RICE UNIVERSITY

Synthesis of Carbon Nanomaterials and Their Applications in the Oilfield

by

Wei Lu

A THESIS SUBMITTED
IN PARTIAL FULFILLMENT OF THE
REQUIREMENTS FOR THE DEGREE

Doctor of Philosophy

APPROVED, THESIS COMMITTEE

James M. Tour, Chair
T. T. and W. F. Chao Professor of
Chemistry, Professor of Mechanical
Engineering & Materials Science and
Professor of Computer Science

W. E. Billups

W. Edward Billups
Professor of Chemistry

Michael S. Wong
Professor of Chemical Engineering and
Professor of Chemistry

HOUSTON, TEXAS
November 2012

ABSTRACT

Synthesis of Carbon Nanomaterials and Their Applications in the Oilfield

by

Wei Lu

This dissertation explores the potential applications of nanotechnology in the oilfield including poly(vinyl alcohol) stabilized carbon black nanoparticles for oil exploration and temperature-responsive carbon black nanoparticles for enhanced oil recovery. Also, it describes the rational design of graphene nanoribbons via intercalating reactive metals into multi-walled carbon nanotubes followed by addition of vinyl monomers or haloalkanes. Efficient production and modification of these aforementioned nanomaterials will make them more attractive for applications in the oilfield and electronics materials.

A method is reported for detecting the hydrocarbon in the porous media with stabilized nanoparticles that are capable of efficiently transporting hydrophobic molecules through oil-containing rocks and selectively releasing them when a hydrocarbon is encountered. Nano-sized carbon black was oxidized and then functionalized with poly(vinyl alcohol) via a coupling reaction between the polymer's hydroxyl groups and the carboxylic groups on oxidized carbon black. Breakthrough curves show that poly(vinyl alcohol)-coated oxidized carbon black was stable in synthetic sea brine at room temperature and could carry the ^{14}C-labeled radioactive tracer 2,2′,5,5′-

tetrachlorobiphenyl through rocks and then released the tracer upon exposure to hydrocarbon.

Due to the temperature-sensitivity of hydrogen bonds, higher molecular weight poly(vinyl alcohol) was used to improve the stability of carbon black nanoparticles in synthetic sea brine at higher temperatures. After sulfation, high molecular weight poly(vinyl alcohol) could stabilized carbon black nanoparticles in American Petroleum Institute standard brine at high temperatures. Those nanoparticles could efficiently transport mass-tagged probe molecules through a variety of oil-field rock types and selectively released the probe molecules into the hydrocarbon-containing rocks. Those proof-of-concept chemical nanoreporters can potentially be used under conditions commonly observed in the reservoir, and aid in the recovery of oil that remains in place.

Amphiphilic carbon nanoparticles have been prepared that are capable of reversibly transferring across the water/oil interface in a temperature-controlled manner. Nano-sized carbon black was oxidized and then functionalized with amphiphilic diblock polyethylene-*b*-poly(ethylene glycol) copolymers that were water-soluble at low-to-moderate temperatures but oil-soluble at higher temperatures. The correlation between the phase transfer temperature and the melting temperature of the hydrophobic block of the copolymers and the weight percent of hydrophilic block were investigated. The amphiphilic nanoparticles were used to stabilize oil droplets for demonstrating potential applications in reducing the water/oil interfacial tension, a key parameter in optimizing crude oil extraction from downhole reservoirs.

Graphene nanoribbons free of oxidized surfaces can be prepared in large batches and 100% yield by splitting multi-walled carbon nanotubes with potassium vapor. If desired, exfoliation is attainable in a subsequent step using chlorosulfonic acid. The low-defect density of these GNRs is indicated by their electrical conductivity, comparable to that of graphene derived from mechanically exfoliated graphite. Additionally, cost-effective and potentially industrially scalable, *in situ* functionalization procedures for preparation of soluble graphene nanoribbons from commercially carbon nanotubes are presented. To make alkane-functionalized graphene nanoribbons, multi-walled carbon nanotubes were intercalated by sodium/potassium alloy under liquid-phase conditions, followed by addition of haloalkanes, while polymer-functionalized graphene nanoribbons were prepared via polymerizing vinyl monomers using potassium-intercalated graphene nanoribbons. The correlation between the splitting of MWCNTs, the intrinsic properties of the intercalants and the degree of graphitization of the starting MWCNTs has also been demonstrated. Those functionalized graphene nanoribbons could have applications in conductive composites, transparent electrodes, transparent heat circuits, and supercapcitors.

Acknowledgments

Earning a Ph.D. in chemistry means a lot to me and this would not have happened without the support of many people I have worked with during my Ph.D. studies at Rice University from 2008 to 2012. I would like to take this opportunity to express my gratitude to the people who have helped me get where I am today.

First of all, I would like to thank my advisor Professor James M. Tour, for giving me the opportunity to join his group and work on exciting projects on nanotechnology for oilfield applications. He not only passed his chemistry knowledge to me but also taught me the importance of presentation. I would also like to thank my committee members, Prof. Michael S. Wong and Prof. W. Edward Billups, for taking time out of their busy schedule to serve on my committee and provide valuable comments and suggestions on my work.

I would also like to express my appreciation to Prof. George Hirasakii, Prof. Clarance Miller, and Maura Puerto who guided me on using appropriate surfactants and polymers for oil recovery and Prof. Mason Tomson and Amy Kan who taught me transport behavior of nanoparticles in the porous media. I am grateful to Prof. Alexander Morgan for use of microcombustion calorimetry and insightful suggestions on developing graphite oxide-based flame retardant additives.

Experimental assistance and training from former and current group members are essential for successful completion of all the research projects I have been involved in. Thank you to Dmitry Kosynki, Jacob Berlin, Jay Lomeda and Amanda Higginbotham for training me on organic chemistry and helpful suggestions. Special thanks should also

be given to Chih-Chau Hwang, Changsheng Xiang, Gedeng Ruan, Zhiwei Peng, Huilong Fei, Daniela Marcano, Gabriel Ceriotti and Loïc Samuel for helping me on the nanoreporter project.

I also benefit a lot from other talented scientists I have worked with on the nanoreporter projects: Jie Yu, Gautam Kini, Ping Zhang and Lunliang Zhang. Thank you to Dustin James and Bo Chen for giving me advice on getting through difficult times before defending my thesis.

Finally, I would like to thank my wife, my parents, my sisters and brothers-in-law for their boundless love and support during my Ph.D. studies. I know that I could not have done it without their endless support and encouragement.

Contents

List of Figures and Schemes

List of Tables

List of Equations

List of Symbols and Abbreviations

ACPA	4,4'-azobis(4-cyanopentanoic acid)
AFM	atomic force microscopy
A-GNRs	alkylated graphene nanoribbons
API	American Petroleum Institute
B-GNRs	butylated-graphene nanoribbons
CCG	chemically converted graphene
CNTs	carbon nanotubes
CVD	chemical vapor deposition
DCC	*N*,*N*'-dicyclohexylcarbodiimide
DLS	dynamic light scattering
DME	1,2-dimethoxyethane
DMF	dimethylformamide
DSC	differential scanning calorimetry
EGA	evolved gas analysis
EOR	enhanced oil recovery
ESI-MS	electrospray mass spectroscopy
fCB	functionalized carbon black
GC-MS	gas chromatography–mass spectrometry
GICs	graphite intercalation compounds
GNRs	graphene nanoribbons
GO	graphene oxide
GONRs	graphene oxide nanoribbons

HD-GNRs	hexadecylated-graphene nanoribbons
H-GNRs	proton functionalized graphene nanoribbons
HsPVA–fCB	highly sulfated polyvinyl alcohol coated functionalized carbon black
LsPVA–fCB	lightly sulfated polyvinyl alcohol coated functionalized carbon black
MAS	magic angle spinning
MWCNTs	multi-walled carbon nanotubes
NMR	nuclear magnetic resonance
NPs	nanoparticles
NTL	Nanotech Laboratories, Inc.
OCB	oxidized carbon black
O-GNRs	octylated-graphene nanoribbons
PAHs	polycyclic aromatic hydrocarbons
PCB	2,2',5,5'-tetrachlorobiphenyl
PCB*	^{14}C-labeled 2,2',5,5'-tetrachlorobiphenyl
PCB*/PVA-OCB	^{14}C-labeled 2,2',5,5'-tetrachlorobiphenyl loaded polyvinyl alcohol-functionalized oxidized carbon black
PE	polyethylene
PE-*b*-PEG	polyethylene-*b*-poly(ethylene glycol)
PE-*b*-PEG-OCB	polyethylene-*b*-poly(ethylene glycol) coated oxidized carbon black
PEG	polyethylene glycol
PEG-HCCs	polyethylene glycol-functionalized hydrophilic carbon clusters

PF-GNRs	polymer-functionalized graphene nanoribbons
PTFE	polytetrafluoroethylene
PVA	polyvinyl alcohol
PVA-OCB	polyvinyl alcohol-functionalized oxidized carbon black
PVs	pore volumes
QMS	quadrupole mass spectrometer
sPVA	sulfated polyvinyl alcohol
sPVA–fCBs	sulfated polyvinyl alcohol coated functionalized carbon black
SS NMR	solid-state ^{13}C nuclear magnetic resonance spectroscopy
SWCNTs	single-walled carbon nanotubes
TEM	transmission electron microscopy
TG/MS	thermogravimetric mass spectrometry
THA	triheptylamine
THA/sPVA–fCBs	triheptylamine loaded sulfated polyvinyl alcohol coated functionalized carbon black
THF	tetrahydrofuran
XRD	X-ray powder diffraction
XPS	X-ray photoelectron spectroscopy

Chapter 1

Engineered Nanoparticles for Hydrocarbon Detection in Oil-field Rocks

This chapter was entirely copied from the reference #1 of this section

1.1. Introduction

Worldwide energy demand continues to increase at a rapid pace. In time, it is desirable to find alternative energy sources to meet this demand, but in the near-term there is a pressing need for improved downhole oil identification. Tracers have long been used to map entry/exit well correlations in the oil-field, but they do not provide any information about the environment between the entry and exit locations. Here we show that nanoparticles can be engineered to detect hydrocarbons in oil-field rocks. These nanoparticles could be used as second generation tracers that not only provide entry/exit

correlations but also indicate whether or not it is worth attempting to recover oil from that area. This is of overarching significance and could have enormous economic impact as oil-fields become more mature and the easily extracted oil is no longer available. Improved methods of assessment of the nano-sized domains within oil-field environments and between drill-holes in particular could have a profound impact in recovery processes. In addition, this detection ability could also be used in contaminated areas.

The transport of small hydrophobic organic molecules through porous media has been studied for many years. In isolation, these hydrophobic molecules adsorb very strongly to nearly all types of soil. However, it has been observed that these hydrophobic chemicals disperse more broadly in the environment than would be expected based on their strong affinity for binding to soil.[2] One possible explanation for this behavior is that organic macromolecules, which possess amphiphilic characteristics, may sequester the hydrophobic small molecules and facilitate their transport by carrying them within the macromolecule.[3,4] Laboratory scale experiments have demonstrated this effect, with some cases, such as the use of β-cyclodextrin, showing highly efficient transport of a variety of hydrophobic aromatic molecules through soil.[5,6] However, selective release of the transported cargo has not been reported and β-cyclodextrin only forms 1 : 1 inclusion complexes with its hydrophobic cargo.

Recently, a new class of compounds, nanomaterials, has been investigated for transport through porous media. Nanomaterials are defined as having at least one dimension of less than 100 nm, and they possess a much larger surface area relative to traditional polymers used for the transport of hydrophobic cargo. Nanomaterials are

expected to have significantly different transport behavior in porous media as a result of their larger size and more rigid shape as compared to polymers, and the design of nanoparticles (NPs) with efficient subsurface transport is an ongoing challenge. Nanomaterials prepared from a variety of precursors, including carbon, iron and silica, have varying abilities to flow through porous media. Water-dispersible aggregates of [C60]fullerenes can flow through sand samples and glass beads, although the breakthrough of the fullerenes is very low at early pore volumes and gradually increases over time.[7,8] The use of a water-soluble fullerene derivative, as opposed to the water dispersible aggregates, showed improved breakthrough for a column of glass beads.[9] Single-walled carbon nanotubes (SWCNTs), which are also prone to aggregation, show limited breakthrough in porous media.[10] Reducing the SWCNTs ability to aggregate by wrapping them with a surfactant or binding humic acid to them improves their mobility in porous media.[11] Similar behavior has been observed for silica and iron, as functionalization of the particles with a hydrophilic polymer, either polyethylene glycol (PEG) or carboxymethyl cellulose, reduces their affinity for aggregation and improves their transport through porous media.[12–15]

We have recently developed NPs with rigid cores of less than 40 nm in length and 1 nm wide consisting of PEG-functionalized hydrophilic carbon clusters (collectively, PEG-HCCs). HCCs are prepared from SWCNTs through a harsh oxidation procedure wherein they become highly oxidized, yet they retain some hydrophobic domains.[16,17] Covalently attaching PEG by coupling polymer chains to many of the carboxylic acids on the surface of the HCCs renders the particles soluble in aqueous solutions.[18] Hydrophobic compounds introduced into an aqueous solution of PEG-HCCs are sequestered on the

hydrophobic domains of the HCC core. This technique was used to load the PEG-HCCs with the hydrophobic chemotherapy drug paclitaxel and deliver it in vivo.[19]

Here we show that this basic design of sequestering a hydrophobic compound in a NP composed of an oxidized carbon core and a polymer shell can be extended to efficiently transport hydrophobic compounds through oil-field rocks and selectively release them when the rock contains oil. In particular, using oxidized carbon black (OCB) as the core and polyvinyl alcohol (PVA) as the shell, efficient transport and selective release of 2,2',5,5'-tetrachlorobiphenyl (PCB) is demonstrated. This NP, PVA-OCB, can be produced on large scale and is expected to be environmentally benign though their environmental fate has not yet been assessed. PVA is biodegradable,[20] and carbon black is naturally abundant in the environment.[21] These readily-prepared NPs bearing cargo could be injected into the subsurface and then recovered and analyzed for the presence of the cargo; release of the cargo would indicate the presence of oil. When used in this manner, the NPs can be described as nanoreporters (Figure 1.1).

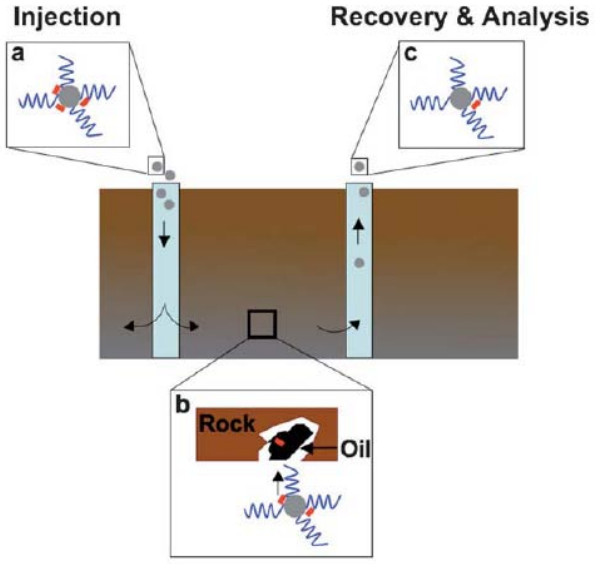

Figure 1.1 Schematic of oil detection by nanoreporters. (a) PVA-OCB NPs (grey circle with blue lines radiating) carrying hydrophobic cargo (red rectangles) are injected into the subsurface. (b) While flowing through the subsurface, the nanoreporters encounter oil and release their hydrophobic cargo into the oil. (c) The nanoreporters are recovered and analyzed for the presence of the cargo; the extent of the cargo's absence in the PVA-OCB indicates the extent of subsurface oil.

1.2. Experimental Procedures

The detailed experimental procedures are provided in Appendix A.

1.3. Results and Discussion

The study was initiated by analyzing the breakthrough of PEG-HCCs in different oil-field rock types. Most previous NP breakthrough studies were done in negatively charged model porous media, such as glass beads and sand. In this paper, we selected two natural rocks for initial study: Berea sandstone and dolomite from an oil-field in Kuwait, in order to evaluate our NPs in a more realistic and more challenging environment. Sandstone is predominantly silica mineral that is negatively charged at neutral pH, but dolomite is a carbonaceous rock, rich in calcium and magnesium, with a net positive charge.[22] Both rock types are common in oil-rich environments. The materials used in this work were obtained from actual field samples. In order to test the flow properties of PEG-HCCs through these materials, the two rock types were separately ground and sieved to provide ~106–250 mm particles that were packed into a glass column. When each packed column was prepared, the volume of liquid contained in the fully saturated

column (the pore volume) was determined. The efficiency of nanomaterial breakthrough was determined by measuring the concentration of nanomaterial in the effluent relative to the concentration in the influent as a function of the amount of solution passed through the column, measured in pore volumes. All of the NPs were injected at a concentration of 20 ppm. A synthetic brine solution designed to be equivalent to seawater was chosen as the aqueous carrier solution for the PEG-HCCs, as seawater is the most commonly used aqueous solution for oil-field work. PEG-HCCs in a seawater solution were able to breakthrough in both rock types (Figure 1.2). While the breakthrough in sandstone

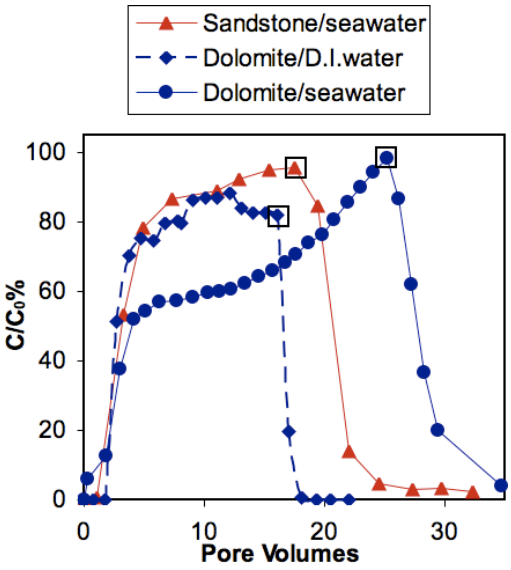

Figure 1.2 Breakthrough of PEG-HCCs in sandstone and dolomite. The percentage of PEG-HCCs in the effluent relative to the influent, as determined by UV absorbance. The black boxes indicate when the flow was switched from the PEG-HCC solution to deionized (DI) water or seawater.

quickly reached greater than 80%, the breakthrough in dolomite initially reached only 60% and then very slowly increased to complete breakthrough. Performing the dolomite

experiment using deionized (DI) water instead of seawater as the aqueous carrier for the PEG-HCCs resulted in rapid breakthrough to an extent >80%. The gradual increase in breakthrough over time when seawater is used and the improved breakthrough in DI water suggests that a significant factor for the retarded breakthrough in dolomite is surface interactions between the PEG-HCCs, the salts in solution and the dolomite surface. The zeta potential of the PEG-HCCs was -35 mV, consistent with carboxylic acids remaining on the surface of the HCC cores. These may be forming the bridging interactions.

In order to improve the breakthrough of the NPs, the polymer shell was changed from PEG to PVA (Scheme 1.1, note only one of each functional group on the HCC core is shown). Fewer carboxylic acids should be left on the HCC core after coupling to PVA as compared to PEG, as for similar levels of polymer coverage, the PVA has many more hydroxyl groups available for coupling. Indeed, the zeta potential of PVA-HCCs was found to be -20 mV as compared to the -35 mV for PEG-HCCs, suggesting that fewer free carboxylic acids remain.

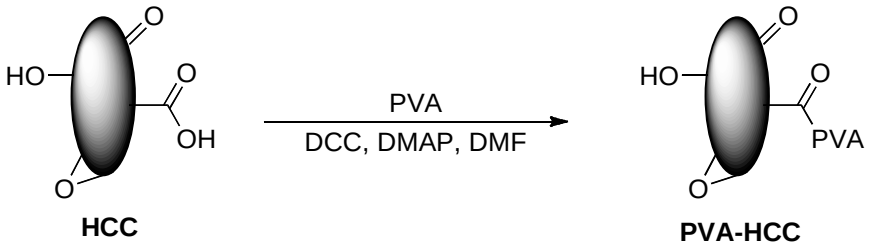

Scheme 1.1 Preparation of PVA-HCC.

If used quickly after being prepared, PVA-HCCs showed comparable breakthrough in sandstone and dramatically improved breakthrough in dolomite relative to PEG-HCCs (Figure 1.3). However, if the NPs were stored for 8 d in the seawater

solution and then used, the breakthrough in dolomite became significantly retarded.

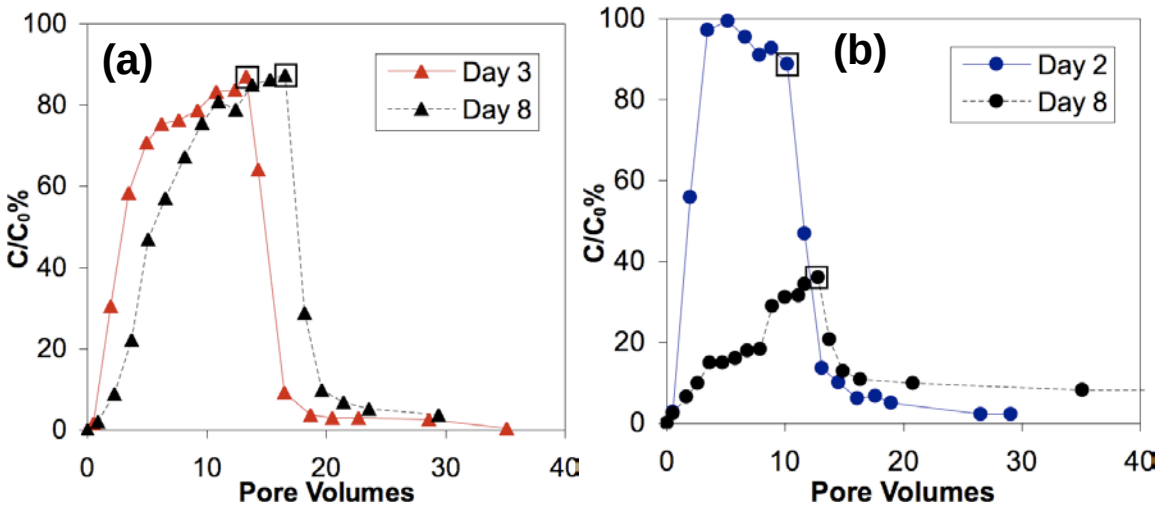

Figure 1.3 (a) Measurement of PVA-HCCs flowing through sandstone. (b) Measurement of PVA-HCCs flowing through dolomite. Between the early experiments and those on day 8, the seawater solution of PVAHCCs was allowed to stand at room temperature. The black boxes indicate that the flow was switched from the PEG-HCC solution to pure synthetic seawater.

In an effort to reduce the NPs aggregation, several alternative carbon nanomaterials were evaluated for use as the core of the NPs, including graphene oxide nanoribbons,[23] graphene oxide flakes[24] and oxidized carbon black (OCB). The graphene materials showed significantly reduced breakthrough (See Appendix A), but the OCB-containing NPs demonstrated efficient breakthrough, improved stability in seawater and the ability to transport and selectively release a hydrophobic reporter molecule. OCB was

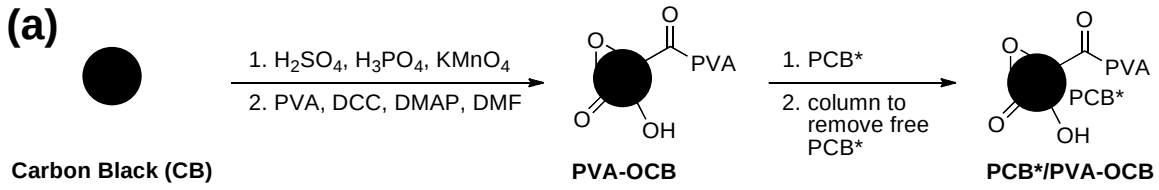

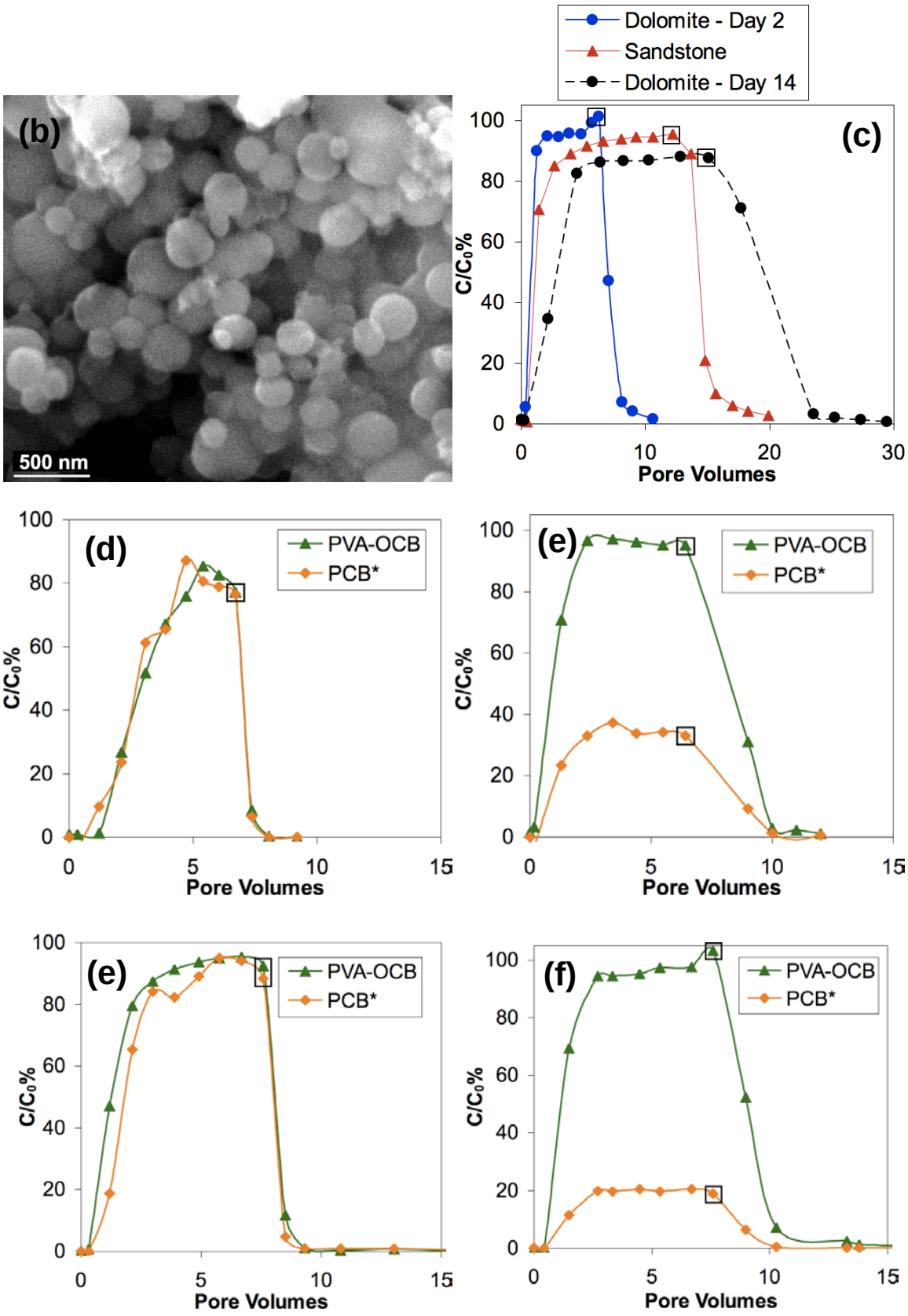
(b)
500 nm
Dolomite - Day 2
Sandstone
Dolomite - Day 14
(c)
C/C0%
Pore Volumes
(d)
PVA-OCB
PCB*
C/C0%
Pore Volumes
(e)
PVA-OCB
PCB*
C/C0%
Pore Volumes
(e)
PVA-OCB
PCB*
C/C0%
Pore Volumes
(f)
PVA-OCB
PCB*
C/C0%
Pore Volumes

Figure 1.4 (a) Synthesis of PVA-OCB and sequestration of PCB*. (b) SEM of PVA-OCB. (c) Breakthrough of PVA-OCBs in sandstone and dolomite immediately after preparation and after 14 d. Breakthrough for both components of PCB*/PVA-OCBs in (d) sandstone, (e) isooctane-containing sandstone, (f) calcite and (g) oil-containing dolomite. The black boxes indicate that the flow was switched from the PEG-HCC solution to pure synthetic seawater.

prepared by treating carbon black with H_2SO_4, H_3PO_4 and $KMnO_4$, an oxidation procedure we recently developed for the preparation of graphene oxide and graphene oxide nanoribbons (Figure 1.4a).[23,24] The OCBs were significantly less oxidized than the HCCs, as the weight loss during thermogravimetric analysis (TGA), which is indicative of the level of oxygen content, was only 17% for OCB while 58% for the HCCs. 2,000 molecular weight (M_W) PVA was coupled to the OCB to provide PVA-OCB particles that were 150 nm in diameter in deionized water as determined by dynamic light scattering. PVA-OCB maintains the spherical shape characteristic of carbon black (Figure 1.4b). When used immediately after preparation, PVA-OCB demonstrated excellent breakthrough in sandstone and dolomite, and even after being left in a seawater solution for 14 d, they demonstrated good breakthrough in dolomite (Figure 1.4c). This is a major improvement over all of the other NPs tested.

The granular filler in the columns had a size from 106 to 250 μm and the porosity was 0.52 for the sandstone column and 0.67 for the dolomite column, suggesting that the pore sizes were tens of microns. Since all of the NPs are significantly smaller than that and were filtered through a 0.45 μm filter prior to introduction to the columns, it is

unlikely that straining of individual NPs is responsible for the different breakthrough properties of the PEG-HCCs, PVA-HCCs and PVA-OCBs in sandstone and dolomite. Instead, NP aggregation plays a large role as this is an equilibrium phenomenon, so even after filtration, larger aggregates can be reformed. Breakthrough is likely reduced by NP aggregates being strained by the columns.[25,26] The retention of NP aggregates blocks smaller pores in the columns resulting in the increased breakthrough seen over time for many conditions. The presence of salt ions promotes aggregation for oxidized carbon nanomaterials, explaining the improved breakthrough when DI water is used instead of seawater. The tendency of these carbon-based NPs to aggregate in the presence of salt ions is a materials property that can be controlled by judicious choice of the polymer coating. The aggregates are also generally retained more by the dolomite than the sandstone, as the dolomite is carbonaceous and can form bridging interactions with the salt ions that are part of the aggregates.

PVA-OCBs can be used as nanoreporters by loading them with hydrophobic cargo and selectively releasing the cargo when the oil-field rock contains hydrocarbons. ^{14}C-labeled 2,2',5,5'-tetrachlorobiphenyl (PCB*) was selected as a model compound because it is extremely hydrophobic, and we have extensive experience monitoring its interaction with porous media. The PCB* was adsorbed onto the PVA-OCBs by mixing them together in synthetic seawater, allowing the solution to equilibrate at 4 ^{o}C and then passing it through a PD-10 desalting column to remove any unbound PCB* (Figure 1.4a, adsorbed formulation PCB*/PVA-OCB). The PCB*/PVA-OCBs were flowed through a sandstone column, and the two components of the nanoreporter were independently monitored; the PCB* in the effluent was measured by its

radioactivity while the PVA-OCB was measured by its UV absorbance at 280 nm (Figure 1.4d). Almost none of the PCB was lost from the PVA-OCBs, as the two measurements of concentration were equal throughout the experiment. Control experiments using just a solution of PCB* or PCB* mixed with PVA showed very low levels of PCB* transport through the sandstone (See Appendix A), indicating that the OCB core of the NPs is required for the efficient transport of PCB*. In order to demonstrate the principle of selective release, a sandstone column was prepared impregnated with 12 wt% of isooctane. When the PCB/PVA-OCBs were flowed through this column, a significant amount of the PCB* was released (Figure 1.4e). In this model system, the PVA-OCBs efficiently transported the hydrophobic reporter molecule through the bare rock and released the reporter molecule when the rock contained oil. A more realistic system with a much reduced amount of hydrophobic organic content was also studied. PCB*/PVA-OCBs were flowed through Iceland spar calcite, a representative carbonaceous material with no bound organic material, and again very little of the PCB* was released (Figure 1.4f). The PCB*/PVA-OCBs were then passed through dolomite from an actual oil reservoir in Kuwait that had been washed with toluene and contained only 0.8 wt% oil, and 80% of the PCB* was released (Figure 1.4g). Thus, hydrocarbons in oil-field rocks can be detected by measuring the amount of hydrophobic cargo our NPs transport through the rocks.

The exact process for PCB* partitioning from PVA-OCBs to the oil phase is ambiguous at this stage. While the adsorption of PCB* onto PVA-OCBs is very strong, there will always be an equilibrium with a small amount of the PCB* desorbed into the surrounding environment. We have previously observed this adsorption/desorption

phenomenon for naphthalene with fullerene NP.[27,28] It is likely that the presence of organic matter (isooctane or crude oil in this study) causes the small amount of desorbed PCB* to partition into the organic phase. This dramatically shifts the equilibrium and results in the unloading of most of the PCB* from the PVA-OCB into the organic phase. This is supported by the fact that for the dolomite column containing crude oil, the total organic content in the column was less than the amount of PVA-OCBs added, but most of PCB* partitioned away from the NPs. Since the PVA-OCBs are soluble in aqueous solutions, but nearly insoluble in organic media, such as isooctane or crude oil, it is likely that when they are at the oil–water interface, they remain in the water. This allows for the efficient recovery observed for the NPs.

1.4. Conclusions

The ability to efficiently transport a hydrophobic molecule through oil-field rock and selectively release it when a hydrocarbon is encountered has potential applications in oil detection down hole. Clearly, PCB* was used only as a proof-of-principle cargo, and much of the benefit of the technique will be realized by selecting appropriate cargo to be transported and released. Oil could be detected by passing reporter-loaded NPs through an area of interest and then recovering the NPs and analyzing them for the amount of reporter retained. This cargo-carrying methodology could also potentially be applied to contaminated subsurface areas where remediation could occur by transporting an agent to assist in the decomposition or removal of hydrophobic pollutants.

1.5. Acknowledgements

We are grateful to the Advanced Energy Consortium (Baker Hughes, Halliburton, Conoco Phillips, BP, OXY, Marathon, Shell, Total, Petrobras, Schlumberger) for financial support.

1.6. References

1. Berlin, J. M.; Yu, J.; Lu, W.; Walsh, E. E.; Zhang, L; Zhang, P.; Chen, W.; Kan, A. T.; Wong, M. S.; Tomson, M. B.; Tour, J. M. *Energy Environ. Sci.,* **2011**, *4*, 505-509.
2. Baker, J. E.; Capel, P. D.; Eisenreich, S. J. *Environ. Sci. Technol.*, **1986**, *20*, 1136-1143.
3. McCarthy, J. F.; Zachara, J. M. *Environ. Sci. Technol.*, **1989**, *23*, 496-502.
4. Enfield, C. G.; Bengtsson, G. *Ground Water*, **1988**, *26*, 64-70.
5. Brussea, M. L.; Wang, X.; Hu, Q. *Environ. Sci. Technol.*, **1994**, *28*, 952-956.
6. Magee, B. R.; Lion, L. W.; Lemley, A. T.; *Environ. Sci. Technol.*, **1991**, *25*, 323-331.
7. Wang, Y.; Li, Y.; Fortner, J. D.; Hughes, J. B.; Abriola, L. M.; Pennell, K. D. *Environ. Sci. Technol.*, **2008**, *42*, 3588-3594.
8. Li, Y.; Wang, Y.; Pennell, K. D.; Abriola, L. M. *Environ. Sci. Technol.*, **2008**, *42*, 7174-7180.
9. Lecoanet, H. F.; Bottero, J.-Y.; Wiesner, M. R. *Environ. Sci. Technol.*, **2004**, *38*, 5164-5169.
10. Jaisi, D. P.; Elimelech, M.; *Environ. Sci. Technol.*, **2009**, *43*, 9161-9166.

11. Wang, P.; Shi, Q.; Liang, H.; Steuerman, D. W.; Stucky, G. G.; Keller, A. A. *Small*, **2008**, *4*, 2166-2170.

12. Lenhart, J. J.; Saiers, J. E. *Environ. Sci. Technol.,* **2002**, *36*, 769-777.

13. Rodriguez, E.; Roberts, M. R.; Yu, H.; Huh, C.; Bryant, S. L. *SPE Annual Technical Conference*, **2009,** SPE 124418.

14. He. F.; Zhang, M.; Qian, T.; Zhao, D. *J. Colloid Interface Sci.,* **2009**, *334*, 96-102.

15. Saleh, N.; Sirk, K.; Liu, Y.; Phenrat, T.; Dufour, B.; Matyjaszewski, K.; Tilton, R. D.; Lowry, G. V. *Environ. Eng. Sci.,* **2007**, *24*, 45-57.

16. Chen, Z.; Kobashi, K.; Rauwald, U.; Booker, R.; Fan, H.; Hwang, W.-F.; Tour, J. M. *J. Am. Chem. Soc.,* **2006**, *128*, 10568-10571.

17. Price, B. K.; Lomeda, J. R.; Tour, J. M. *Chem. Mater.,* **2009,** *21,* 3917-3923.

18. Stephenson, J. J.; Hudson, J. L.; Leonard, A. D.; Price, B. P.; Tour, J. M. *Chem. Mater.,* **2007**, *19*, 3491-3498.

19. Berlin, J. M.; Leonard, A. D.; Pham, T. T.; Daisuke, S.; Marcano, D. C.; Yan, S.; Fiorentino, S.; Milas, Z. L.; Kosynkin, D. V.; Price, B. K.; Lucente-Shultz, R. M.; Wen, X.; Raso, M. G.; Craig, S. L.; Tran, H. T.; Myers, J. N.; Tour, J. M. .*ACS Nano,* **2010**, *4*, 4621-4636.

20. Chiellini, E.; Corti, A.; D'Antone, S.; Solaro, R. *Prog. Polym. Sci.,* **2003**, *28*, 963–1014.

21. Nguyen, B. T.; Lehmann, J.; Kinyangi, J.; Smernik, R.; Riha, S. J.; Engelhard, M. H. *Biogeochemistry,* **2009**, *92*, 163-176.

22. Kan, A. T.; Yan, L.; Bedient, P. B.; Oddo, J. E.; Tomson, M. B. *SPE,* **1991,** 747, SPE 21714.

23. Higginbothan, A. L.; Kosynkin, D. V.; Sinitskii, A.; Sun, Z.; Tour, J. M. *ACS Nano*, **2010**, *4*, 2059-2069.

24. Marcano, D. M.; Kosynkin, D. V.; Berlin, J. M.; Sinitskii, A.; Sun, Z.; Alemany, L. B.; Lu, W.; Tour, J. M. *ACS Nano,* **2010**, *4*, 4806-4814.

25. Jaisi, D. P.; Elimelech, M. *Environ. Sci. Technol.,* **2009**, *43*, 9161-9166.

26. Elimelech, M.; Gregory, J.; Jia, X.; Williams, R. A. *Particle Deposition and Aggregation - Measurement, Modeling and Simulation*. Elsevier; 1998.

27. Cheng, X. K.; Kan, A. T.; Tomson, M. B. *J. Chem. Eng. Data,* **2004**, *49*, 675–683.

28. Cheng, X. K.; Kan, A. T.; Tomson, M. B. *J. Mater. Res.;* **2005**, *20*, 3244-3254.

1.7. Experimental Contributions

My contribution to the experimental work in this chapter is the following: experiment design and preparation of PVA-OCB NPs and characterization of those nanoparticles by Raman, TGA, SEM, XPS, and UV spectroscopy. Dr. Jie Yu built the column and studied the transport behavior of PVA-OCB NPs. Dr. Jacob M. Berlin assisted in interpretation of the data analysis. Assistance in column studies and preparation of PVA-OCB NPs was received from Lunliang Zhang, Ping Zhang and Erin E. Walsh.

Chapter 2

Highly Stable Carbon Nanoparticles Designed for Downhole Hydrocarbon Detection

This chapter was entirely copied from Reference #1 of this section

2.1. Introduction

As energy demand continues to increase it is desirable to produce as much oil as possible from existing and new oil wells. Tracers have long been used to map entry/exit well correlations in the oil-field, but they do not provide any information about the environment between the entry and exit locations. Here we show that nanoparticles possessing functionalized carbon black (fCB) cores and sulfated polyvinyl alcohol (sPVA) addends were designed to transport hydrocarbon detection molecules through subsurface rock formations. The sPVA–fCBs are stable under high-temperature and

salinity conditions and are transported through a variety of oilfield rock types. A non-radioactive probe molecule that is easily detectable by mass spectrometry, triheptylamine (THA), was adsorbed onto the sPVA–fCBs. The THA was selectively released when the nanoparticles were passed through a column of isooctane-containing crushed rock, providing both entry and exit correlations and a measure of oil content. This study simulates detection and quantitative analysis of the hydrocarbon content in downhole rock formations, which is a critically needed assessment in older oilfields.

Nanomaterials have a much larger surface area relative to traditional polymers presently used for the transport of hydrophobic cargo and are expected to have significantly different transport behavior in porous media as a result of their more rigid structures.[2] The design of nanoparticles (NPs) with efficient terrestrial subsurface transport is an ongoing challenge. For example, water-dispersible aggregates of C_{60} fullerenes can flow through sand samples and glass beads, but the breakthrough of the fullerenes is very low at early pore volumes and gradually increases over time.[2,3] The use of a water-soluble fullerene derivative, as opposed to the water-dispersible aggregates, showed improved breakthrough for a column of glass beads.[4] Single-walled carbon nanotubes (SWCNTs) can also be either wrapped by a surfactant or bound with humic acid, improving their mobility in porous media.[5] Similar behavior has been observed for silica and iron, as functionalization of the particles with a hydrophilic polymer, either polyethylene glycol (PEG) or carboxymethyl cellulose, reduces their affinity for aggregation and improves their transport through porous media.[6–9]

Injection of NPs through downhole porous media represents an innovative approach for subsurface oil detection and enhanced oil recovery (EOR) due to their

unique transport properties.[10,11] We have evaluated several alternative carbon materials for use as the core of the NPs to deliver probe molecules to downhole rocks, including graphene oxide nanoribbons,[12] graphene oxide flakes,[13] carbon nanotubes and oxidized carbon black (OCB).[14] The latter structure, OCB, is derived from the readily available and non-toxic carbon black, making it most attractive. Furthermore, the polyvinyl alcohol modified OCB (PVA–OCB) NPs demonstrated the best breakthrough efficiency and stability in seawater. Unfortunately, they still suffered from thermal stability problems, such as being prone to agglomeration in seawater at higher temperatures (70 ºC), and they also demonstrated poor breakthrough efficiency in certain charged porous media such as dolomite and calcite rocks.[14] Therefore, designing alternative NPs that can simultaneously endure high temperature and high salinity, and are capable of being transported through a variety of porous media, is an important goal.

One possible method to enhance the thermal stability of the PVA–OCB NPs was to choose appropriately sized molecular weight PVA for functionalization, thereby keeping the PVA–OCB NPs stable at higher temperature. Since different rocks have different surface properties, the negatively charged OCB NPs demonstrated lower mobility in positively charged porous media such as dolomite or calcite rocks. Instead of OCB-containing NPs, our approach here to solving the mobility problem is to use a carboxyl group-functionalized carbon black (fCB) as the NP core. The fCB is less oxidized than the OCB core, resulting in a surface charge close to zero for fCB-containing NPs in neutral aqueous solution. Thus the PVA-modified fCB exhibits improved performance when moving through charged rocks. Because ionic surfactants are not as temperature sensitive as non-ionic surfactants,[15] the PVA–fCB NPs were also

sulfated to provide NPs with slightly ionic properties. Sulfated PVA–fCB (sPVA–fCB) NPs used here show tolerance against agglomerating under high temperature and high salinity conditions, and are capable of breaking through most subsurface rocks such as sandstone, dolomite and calcite. This finding is extraordinary and it has implications in downhole oil detection, enhanced oil recovery and environmental remediation of organic-contaminated land.

Radioactive 2,2',5,5'-tetrachlorobiphenyl (PCB*) was used in our first laboratory simulations of hydrocarbon detection by PVA–OCBs,[14] however the use of PCB* in the field is unacceptable.[16] Thus in the present research, triheptylamine (THA) was used instead of PCB*. The THA/sPVA–fCBs (here we use the convention that ‘‘/’’ indicates a non-covalent attachment while ‘‘–’’ indicates a covalent attachment) were found to efficiently transport THA through columns that simulate subsurface formations and selectively release the THA into hydrocarbon containing rocks. THA/sPVA–fCBs could be used as second generation nanoreporters that not only provide subsurface formation entry/exit correlations but also an assessment of stranded downhole oil content.

2.2. Experimental Procedures

The detailed experimental procedures are provided in Appendix B.

2.3. Results and Discussion

Oil production can be enhanced if the degree of oil content in the downhole environment can be determined. Presently, the oil industry uses ‘‘tracers’’ which only give information regarding entry and exit locations, but no information regarding

downhole oil content. Our recently disclosed approach was the injection of a nanoreporter into the subsurface formation that would be recovered at the production well and analyzed for information about the subsurface oil content.[14] Figure 2.1 outlines the use of a nanoreporter that can be extended to efficiently transport hydrophobic compounds (probe molecules) through rock formations followed by selectively releasing them when the rock contains oil. The hydrophobic compound serves as a probe during its

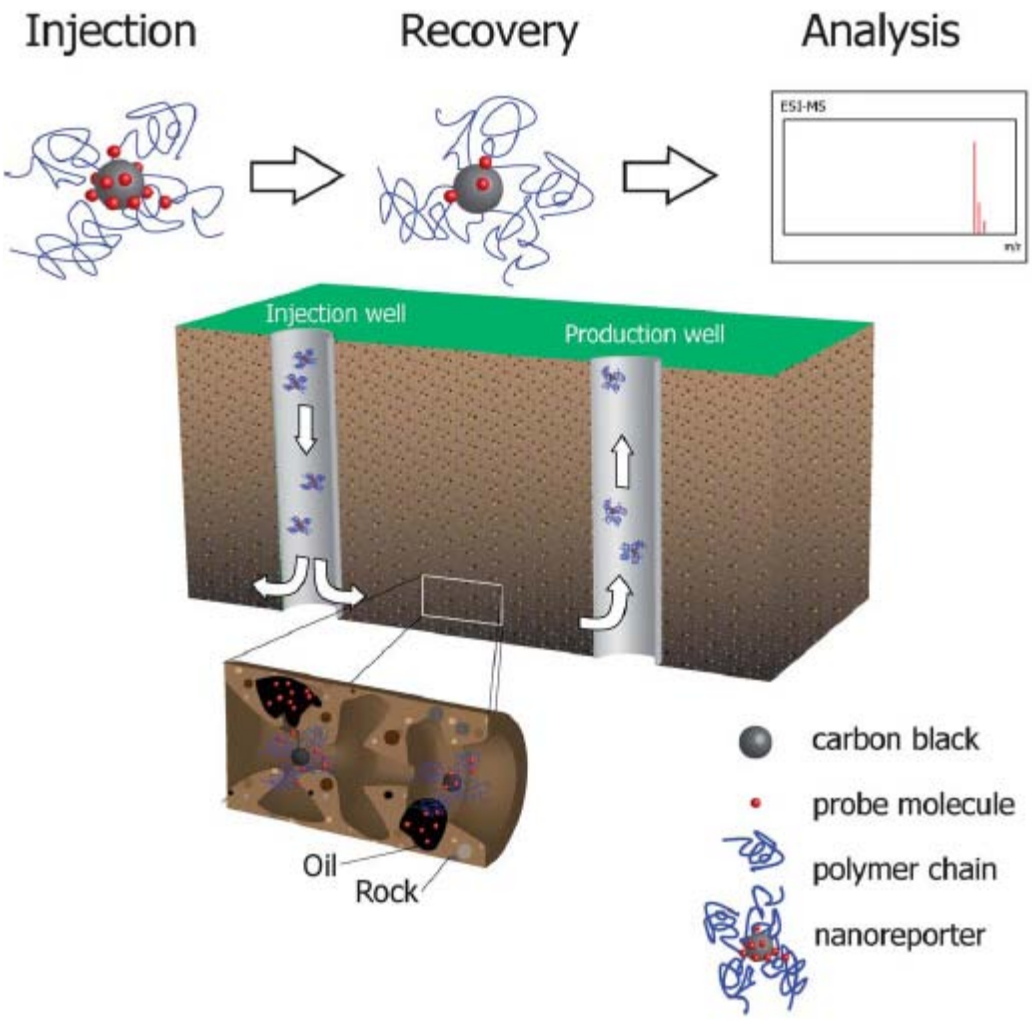

Figure 2.1 Schematic diagram of subsurface oil detection by nanoreporters. Nanoreporters transport probe molecules through downhole rocks followed by selectively

releasing them when the rock contains oil. The interrogation of the nanoreporter at the production well will give quantitative information of the oil content based upon the amount of the probe molecule remaining on the nanoreporter.

downhole journey, reflecting the oil content in the oilfield rocks. If more oil is present, more probe molecules are released from the nanoreporter, and interrogation of the nanoreporter at the production site will give quantitative information regarding the oil content based upon the amount of probe molecules remaining on the nanoreporter. To develop a useful nanoreporter, the carrier should be stable to the subsurface conditions, able to endure harsh conditions such as high temperatures and salinities and should have mobility through different rocks.

Accordingly, a new type of NP was designed and synthesized to solve the problem that the OCB-containing NPs had relatively poorer mobility in positively charged rocks such as dolomite or calcite due to electrostatic attraction. Since the CB lacks active groups on its surface, it is difficult to directly graft polymers onto its surface without any pretreatment. Hence, a radical initiator 4,4'-azobis(4-cyanopentanoic acid) (ACPA) was used to introduce carboxyl groups onto the CB, forming carboxyl group functionalized CB (fCB) (Scheme 2.1a).[17] The grafting of PVA onto the fCB surface was achieved by the condensation of hydroxyl groups of the PVA with carboxyl groups on the fCB using a *N*,*N*'-dicyclohexylcarbodiimide (DCC) coupling reaction (Scheme 2.1b). Unbound PVA was removed after dialysis against running DI water. Finally the PVA-grafted fCB (PVA–fCB) was obtained.

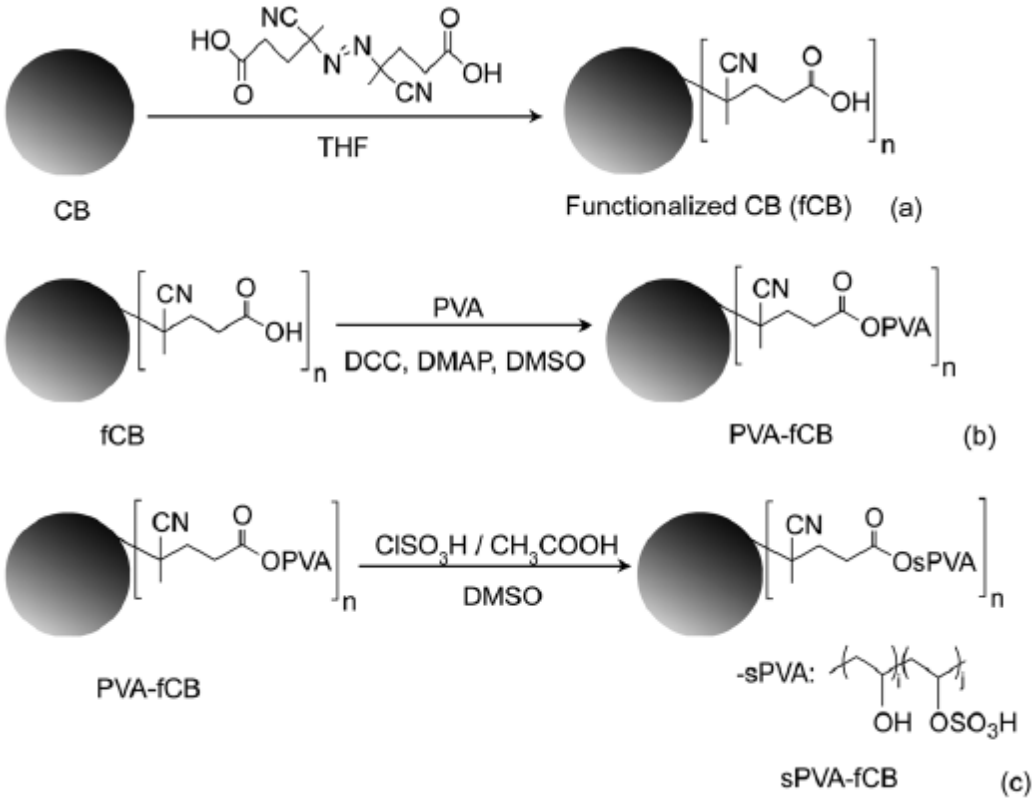

Scheme 2.1 Synthesis of (a) functionalized carbon black (fCB); (b) PVAmodified fCB (PVA–fCB) and (c) sulfated PVA–fCB (sPVA–fCB). Sulfation yields units with -OSO_3H pendants. The particle size of the carbon black is ~15 nm.

For optimization, we further changed the surface properties of the PVA–fCB NP by sulfation (Scheme 2.1c).[18] It has been demonstrated that sulfation could significantly improve the stability of surfactants in high-temperature and high-salinity environments.[19] Here, 3.0 mL 1 M $ClSO_3H$ was added to the as-synthesized PVA–fCB in DMSO and then the mixture was heated at 60 ºC for 30 min to obtain lightly sulfated PVA–fCB (LsPVA–fCB). Highly sulfated PVA–fCB (HsPVA–fCB) was prepared by adding 4.5 mL 1 M ClSO3H and heating for 60 min at 75 ºC.

Figure 2.2 shows ATR-IR and XPS spectra for the PVA(50k)–fCB NPs before and after sulfation. In addition to the vibrational bands that are in common, such as ν_{O-H} and ν_{C-H}, the peaks at 1024 cm^{-1}, which are only found in the LsPVA(50k)–fCB and the HsPVA(50k)–fCB, are attributed to S=O stretching from the sulfated PVA.[18] The peak intensity then reflects the different extent of sulfation. The S2p XPS spectra of the LsPVA–fCB and the HsPVA–fCB is further evidence that the HsPVA–fCB has almost twice the sulfur content of the LsPVA–fCB (2.2 atomic% vs. 1.3 atomic%, respectively, Figure 2.2e and f, insets).

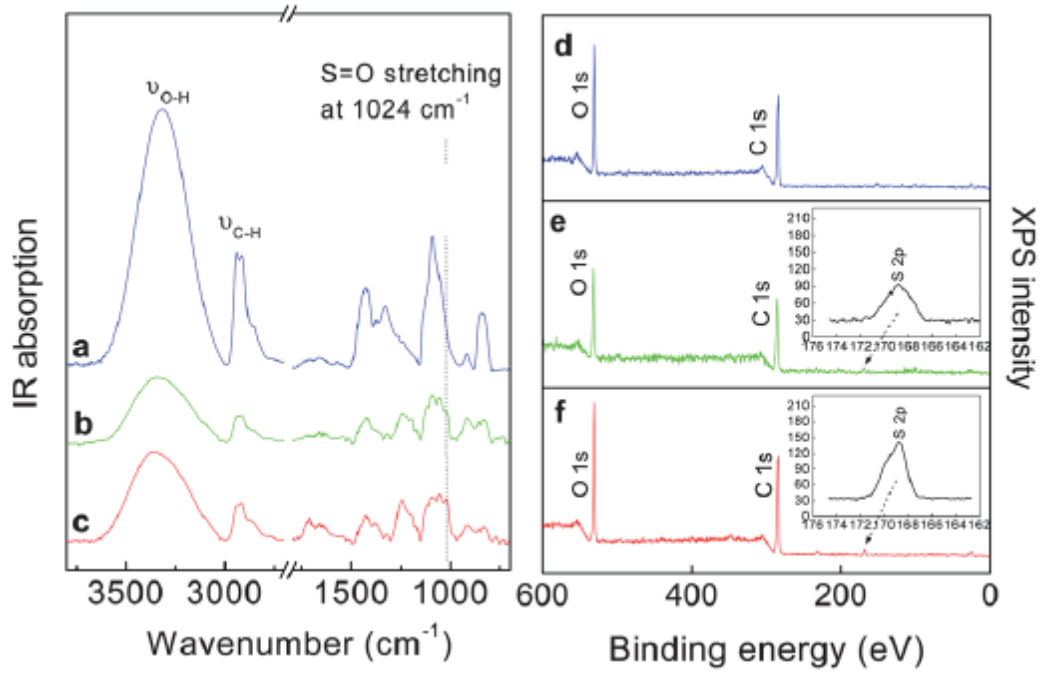

Figure 2.2 ATR-IR spectra of the (a) PVA(50k)–fCB; (b) LsPVA(50k)–fCB and (c) HsPVA(50k)–fCB. XPS spectra of (d) the PVA(50k)–fCB; (e) LsPVA(50k)–fCB; and (f) HsPVA(50k)–fCB. The insets in (e) and (f) are the high resolution S2p XPS spectra of LsPVA(50k)–fCB and HsPVA(50k)–fCB NPs, respectively. All XPS peaks were referenced to the C=C peak at 284.8 eV.

Thermogravimetric analysis (TGA) can be further used to provide evidence for PVA or sPVA on the fCB core. Figure 2.3 shows typical TGA plots from the LsPVA(50k)–fCB, the HsPVA(50k)– fCB and the PVA(50k)–fCB NPs. Prior to running the TGA, the NPs were heated at 120 ºC to remove adsorbed water and then cooled to 30

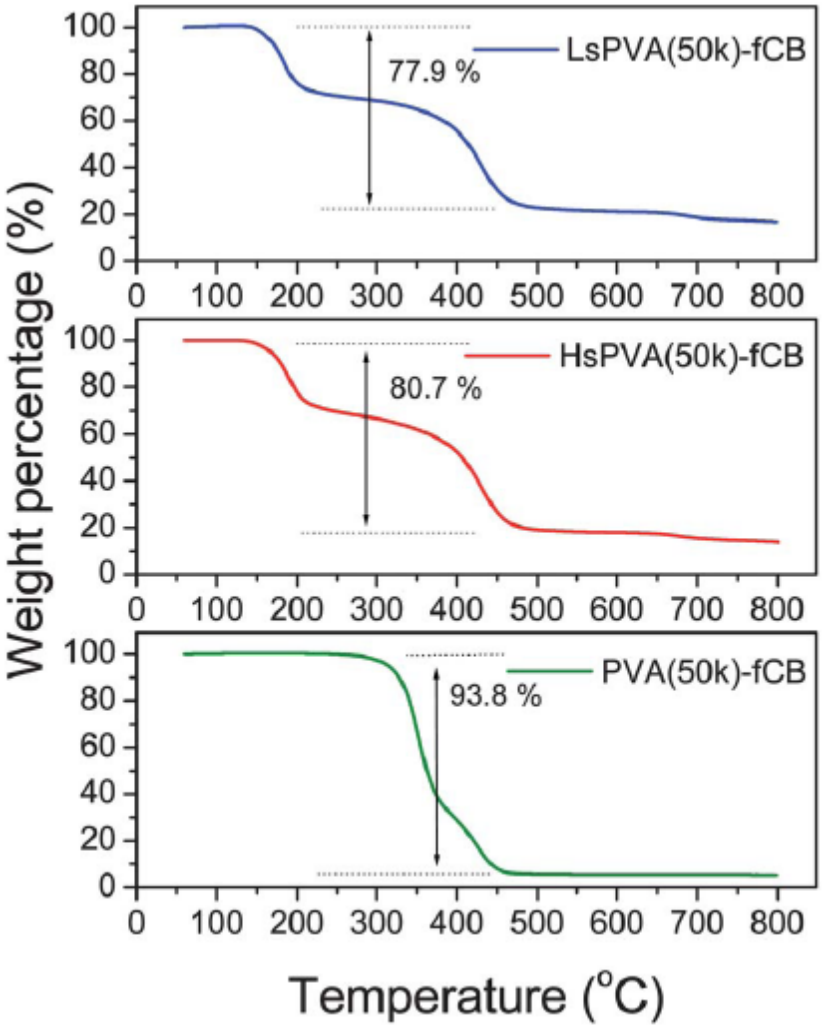

Figure 2.3 Thermogravimetric analysis (TGA) of the LsPVA(50k)–fCB, the HsPVA(50k)–fCB and the PVA(50k)–fCB NPs. Samples were pretreated at 120 ºC for dehydration prior to being heated to 800 ºC at a rate of 3 ºC min^{-1} in Ar.

ºC under argon. The sample was then heated to 800 ºC at a rate of 3 ºC min^{-1}. The TGA indicated that the weight loss of the PVA–fCB (94%) was slightly higher than the PVA–OCB (86%) recorded in our previous report,[14] which indicates that the fCB cores are viable replacements for the OCB cores due to their high degrees of functionalization. Compared to the PVA–fCB, both highly and lightly sulfated PVA–fCB NPs are expected to have larger weight loss due to the addition of sulfate groups. However, the TGA weight loss for the LsPVA–fCB and HsPVA–fCB NPs was 78% and 81%, respectively. The PVA polymers were grafted onto the fCB surface via carboxylic ester bonds. The sulfation agent, chlorosulfonic acid, not only sulfates the PVA, but it could also damage the carboxylic esters. We speculate that part of the grafted PVA was lost during the sulfation process. After dialysis in running DI water, these unbound PVA were therefore removed, leading to the diminished PVA weight loss in the sPVA–fCB NPs.

Figure 2.4 shows SEM images of three different fCB-containing NPs. 50,000 molecular weight PVA was coupled to the fCB to provide PVA(50k)–fCB NPs with a particle size from 200 to 300 nm as shown in Figure 2.4a. These NPs appear agglomerated because they were precipitated from acetone. Even so, each NP has the spherical shape of carbon black. After the PVA–fCB NP was lightly sulfated by $ClSO_3H$, the resulting LsPVA(50k)–fCB has a particle size distribution in a range between 100 and 200 nm. The HsPVA(50k)–fCB particles are almost twice as large (200 – 400 nm) as the LsPVA(50k)–fCB. The zeta potential (ξ) of HsPVA(50k)–fCB was -52 mV; they are much more negatively charged than LsPVA(50k)–fCB ($\xi \sim$ -10 mV) and PVA(50k)–fCB ($\xi \sim$ 0 mV). These negatively charged sulfated PVA polyelectrolytes carry a high net

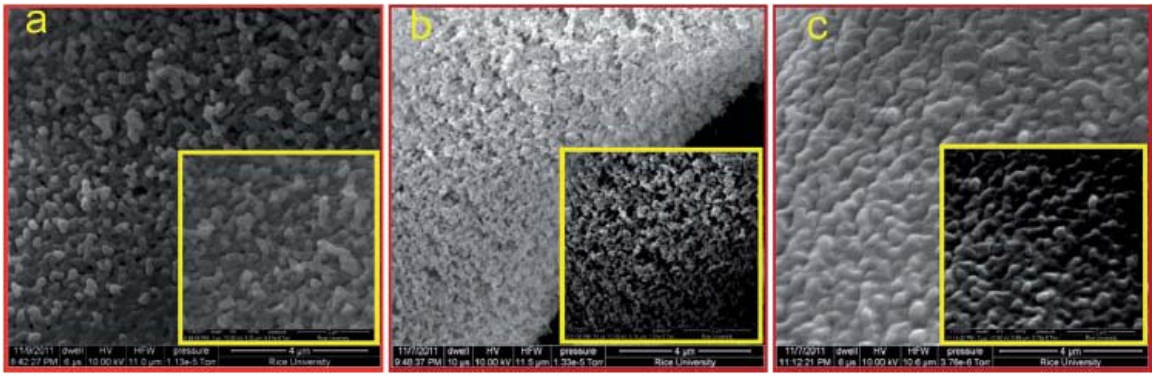

Figure 2.4 SEM images and enlarged insets of (a) PVA(50k)–fCB; (b) LsPVA(50k)–fCB and (c) HsPVA(50k)–fCB. The scale bar for each main image is 4 μm and 2 μm for each inset.

charge; the particle size of the HsPVA–fCB NPs is larger than that of PVA–fCB or LsPVA–fCB NPs because the expansion of the polyelectrolyte particle increases with the higher degree of ionization due to Columbic repulsion between the ionized groups. Dynamic light scattering (DLS) data of the NPs in DI H_2O at 25 ºC also support the SEM results for particle size trends (see Appendix B).

In the next phase of research, a different brine solution, certified by the American Petroleum Institute (API), was used to disperse the fCB NPs. API standard brine (pH 6.4) has much higher salinity than the synthetic seawater typically used to disperse the OCB NPs in our previous work, providing a more vigorous environment for maintaining dissolution. As Figure 2.5a shows, when the temperature was elevated to 100 ºC, the PVA(50k)–fCB NPs that were stable in synthetic seawater quickly precipitated and could not be redispersed in the API standard brine solution on cooling to room temperature. The LsPVA(50k)–fCB NPs did not precipitate but were stable at 100 ºC (Figure 2.5b).

However, the HsPVA(50k)–fCB was unstable in the API brine and formed a suspension (Figure 2.5c), indicating that light sulfation produces the best results. The DLS data over

Figure 2.5 Photographs taken of the (a) PVA(50k)–fCB; (b) LsPVA(50k)–fCB and (c) HsPVA(50k)–fCB at 100 ºC. All NPs were suspended in API standard brine solution. The API standard brine solution was composed of 90% H_2O, 8% NaCl and 2% $CaCl_2$.

a temperature range of 25–70 ºC (instrument limit) confirm the non-aggregation of the LsPVA(50k)–fCB (See Figure B1 in the Appendix B).

In order to evaluate the fCB-containing NPs under more realistic conditions, transport of these NPs through porous media that mimic natural rocks in oil-fields[20] was attempted. Sandstone and calcite, predominantly silica and calcium carbonate, which are

often found in oil-rich environments, were ground and sieved to ~106 to 250 µm particles, then packed into a glass column. Sandstone is composed of silica mineral which is negatively charged at neutral pH, whereas calcite is a carbonate mineral with a positive charge. After each column was prepared, the volume of liquid contained in the fully saturated column (pore volume) was calculated. The breakthrough efficiency of the PVA–fCB NPs was estimated by measuring the concentration of the PVA–fCB in the effluent (C) relative to the concentration in the influent (C_0) as a function of the amount of solution passed through the column measured in pore volumes (PVs). The API brine was used to evaluate the breakthrough performance the fCB NPs. Figure 2.6 demonstrates the relative breakthrough efficiencies of three different fCB NPs when they were passed through either sandstone- or calcite-packed columns at 70 ºC. The LsPVA(50k)–fCB NPs in API brine showed breakthrough in both rock types in spite of the harsh environment. The breakthrough in the sandstone quickly reached greater than 95% at ~ 4 PV, while the breakthrough in the calcite initially approached only 85 % at

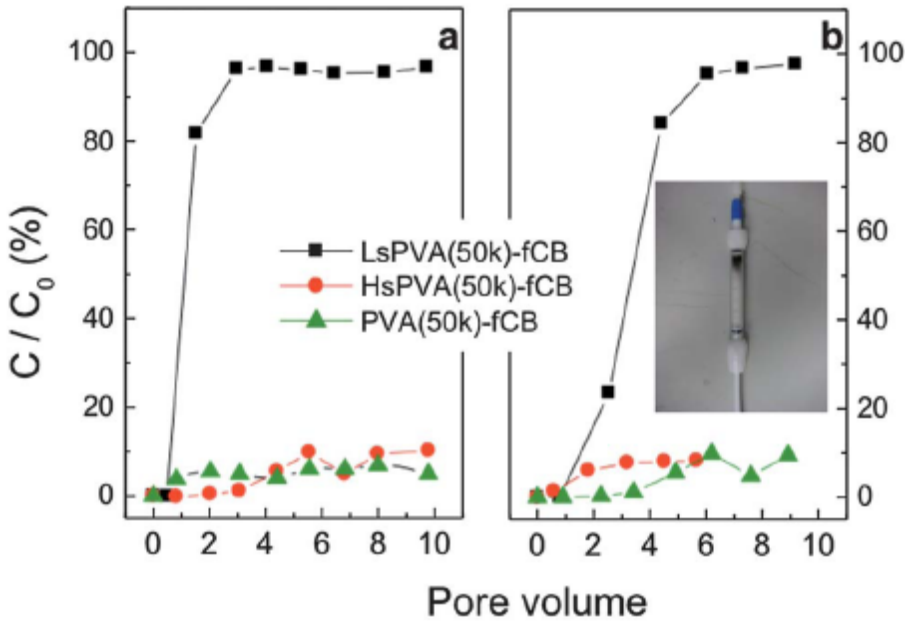

Figure 2.6 Breakthrough tests of PVA(50k)–fCB, LsPVA(50k)–fCB and HsPVA(50k)–fCB NPs in (a) sandstone and (b) calcite-packed columns at 70 ºC. API standard brine solution was used as aqueous carrier solution, and NPs were injected into column at a flow rate of 8 mL h^{-1} and a linear velocity of 9.3 m per 24 h. The inset in (b) shows that the HsPVA(50k)–fCB NPs block the column (black band at the top of the column), resulting in little breakthrough after ~ 6 PV.

similar PV and then gradually increased to complete breakthrough. The phenomenon that retards NP breakthrough in the calcite could be attributed to the bridging surface interactions between the LsPVA–fCB NPs, the salts in brine solution and the calcite surface. The ξ of the LsPVA(50k)–fCB was -9.6 mV, while the HsPVA(50k)–fCB was -51.5 mV, providing a rationale for the fact that HsPVA(50k)–fCB NPs blocked the column and had poorer transporting performance in both rocks (see Figure 2.6 inset). HsPVA–CB NPs started to aggregate due to its high ξ, leading to intermolecular bridging with calcium ions. The LsPVA–fCB NPs were largely unaffected due to the lower charge and lower concentration of sulfate groups. Although the PVA(50k)–fCB NPs had almost zero surface charge, the presence of highly concentrated salts in the API brine apparently causes the PVA–fCB to become unstable. Compared to the fCB-based NPs, the OCB surface is highly negatively charged (ξ = -30.0 mV), probably due to the functionality introduced by the oxidative synthesis. However, the negatively charged surface is apparently shielded by the grafted polymer (PVA), decreasing the ξ of the PVA(50k)–OCB to -0.6 mV, similar to that of the PVA(50k)–fCB. The sulfation then produced a negatively charged NP (ξ = -34.8 mV) for the HsPVA(50k)–OCB. Strong interactions

between the HsPVA(50k)–OCBs, the electrolytes in the brine and the positively charged rocks retard the breakthrough efficiency of the sPVA(50k)–OCBs.

Based on the testing data, the LsPVA–fCB NPs are good candidates for hydrocarbon detection due to their thermal stability and efficient mobility under critical environments. Thus, instead of the radioactive molecule PCB*, triheptylamine (THA) was selected as a model compound for hydrocarbon detection. The THA was adsorbed onto the LsPVA(50k)–fCB NPs to yield the THA/LsPVA(50k)–fCB nanoreporter by mixing THA (~ 5 µL) with 50 mL LsPVA(50k)–fCB aqueous solution. After stirring for 1 day, the resulting solution was passed through a size exclusion column (PD-10) in order to remove any unbound THA. The remaining THA was adsorbed on the hydrophobic domains of the LsPVA(50k)–fCB, so that it was not available for removal by the PD-10 column. A control experiment was done using a brine solution of THA without any LsPVA(50k)–fCB NPs. The result showed extremely low levels of THA after the PD-10 column filtration, which means that the fCB core of NPs is required for the efficient transport of THA through the PD-10 column.

For laboratory detection and quantitative analysis of the hydrocarbon content in downhole rocks, the THA/LsPVA(50k)–fCB nanoreporter was first diluted to ~20 ppm with the API brine and the solution was pumped through a calcite-packed column by an automatic injection system (Scheme 2.2). The recovered solution was dual monitored by UV-vis and electrospray mass spectroscopy (ESI-MS). The LsPVA(50k)–fCB NP in the effluent was measured by its UV absorbance at 232 nm, while the ESI-MS THA detection was observed by the protonated molecular ion (m/z = 312.4).

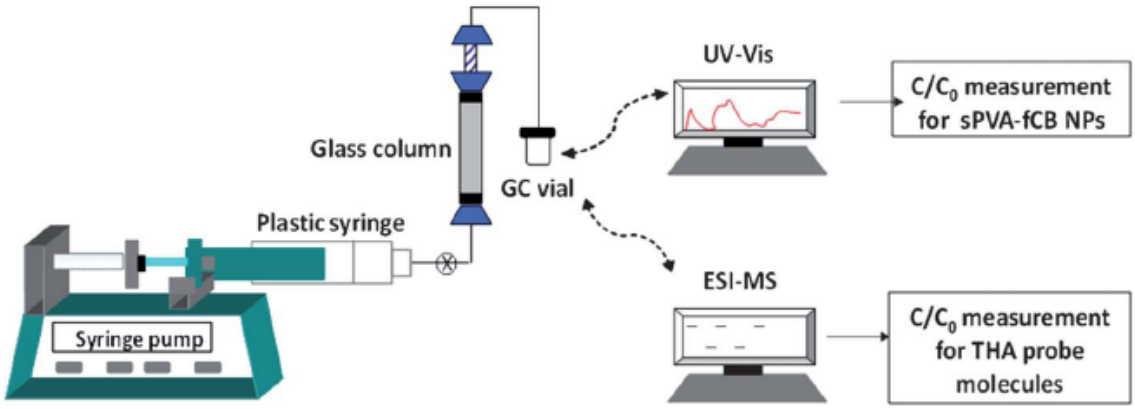

Scheme 2.2 Configuration of the apparatus for laboratory detection and quantitative analysis of the hydrocarbon content in downhole rocks. A 20 ppm solution of THA/LsPVA–fCB in API brine was loaded into the plastic syringe and it was pumped through a calcite-packed column with a given concentration of isooctane and the breakthrough volume was measured. The effluent was recovered and analyzed independently. The C/C_0 of the LsPVA(50k)–fCB NP was measured by its UV absorbance at 232 nm, while the C/C0 of the THA was measured by ESI-MS by observing the protonated molecular ion (m/z = 312.4).

The THA/PVA(50k)–fCB nanoreporters were subsequently pumped through a calcite column impregnated with isooctane from 0 to 52% ‘‘oil saturation’’ to simulate trapped oil in the formation. Oil saturation is a measurement of the degree of saturation of reservoir pore structure by reservoir oil; in this case, it is a measure of the degree of column pore saturation by the isooctane. The 52% oil saturation corresponds to 10 wt% isooctane. Based on the results, the pore volume breakthrough of the LsPVA(50k)–fCB NPs was independent of the isooctane oil saturation concentration, showing >95% breakthrough after 5 pore volumes. However, the amount of THA that was released from

the THA/LsPVA(50k)–fCB NPs (Figure 2.7b and c) depended directly on the isooctane oil saturation concentration in the column (Figure 2.7d).

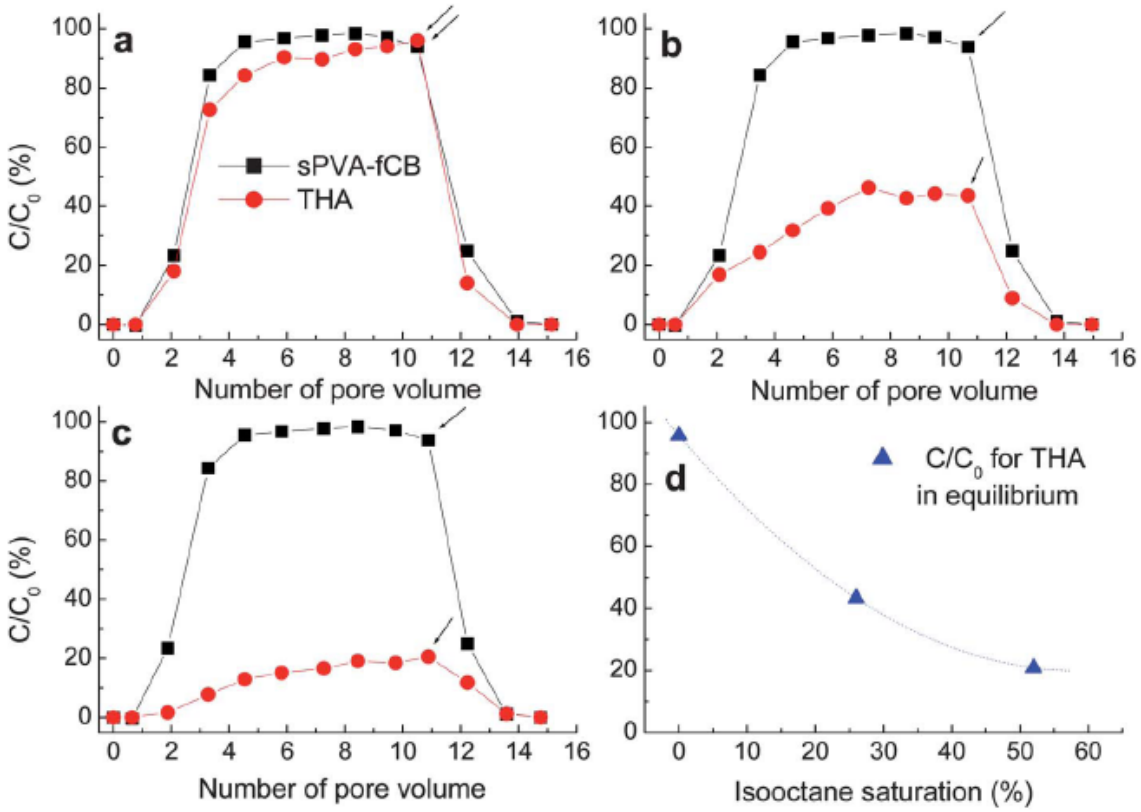

Figure 2.7 Breakthrough of THA/LsPVA(50k)–fCB nanoreporters in calcite-packed columns at 25 ºC (a) without isooctane; (b) with 26% isooctane oil saturation in the column and (c) with 52% isooctane oil saturation in the column. The black arrows indicate when the flow was switched from the THA/LsPVA–fCB solution to API brine. (d) Correlation between the C/C_0 value of THA and isooctane saturation in calcite columns.

In our previous work, the PVA–OCB NPs demonstrated an ability to deliver the hydrophobic PCB* through rock columns and selectively release PCB* into the oil

phase.[14] The LsPVA(50k)–fCB NPs here also efficiently transport the masstagged THA probe molecules through downhole porous media for hydrocarbon detection despite higher temperature and salinity in most types of rocks.

2.4. Conclusions

In summary, we solved the stability problem of the PVA–OCB NPs at high temperatures by choosing appropriately sized (molecular weight) PVA for functionalization. The OCB core was replaced by the fCB composite core without changing its intrinsic properties. After sulfation, the sPVA–fCB NPs exhibited stability at the high temperature and high salinity conditions expected in the downhole rock environment. The sPVA–fCB NPs efficiently transported mass-tagged probe molecules through a variety of oil-field rock types and selectively released the probe molecules into hydrocarbon-containing rocks. Based on the recovery of nanoreporters, one could quantitatively analyze the stranded downhole oil content.

2.5. Acknowledgements

This work was supported by Sandia National Laboratory, Nalco Energy Services and the Advanced Energy Consortium (BG Group, Halliburton, ConocoPhillips, BP, Occidental Oil and Gas, Marathon, Shell, TOTAL, Petrobras, Schlumberger).

2.6. References

1. Hwang, C.-C.; Wang, L.; Lu, W.; Ruan, G.; Kini, G. C.; Xiang, Ch.; Samuel, E. L. G.; Shi W.; Kan, A. T.; Wong, M. S.; Tomson, M. B.; Tour, J. M. *Energy. Environ. Sci*. **2012**, *5*, 8304-8309.
2. Wang, Y.; Li, Y.; Fortner, J. D.; Hughes, J. B.; Abriola, L. M.; Pennell, K. D.; *Environ. Sci. Technol.,* **2008**, 42, 3588-3594.
3. Li, Y.; Wang, Y.; Pennell, K. D.; Abriola, L. M. *Environ. Sci. Technol.,* **2008**, *42,* 7174-7180.
4. Lecoanet, H. F.; Bottero, J.-Y.; Wiesner, M. R. *Environ. Sci. Technol.,* **2004**, *38*, 5164-5169.
5. Wang, P.; Shi, Q.; Liang, H.; Steuerman, D. W.; Stucky, G. G.; Keller, A. A. *Small*, **2008**, *4*, 2166-2170.
6. Lenhart, J. J.; Saiers, J. E. *Environ. Sci. Technol.,* **2002**, *36*, 769-777.
7. Rodriguez, E.; Roberts, M. R.; Yu, H.; Huh, C.; Bryant, S. L. *Annu. Tech. Conf. - Soc. Plast. Eng.,* **2009,** 124418.
8. He, F.; Zhang, M.; Qian, T.; Zhao, D. J. *J Colloid Interface Sci.,* **2009,** *334,* 96-102.
9. Saleh, N.; Sirk, K.; Liu, Y.; Phenrat, T.; Dufour, B.; Matyjaszewski, K.; Tilton, R. D.; Lowry, G. V. *Environ. Eng. Sci.,* **2007**, *24*, 45-57.
10. Ju, B.; Fan, T.; Ma, M. *China Particuol.,* **2006,** *4*, 41-47.
11. Barari, M.; Abdollahi, M.; Hemmati, M. *Iran. Polym. J.,* **2011,** *20,* 65-76.
12. Higginbotham, A. L.; Kosynkin, D. V.; Sinitskii, A.; Sun, Z.; Tour, J. M. *ACS Nano,* **2010,** *4*, 2059-2069.
13. Marcano, D. M.; Kosynkin, D. V.; Berlin, J. M.; Sinitskii, A.; Sun, Z.; Alemany, L. B.; Lu, W.; Tour, J. M. *ACS Nano,* **2010,** *4*, 4806-4814.

14. Berlin, J. M.; Yu, J.; Lu, W.; Walsh, E. E.; Zhang, L.; Zhang, P.; Chen, W.; Kan, A. T.; Wong, M. S.; Tomson, M. B.; Tour, J. M. *Energy Environ. Sci.,* **2011,** *4,* 505-509.

15. Lyklema, J. *Fundamentals of Interface and Colloid Science: Soft Colloids,* Elsevier, New York, 2005, vol. 5.

16. Environmental Protection Agency, http://edocket.access.gpo.gov/

17. Chen, J.; Tsubokawa, N. *J. Appl. Polym. Sci.*, **2000,** *77*, 2437-2447.

18. Shen, C. C.; Joseph, J.; Lin, Y. C.; Lin, S. H.; Lin, C. W.; Hwang, B. J. *Desalination,* **2008,** *233*, 82-87.

19. Hirasaki, G. J.; Miller, C. A.; Puerto, M. *SPE Reservoir Eval. Eng.,* **2011,** *16,* 889-907.

20. Folk, R. L. *Petrology of Sedimentary Rocks*, Hemphill Publishing Company, Austin Texas, 1981.

2.7. Experimental Contributions

My contribution to the experimental work in this chapter is the following: experiment design and preparation of fCB and sulfation of PVA. Chih-Chau Hwang characterized the nanoparticles and studied the sequestration and releasing behavior of mass spec tags. Lu Wang built the column and studied the transport behavior of sPVA-fCB NPs. Assistance in column studies and preparation of sPVA-fCB NPs was received from Gedeng Ruan, Gautam C. Kini, Changsheng Xiang, Errol L. G. Samuel, and Wei Shi.

Chapter 3

Toward Enhanced Oil Recovery: Temperature-Driven Reversible Migration of Amphiphilic Nanoparticles Across the Water/Oil Interface

3.1. Introduction

A fundamental understanding of the physical and chemical properties of the water/oil interface is a critical aspect of environmental and energy-related research, along with its relevance in biology systems.[1] Recently, nanoparticles (NPs) at or transporting across the liquid/liquid interface, especially the water/oil interface, have been investigated for potential applications in phase transfer catalysis,[2] fuel cells[3] and enhanced oil recovery (EOR).[4] For this, NPs must have amphiphilic moieties to make them soluble in both of the two immiscible phases. The initial development of NP phase-transfer used water-soluble metal NPs that were transferred from the aqueous phase to the organic phase in the presence of a phase-transfer reagent and a reducing reagent.[5,6] Later,

phase-transfer of NPs was carried out by ligand exchange[7,8] followed by electrostatic interaction,[9] lipid-based amphiphilic surface coating[10] and bilayer stabilization.[11–13] However, transfers from the aqueous phase to the oil phase or *vice versa* is always irreversible by the aforementioned methods. Consequently, much effort has been devoted to exploring the reversible transfer of NPs across the interface when triggered by external stimuli. Reversibly moving surfactant-stabilized NPs across the water/oil interface can be achieved by tuning pH-induced acid-base interactions of the surfactants[14,15] or by using the temperature-driven hydrophobic effect of small organic molecules, which lacks versatility.[16] The first example of using intrinsically temperature-responsive polymer brushes for reversible transport of NPs across the water/ethyl acetate interface was reported by Li *et al*., who exploited the thermally induced hydration/dehydration effect of poly(methoxytri(ethylene glycol) methacrylate).[17] Similarly, Edwards *et al*. developed sophisticated branched water-soluble copolymers based on 2-(2-methoxyethoxy) ethyl methacrylate and oligo(ethylene glycol) methacrylate for initiating the reversible transfer across the interface by taking advantage of "salting out" oligo(ethylene glycol) at low to elevated temperatures.[18] However, the correlation between the phase transfer and the physical characteristics of the polymer coatings, such as molecular weight, melting temperature and the weight percent of the hydrophilic block, has not yet been adequately investigated. Here, we demonstrate the rational design and synthesis of temperature-responsive NPs that are capable of reversibly migrating across the water/oil interface by choosing amphiphilic diblock copolymers with the appropriate content and molecular weight of the hydrophilic block. Also demonstrated is a new type of stimuli-responsive amphiphilic diblock copolymer with aqueous solubility at low-to-moderate temperatures

and oil solubility at higher temperatures for the reversible phase transfer, in combination with the known decrease in hydrophilic block water-solubility *via* dehydration.[16–19] This temperature responsiveness can be finely tuned based upon the polymer molecular weight. This opens for door for temperature-induced spontaneous phase separation of a surfactant back to the aqueous phase, as has been long-sought in EOR applications.[20] And since the NP cores are made from inexpensive and non-toxic carbon black, this could lead to environmentally accepted systems.

3.2. Experimental Procedures

The detailed experimental procedures are provided in the Appendix C.

3.3. Results and Discussion

Amphiphilic carbon-based NPs were prepared that could migrate to the oil phase at the temperature corresponding to the melting temperature of the hydrophobic block of the diblock copolymers. Inexpensive and non-toxic oxidized carbon black (OCB)[21] was used as the core and polyethylene-*b*-poly(ethylene glycol) (PE-*b*-PEG) diblock copolymers were used as the shell, as shown in Figure 3.1a. The OCB was prepared by $KMnO_4$ oxidation of 30-40 nm carbon black as we described previously.[21] (See the Appendix C materials and methods for the preparation of OCB and PE-*b*-PEG-OCB). The diblock copolymers used here are composed of hydrophilic blocks that form ester linkages with the OCB, and hydrophobic blocks that are oil-soluble at higher temperatures.[22] Though the ester linkages are less susceptible to hydrolysis than typical esters due to their steric hindrance near the NP carbon cores, in the future amides and

hindered amides might be preferred to enhance high temperature stability. PE blocks collapse in the aqueous phase

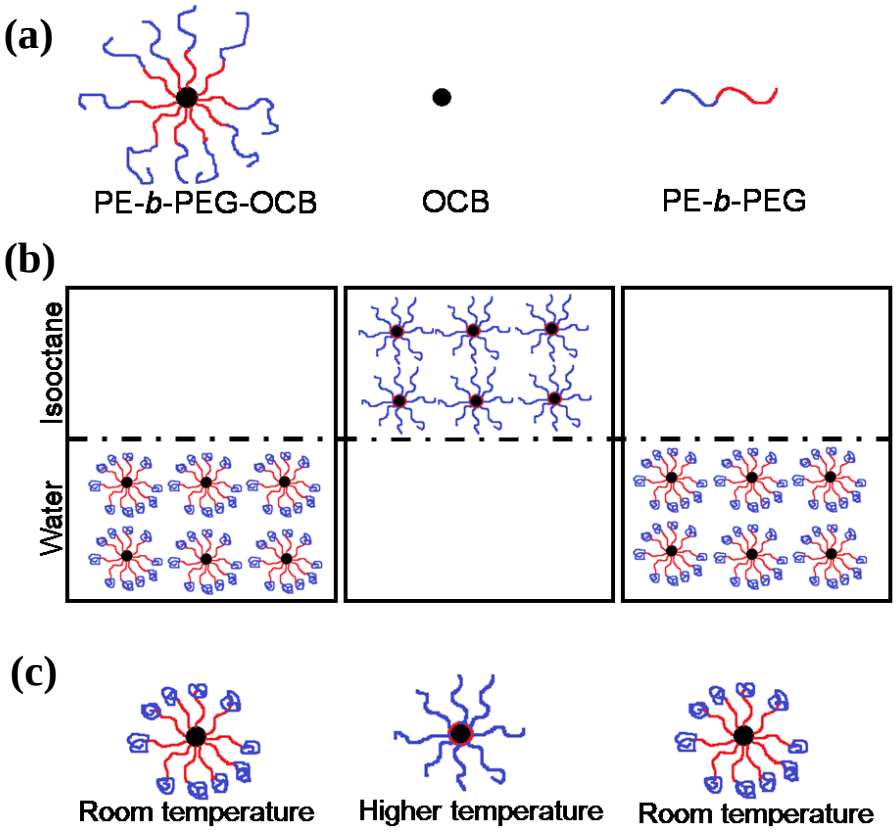

Figure 3.1 (a) Chemical structures of PE-*b*-PEG-OCB. The polymer is attached by an ester linkage to the OCBs. (b) A schematic illustration of the reversible phase transfer of amphiphilic OCB across the water/oil interface based on the temperature-dependent solubility of the hydrophobic block of the diblock copolymer and (c) the corresponding structures of the amphiphilic OCB in the aqueous phase and the oil phase.

but splay in the oil phase due to their oil solubility at higher temperature, while PEG blocks collapse in the oil phase but splay in the aqueous phase, as shown in Figure 3.1. Upon heating to 110 ºC, the PE-*b*-PEG-OCB NPs could migrate from synthetic sea brine

(See the Appendix C for the composition of the sea brine) in 20 min by vigorous stirring (Figure 3.2a, b) or in 12 h without stirring. The NPs migrated back to the aqueous

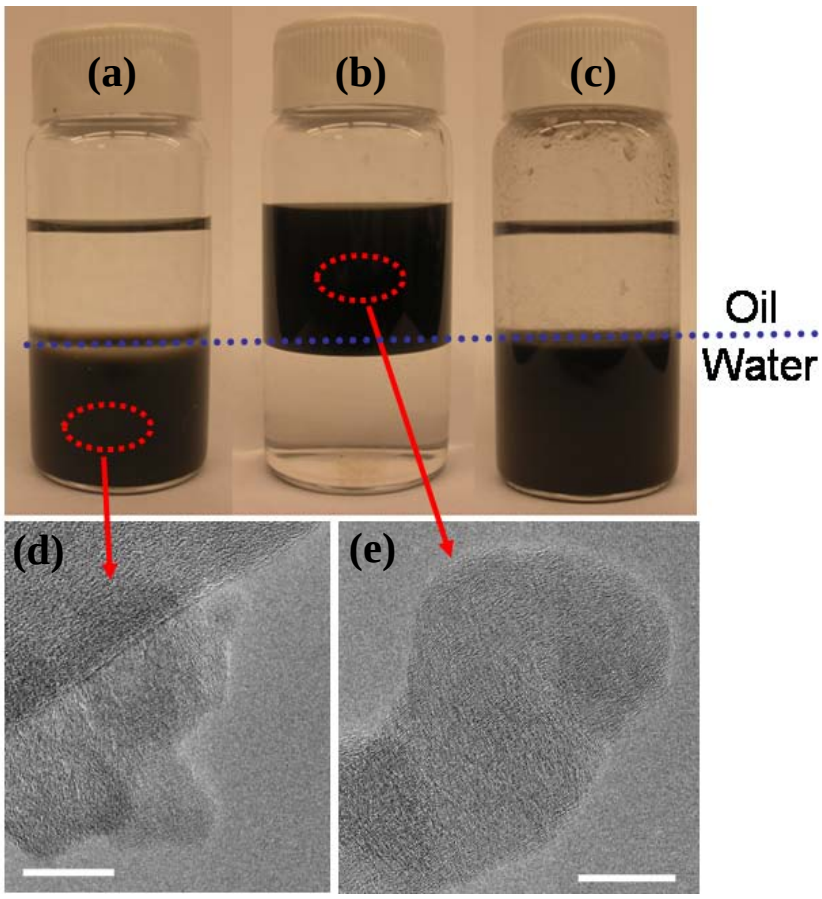

Figure 3.2 Photographs of a two-phase mixture of PE-*b*-PEG-OCB/synthetic sea brine solution (the concentration of OCB in sea brine was 50 mg/L, 1400 M_n PE-b-PEG (50 wt% PEG content)) and isooctane (a) before and (b) after phase transfer caused by heating at 110 ºC. (c) The former mixture after agitation at room temperature for 1 h. TEM images of PE-*b*-PEG-OCB extracted from (d) the synthetic sea brine and (e) the isooctane phase. The scale bars in (d-e) are 20 nm. The starting and fuctionalized individual carbon black is between 30-40 nm in diameter but it stays in the form of clusters composed of 3-5 individual carbon black nanoparticles.[23] The linear structure in

the top-left of (d) is part of the carbon TEM grid. See Table C1 in the Appendix C for the effective diameter of PE-*b*-PEG-OCB by dynamic light scattering in DI water and sea brine.

phase upon cooling, as illustrated in Figure 3.2c. The phase-transfer process was accompanied by a change in the color of the mixtures: the aqueous phase in Figure 3.2 was black before phase transfer and became colorless after phase transfer, whereas the oil phase was colorless before phase transfer and became black after phase transfer. Transmission electron microscopy (TEM) was used to examine the size of PE-*b*-PEG-OCB NPs in the aqueous and oil phases. Figures 3.2d and 3.2e show the TEM images of the NPs before and after phase transfer, respectively. The spots highlighted in red are the carbon black cores and the amorphous domains surrounding those black cores are likely the diblock copolymers. No observable aggregation or size change could be identified, compared to the OCB (See Figure C1 in the Appendix C for TEM image of OCB). We also investigated the transfer efficiency of amphilphilic OCB through the interface by calculating the amount of NPs in the sea brine after phase transfer (See Figure C2 in the Appendix C) and it was found using UV-spectroscopy that only 6% of the NPs remained in the aqueous phase.

Since no phase transfer was observed at low-to-moderate temperatures, we studied the temperature-dependent solubility of amphiphilic OCB in isooctane at higher temperatures. As shown in Figures 3.3a and 3.3b, PE-*b*-PEG-OCB NPs were well-dispersed in isooctane at higher temperatures but precipitated as soon as the oil bath was removed, implying a temperature-dependent solubility in the oil phase. Shown in Figure

3.3c is the differential scanning calorimetry (DSC) measurement of 1400 M_n PE-*b*-PEG. The characteristic melting peak at 105 ºC is obvious, corresponding to the main crystalline phase of the PE block; the shoulder peak at 94 ºC corresponds to a secondary, less ordered crystalline phase associated with the PE block.[24]

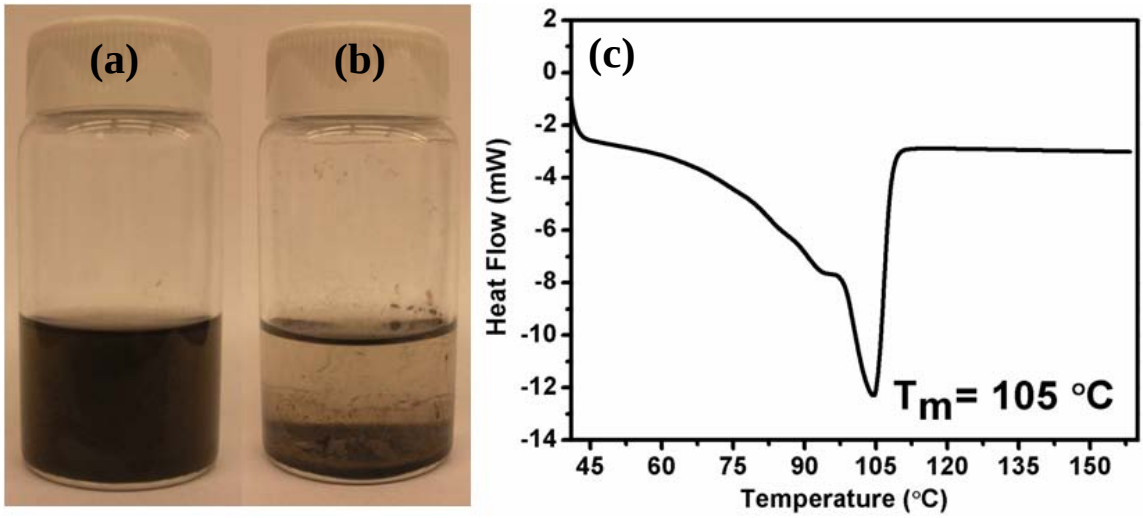

Figure 3.3 Photographs of 1400 M_n PE-*b*-PEG-OCB/isooctane mixture at (a) 105 ºC and (b) when the T < 105 ºC (T = 25 °C shown). The concentration of OCB was ~50 mg/L. (c) DSC curve of 1400 M_n PE-*b*-PEG.

The phase transport also occurred at a lower temperature (90 ºC) but took approximately 1 week to complete (See Figure C3 in the Appendix C for photos), indicating that transport across the interface is dependent on the kinetics of the PE-*b*-PEG dissolution in the isooctane phase. To determine if the phase transfer could be solely driven by temperature, we mixed a PE-*b*-PEG-OCB/deionized water (DI water) solution with an equal volume of isooctane in a sealed ampoule to prevent fluid solvent loss (See the Appendix C for the ampoule sealing procedure). Upon heating at 110 ºC, PE-*b*-PEG-

OCB NPs transferred from the DI water into the oil phase without the presence of salt ions (Figure 3.4), in contrast to the previous work in which salt ions were required to lower the solubility of the oligo(ethylene glycol) methacrylate block and thus drive the

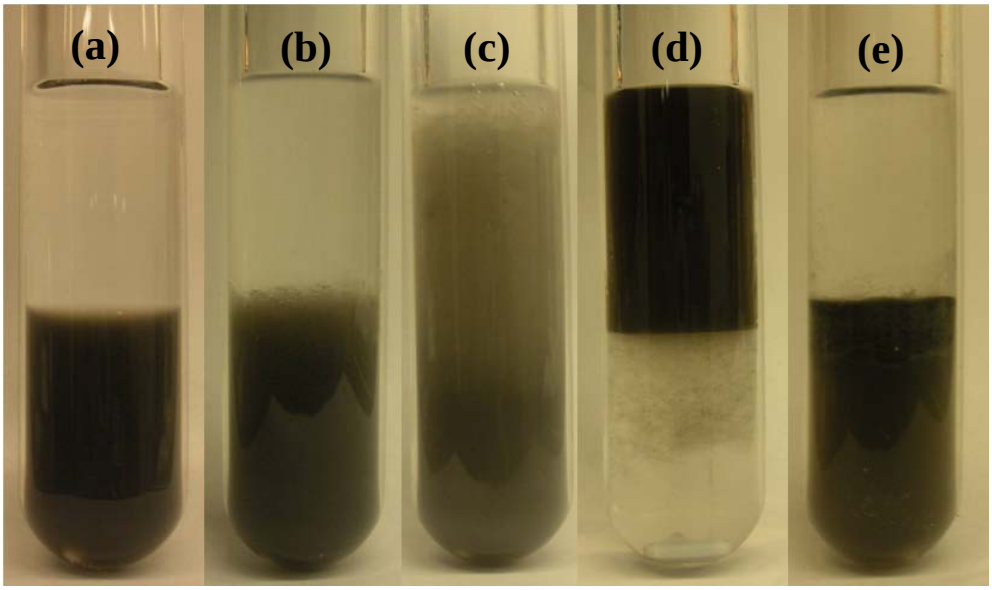

Figure 3.4 Sequential photographs of the reversible transfer of PE-*b*-PEG-OCB through the water/oil interface. (a) The two-phase mixture of PE-*b*-PEG-OCB/DI water solution (the concentration of OCB in water was 50 mg/L, 1400 M_n PE-*b*-PEG was used) and isooctane; (b) after being heated at 110 ºC for 1 h, (c) 6 h, and (d) 26 h. Since 1400 M_n PE-*b*-PEG contains poly(ethylene glycol) homopolymer contamination[25] that was not soluble in either isooctane or water at higher temperature, the OCB coated by the homopolymer formed a less well-defined transition layer in the aqueous phase in (d). (e) The resulting solution after being stirred at room temperature for 24 h.

NPs into the oil phase.[18] The sequential photographs indicate that the formation of isooctane droplets (Figure 3.4b) at the interface was the first step for phase transfer: oil-in-water droplets were formed (Figure 3.4b) and gradually dissolved in the oil layer

(Figures 3.4c and 3.4d) as a result of the increased oil-solubility of PE blocks at higher temperature. This further confirms that the solubility-dependent phase-transfer process is controlled by temperature. Introducing the salt could increase the rate of the phase transport process (Figure 3.2). Finally, in Figure 3.4e, the NPs migrate back to the aqueous phase upon cooling to room temperature.

Although the reversible phase transfer of polymer-coated NPs across the liquid/liquid interface has been demonstrated based on the temperature-driven hydration/dehydration of the surfactant coatings, the important link between the intrinsic properties of the polymer coating and the corresponding phase transfer has been less explored. Here we demonstrate a correlation between the characteristic properties of polymer coatings and the temperature-driven phase transfer process. Exploring the dependency of melting temperature on the molecular weight, PE-*b*-PEG diblock copolymers with M_n ~ 2250, 920, and 575 were used for tuning the phase transfer temperature. The characteristics of PE-*b*-PEG diblock copolymers are listed in Table 1.

Table 3.1 Characteristics of PE-*b*-PEG diblock copolymers

M_n	EO Content[a]	T_m (°C)[b]
575	20 %	88
920	50 %	86
1400	50 %	105
2250	80 %	92

[a]wt% of the PEG block. [b]Melting temperature of the PE block. DSC curves of 575, 920 and 2250 M_n PE-*b*-PEG are given in Figures C5-C7 in the Appendix C.

Figure C4 in the Appendix C shows that 920 M_n PE-*b*-PEG-coated OCB reversibly moved across the water/oil interface at 90 ºC in 1 h. However, 575 M_n PE-*b*-PEG-coated OCB was not water-soluble and 2250 M_n PE-*b*-PEG-coated OCB did not move into the isooctane phase even when heated at 110 ºC for 1 h. The common features of the diblock copolymers that are capable of moving the OCB through the water/oil interface is that they have an equal wt% of hydrophobic and hydrophilic blocks: 920 M_n PE-*b*-PEG and 1400 M_n PE-*b*-PEG both have 50 wt% of poly(ethylene oxide) in the backbone, as shown in Table 3.1. 575 Mn PE-*b*-PEG only has 20 wt% poly(ethylene oxide) in the backbone and the corresponding PE-*b*-PEG-OCB was insoluble in water; 2250 M_n PE-*b*-PEG only has 20 wt% polyethylene in the backbone and, therefore, the corresponding PE-*b*-PEG-OCB did not move into the isooctane phase even at 110 ºC (as seen in Figure 3.5), because of the insufficient PE block content. Though the number of polymer systems

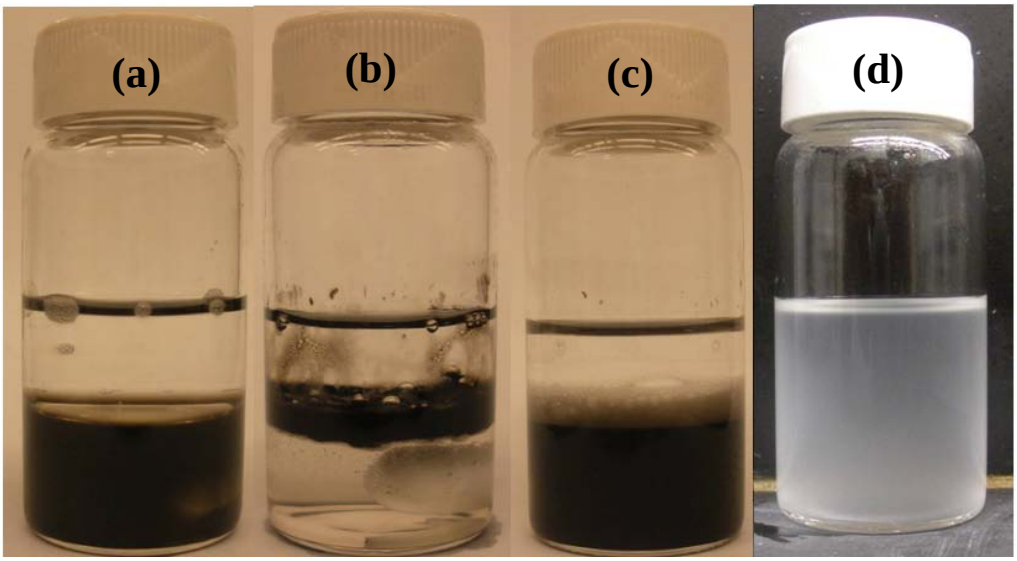

Figure 3.5 Photographs of a two-phase mixture of PE-*b*-PEG-OCB/synthetic sea brine solution (the concentration of OCB in the synthetic sea brine was 50 mg/L, functionalized by 2250 M_n PE-*b*-PEG) and isooctane (a) before and (b) after being heating at 110 ºC for

1 h. (c) The mixture after agitation at room temperature for 1 h. (d) 2250 M_n PE-*b*-PEG in isooctane (500 mg/12 mL isooctane) being heated at 110 ºC for 1 h after shaking. The turbid solution indicates the low solubility of 2250 M_n PE-*b*-PEG in the isooctane and thus the corresponding PE-*b*-PEG-OCB NPs could not be dissolved in the oil phase at higher temperature.

investigated here is not sufficiently conclusive, it could suggest that reversible phase transport triggered by temperature-dependent oil-solubility is facilitated by diblock copolymers with nearly equal wt% of hydrophobic and hydrophilic blocks.

Due to its amphiphilicity, the PE-*b*-PEG-OCB was used to stabilize oil droplets for potential applications in reducing water/oil interfacial tension. Equal volumes of PE-*b*-PEG-OCB NP solution and isooctane were magnetically stirred overnight. Successful emulsification was obtained with the 920 M_n and 1400 M_n PE-*b*-PEG copolymer-coated NPs. Stable oil-in-water emulsions were verified by optical microscopy (Figure 3.6) and a bimodal distribution of stable oil-in-water emulsion droplets was observed in the image. Most droplets were 30-60 μm in diameter, but smaller droplets with diameters ranging from 1 to 10 μm were also present. The interfacial tension of the mixture of 920 M_n PE-*b*-PEG-OCB and isooctane was measured and the interfacial tension was lowered from 50 mN/m to 0.1 mN/m as the temperature was raised from room temperature to 70 ºC. Systematic studies are underway to better understand the correlation between the reduction of the interfacial tension and the temperature-responsiveness of the NPs for use in the EOR process where trapped oil is flushed from sediments in Pickering-type emulsion.[26]

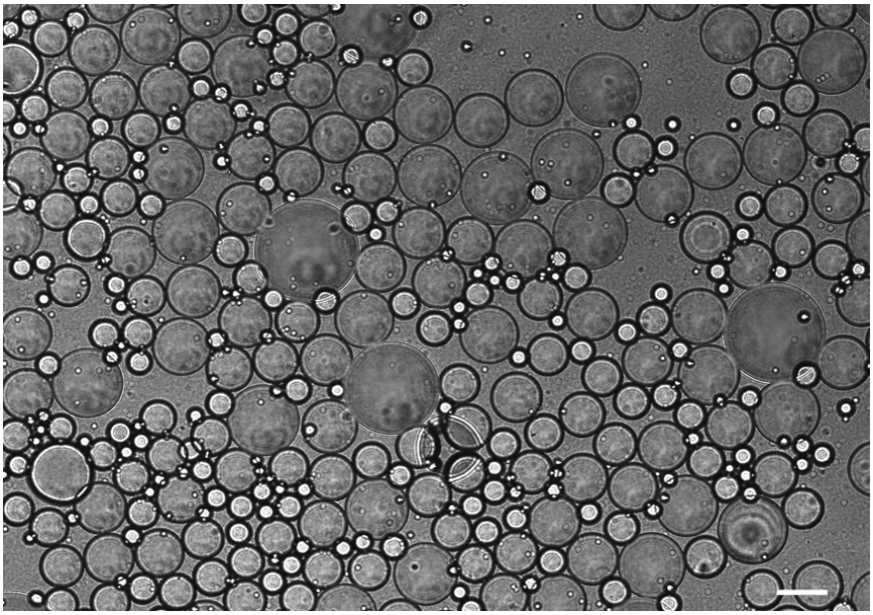

Figure 3.6 Optical micrograph of emulsified isooctane droplets in water stabilized by 1400 M_n PE-*b*-PEG coated OCB. The scale bar is 50 μm.

3.4. Conclusions

In conclusion, we have shown that diblock copolymer-coated carbon black NPs will reversibly transfer across the water/oil interface in a process solely driven by temperature. Introducing salt ions could accelerate the phase-transfer process due to the lower solubility of the copolymers in water, and since synthetic sea brine solutions are commonly used in the oil recovery industry, the compatibility of the NPs in that medium is of significance. Also shown here is that, contrary to hydration/dehydration-induced phase transfer due to an increased in temperature, the solubility of the hydrophobic blocks increases as the temperature increases, favoring the transport of the NPs into the isooctane phase. More importantly, a correlation between the phase-transfer behavior and the intrinsic properties of the copolymers is described. Through emulsification of oil

droplets with amphiphilic NPs, we have demonstrated the potential applications of those polymer-coated NPs for reducing interfacial tension. The flexibility of choosing diblock copolymers with different molecular weights enables systematic variations in the temperatures at which phase transfer occurs, thus suggesting engineering of the stabilization of oil droplets for potential applications in EOR where cooling upon reaching surface temperature would spontaneously move the amphiphilic NPs back to the aqueous phase for simple re-use. Taking advantage of temperature-dependent solubility, the present approach could also open new directions for designing temperature-responsive polymers in the applications of phase-transfer catalysts.

3.5. Acknowledgements

This work was supported by Nalco Energy Services and the Advanced Energy Consortium (BG Group, Halliburton, ConocoPhillips, BP, Occidental Oil and Gas, Marathon, Shell, TOTAL, Petrobras, Schlumberger).

3.6. References

1. Benjamin, I. *Annu. Rev. Phys. Chem.* **1997**, *48*, 407-451.
2. C. M. Starks, C. L. Liotta, M. H. *Phase-Transfer Catalysis Fundamentals, Applications and Industrial Perspectives*; Chapman & Hall: New York, 1994.
3. W. Mitchell Jr. *Fuel Cells*; Academic Press: New York, 1963.
4. O'Brien, B. M. *J. Am. Oil Chem. Soc.* **1980**, *59*, 839-852.

5. Brust, M.; Walker, M.; Bethell, D.; Schiffrin, D. J.; Whyman, R. *J. Chem. Soc. Chem. Commun.* **1994**, 801-802.

6. Meguro, K.; Torizuka, M.; Esumi, K. *Bull. Chem. Soc. Jpn.* **1988**, *61*, 341-345.

7. Woehrle, G. H.; Brown, L. O.; Hutchison, J. E. *J. Am. Chem. Soc.* **2005**, *127*, 2172-2183.

8. Caragheorgheopol, A.; Chechik, V. *Phys. Chem. Chem. Phys.* **2008**, *10*, 5029-41.

9. Crooks, R. M.; Zhao, M.; Chechik, V. *J. Am. Chem. Soc.* **1999**, *121*, 4910-4911.

10. Dubertret, B.; Skourides, P.; Norris, D. J.; Noireaux, V.; Brivanlou, A. H.; Libchaber, A. *Science* **2002**, *298*, 1759-1762.

11. (a) Shen, L. F.; Laibinis, P. E.; Hatton, T. A. *Langmuir* **1999**, *15*, 447-453. (b) Bagaria, H. G.; Kini, G. C.; Wong, M. S. J. Phys. Chem. C **2010**, *114*, 19901-19907.

12. Prakash, A.; Zhu, H.; Jones, C. J.; Benoit, D. N.; Ellsworth, A. Z.; Bryant, E. L.; Colvin, V. L. *ACS Nano* **2009**, *3*, 2139-2146.

13. Wang, Y.; Wong, J. F.; Teng, X.; Lin, X. Z.; Yang, H. *Nano Letters* **2003**, *3*, 1555-1559.

14. Jiang, H.; Jia, J. *J.Mater. Chem.* **2008**, *18*, 344-349.

15. Imura, Y.; Morita, C.; Endo, H.; Kondo, T.; Kawai, T. *Chem.Ccommu.* **2010**, *46*, 9206-9208.

16. Qin, B.; Zhao, Z.; Song, R.; Shanbhag, S.; Tang, Z. *Angew. Chem. Int. Ed.* **2008**, *47*, 9875-9878.

17. Li, D.; Zhao, B. *Langmuir* **2007**, *23*, 2208-2217.

18. Edwards, E. W.; Chanana, M.; Wang, D.; Möhwald, H. *Angew. Chem. Int. Ed.* **2008**, *120*, 326-329.

19. Kuckling, D.; Adler, H.-J. P.; Arndt, K.-F.; Ling, L.; Habicher, W. D. *Macromol. Chem. Phys.* **2000**, *201*, 273-280.

20. Hirasaki, G. J.; Miller, C. A.; Puerto, M. *SPE Journal* **2011**, *16*, 889-907.

21. Berlin, J. M.; Yu, J.; Lu, W.; Walsh, E. E.; Zhang, L.; Zhang, P.; Chen, W.; Kan, A. T.; Wong, M. S.; Tomson, M. B.; Tour, J. M. *Energy Environ. Sci.* **2011**, *4*, 505-509.

22. Shen, Y.; Zhu, S.; Pelton, R. *Macromolecules* **2001**, *34*, 3182-3185.

23. Lahaye, J.; Dolle-Ehrburger, F. *Carbon* **1994**, *32*, 1319-1324.

24. Sertchook, H.; Elimelech, H.; Makarov, C.; Khalfin, R.; Cohen, Y.; Shuster, M.; Babonneau, F.; Avnir, D. *J. Am. Chem. Soc.* **2007**, *129*, 98-108.

25. Sun, L.; Liu, Y.; Zhu, L.; Hsiao, B. S.; Avila-Orta, C. A. *Polymer* **2004**, *45*, 8181-8193.

26. (a) Pickering, S. U. *J. Chem. Soc., Trans.* **1907**, *91*, 2001-2021. (b) Ju, B.; Fan, T.; Ma, M. *China Particuology*, **2006**, *4*, 41-46.

3.7. Experimental Contributions

My contribution to the experimental work in this chapter is the following: experiment design and characterizations of PE-*b*-PEG-OCB and investigation of phase-transfer behavior of those amphiphilic nanoparticles. Gautam Kini measured the interfacial tension of the mixture of 920 M_n PE-*b*-PEG-OCB and isooctane under

different temperatures. Assistance in preparation and characterization of PE-*b*-PEG-OCB was received from Chih-Chau Hwang, Zhiwei Peng and Gedeng Ruan.

Chapter 4

Highly Conductive Graphene Nanoribbons by Longitudinal Splitting of Carbon Nanotubes Using Potassium Vapor

This chapter was entirely copied from Reference #1 of this section

4.1. Introduction

Graphene holds great promise for the fabrication of microelectronic devices. It is a zero-bandgap semiconductor demonstrating ballistic conductance over distances approaching several micrometers.[2-6] We have recently shown that multi-walled carbon nanotubes (MWCNTs) and single-walled carbon nanotubes (SWCNTs) can be selectively unzipped lengthwise by the action of acidic potassium permanganate to form straight-edged graphene oxide nanoribbons (GONRs).[7] Effectively using graphene can be

hampered because the ballistic charge transport drops by several orders of magnitude if the sp^2 carbon network of ideal graphene is disrupted by even a relatively small number of defects.[8-12] The requisite low-defect material has only been available through treatments avoiding preliminary oxidation of graphite, including micromechanical cleavage,[2] chemical vapor deposition (CVD) on atomically flat surfaces of metal single crystals,[13,14] CVD on nickel[15] or copper foil,[16] or partial sublimation of silicon from the silicon face of SiC single crystals in high vacuum.[17] Splitting CNTs can directly produce graphene nanoribbons (GNRs) with high length-to-width ratios and dimensions exactly predetermined by the initial CNT length and diameter.[7] GNRs narrower than 10 nm have nonzero band gaps inversely dependent upon their widths and are suitable for fabrication of low-voltage field effect transistors with up to 10^7 on/off ratios,[3] while the wider ribbons exhibit high electrical conductance characteristic of large graphene flakes and could be useful for bulk applications, such as flexible transparent electrodes. The high aspect ratio of wide GNRs might make them particularly attractive for carbon fiber spinning[18] and formulation of conductive polymer composites.[19]

To date, MWCNTs and SWCNTs have been unzipped to nanoribbons by treatment with permanganate in concentrated sulfuric acid.[7] Additionally, GNRs have been obtained by the cutting action of catalytic metal nanoparticle to give low yields of GNRs consisting of 50-100 layers,[20] by treatment of MWCNTs with a solution of lithiumin liquid ammonia[21] and by plasma etching of polymer masked nanotubes.[22] The permanganate treatment, being a scalable process, produces heavily oxidized GONRs similar in chemical structure to graphene oxide (GO). While the majority of oxygen-containing functional groups can be removed from the basal plane of the GO ribbons by

reduction, a small but significant fraction of defects persists even after annealing in hydrogen at 900 ºC, resulting in lower electrical conductance dominated by a Mott variable range hopping mechanism instead of the desirable ballistic transport.[23] While oxidative defects are not introduced by the lithium/liquid ammonia intercalation-driven opening,[21] the process fails with pristine nanotubes; a preliminary treatment of the MWCNTs with a strong oxidant is required to induce defects that permit intercalation of the ammonia-solvated lithium rendering defective ribbons that only partially unwrap from the tubular state.

4.2. Experimental Procedures

SEM imaging was performed on a JEOL-6500 field-emission microscope. AFM images were obtained with a Digital Instruments nanoscope IIIa, operating in tapping mode, using Si tips n-doped with 1-10 Ωcm phosphorus (Veeco, MPP-11100-140) at a scan rate of 0.5 Hz and a resolution of 512 x 512. XPS was performed on a PHI Quantera SXM scanning X-ray microprobe. Raman spectroscopy was performed on a Renishaw Raman microscope using a 633 nm HeNe laser. Fabrication of graphene devices was performed by tracking individual GNRs on the surface of highly doped Si substrates, covered with 500 nm-thick thermal SiO_2 layer, by SEM (JEOL-6500 microscope), and followed by patterning of 20 nm-thick Pt contacts by standard electron beam lithography, as described previously in detail.[23] The electrical transport properties were tested using a probe station (Desert Cryogenics TT-probe 6 system) under vacuum with chamber base pressure below 10^{-5} Torr. The IV data were collected by an Agilent 4155C semiconductor parameter analyzer.

Reaction of MWCNTs with Potassium. MWCNTs were provided by Mitsui & Co. (lot no. 05072001K28) and were used without any further treatment. The synthesis of potassium split MWCNTs was performed by melting potassium over MWCNTs under vacuum (0.05 Torr) as follows: MWCNTs (1.00 g) and potassium pieces (3.00 g) were placed in a 50 mL Pyrex ampule that was evacuated and sealed with a torch. (Caution: Potassium and sealing of the potassium-loaded ampule should be handled with utmost care due to the highly reactive nature of potassium metal. Users should wear safety glasses and a face shield, and all operations should be done in a sash-equipped fume hood when handling this reagent. Likewise, final quenching of potassium and its derivatives should be done with the utmost of care under an inert atmosphere.) The reaction mixture was kept in a furnace at 250 ºC for 14 h. (Pyrex glass turns dark-brown when exposed to potassium vapor at 350 ºC. This color disappears upon quenching with ethanol, but the glass surface shows visible signs of corrosion. Higher temperatures were not explored for safety reasons). The heated ampoule containing a golden-bronze colored potassium intercalation compound and silvery droplets of unreacted metal was cooled to room temperature, opened in a drybox or in a nitrogen-filled glovebag, and then mixed with ethyl ether (20 mL). Ethanol (20 mL) was slowly added into the mixture of ethyl ether and potassium-intercalated MWCNTs at room temperature with some bubbling observed; much of the heat release was dissipated by the released gas (hydrogen). The quenched product was removed from the nitrogen enclosure and collected on a polytetrafluoroethylene (PTFE) membrane (0.45 μm), washed with ethanol (20 mL), water (20 mL), ethanol (10 mL), ether (30 mL), and dried in vacuum to give longitudinally split MWCNTs as a black, fibrillar powder (1.00 g).

Exfoliation of Potassium Split MWCNTs with Chlorosulfonic Acid. The potassium split MWCNTs tubes (10 mg) were dispersed in chlorosulfonic acid (15 mL, Sigma-Aldrich) under bath sonication using an ultrasonic jewelry cleaner (Cole-Parmer, EW-08849-00) for 24 h. (Caution: Chlorosulfonic acid must be handled with care since it is a corrosive liquid and reacts violently with water to form HCl and H_2SO_4. Users should wear protective gloves, a rubber smock, safety goggles, and a full-face shield, and all experiments should be performed in a sash-equipped and acid-approved fume hood.) The mixture was quenched by pouring onto ice (50 mL), and the suspension was filtered through a PTFE membrane (0.45 μm). The filter cake was dried under vacuum. The resulting black powder was dispersed in dimethylformamide (DMF) and bath sonicated for 15 min to prepare a stock solution for microscopy analysis.

Supporting Information (Appendix D): Additional XPS and UV-vis analytical spectra and TEM and SEM images of GNRs. Details of simulations of splitting and exfoliation of MWNTs.

4.3. Results and Discussion

Here, we investigate a hypothesis that thermal motion of a carbon framework in MWCNT sidewalls at elevated temperatures might create large enough transient openings for the alkali metal atoms to penetrate. In this process, potassium and MWCNTs, with a starting outside diameter of 40-80 nm and approximately 15-20 inner nanotube layers,[7] are sealed in a glass tube, heated in a furnace at 250 ºC for 14 h, and followed by quenching with ethanol to effect the longitudinal splitting process in 100% yield, as depicted in Figure 4.1a and b. Intromission of potassium atoms results in the formation of

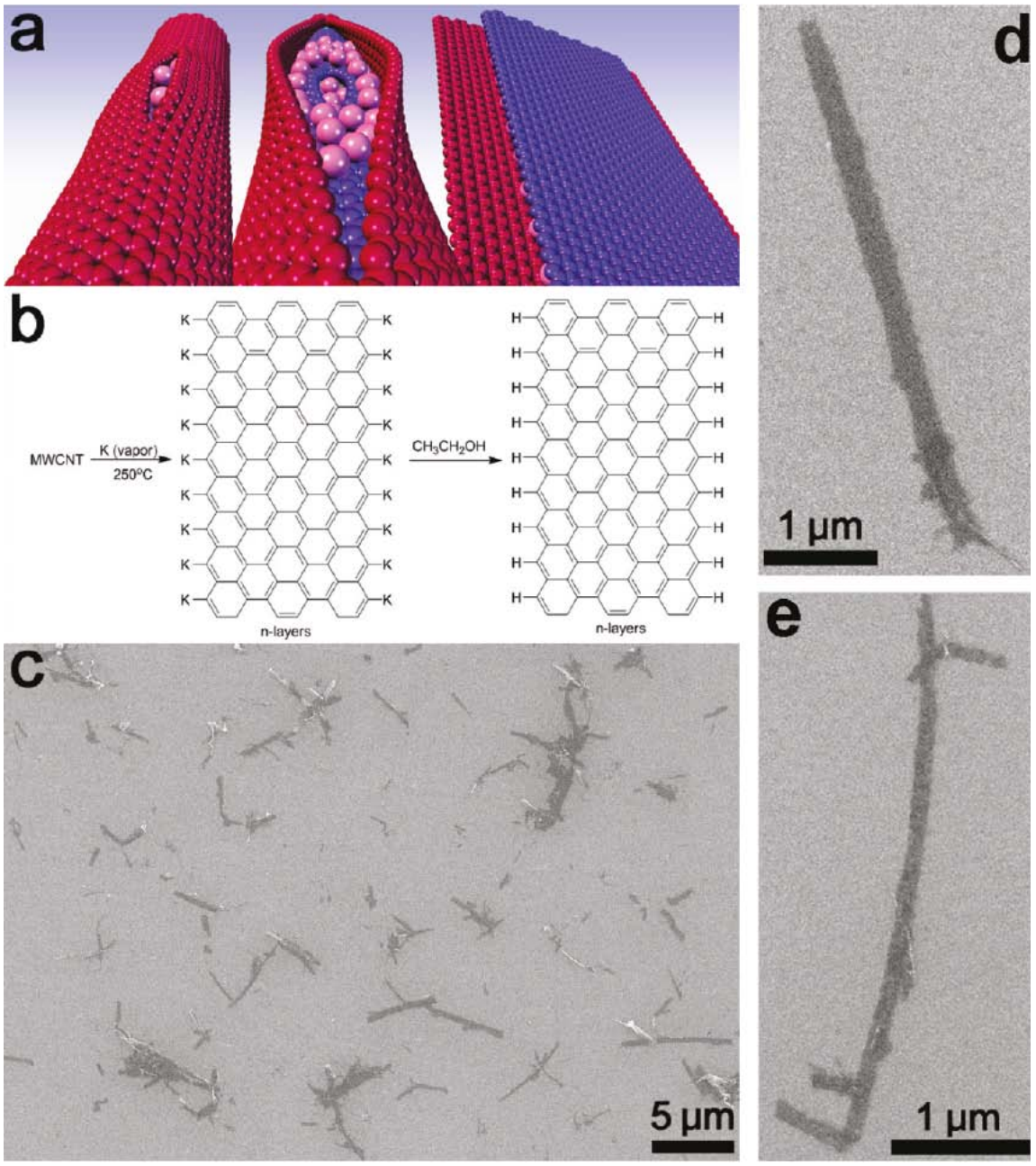

Figure 4.1 Schematic of the splitting process and SEM images on a Si/SiO_2 surface of GNRs produced by potassium splitting. (a) Schematic of potassium intercalation between the nanotube walls and sequential longitudinal splitting of the walls followed by unraveling to a nanoribbon stack. The potassium atoms along the periphery of the ribbons are excluded for clarity; see Figures D6-D9, Appendix D for more details. (b) Chemical

schematic of the splitting processes where ethanol is used to quench the aryl potassium edges; only a single layer is shown for clarity, while the actual number of GNR layers correlates with the number of concentric tubes in the MWCNT. (c) Overview of a large area showing complete conversion of MWCNTs to GNRs. (d, e), Images of isolated GNR stacks demonstrating characteristic high aspect ratios and predominantly parallel edges.

intercalation compounds within the interstices of MWCNT sidewalls as commonly observed with other forms of graphitic carbon;[24,25] however, in the case of the MWCNTs used here, the splitting could be further assisted by the generation of H_2 upon the ethanolic quench.[26] Under sonication in chlorosulfonic acid, the split MWCNTs are further exfoliated to form GNRs. The use of high-quality pristine carbon nanotubes as GNR precursors allows production of material free from oxidative damage and with conductivities paralleling the properties of the best samples of mechanically exfoliated graphene (measured on SiO_2 substrates). This simple, scalable, and inexpensive technique provides multigram quantities of stacked GNRs that can be further exfoliated with the aid of acid and mild bath sonication.

Scanning electron microscopy (SEM) and atomic force microscopy (AFM) were used to image the ribbon structures. SEM images in Figure 1 show the GNRs with widths of 130-250 nm and a length of 1-5 μm. AFM imaging (Figure 4.2) shows a thin graphene ribbon derived from the longitudinal splitting process. These results clearly indicate that MWCNTs were successfully split and then exfoliated to form GNRs after potassium intercalation followed by bath sonication in chlorosulfonic acid.

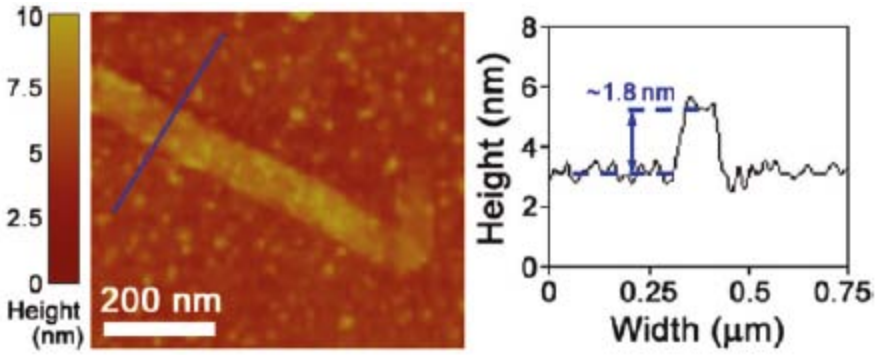

Figure 4.2 AFM image of a thin GNR with an average thickness of ~1.8 nm. The left panel shows a GNR with a folded end (lower-right portion), and the right panel shows the height of the ribbon along the blue line in the left panel. The GNR is likely a trilayer.

There was an increase in the ratio of intensities of Raman bands located around 1350 (D band) and 1580 cm^{-1} (G band) in comparison with the starting material (Figure 4.3). The D/G ratio[27] is commonly used as a measure of imperfection in the graphene lattice, as it corresponds to the relative population of sp^3-hybridized carbon atoms and it is also indicative of the abundance of edge atoms in the otherwise pristine flakes of mechanically exfoliated graphite.[2] The disordered structure introduced during the splitting and exfoliation process leads to the broadening of the G band[27,28] and the 2D band[29] as well as the combination mode[30] D + G band at about 2906 cm^{-1}.

To investigate the electrical properties of the GNRs derived from split tubes, several electronic devices were built on Si-SiO_2 and tested. The GNRs used for the device fabrication were 3.5-5 nm thick. All devices exhibited large conductivities ranging from ~70 000 to ~95 000 S/m, values that are comparable to other reported nanoribbons devices prepared from exfoliated graphene,[3,22] as seen in Figure 4.4. However, they

showed only little gate effect, presumably due to the large number of layers in these GNRs and their high metal-like conductivity.

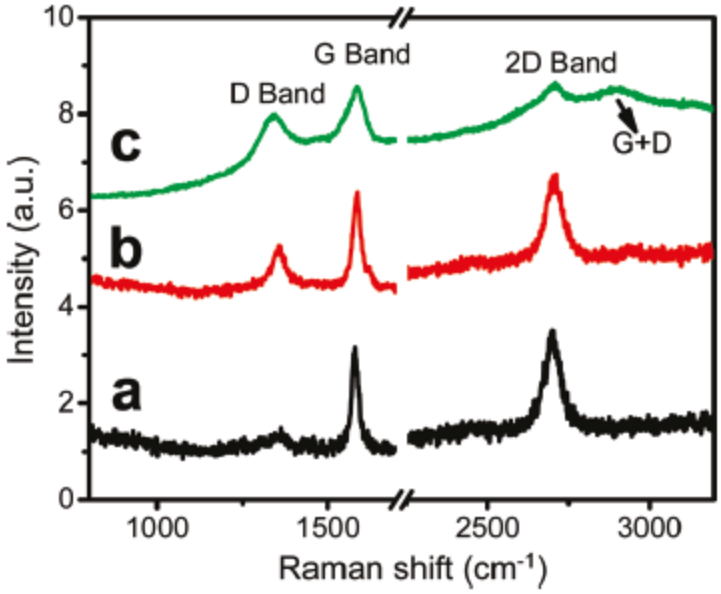

Figure 4.3 Raman spectra (excitation at 514 nm) of starting MWCNTs and splitting products. (a) Pristine MWCNTs. (b) MWCNTs treated with potassium at 250 ºC generating split nanotroughs. (c) GNRs obtained after bath sonication of the material in (b) with chlorosulfonic acid for 24 h.

X-ray photoelectron spectroscopy (XPS) was also performed to determine whether the increase in the intensity of D band was caused by oxidation. No signals corresponding to C-O and C=O groups were observed in the high-resolution XPS C1s spectra (see Figures D3 and D4 in the Appendix D). Thus, we conclude that the observed increase in the D/G ratio was solely attributable to the emergent edge carbon atoms and not an oxidative process. These MWCNT reductively derived GNRs are unlike chemically converted graphene (CCG) that is prepared by the reduction of GO. That

latter protocol produces domains of graphene that are divided by defect boundaries, even upon extensive removal of oxygenation, resulting in their inferior electrical transport properties.[5]

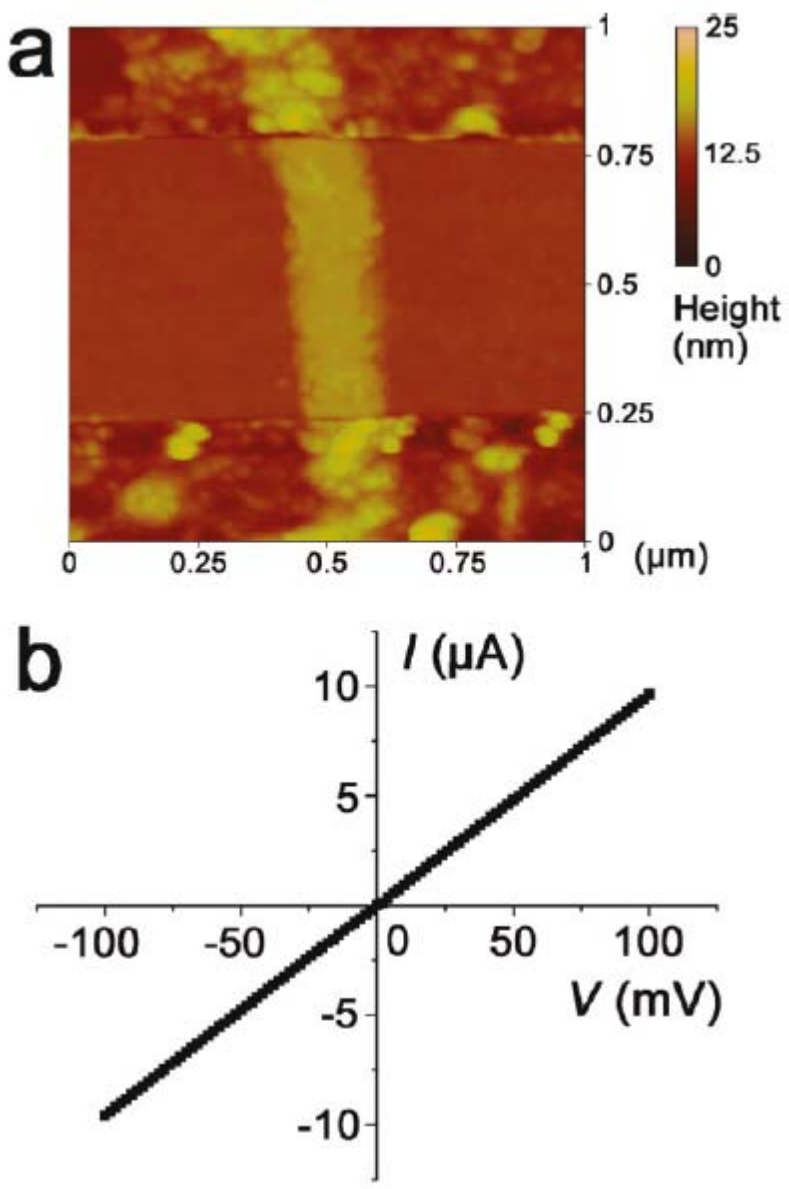

Figure 4.4 Appearance and electrical properties of a device made from a thin (3.8 nm) GNR stack. (a) AFM image of a GNR (~5-layered) with 0.5 μm-spaced platinum

electrodes shown spanning horizontally at top and bottom. (b) Electrical properties (conductivity 80 000 S/m) of the GNR shown in (a).

Before we discuss the possible mechanism for splitting MWCNTs to form GNRs, let us briefly recall here the earlier experimental results on intercalation of alkali metals in graphite and carbon nanotubes. Graphite has a well-known propensity to form layered, stage I intercalation compounds when exposed to all molten alkali metals, except sodium, at moderately elevated temperatures. Intercalation of sodium proceeds anomalously as it requires using another metal, such as potassium, as a cointercalant or an application of high pressure (~2000 bar)[24] at which unusual double layers of intercalated metal can develop.[31] While the interaction of both MWCNTs and SWCNTs with alkali metals have been previously studied, no phenomena other than penetration of metal atoms into the spaces between individual nanotubes in nanotube bundles have been observed,[32,33] except by Cano-Márquez et al.,[21] where partial splitting of oxidatively cut MWCNTs arose after treatment with lithium dissolved in liquid ammonia, followed by quenching and thermal shocking. Unfortunately, when they intercalate alone, without a solvating shell of ammonia molecules, lithium atoms expand the interplanar distance in graphite from 0.335 nm to only 0.373 nm in C_6Li, the saturated stage I intercalation compound.[24] Such a small increase in the interstitial distance between the two outermost shells of a MWCNT would not likely provide enough strain in the carbon-carbon bonds to induce breakage at moderately elevated temperatures, and experimentally no splitting with lithium was observed.

Thus, we investigated the next larger metal, sodium. Although it is known that sodium does not well-intercalate into graphite,[24] we had to prove experimentally that

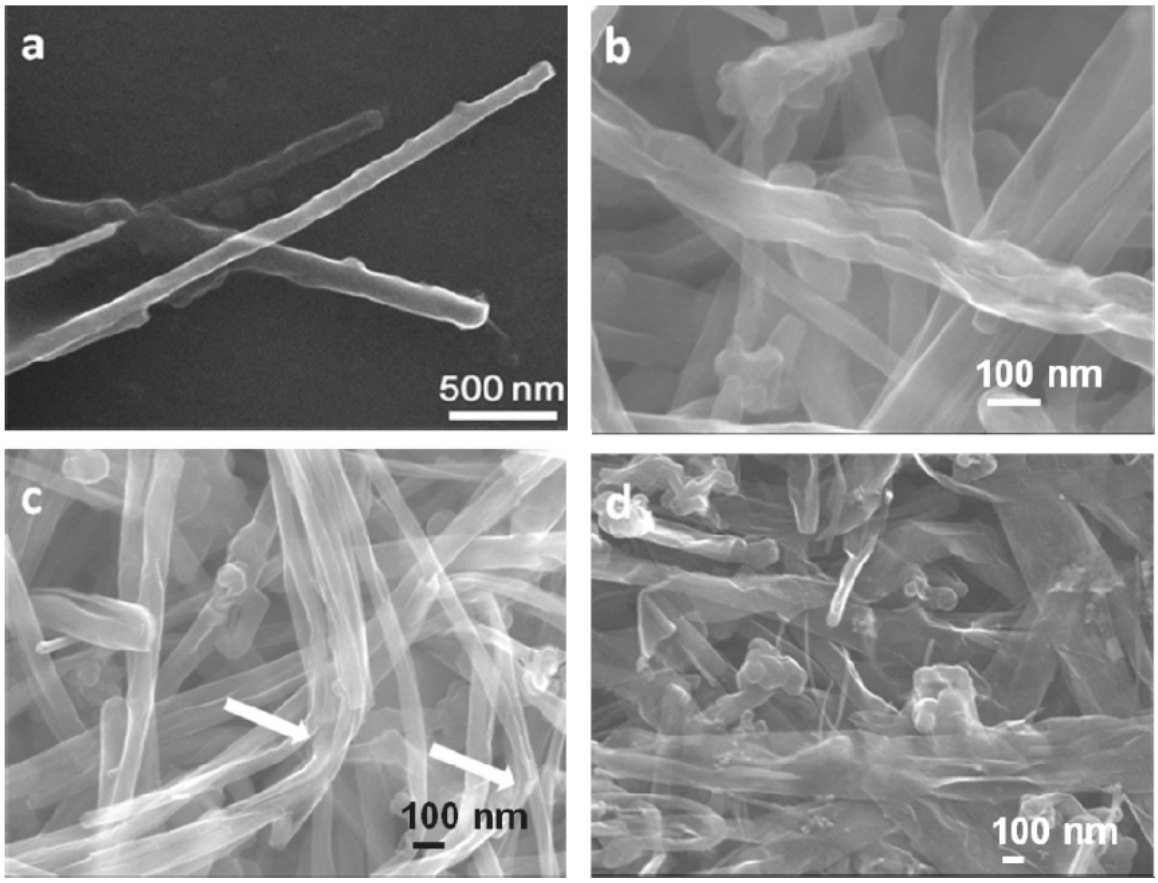

Figure 4.5 SEM images of MWCNTs treated with sodium and potassium. (a) MWCNTs recovered after treatment with sodium at 250 ºC for 14 h showing no splitting. (b and c) MWCNTs treated with K at 250 ºC for 14 h demonstrating a "split-log" appearance. Arrows indicate areas of high flexibility not observed in pristine MWCNT samples. (d) Potassium-treated MWCNTs after bath ultrasonication in chlorosulfonic acid for 24 h. Nearly complete conversion to stacks of straight-edged nanoribbons is evident.

MWCNTs were also poor targets for sodium intercalation. When MWCNTs were exposed to molten sodium and its vapor at 150-400 ºC, no changes in sample appearance, nanotube morphology, or spectroscopic properties were observed. A representative SEM image of MWCNTs treated with sodium at 250 ºC is shown in Figure 4.5a. Bond

incommensurability is not thought to be an issue here because the MWCNTs interact not with solid sodium but with either molten or vaporized metal where those bonds are already broken.

Contrary to the results with lithium and sodium, the change in the nanotube behavior was dramatic when potassium was used (Figure 4.5b-d). The silvery luster of potassium rapidly changed at 150 ºC to a uniform appearance of shiny golden-bronze color, as is seen for C_8K.[24] To obtain efficient intercalation, the reaction tube was heated for 14 h at temperatures varying from 150 to 350 ºC, and the 250 ºC temperature was chosen for preparative purposes as the MWCNT splitting was complete at this temperature, while the Pyrex glass tube was not substantially corroded. The recovered product had much higher apparent density than the starting material, likely due to greater flexibility of the GNRs in comparison with the high-persistence length pristine MWCNTs. The enhanced suppleness of the nanotubes, resulting in bending and looping, was evident in the SEM images along with a "split-log" nanotrough appearance of individual MWCNTs (Figure 4.5 b and c). Formation of such curled nanotrough structures might be attributed to the incomplete splitting of MWCNTs. However, more likely, flattening of the resulting nanotrough is slow under the conditions employed due to the robust C-C bonds at the curled areas and the interlayer van der Waals interactions that would need to be overcome as the layers slide past each other upon flattening. Furthermore, fast deintercalation of the metal, as previously observed in the corresponding compounds of graphite,[26] could limit the entry of ethanol into the interstitial space. And since the initial study was performed in order to eliminate the

exposure of the MWCNTs or subsequent GNRs to any oxidizing media, other means of exfoliation were sought.

After trying many organic solvents such as 1,2-dichlorobenzene and dimethylformamide, which did not induce the flattening and exfoliation, we chose chlorosulfonic acid as it has been shown to promote efficient exfoliation of bulk graphite

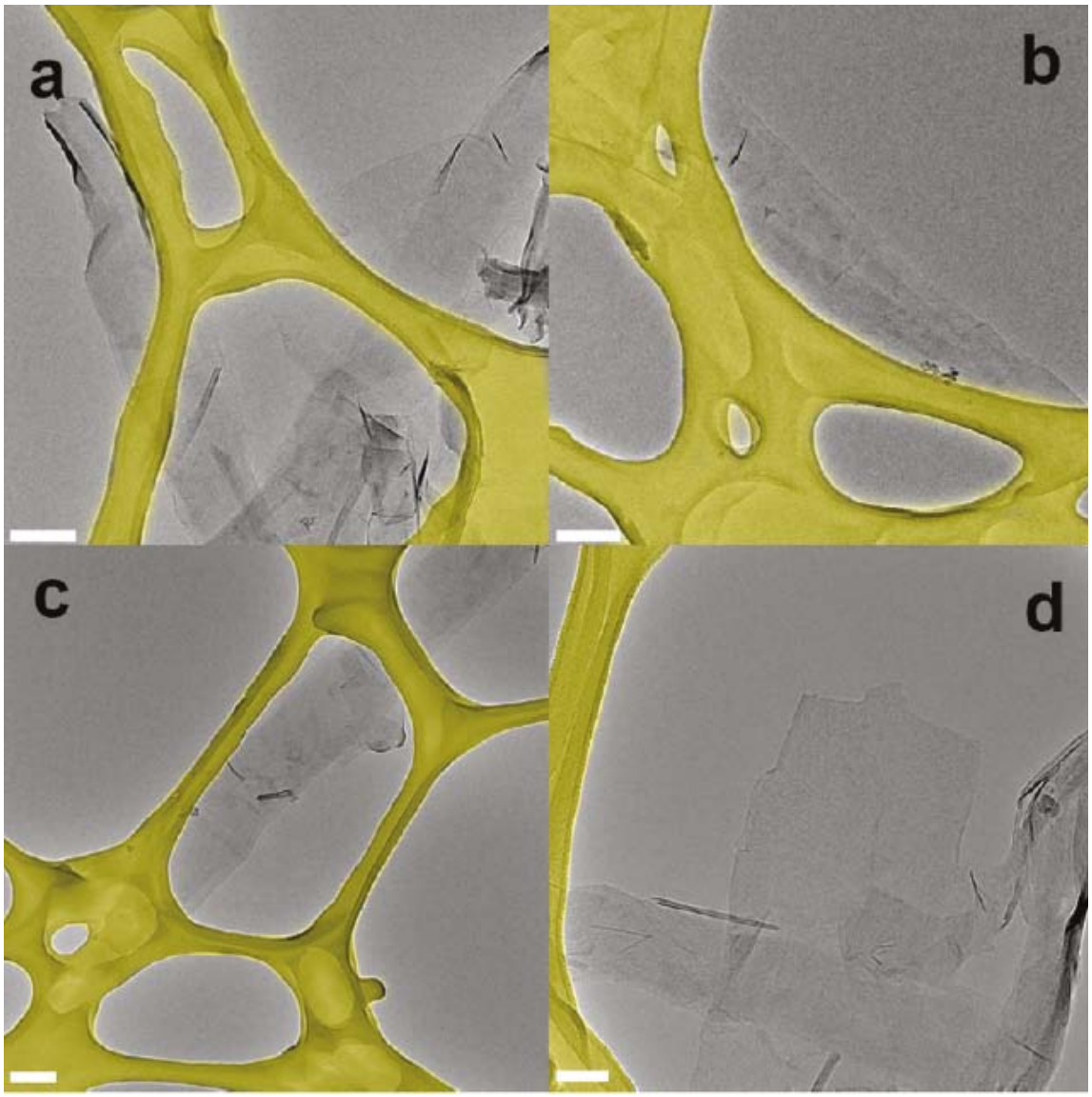

Figure 4.6 TEM images of GNRs obtained after sonication in chlorosulfonic acid for 24 h. (a-c) Few-layer GNRs. (d) Monolayer graphene nanoribbon. All scale bars are 200 nm,

except for that in (d) (100 nm). The lacey carbon grid in the images is highlighted in yellow to make the GNRs more distinguishable. Complete exfoliation of MWCNTs to form GNRs is evident.

to few-layer graphene; a superacid, such as chlorosulfonic acid, could protonate the split sidewalls of MWCNTs and thus induce electrostatic repulsive forces, which would facilitate exfoliation of split MWCNTs under sonication.[34] Therefore, we used a bath sonicator for 24 h to induce exfoliation in chlorosulfonic acid. Figure 4.5d shows the nanoribbons formed from exfoliation of split MWCNTs in chlorosulfonic acid under bath sonication. The advantage of bath sonication in the presence of a superacid was that electrostatic repulsive forces on the edges of split MWCNTs could overcome the van der Waals forces between the graphene layers, resulting in exfoliated GNRs. In order to distinguish the number of layers of GNRs, we carefully characterized the obtained sample using transmission electron microscopy (TEM). The TEM images in Figure 4.6 reveal that few-layered GNRs were obtained in the present case (see Appendix D for high-resolution TEM images).

To further interpret the splitting of MWCNTs by potassium vapor, we used molecular dynamics to model the intercalation reaction. The simulation generates a MWCNT with a 30-atom cluster of potassium atoms, one atom thick, inserted into the interstitial void immediately beneath its outermost sidewall (see the Appendix D). The propagation of a cleft in the sidewall should begin in a carbon “blister” formed around the intercalated potassium and would be driven by the concentration of strain at the tips of the fissure, aided by Coulomb repulsion of negative charges congregated at its edges

and additionally enhanced by the buttressing interaction of carbon-potassium bonds decorating the newly formed edges. As the cleft expands, the surface of the nanotube wall one level closer to the core becomes exposed to potassium and, therefore, amenable to the intercalation-induced splitting.

Further simulation using rubidium and cesium with their larger ionic radii and lower ionization potentials shows that these metals should be even more effective at inducing MWCNT splitting than potassium. But the practical use of these metals is rather difficult owing to their pyrophoric nature and high costs. Interestingly, according to the simulation, SWCNTs should be immune to splitting by alkali metals, as their inner diameters, typically exceeding 0.7 nm, are large enough to accommodate any alkalimetals without inducing additional strain in the sidewall of the tube. SWCNT splitting was not experimentally observed.

4.4. Conclusions

In conclusion, we have demonstrated a chemical route to produce bulk quantities of low-defect, highly conductive graphene nanoribbons and longitudinally split MWCNTs by exposing pristine nanotubes to hot potassium vapor followed by protonation. This was followed by bath sonication in chlorosulfonic acid to effect exfoliation of the highly stacked GNRs. Since the process does not require any oxidation, the less defective GNRs could result in intriguing electronic or spin properties. The GNRs could also be an attractive material for reinforcing polymers,[19] as the potassium-carrying reactive edges could facilitate the attachment of electrophiles or polymer chains

to improve interfacial interaction for load transfer. Consequently, the present procedure opens up new directions for preparation of GNRs and subsequent applications.

4.5. Acknowledgements

Mitsui & Co., Ltd. generously donated the MWCNTs. The work was funded by AFOSR (FA9550-09-1-0581), the AFOSR through University Technology Corporation (09-S568-064-01-C1), the Office of Naval Research Graphene MURI Program (00006766), and M-I SWACO, LLC. Gorka Pera gratefully acknowledges the award of a Formacion Profesorado Universitario fellowship from Ministerio de Educacion y Ciencia.

4.6. References

1. Kosynkin, D. V.; Lu, W.; Sinitskii, A.; Pera, G.; Sun, Z.; Tour, J. M. *ACS Nano* **2011**, *5*, 968-974.

2. Novoselov, K. S.; Geim, A. K.; Morozov, S. V.; Jiang, D.; Zhang, Y.; Dubonos, S. V.; Grigorieva, I. V.; Firsov, A. A. *Science* **2004**, *306*, 666-669.

3. Li, X.; Wang, X.; Zhang, L.; Lee, S.; Dai, H. *Science* **2008**, *319*, 1229-1232.

4. Yang, L.; Park, C. H.; Son, Y. W.; Cohen, M. L.; Louie, S. G. *Phys. Rev. Lett.* **2007**, *99*, 186801-186804.

5. Cómez-Navarro, C.; Meyer, J. C.; Sundaram, R. S.; Chuvilin, A.; Kurasch, S.; Burghard, M.; Kern, K.; Kaiser, U. *Nano Lett.* **2010**, *10*, 1144–1148.

6. Novoselov, K. S.; S.; Geim, A. K.; Morozov, S. V.; Jiang, D.; Katsnelson, M. I.; Grigorieva, I. V.; Dubonos, S. V.; Firsov, A. A. *Nature* **2005**, *438*,197-200.

7. Kosynkin, D. V.; Higginbothan, A. L.; Sinitskii, A.; Lomeda, J. R.; Dimiev, A. *Nature* **2009**, *458*, 872-876.

8. Lusk, M. T.; Carr, L. D. D. *Phys. Rev. Lett.* **2009**, *100*, 175503.

9. Chen, H. J.; Cullen, W. G. ; Jang, C. ; Fuhrer, M. S. ; Williams, E. D. *Phys. Rev. Lett.* **2009**, *102*, 236805.

10. Campos-Delgado, J.; Kim, Y. A.; Hayashi, T.; Morelos-Gómez, A.; Hofmann, M.p; Muramatsu, H.; Endo, M.; Terrones, H.; Shull, R. D.; Dresselhaus, M. S.; Terrones, M. *Chem. Phys. Lett.* **2009**, *469*, 177-182.

11. Coleman, V. A.; Knut, R. ; Grennberg, H. ; Jansson, U. ; Quinlan, R. ; Holloway, B. C. ; Sanyal, B. ; Eriksson, O. *J Phys. D Appl. Phys.* **2008**, *41*, 062001.

12. Hashimoto, A.; Suenaga, K.; Gloter, A.; Urita, K.; Iijima, S. *Nature* **2004**, *430*,870-873.

13. Eizenberga, M. ; Blakely, J. M. M. *Surface Science* **1979**, *82*, 228-236.

14. Aizawa, T.; Souda, R.; Otani, S.; Ishizawa, Y. *Phys. Rev. Lett.* ***1989,*** *64,* 768-771.

15. Kim, K. S.; Zhao, Y.; Jang, H.; Lee, S. Y.; Kim, J. M.; Kim, K. S.; Ahn, J.-H.; Kim, P.; Choi, J.-Y.; Hong, B. H. *Nature* **2009**, *457*, 706-710.

16. Li, X.; Cai, W.; An, J.; Kim, S. ; Nah, J. ; Yang, D.; Piner, R.; Velamakanni, A.; Jung, I.; Tutuc, E.; Banerjee, S. K.; Colombo, L.; Ruoff, R. S. *Science,* **2009,** *324,* 1312-1314.

17. Berger, C.; Song, Z.; Li, X.; Wu, X.; Brown, N.; Naud, C.; Mayou, D.; Li, T.; Hass, J.; Marchenkov, A. N.; Conrad, E. H.; First, P. N.; de Heer W. A. *Science* ***2006,*** *312***,** 1191-1196.

18. Ericson, L. M.; Fan, H.; Peng, H.; Davis, V. A.; Zhou, W.; Sulpizio, J.; Wang, Y.; Booker, R.; Vavro, J.; Guthy, C. et al. *Science*, **2004,** *305*,1447-1450.

19. Stankovich, S.; Dikin, D. A.; Dommett G. H. B.; Kohlhaas, K. M.; Zimney, E. J.; Stach, E. A.; Piner, R. D.; Nguyen, S. T.; Ruoff, R. S. *Nature*, **2006,** *442*, 282-286.

20. Elías, A. L.; Botello-Méndez, A. R.; Menese-Rodríguez, D.; González, V. J.; Ramírez-González, D.; Ci, L.; Muñoz-Sandoval, E.; Ajayan, P. M.; Terrones, H.; Terrones, M. *Nano Lett.* **2010**, *10*, 366-372.

21. Cano-Márquez, A. G.; Rodríguez-Macías, F. J.; Campos-Delgado, J.; Espinosa-González, C. G.; Tristán-López, F.; Ramírez-González, D.; Cullen, D. A.; Smith, D. J.; Terrones, M.; Vega-Cantú, Y. I. *Nano Lett.* **2009**, *9*, 1527–1533.

22. Jiao, L.; Zhang, L.; Wang, X.; Diankov, G.; Dai, H. *Nature* **2009**, *458*, 877-880.

23. Sinitskii, A.; Fursina, A. A.; Kosynkin, D. V.; Higginbotham, A. L.; Natelson, D.; Tour, J. M. *Appl. Phys. Lett.* **2009**, *95***,** 253108.

24. Novikov, Y. N.; Vol'pin, M. E. *Russ. Chem. Rev.* **1971**, *40*, 733-746.

25. Valles, C.; Drummond, C.; Saadaoui, H.; Furado, C. A.; He, M.; Roubeau, O.; Ortolani, L.; Monthioux, M.; Pénicaud, A. *J. Am. Chem. Soc.* **2008**, *47*, 15802-15804.

26. Viculis, L. M.; Mack, J. J.; Kaner, R. B. *Science* **2003**, *299*, 1361.

27. Ferrari, A. C.; Robertson, J. *Phys. Rev. B* **2000,** *61*, 14095-14107.

28. Kudin, K. N.; Ozbas, B.; Schniepp, H. C.; Prud'home, R. K.; Aksay, I. A.; Car, R. *Nano Letters* **2008**, *8*, 36-41.

29. Vidano, R.; Fischbach, D. B. *J Amer Cera Soc* **1978**, *61*, 13-17.

30. Campos-Delgado, J.; Romo-Herrera, J. M.; Jia, X.; Cullen, D. A.; Muramatsu, H.; Kim, Y. A.; Hayashi, T.; Ren, Z.; Smith, D. J.; Okuno, Y. et. al. *Nano Letters* **2008**, *8*, 2773-2778.

31. Suzuki S.; Maeda F.; Watanabe Y.; Ogino T. *Phys. Rev. B* **2003**, *67*, 115418.

32. Duclaux L.; Salvetat, J. P.; Lauginie, P.; Cacciaguera, T.; Faugère A. M.; Goze-Bac, C.; Bernier, P. *J Phys. Chem. Solids* **2003,** *64*, 571-581.

33. Guerarda, D.; Herolda, A. *Carbon* **1975**, *13*, 337-345.

34. Behabtu, N.; Lomeda, J. R.; Green, M. J.; Higginbotham, A. L.; Sinitskii, A.; Kosynkin, D. V.; Tsentalovich, D.; Parra-Vasquez, A. N. G.; Schmidt, J.; Kesselman, E.; Cohen, Y.; Talmon, Y.; Tour, J. M.; Pasquali, M. *Nat. Nanotech.* **2010**, *5*, 406-411.

4.7. Experimental Contributions

My contribution to the experimental work in this chapter is the following: optimization of the synthesis of GNRs via sonicating split MWNTs in chlorosulfonic acid and characterizations of those materials by XPS, SEM, Raman spectroscopy and UV-vis spectroscopy. Dmitry V. Kosynkin developed the idea of splitting MWNTs via intercalation of potassium metal and used molecular dynamics to model the intercalation reaction. Alexander Sinitskii measured the thickness and conductivity of GNRs. Zhengzong Sun imaged GNRs using TEM. Assistance in preparation of GNRs was received from Gorka Pera.

Chapter 5

In Situ Intercalation Replacement and Selective Functionalization of Graphene Nanoribbon Stacks

This chapter was entirely copied from Reference #1 of this section

5.1. Introduction

Graphene is a stable 2D material that holds great promise due to its having extraordinary electrical, mechanical, and thermal properties. Thus it is a potential building block for electronic devices. The abundance of carbon and its low toxicity are additional driving forces for the scientific community to search for applications of graphene in energy-related devices such as ultracapacitors, Li-ion batteries and solar cells and for catalysis.[2] However, two important issues need to be solved to realize the use of

graphene and its derivatives in those future applications: (a) bulk preparation of high quality graphene-based nanomaterials and (b) functionalization and incorporation of these materials into devices.

Since the report in 2004,[3] many different methods have been developed to yield graphene nanomaterials. These methods can be divided into bottom-up and topdown strategies.[2] Bottom-up strategies include chemical vapor deposition (CVD) growth[4,5] and organic synthesis.[6] Both methods can deliver high quality and relatively low-defect materials but they are hard to scale-up and process. On the other hand there is the scalable top-down approach where graphite or carbon nanotubes (CNTs) are used as a starting material. The most common preparation method of bulkquantity graphene is by exfoliation of oxidized graphite[7,8] with subsequent reduction[9] or high temperature annealing to produce more highly conjugated material.[10] The disadvantage of this method is the irreversible damage to the graphene basal plane and its consequently lower conductivity. High quality monolayer to few-layer graphene has been obtained in bulk quantities using different intercalation and thermal expansion techniques.[11-13] When tuning the physical properties and minimizing defects, one must also consider the shape of the material that is inherently governed by the graphite precursor for top-down approaches. It was reported that the width and edges of the graphene play important roles in defining the material's electronic properties.[14] CNTs are known precursors for production of bulk quantities of well-defined graphene nanoribbons (GNRs). To date several unzipping methods with reasonable yields have been reported.[15-19] Because of their high carbon aspect ratio, which is advantageous for mechanical processing, GNRs are good candidates for applications in energy related devices,1 catalysis, transparent

touch screens,[20] carbon fiber spinning,[21] formation of conductive polymer composites,[22] and low-loss-high permittivity composites.[23] When dealing with applications, the material should be available in bulk quantities and should be easily processable, since most of the applications require preparation of well-dispersed solutions or suspensions. Pristine graphene materials are very difficult to disperse, thus functionalization is generally required.

Layered carbon materials such as graphite or multiwalled carbon nanotubes (MWCNTs) are stable because of their fully π-conjugated aromatic system. Traditional organic synthetic approaches are thus limited to certain reactions. Polycyclic aromatic hydrocarbons (PAHs), close chemical relatives to graphene-based materials, are susceptible to electrophilic substitutions, nucleophilic and free radical reactions, addition reactions, reductions, oxidations, and rearrangements.[24] All of these reactions could be used for functionalization of graphene. However, the current graphene literature reports are limited mostly to oxidation, hydrogenation, and reductive functionalization methods. These methods generally produce a product with the desired physical properties such as solubility and dispersibility. The degree of functionalization in these cases is relatively high, mostly because the basal planes are functionalized, but functionalization of the basal plane inevitably leads to a suppressed conductivity as the π-conjugation is disturbed. Selective edge functionalization might be a solution to this problem. However, edge functionalization would likely only have an impact on physical properties in materials with high edge-to-basal plane carbon ratios such as in GNRs.

In the present study we further investigate the hypothesis that potassium intercalation between the walls of commercial MWCNTs would longitudinally split the

walls and furnish active carboanionic edges of the ribbons.[19] The increased reactivity of the edges compared to the basal plane would therefore preferably functionalize the edges of GNRs with desired electrophiles. Selective functionalization would introduce improved solubility without sacrificing conductivity. Further we investigate the replacement of intercalated metal with haloalkanes that then serve as intercalants in the resulting functionalized GNRs.

5.2. Experimental Procedures

Materials. Reactions were performed in dried glassware under an N_2 atmosphere unless stated otherwise. Reagent grade 1,2-dimethoxyethane was degassed with Ar, refluxed over sodium in an N_2 atmosphere, and freshly distilled. Other solvents were used without further distillation. Mitsui MWCNTs were received from Mitsui & Co. (lot no. 05072001K28). NTL-M grade MWCNTs were donated by Nanotech Laboratories, Inc. (5T10M10). All other commercially available reagents were used as received. Liquid Na/K alloy was prepared in a vial inside of a N_2 glovebox by pressing together freshly cut K (1 mol equiv) and Na (0.22 mol equiv) chunks using tweezers to facilitate the melting process. Amounts of liquid Na/K alloy indicated are by volume. Caution: All synthetic steps involving Na/K alloy should be carried out with extreme caution under strict exclusion of air or moisture and under inert gas and appropriate personal protection (hood, blast shields, face shield, protective and fire resistant clothing) should be used and worn at all times. 1-Iodohexadecane, 1-iodooctane, and 1-iodobutane were all obtained from Sigma-Aldrich and used as received without further purification. In-house deionized water was used during purification of the products.

Synthesis of Functionalized Graphene Nanoribbons Stacks and Intercalation Replacement. A sample of MWCNTS (100 mg, 8.3 mmol) was added to an oven-dried 250 mL round-bottom flask containing a magnetic stir bar. The vessel was then transferred to a N_2 glovebox where freshly distilled 1,2-dimethoxyethane (35 mL) and liquid Na/K alloy (0.29 mL) were added. The flask containing the suspension was then sealed with a septum and transferred out of the glovebox where the suspension was dispersed by a short 5 min ultrasonication (using ultrasonic cleaner Cole-Parmer model 08849-00) to yield a dark greenish to red suspension. After ultrasonication, the reaction mixture was vigorously stirred (450 rpm) at room temperature for 3 d. The reaction suspension was then quenched by the addition of the 1-iodoalkane (8.75 mmol) through a syringe and left to stir at room temperature for an additional day. Methanol (20 mL, 500 mmol) was then added to quench any excess Na/K alloy, and the mixture was stirred at room temperature for 10 min. For workup, the reaction mixture was filtered over a 0.45 μm pore size PTFE membrane. The filter cake was successively washed with THF (100 mL), i-PrOH (100 mL), H_2O (100 mL), i-PrOH (100 mL), THF (100 mL) and Et_2O (10 mL). Then Soxhlet extraction with THF was used for 3 d, and the product was dried in vacuum ($\sim 10^{-2}$ mbar) for 24 h.

Electron Microscopy. Samples were dispersed in chlorobenzene and bath sonicated using an ultrasonic cleaner for 15 min for a quick dispersion. A drop was cast on a 100 nm SiO_2/Si substrate, and large area low resolution images were taken at 20 kV under FEI Quanta 400 ESEM FEG scanning electron microscope and under a JEOL-6500 field-emission microscope.

Conductivity Measurements. Fabrication of HD-GNR devices was performed by tracking individual GNRs on the surface of 500 nm-thick thermal SiO_2 layer-covered highly doped Si substrates by SEM (JEOL-6500 microscope), followed by the patterning of 20 nm-thick Pt contacts by standard electron beam lithography. The electrical transport properties were tested using a probe station (Desert Cryogenics TT-probe 6 system) under vacuum with a chamber base pressure below 10^{-5} Torr. The *I-V* data were collected by an Agilent 4155C semiconductor parameter analyzer.

Evolved Gas Analysis (EGA) Experimental Part. Thermogravimetric measurements were performed on a Netzsch 449 F3 Jupiter instrument under a dynamic Ar (5.0) flow with a flow rate of 60 mL/min in a temperature range from 25 to 900 ºC. A heating rate of 10 K/min was used. About 5 mg of sample was placed in an alumina (Al_2O_3) crucible. Simultaneously mass spectrometry was performed on MS 403C Aëolos with a SEM Chenneltron detector and system pressure of 2 x 10^{-5} mbar. Gasses that evolved under TG heat treatment were transferred to the mass spectrometer through transfer capillary, quartz ID 75 μm, which was heated up to 220 ºC. The upper limit of the mass spectrometer detector was 100 AMU.

XRD. X-ray powder diffraction (XRD) was performed using a Rigaku D/Max 2550 diffractometer with Cu KR radiation (λ = 1.5418 Å). Where necessary the data obtained were analyzed and processed using the Jade 9 software package.

GC-MS. Gas chromatography–mass spectrometry (GC-MS) was performed on Agilent Technologies 6890N Network GC system coupled to an Agilent 5973 network mass selective detector.

SS ^{13}C NMR Spectroscopy. Spectra were obtained at 50.3MHz ^{13}C on a Bruker Avance 200 spectrometer with a probe for magic angle spinning (MAS) of rotors 4 mm in diameter. Chemical shifts are relative to the carbonyl carbon in glycine defined as 176.46 ppm.[25] Both samples in Figure 5.6 were dispersed in silica (10 wt % sample, 90 wt % silica). Parameters for the ^{1}H-^{13}CCP spectrum of functionalized and intercalated HD-GNRs (red curve in Figure 5.6): 7.6 kHz MAS (so that any spinning sidebands are at multiples of +151 or -151 ppm from a centerband), 90º ^{1}H pulse = 2.4 μs, contact time = 1 ms with ramped amplitude proton pulse, FID = 32.8 ms with spinal64 decoupling, relaxation delay =5 s, number of scans =40 400, line broadening = 50 Hz (1 ppm) used in processing the FID. Parameters for the ^{1}H-^{13}C CP/dipolar dephasing spectrum of functionalized and intercalated HD-GNRs (black curve in Figure 5.6): as above except that a pair of 25-μs dephasing periods with a central 8.3-μs, 180º ^{13}C refocusing pulse immediately preceded FID acquisition. Parameters for the ^{1}H-^{13}C CP spectrum of functionalized and intercalated HD-GNRs heated at 900 ºC for 20 min (blue curve in Figure 5.6) are the same as for the unheated sample (red curve) except for 85 000 scans. Parameters for the ^{1}H-^{13}C CP spectrum of 100% silica (control sample) are the same except for 55 000 scans; no signal was detected.

Raman Spectroscopy. The Raman spectra were acquired using a Renishow Raman RE01 microscope with 40 × lens; 514 nm wavelength laser was used for excitation.

Additional synthesis details, optical, SEM, AFM images, conductivity measurements, TGA, GC-MS, and XRD of the described materials are given in the Appendix E.

5.3. Results and Discussions

The reaction scheme for the selective edge *in situ* functionalization is depicted in Figure 5.1. In the first step commercially available MWCNTs (Nanotech Laboratories, Inc. (NTL) or Mitsui & Co.) were treated with Na/K alloy in 1,2-dimethoxyethane (DME) for several days. Since K (but not Na) can be easily intercalated into graphene galleries[26] and Englert *et al*. have shown that K can be successfully intercalated into

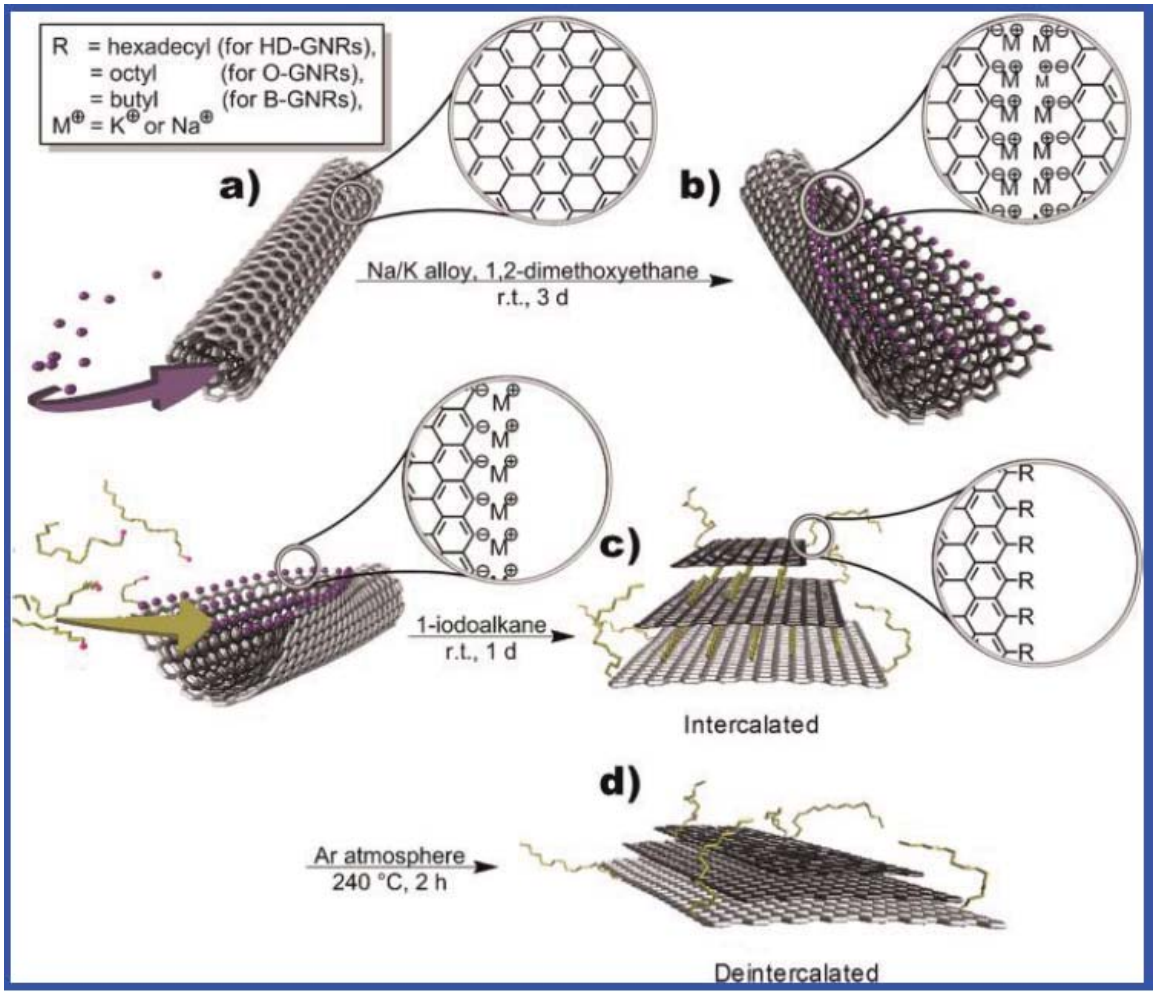

Figure 5.1 Proposed scheme for the in situ intercalation replacement and selective functionalization of GNRs: (a) intercalation of potassium between the walls of MWCNTs; (b) splitting process of MWCNTs and formation of active carboanionic edges

($M = K^+$ or Na^+); (c) in situ functionalization and intercalation of GNRs with alkyl groups; (d) deintercalation of functionalized GNRs.

graphite flakes using the above conditions,[27] we also expected K to intercalate between the walls of the MWCNTs. Our previous work has shown that the intercalation of the K is accompanied by partial longitudinal cracking of the walls as they tend to swell.[19] Under the conditions used, the edge atoms should be in the reduced carboanionic form and thus very reactive and susceptible to electrophilic attack. This reductive splitting can be visualized as the reaction mixture changes color from a dark black or brown color to a finely dispersed green or red suspension. The next step is the *in situ* functionalization; iodoalkanes (1-iodohexadecane, 1-iodooctane, and 1-iodobutane) are added to the reaction mixtures, presumably reacting with the active sites on the edges of the GNRs. As the reaction proceeds, the green or red color disappears. To produce proton functionalized GNRs (H-GNRs) we quenched the reaction mixture with methanol (described in detail in the Appendix E). To attain the intercalated compounds with a formula as close as possible to KC_8 or stage 1,[19] an excess of Na/K was used. Accordingly, it was necessary to add an excess of the iodoalkanes. This leads to side reactions, not just in the reaction solution, but also between the walls of the MWCNTs. The side products include alkanes, alkenes, and dimers of alkanes. SEM images clearly indicate that MWCNTs split to GNRs (Figure 5.2) in high yields. To quench any active species that were remaining, we treated the reaction mixture with methanol. The crude materials, hexadecylated-GNRs (HD-GNRs), octylated-GNRs (O-GNRs), and butylated-GNRs (B-GNRs), were collected by filtration using 0.45 μm PTFE-membranes and the filter cakes were washed with

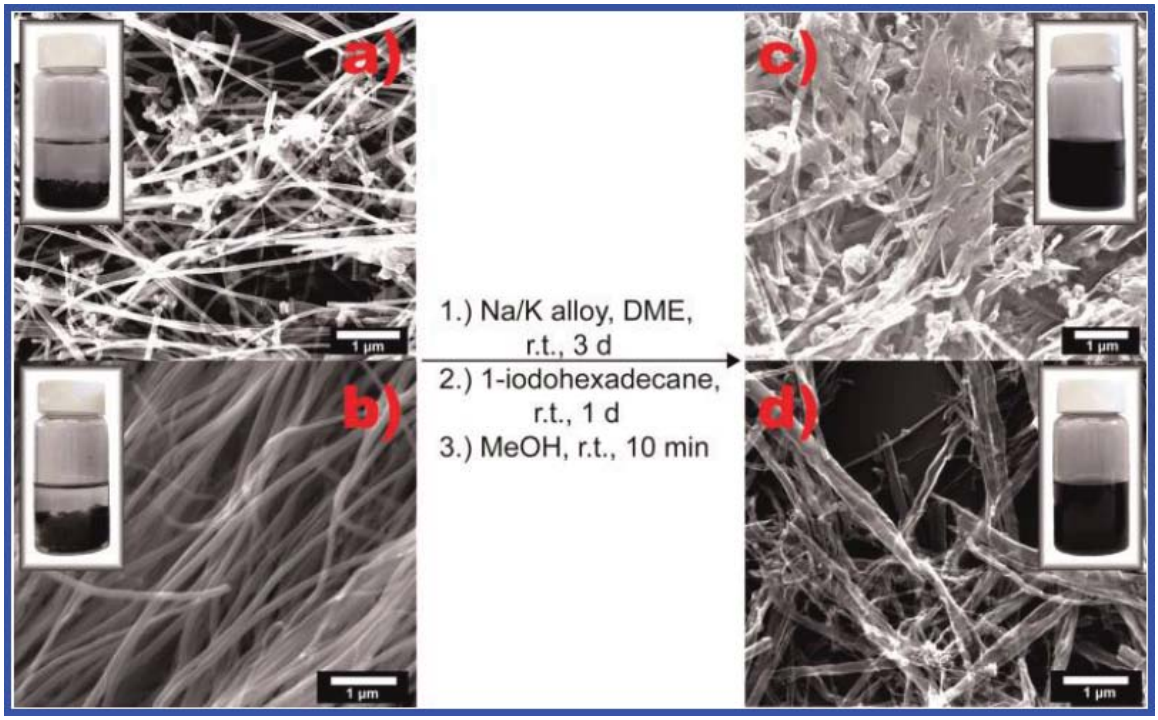

Figure 5.2 Solubility test. SEM images showing the splitting and functionalizing of commercially available MWCNTs and the photographic difference in solubility between functionalized GNRs and pristine MWCNTs: (a) pristine Mitsui MWNTs and a 0.1 mg/mL suspension in chloroform; (b) pristine NTL MWNTs and a 0.1 mg/mL suspension in chloroform; (c) Mitsui-originated HD-GNRs and a 0.1 mg/mL stable dispersion in chloroform; (d) NTL-originated HD-GNRs and a 0.1 mg/mL stable dispersion in chloroform.

organic solvents and water and then underwent Soxhlet extraction to remove the majority of the physisorbed impurities. Before analysis, all of the products were dried in vacuum (~10^{-2} Torr) at 60 °C for 24 h. To the best of our knowledge, a similarly efficient *in situ* one-pot method of converting MWCNTs to functionalized GNR stacks has not been reported. The efficiency of the synthesis and possible scale-up makes it further attractive.

5.3.1. Bulk Properties

The solubility of pristine graphitic materials is in general known to be poor. For bulk purposes, dispersing of the material is of great importance. For our solubility study, we focused on HD-GNRs. HD-GNRs exhibit an improvement in solubility and dispersibility in chloroform after a short sonication using simple ultrasonic cleaner. In Figure 5.2, where starting MWCNTs were compared to HD-GNRs, the difference is apparent. HD-GNRs show stable dispersions in chloroform for weeks, while MWCNTs cannot be dispersed using the same conditions. We have also performed solubility test for HD-GNRs and MWCNTs at 0.1 mg/mL concentrations in different solvents (Figure E1 in the Appendix E). HD-GNRs are well dispersible in common organic solvents such as 2-propanol, acetone, ethyl acetate, diethyl ether, chloroform, hexane, and chlorobenzene. After 1 h, HD-GNRs settle out in hexanes and diethyl ether, while remaining dispersed in the other solvents. Four days of shelf aging resulted in sedimentation of all of the suspensions except when in chloroform and chlorobenzene, which stayed well-dispersed for weeks. A low magnification SEM image and optical microscope image of drop cast HD-GNRs on a SiO2/Si substrate show well-dispersed material (Figure E2 in the Appendix E). However, the starting material MWCNTs showed sedimentation in all solvents tested in less than 1 h. Thus HD-GNRs are good candidates for applications where organic dispersibility is important.

5.3.2. Conductivity

A desirable property in functionalized GNRs is the retention of conductivity especially if they are to be used in transparent electrodes or energy-related devices such

as ultracapacitors, Li-ion batteries, and solar cells. We have fabricated a single HD-GNR device by depositing 20 nm thick Pt contacts on opposite ends of GNR stacks using

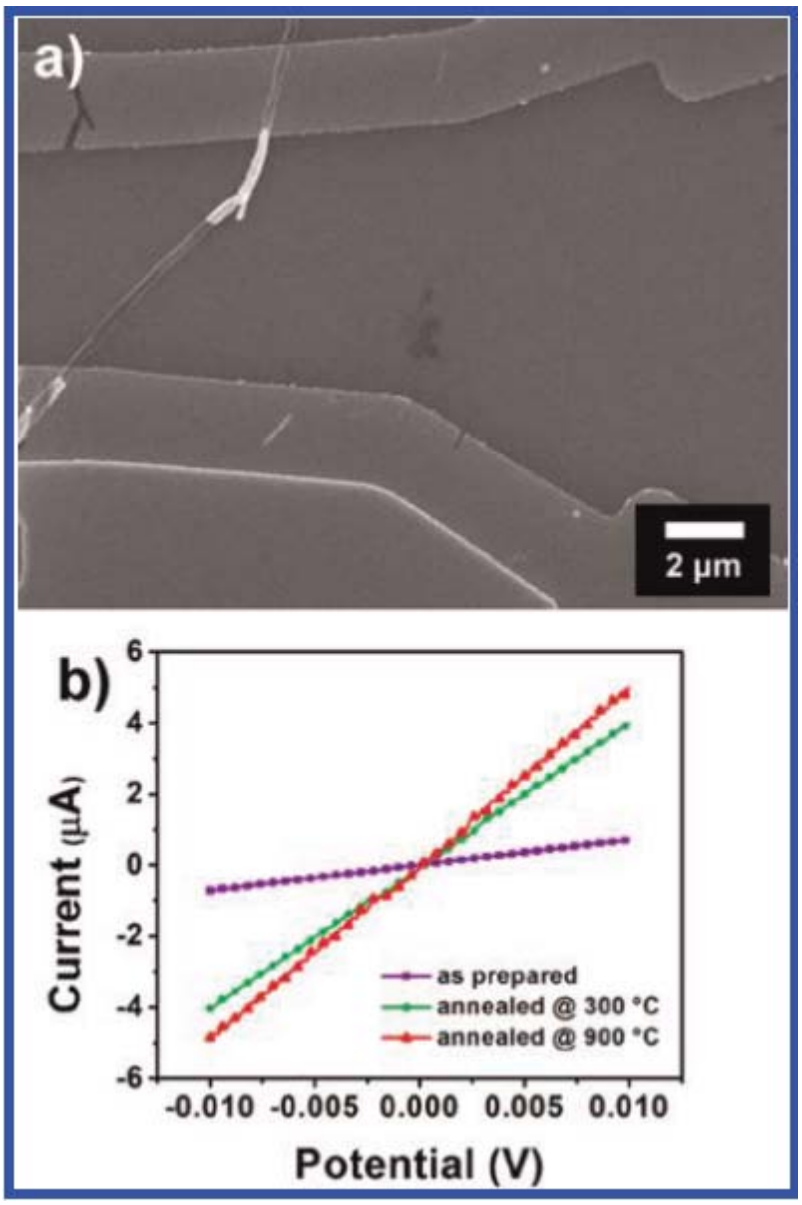

Figure 5.3 Fabricated device and conductivity measurements: (a) SEM image of a device made from HD-GNRs stack; NTL-originated MWCNTs and Pt electrodes; (b) change in electrical properties after different thermal treatment compared to as-prepared HD-GNRs.

lithography (Figure 5.3a). The HD-GNR stack used in the device was 7.9 μm long, ~300 nm wide (Figure E3 in the Appendix E), and ~30 nm thick. The thickness was estimated from the AFM image (Figure E4 in the Appendix E). The as-prepared, single ribbon device exhibited a conductivity of 600 S/cm (Equation E1 and Table E1 in the Appendix E). The conductivity increased almost six times to 3540 S/cm when the device was annealed at 300 °C. There are at least two reasons for such a difference in conductivity between the as-prepared sample and the sample annealed at 300 °C. The conductivity could be partially increased due to improved contact between the electrodes and the GNR stack. However, previous work on graphene materials with Pt-contacts shows that the good wetting of the carbon with Pt leads to a low-barrier contact,[19] thus the main contribution is probably due to deintercalation of hydrocarbons (but not necessarily defunctionalization) from the graphene galleries. The intercalated graphene galleries are electrically isolated from each other, as alkanes are known insulators; deintercalation reinstates the interaction between the graphene layers. A control experiment where HD-GNRs were heated at 300 °C for 2 h showed that their solubility in chloroform after annealing was comparable to the as-prepared HD-GNRs. The latter result speaks in favor of the HD functional groups staying intact at temperatures up to 300 °C. When the device was further heated to 900 °C, a temperature at which the HD functional groups are expected to have cleaved from the GNRs, the conductivity increased to 4260 S/cm. This small increase could indicate that edge functionalization does not substantially disturb the conductivity of the graphene basal planes. The conductivities of the functionalized HD-GNRs are comparable to previous literature reports on pristine materials such as graphite (200–8300 S/cm),[28] CNTs (1000–100000 S/cm),[29] and GNRs (~800 S/cm)[14, 19, 30] and

thus interesting for further study. Bulk conductivities of as-prepared samples were also measured using four-point probe measurement on pressed pellet. Similarly, relatively high conductivity ranging from 145 to 175 S/cm was observed, which is only 2.5 times smaller than conductivities of the starting material MWCNTs (Figure E5, Scheme E1 and Equation E2 in the Appendix E).

5.3.3. Evolved Gas Analysis (EGA)

Confirming edge functionalization *versus* intercalation remains challenging due to the expected low degree of edge carbons to nonedge carbons. The average GNRs stack with 250 nm width × 2.7μm length dimensions (estima ted from the SEM image, Figure E3 in the Appendix E) should have only 0.05 atomic % of edge carbons in GNRs (Figure E6 in the Appendix E). If all of the edge carbons are functionalized then the functional groups would contribute 1 wt % of the total weight to the HD-GNRs; 0.5 wt % if considering O-GNRs, and 0.25 wt % if considering B-GNRs. Since the expected degree of functionalization is low, we have used thermogravimetric analysis (TGA) coupled with a quadrupole mass spectrometer (QMS) to detect thermalized products. The sensitivity of QMS should give some insight into the quantitative nature of the alkylated graphene nanoribbons (A-GNRs). The TGA of HD-GNRs shows a total weight loss of 37% in the range between 40 and 900 °C, which is far above the expected value of 1% (Figure 5.4a). The reference compound, hexadecane, has a specific fragmentation pattern, with high abundance fragments with decreasing intensities at m/z = 57, 43, 71, 85, 29, and 99. Similar patterns are expected for octane m/z 43, 57, 29, 85, 71 and for butane m/z 43, 29, 15, 57. These fragments were also found in the evolved gases during the TGA, indicating

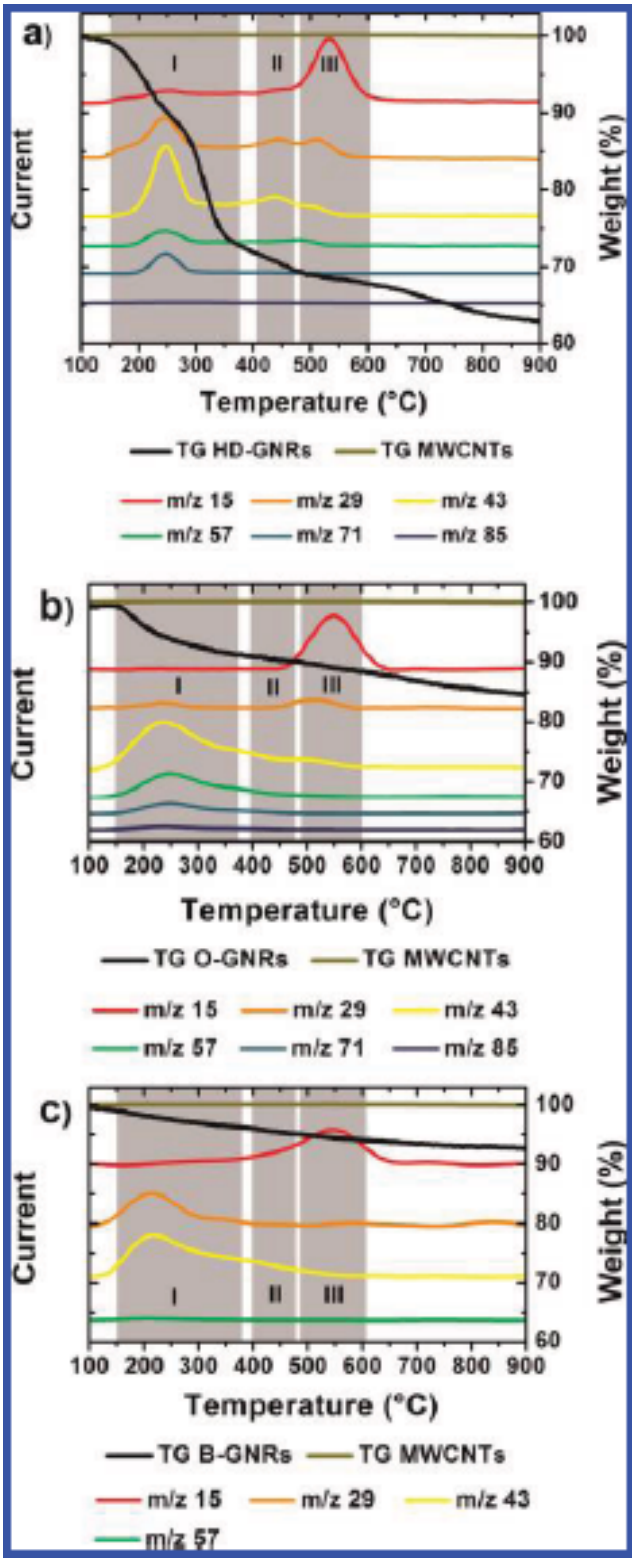
a)
I
II
III
Current
Weight (%)
100
90
80
70
60
100 200 300 400 500 600 700 800 900
Temperature (°C)
TG HD-GNRs
TG MWCNTs
m/z 15
m/z 29
m/z 43
m/z 57
m/z 71
m/z 85
b)
I
II
III
Current
Weight (%)
100
90
80
70
60
100 200 300 400 500 600 700 800 900
Temperature (°C)
TG O-GNRs
TG MWCNTs
m/z 15
m/z 29
m/z 43
m/z 57
m/z 71
m/z 85
c)
I
II
III
Current
Weight (%)
100
90
80
70
60
100 200 300 400 500 600 700 800 900
Temperature (°C)
TG B-GNRs
TG MWCNTs
m/z 15
m/z 29
m/z 43
m/z 57

Figure 5.4 Evolved gas analysis. Different colors represent fragments with m/z that correspond to alkane fragments. Black and gold curves represent the TGA profile of functionalized GNRs and pristine MWCNTs, respectively. Gray rectangles represent region I, region II, and region III, respectively. (a) TGA-MS of HD-GNRs; (b) TGA-MS of O-GNRs, and (c) TGA-MS of B-GNRs.

that alkyl groups are present in the A-GNRs samples (Figure 5.4). However, there are three distinct temperature ranges during which the alkyl groups are present in the off-gas from HD-GNR thermolysis products (Figure 5.4a). The first is the range between 154 and 374 °C (region I), where the weight loss is 26%. The second range is between 400 and 474 °C with a weight loss of 2% (region II) while the range between 480 and 612 °C had a 2% weight loss (region III). Region I is assigned to deintercalation of alkanes; see what follows for further explanation. Regions II and III were assigned to covalently bound alkyl groups, most likely hexadecyl. The temperature interval for region II corresponds with previous reports on covalently attached organic moieties on different carbon substrates.[27, 31] The mass spectrometer detection limit is up to 100 atomic mass units; thus the molecular ion corresponding to the hexadecyl moiety could not be detected. Fragments *m*/*z* 29, 15, 43, 57, 85, and 71 that are present in region II are indications that fragmentation due to thermal cleavage of the hexadecyl group is most likely occurring. The major fragments present in region III are the methyl and ethyl groups (*m*/*z* 15, 29) which could be the remainder of the hexadecyl group bound directly to the graphene substrate. Similar results were obtained for O-GNRs and B-GNRs (Figure 5.4b,c), where we observed 7 wt % loss between 139 and 293 °C, and 4 wt % between 121 and 247 °C

for region I, respectively. Region II between 448 and 526 °C for O-GNRs shows a 1 wt % loss, while region III between 526 and 628 °C had a 1.3 wt % loss. B-GNRs show 1.3 wt % loss for region II between 328 and 453 °C and 1.7 wt % for region III between 453 and 636 °C. According to this data and the assumption that regions II and III correspond to the same functional groups but have different fragmentation temperatures, the degree of functionalization is 4.6% for HD-GNRs, 2.3% for O-GNRs, and 3% for B-GNRs. The reason for the discrepancy between the estimated degree of edge functionalization and the actual degree of functionalization is unclear.

To exclude the reaction between solvent and active GNRs, the EGA of methanol-quenched, thus hydrogen terminated, GNRs (H-GNRs) was also done. TGA-MS analysis confirmed the absence of all fragments except *m*/*z* 15, the methyl fragment between 400 and 600 °C (Figure E7 in the Appendix E). The methyl fragment could be the result of rearrangements with successive cleavage on defects and edges where carbons are expected to be hydrogen-terminated or from trace methanol.[15]

5.3.4. X-ray Powder Diffraction (XRD) Analysis

For direct evidence of deintercalation in region I, HD-GNRs thermally treated at temperatures of 240, 530, and 900 °C were prepared, and XRD diffractograms were recorded and analyzed (Figure 5.5a). The total weight loss for the sample heated at 240 °C for 2 h was 26%, which corresponds to the weight loss in region I in Figure 5.4a. For the sample heated at 530 °C for 2 h, the weight loss was 32%, and for the sample heated at 900 °C for 20 min, the weight loss was 39% (for the TGA plots of the thermally treated HD-GNRs samples see the Appendix E Figure E8).

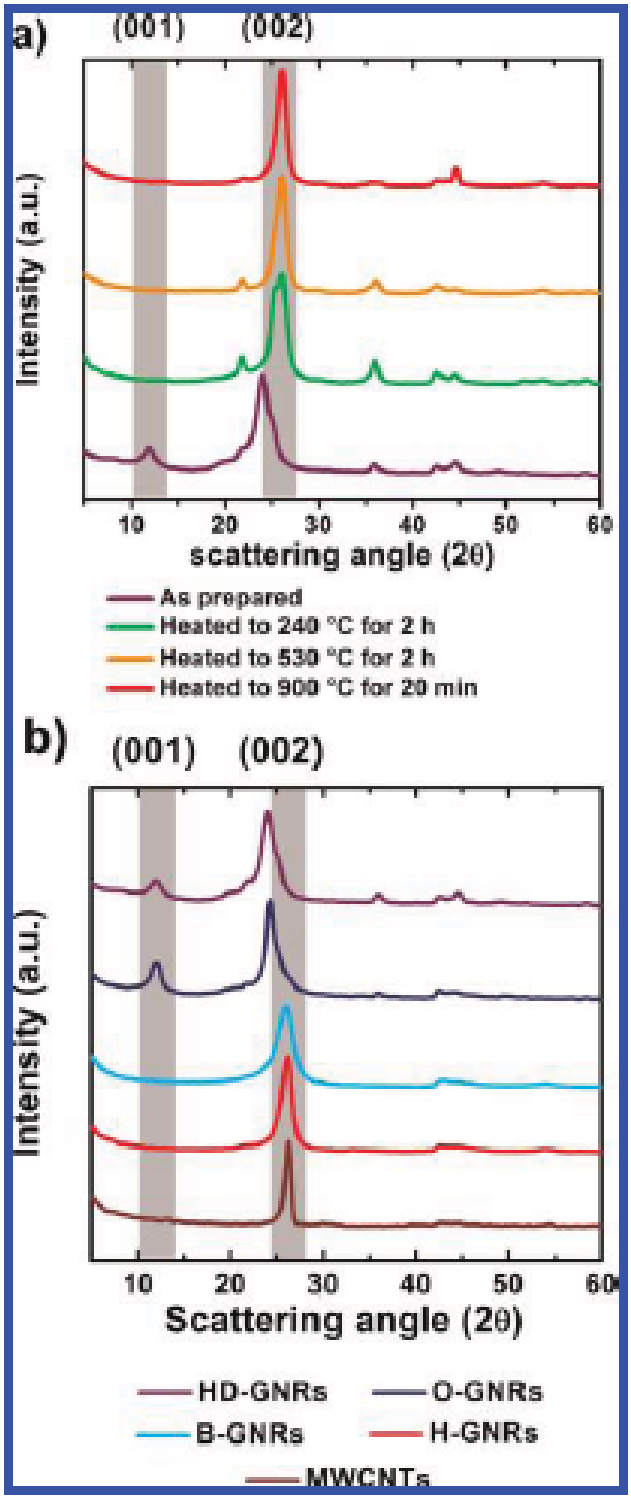

Figure 5.5 Powder diffraction patterns. (a) Comparison of as-prepared intercalated HD-GNRs and thermally treated HD-GNRs where deintercalation is observed. (b)

Comparison of functionalized HD-GNRs, O-GNRs, B-GNRs, GNRs, and MWCNTs. Peaks at 21.8°, 25.3°, 35.9°, 42.4°, 44.4°, 51.8°, 56.8°, and 58.4° 2θ angle correspond to low concentrations of KI impurity, which could not be removed.

The XRD diffractogram for the as-prepared sample contains well-pronounced diffraction lines at 12.0° and 24.2° 2θ angle, which correspond to the (001) and (002) signals of a stage 1 intercalation compound, respectively. The calculated *c*-axis repeat distance (I_c) is 0.738 nm, which is the typical spacing (d_s) between the two carbon layers sandwiching the layer of intercalant. As one can see from Figure 5.5a, both the 12.0° and 24.2° signals disappear after heating at 240 °C. The new diffraction line at 26.2° 2θ angle corresponding to the (002) signal of graphite appears instead.

The sample heated to 240 °C and then cooled to room temperature can be considered an intermediate state between the fully intercalated as-prepared sample and the one heated for 2 h at 240 °C. The weight loss during heating to 240 °C was ~12% (Figure E8 in the Appendix E). The sample that was heated and then cooled contains both the 24.2° signal and the 26.2° signal in a ratio of ~1:2 (Figure E12 in the Appendix E). Interestingly, no intermediate stage compound was detected in the sample. This is very unusual for graphite intercalation compounds (GICs), where graphite gradually intercalates and then gradually deintercalates, sequentially going through all the stage numbers.[26] Instead we detect only the two states, the stage 1 GIC and the nonintercalated graphitic GNRs. We suggest that the mixed stage comes from different GNRs. Individual GNRs probably deintercalate quickly and completely; the observed “mixed stage” is simply a mixture of completely intercalated and completely deintercalated individual

GNR stacks. Samples heated at temperatures of 530 and 900 °C are completely deintercalated and give diffractograms identical to H-GNRs or the starting material MWNTs (Figure 5.5b). Since weight losses of 7% and 4% were also observed for O-GNRs and B-GNRs in region I, XRD diffractograms were also recorded for as-prepared samples. However, O-GNRs show similar intercalation compounds as HD-GNRs, with I_c spacing between graphene layers of 0.731 nm. Interestingly, B-GNRs do not show any intercalation (Figure 5.5b), since the diffractograms are identical to H-GNRs or MWNTs. The reason might be in the size of the intercalant. In the case of HD-GNRs, it is expected to be at least 16 or 32 carbon chains (the latter is the dimer product). Hexadecane and octane are higher boiling point liquids while dotriacontane is a solid. On the other hand butane is a gas which is likely too volatile and mobile to form a stable GIC. For HD-GNRs, the proposed major intercalant is dotriacontane, but others cannot be excluded. The synthesis of HD-GNRs, as discussed earlier, leads to side products that are also potential intercalents. Two control experiments produced evidence that dotriacontane is indeed the main component. In the first control experiment 1-iodohexadecane was added into the dispersion of Na/K in DME (See the Appendix E for details). Gas chromatography–mass spectrometry (GC–MS) showed the presence of 1-hexadecene and hexadecane as minor components (21% and 19%, respectively) and dotriacontane as the major component (60%) of the reaction mixture. Another experiment with as-prepared HD-GNRs was done. HD-GNRs were heated at 150 °C in vacuum. A coldfinger cooled to 0 °C was connected to the system to capture products that were released. Analysis of the collected vapors using GC–MS again showed dotriacontane as the major component (45%). Other components detected were 1-hexadecene (6%), hexadecane (35%), and

starting material 1-iodohexadecane (13%, for the GC–MS analysis see the Appendix E Figure E9).

5.3.5. X-ray Powder Diffraction (XRD) Analysis Solid-State ^{13}C Nuclear Magnetic Resonance Spectroscopy (SS NMR)

To further investigate the nature of the intercalent, two types of magic angle spinning (MAS) NMR experiments were performed. The relatively high conductivity of HD-GNRs caused severe probe tuning problems, which initially prevented useful ^{1}H–^{13}C cross-polarization (CP) and direct ^{13}C pulse spectra from being obtained. However, dispersing the sample in silica (an approach previously used to obtain a ^{13}C spectrum of graphite[32]) enabled the ^{13}C and ^{1}H channels to be properly tuned on a sample of 10 wt % HD-GNRs and 90 wt % silica.

In the CP spectrum of the unheated material (Figure 5.6, red spectrum), two broad, overlapping bands are evident. The band centered at about 90 ppm is thought to be from several types of carbons: graphene sheet sp^2 C–H carbons, graphene sheet sp^2 carbons that are either on or near the edge of the sheet or near a covalently bound hexadecyl group or intercalated alkane and thus are capable of being cross polarized, and from the downfield tail of the signal from the methylene carbons in covalently bound hexadecyl groups and in intercalated side products (*e.g.*, hexadecane, 1-hexadecene, and dotriacontane). The band centered at about 90 ppm is unusually broad and shielded, as is the signal from the carbons detected in a direct ^{13}C pulse spectrum of graphite dispersed in silica.[32] The breadth of the band centered at about 90 ppm can be at least partially attributed to the inability of MAS to completely remove the anisotropy of the magnetic

susceptibility in the graphene sheets,[32,33] while the shielding can be attributed to the diamagnetic shift in the δ_{33} component of the shielding tensor of the numerous graphene carbons in a very large condensed aromatic ring system.[33] This broadening and shielding is reminiscent of what is observed as graphite oxide is steadily reduced and becomes increasingly like graphite.[34]

The band centered at about 0 ppm is thought to be from the methylene carbons indicated above and from the upfield tail of the signal from graphene sheet sp^2 carbons. The band centered at about 0 ppm is also unusually shielded, as would be expected if the covalently bound hexadecyl groups or intercalated alkanes are sandwiched between the graphene sheets and thus are subjected to a large diamagnetic susceptibility resulting from delocalized electrons (a π-electron ring current) in the graphene sheets. Indeed, a less dramatic shielding effect but much better resolution is observed with anthracite bearing dodecyl groups on the edges.[35] In contrast, the central methylene carbons in the methylene chains constrained to be above an aromatic ring in molecules such as [12]-paracyclophane[36] and various 1,*n*-dioxa[*n*](2,7)pyreneophanes[37] experience only a very small ring current shielding effect. The much weaker signal from the methyl carbons in the HD-GNRs is not recognizable.

The 50-μs dephasing period in the dipolar dephasing experiment on the unheated material (Figure 5.6, black spectrum) strongly attenuates the band centered at about 90 ppm and completely eliminates the band centered at about 0 ppm. Since this dephasing period is designed to eliminate CH and CH_2 signals with minimal attenuation of quaternary carbon signals,[35] the less shielded band in the basic (red) CP spectrum has significant contributions from graphene sheet sp^2 C–H carbons and the downfield tail of

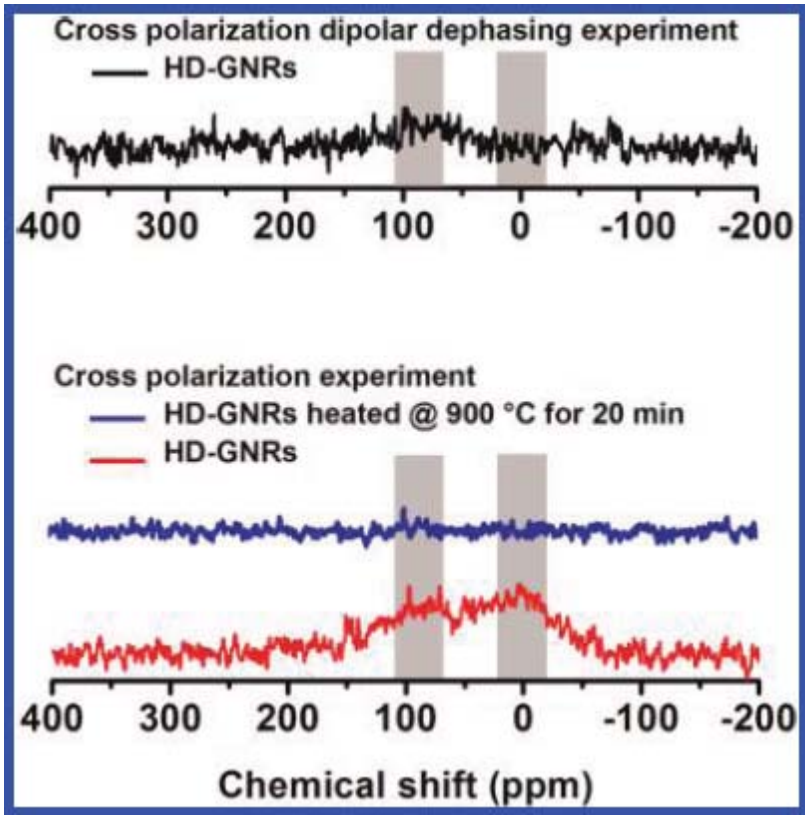

Figure 5.6 SS NMR. Cross-polarization experiment of functionalized and intercalated HD-GNRs (red curve) and defunctionalized and deintercalated HD-GNRs after heating at 900 ºC for 20 min (blue curve). Cross-polarization dipolar dephasing experiment of functionalized and intercalated HD-GNRs (black curve).

the signal from the various methylene carbons, while the more shielded band in the basic CP spectrum is consistent with the various methylene carbons and the upfield tail of the signal from graphene sheet sp^2 C–H carbons. The relatively immobile nature of the covalently bound hexadecyl groups and intercalated alkanes results in a correspondingly strong $^{1}H–^{13}C$ dipole–dipole interaction that both makes it possible for these methylene groups to cross polarize (red spectrum) and then to have the signal rapidly decay (black

spectrum). The very weak signal centered at about 90 ppm in the dephasing experiment may result from the attenuated signal from graphene sheet sp^2 carbons that poorly cross polarized.

The CP spectrum of the heated material (Figure 5.6, blue spectrum) shows no signal above the noise. As seen from the conductivity, TGA, and XRD results, defunctionalization and deintercalation at this temperature is complete. With no covalently bound hexadecyl groups or intercalated alkanes remaining, no NMR signal is detected. The importance of these hexadecyl groups and alkanes for generating the signals in the spectrum of the unheated material (red spectrum) is evident.

5.3.6. Raman Spectroscopy

The Raman spectrum of the as-prepared sample is significantly enhanced compared to the heated samples (Figure 5.7). This is an additional argument in support of formation of the intercalation compound. It is known that when several species are intercalated into graphite, or simply physisorbed on the graphene surface, the Raman spectra are enhanced.[38,39] No blue-shift of the G-peak is detected, however. This suggests that the intercalant in HD-GNRs is neutral toward carbon and does not charge the carbon layers. The spectrum of the as-prepared sample contains a D-peak at ~1360 cm^{-1} of very high intensity and the G+D peak at ~2950 cm^{-1}. This suggests that significant disorder in the system was induced by splitting[18] and intercalation. This is rather unusual, because for most of the known GIC compounds, intercalation does not cause appearance of the D-band. The D-band gradually decreases with heating and is finally of the same magnitude as nonintercalated split GNRs. The D/G ratio can be considered a measure of disorder.

The fact that it decreases suggests that disorder induced by the intercalant decreases when the intercalant is removed. The 2D peak in both the parent MWCNTs and GNRs is single-Lorentzian, suggesting no AB stacking. This is quite natural, since the walls in MWCNT have different chiralities. They retain their structure after splitting. Hence, the layers in the GNR have some degree of single-layer character.

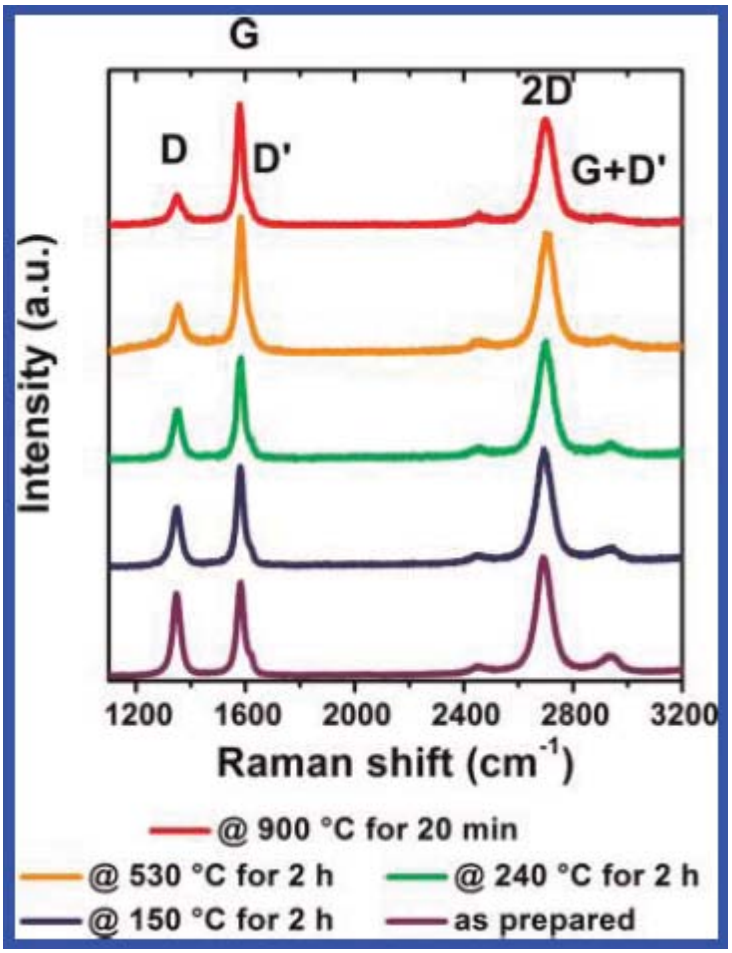

Figure 5.7 Raman spectra. Comparison of thermally treated HD-GNRs with as-prepared sample.

We hypothesize that intercalation is possible only when the reaction of intercalated K and 1-iodoalkane occurs between graphene sheets. The byproduct KI is

forced out, while newly formed alkanes and alkenes (as well as covalently bound alkyl groups) take their places between sheets. For this process the term “replacement-driven intercalation” is introduced. To partially confirm the latter, we performed a control experiment, where instead of 1-iodohexadecane, hexadecane was used (See the Appendix E for details). Under the same reaction conditions, no intercalation was observed, and that was confirmed by XRD (Appendix E Figure E10), where the (002) signal was observed at 26.2° 2θ angle, which corresponds to nonintercalated material, and by TGA, where we observed a weight loss of ~2% in the region between room temperature and 800 °C (Appendix E Figure E11).

5.4. Conclusions

A high yielding conversion of commercially available MWCNTs to *in situ* functionalized GNR stacks was achieved by a reductive method. GNRs bearing long alkyl chains are well-dispersible in organic solvents such as alcohols, ketones, ethers, and alkanes. Particularly stable dispersions are produced in chloroform or chlorobenzene. HD-GNRs exhibit relatively high GNR conductivity as well as bulk material conductivity. The conductivity of ~3540 S/cm of single deintercalated HD-GNR was achieved through minimal interruption of the conjugated π-system of the basal plane. Therefore we propose that functionalization occurs preferably on the edges of graphene. The concept of edge functionalization was partially supported by EGA, enhanced solubility, and relatively high conductivity of single and bulk-functionalized material. Replacement of intercalated addends was observed and thoroughly investigated for the HD-GNRs and O-GNRs. TGA-MS showed deintercalation of alkanes and alkenes at

temperatures between 140 and 300 °C. XRD revealed a stage 1 intercalation compound for the as-prepared samples. Interestingly, no intermediate stage compounds were detected. GC–MS showed dotriacontane as a major intercalant compound in HD-GNRs. Further, solid-state ^{13}C nuclear magnetic resonance spectra of HD-GNRs were consistent with the presence of methylene carbons in covalently bound hexadecyl groups and intercalated alkanes, as the signal attributed to the methylene carbons is unusually shielded and disappears after the sample is deintercalated and defunctionalized by heating. Similarly, Raman spectroscopy for the as-prepared sample indicated the intercalation compound. XRD and Raman spectroscopy revealed that thermal treatment of intercalated HD-GNRs up to ~ 300 °C leads to full deintercalation. However, covalently bound functional groups are stable at that temperature and still provide enhanced solubility, as the deintercalated HD-GNRs are still soluble in organic solvents. Functionalized GNRs with enhanced properties such as dispersibility and conductivity should be of great interest for bulk application as well as further basic research since improved processability and scale-up is possible. Possible fields of application are catalysis, ultracapacitors, transparent touch screens, carbon fiber spinning, formation of conductive polymer composites, and low-loss, high-permittivity composites. Further, the intercalation and functionalization principle could be used in the field of organic-based Li-ion batteries where the intercalant or addend would bear the redox center, as the method enables variations in functional addends.

5.5. Acknowledgements

We thank MI-SWACO, the Advanced Energy Consortium (BG Group, Halliburton, Conoco Phillips, bp, OXY, Marathon, Shell, Total, Petrobras, Schlumberger), the AFOSR (FA9550-09-1-0581), Center of Excellence Low Carbon Technologies, Slovenia (CO NOT), Center of Excellence Advanced Materials and Technologies for the Future, Slovenia (CO NAMASTE), the Lockheed Martin Corporation through the LANCER IV Program, NSF (CHE 0947054), and the ONR MURI program (Grant Nos. 00006766, N00014-09-1-1066) for funding. We thank Drs. A. Tanioka and M. Endo for the donation of the Mitsui MWCNTs, and Nanotech Laboratories, Inc. for the NTL MWCNTs.

5.6. References

1. Genorio, B.; Lu, W.; Dimiev, A. M.; Zhu, Y.; Raji, A.-R. O.; Novosel, B.; Alemany, L. B.; Tour, J. M. *ACS Nano* **2012**, *6*, 4231-4240.
2. Luo, B.; Liu, S.; Zhi, L. *Small* **2011**, *8*, 630-646.
3. Novoselov, K. S.; Geim, A. K.; Morozov, S. V.; Jiang, D.; Zhang, Y.; Dubonos, S. V.; Grigorieva, I. V.; Firsov, A. A. *Science* **2004**, *306*, 666– 669.
4. Li, X.; Cai, W.; An, J.; Kim, S.; Nah, J.; Yang, D.; Piner, R.; Velamakanni, A.; Jung, I.; Tutuc, E.; Banerjee, S. K.; Colombo, L.; Ruoff, R. S. *Science* **2009**, *324*, 1312– 1314.
5. Yu, Q.; Jauregui, L. A.; Wu, W.; Colby, R.; Tian, J.; Su, Z.; Cao, H.; Liu, Z.; Pandey, D.; Wei, D.; Chung, T. F.; Peng, P.; Guisinger, N. P.; Stach, E. A.; Bao, J.; Pei, S.-S.; Chen, Y. P. *Nat. Mater.* **2011**, *10*, 443– 449

6. Wu, J.; Pisula, W.; Müllen, K. *Chem. Rev.* **2007**, *107*, 718-747.

7. Hummers, W. S.; Offeman, R. E.; *J. Am. Chem. Soc.* **1958**, *80*, 1339-1339.

8. Marcano, D. C.; Kosynkin, D. V.; Berlin, J. M.; Sinitskii, A.; Sun, Z.; Slesarev, A.; Alemany, L. B.; Lu, W.; Tour, J. M. *ACS Nano* **2010**, *4*, 4806-4814.

9. Stankovich, S.; Dikin, D. A.; Piner, R. D.; Kohlhaas, K. A.; Kleinhammers, A.; Jia, Y.; Wu, Y.; Nguyen, S. T.; Ruoff, R. S. *Carbon* **2010**, *4*, 4806-4814.

10. Becerril, H. A.; Mao, J.; Liu, Z.; Stoltenberg, R. M.; Bao, Z.; Chen, Y. *ACS Nano* **2008**, *2*, 463-470.

11. Li, X.; Zhang, G.; Bai, X.; Sun, X.; Wang, X.; Wang, E.; Dai, H. *Nat. Nanotechnol.* **2008**, *3*, 538-542.

12. Lee, J. H.; Shin, D. W.; Makotchenko, V. G.; Nazarov, A. S.; Fedorov, V. E.; Kin, Y. H.; Choi, J.-Y.; Kin, J. M.; Yoo, J.-B. *Adv. Mater.* **2009**, *21*, 4383-4387.

13. Shih, C.; Vijayaraghavan, A.; Krishnan, R.; Sharma, R.; Han, J. H.; Ham, M. H.; Jin, Z.; Lin, S.; Paulus, G. L. C.; Reuel, N. F.; Wang, Q. H.; Blankschtein, D.; Strano, M. S. *Nat. Nanotechnol.* **2011**, *6*, 439-445.

14. Li, X.; Wang, X.; Zhang, L.; Lee, S.; Dai, H. *Science* **2008**, *319*, 1229-1232.

15. Kosynkin, D. V.; Higginbotham, A. L.; Sinitskii, A.; Lomeda, J. R.; Dimiev, A.; Price, B. K.; Tour, J. M. *Nature* **2009**, *458*, 872-876.

16. Jiao, L.; Wang, X.; Diankov, G.; Wang, H.; Dai, H. *Nat. Nanotechnol.* **2010**, *5*, 321-325.

17. Wang, J.; Ma, L.; Yuan, Q.; Zhu, L.; Ding, F. *Angew. Chem., Int. Ed.* **2011**, *50*, 1-6.

18. Cano-Máquez, A. G.; Rodríguez-Macías, F. J.; Campos-Delgado, J.; Espinosa-González, C. G.; Tristán-López, F.; Ramírez-González, D.; Cullen, D.; Smith, D. J.; Terrones, M.; Vega-Cantú, Y. I. *Nano Lett.* **2009**, *9*, 1527-1533.

19. Konsynkin, D. V.; Lu, W.; Sinitskii, A.; Pera, G.; Sun, Z.; Tour, J. M. *ACS Nano* **2011**, *5*, 968-974.

20. Zhu, Y.; Sun, Z.; Yan, Z.; Jin, Z.; Tour, J. M. *ACS Nano* **2011**, *5*, 6472-6479.

21. Ericson, L. M.; Fan, H.; Peng, H.; Davis, V. A.; Zhou, W.; Sulpizio, J.; Wang, Y.; Booker, R.; Vavro, J.; Guthy, C. *et al. Science* **2004**, *305*, 1447-1450.

22. Stankovich, S.; Dikin, D. A.; Dommett, G. H. B.; Kohlhass, K. M.; Zimney, E. J.; Stach, E. A.; Piner, R. D.; Nguyen, S. T.; Ruoff, R. S. *Nature* **2006**, *442*, 282-286.

23. Dimiev, A.; Lu, W.; Zeller, K.; Crowgey, B.; Kempel, L. C.; Tour, J. M. *ACS App. Mater. Interfaces* **2011**, *3*, 4657-4661.

24. Harvey, R. G. *Polycyclic Aromatic Hydrocarbons;* Wiley-VCH, Inc.: New York, 1997; p 667.

25. Hayashi, S.; Hayamizu, K. *Bull. Chem. Soc. Jpn.* **1991**, *64*, 685-687.

26. Dresselhaus, M. S.; Dresselhaus, G. *Adv. Phys.* **2002**, *51*, 1-186.

27. Englert, J. M.; Dotzer, C.; Yang, G.; Schmid, M.; Papp, C.; Gottfried, J. M.; Steinruck, H.-P.; Spiecker, E.; Hauke, F.; Hirsch, A. *Nat. Chem.* **2011**, *3*, 279-286.

28. American Institute of Physics. *American Institute of Physics Handbook;* McGraw-Hill, 1972.

29. Ebbesen, T. W.; Lezec, H. J.; Hiura, H.; Bennett, J. W.; Ghaemi, H. F.; Thio, T. *Nature* **1996**, *382*, 54-56.

30. Jiao, L.; Zhang, L.; Wang, X.; Diankov, G.; Dai, H. *Nature* **2009**, *458*, 877-880.

31. Sun, Y.; Mukherjee, A.; Kuznetsov, O.; Thaner, R.; Alemany, L. B.; Billups, W. E. *Energy Fuels* **2011**, *25,* 1571-1577.

32. Jiang, Y. J.; Solum, M. S.; Pugmire, R. J.; Grant, D. M.; Schobert, H. H.; Pappano, P. J. *Energy Fuels* **2002**, *16,* 1296-1300.

33. Pugmire, R. J.; Solum, M. S.; Jiang, J.; Sarofim, A. F.; Veranth, J.; Schobert, H. H.; Pappano, P. J. *Prepr. Symp.-Am. Chem. Soc., Div. Fuel Chem.* **2002**, *47,* 733-735.

34. Gao, W.; Alemany, L. B.; Ci, L.; Ajayan, P. M. *Nat. Chem.* **2009**, *1,* 403-408.

35. Sun, Y.; Kuznetsov, O.; Alemany, L. B.; Billups, W. E. *Energy Fuels* **2011**, *25,* 3997-4005.

36. Levin, R. H.; Roberts, J. D. *Tetrahedron Lett.* **1973**, *14,* 135-138.

37. Bodwell, G. J.; Bridson, J. N.; Cyrañski, M. K.; Kennedy, J. W. J.; Krygowski, T. M.; Mannion, M. R.; Miller, D. O. *J Org. Chem.* **2003**, *68,* 2089-2098.

38. Eklund, P. C.; Mahan, G. D.; Splar, J. G.; Zhang, J. M.; Arakawa, E. T.; Hoffman, D. M. *Phys. Rev. B* **1988**, *37,* 691-698.

39. Jung, N.; Crowther, A. C.; Kim, N.; Kim, P.; Brus, L. *ACS Nano* **2010**, *4,* 7005-7013.

5.7. Experimental Contributions

My contribution to the experimental work in this chapter is the following: experiment design and characterizations of functionalization of graphene nanoribbon stacks with Bostjan Genorio. Yu Zhu fabricated and tested GNRs devices and Barbara Novosel performed TG-MS measurements. Assistance in preparation and characterizations

of graphene nanoribbon stacks was received from Ayrat M. Dimiev, Abdul-Rahman O. Raji and Lawrence B. Alemany.

Chapter 6

Polymerization-Assisted Splitting and Exfoliation of Carbon Nanotubes for One-Pot Synthesis of Polymer-Functionalized Graphene Nanoribbons

6.1. Introduction

Due to their interesting electronic and mechanical properties,[1] graphene nanoribbons (GNRs) have attracted attention for use in the preparation of conductive composites, and several techniques have been explored to fabricate bulk quantities of functionalized GNRs. GNRs have been obtained through oxidative unzipping of multi-walled carbon nanotubes (MWCNTs) using potassium permanganate and sulfuric acid,[2] and by intercalating lithium into MWCNTs followed by thermal expansion[3] and by longitudinal splitting of MWCNTs using

transition metal clusters.[4] GNRs have also been prepared via intercalation of potassium into MWCNTs[5,6] or expansion of MWCNTs using molecular nitrogen.[7] In order to produce conductive and mechanically reinforced GNR composites, the GNRs must be well-dispersed in the polymer matrix, and to this end, functionalization of the GNRs is key. However, these existing approaches do not generate bulk quantities of GNRs functionalized with addends that render the product evenly dispersible in polymer matrices. Here, we demonstrate that, in analogy to the intercalation chemistry of graphite, potassium intercalation into MWCNTs followed by *in situ* reaction with vinyl monomers results in exfoliation of the MWCNTs and subsequent splitting into polymer-functionalized GNRs (PF-GNRs) in a one-pot solution-based process. These polymer addends provide enhanced integration between the GNRs and polymer matrices. Furthermore, since polymerization is initiated from GNR edges, the basal planes can remain sp^2-hybridized. This stands in contrast to the covalent functionalization and carbon nanotubes where the functionalized nanotubes must contain sp3-hybridized carbons at all functionalization sites. We also correlate the exfoliation of MWCNTs with the structural characteristics of the starting materials and the intrinsic properties of the intercalants. This scalable and low-cost approach to functionalized GNRs produces materials that could be useful for transparent electrodes and heat circuits, electroactive polymer/graphene supercapcitors, and conductive nanocomposites.

6.2. Experimental Procedures

MWCNTs were obtained from Mitsui &Co. (lot no. 05072001K28), NanoTechLabs, Inc. (lot no. #5T10M10), or Bayer MaterialScience (lot no. C720P) and

they were used as received. THF was treated with potassium hydroxide for several days, degassed and freshly distilled over sodium/benzophenone under nitrogen atmosphere. Styrene was passed through a neutral alumina column and then degassed before use. Isoprene was distilled under a nitrogen atmosphere. All chemicals were purchased from Sigma-Aldrich unless specified.

TG-MS measurements were performed using a Netzsch449 F3 Jupiter®instrument under a dynamic Ar (99.999 %) flow with a flow rate of 60 mL/min in a temperature range from 25°C to 900°C. A heating rate of 10 °C/min was used. About 5 mg of the sample was placed in an alumina (Al_2O_3) crucible. Simultaneous MS used a MS 403CAëolos® with a detector secondary electron multiplier Chenneltron at a system pressure of $2x10^{-5}$ mbar. Gasses evolved under TG heat treatment were transferred to a MS detector using a quartz transfer capillary with an inside diameter of 75 µm that was heated to 220 °C. The upper limit of the MS detector was 100 AMU. Raman spectroscopy was done using a Renishaw Raman RE01 microscopy with a 514.5 nm laser. The PF-GNRs were dispersed in *ortho*-dichlorobenzene using mild bath sonication (Cole-Parmer, EW-08849−00), the suspension was drop-cast onto Si chips with a 500 nm-thick SiO_2 layer, then the solvent was evaporated upon heating, and the sample was imaged using a JEOL 6500 field-emission microscope and 2100F field emission gun transmission electron microscope.

To prepare PF-GNRs, 0.1 g of alkali metal (Li, Na, or K), 0.256 g of naphthalene and 50 mg of MWCNTs (Mitsui MWCNTs, NTL MWCNTs or Baytubes) were added to a 100 mL oven dried Schlenk flask. 50 mL of THF was added. The flask was capped with a septum and the suspension was subjected to three freeze-pump-thaw cycles to remove

oxygen. The reaction mixture was stirred at room temperature for 3 d and 20 mL of monomer (styrene or isoprene) was added dropwise while cooling in a dry ice/acetone bath. The mixture was stirred at room temperature for 1 day and then the reaction mixture was quenched by 20 mL of anhydrous ethanol. The gray precipitate was filtered through a polytetrafluoroethylene (PTFE) membrane (0.45 μm), followed by extraction with boiling chloroform in a Soxhlet extractor for 1 week to remove unbound polymer. The final product (55 mg of PF-GNRs) was collected on a PTFE membrane (0.45 μm), washed with THF (3 × 100 mL), ethanol (3 × 100 mL), DI water (3 × 100 mL), and acetone (50 mL), ether (50 mL), and dried in vacuum oven at 60 ºC overnight.

6.3. Results and Discussion

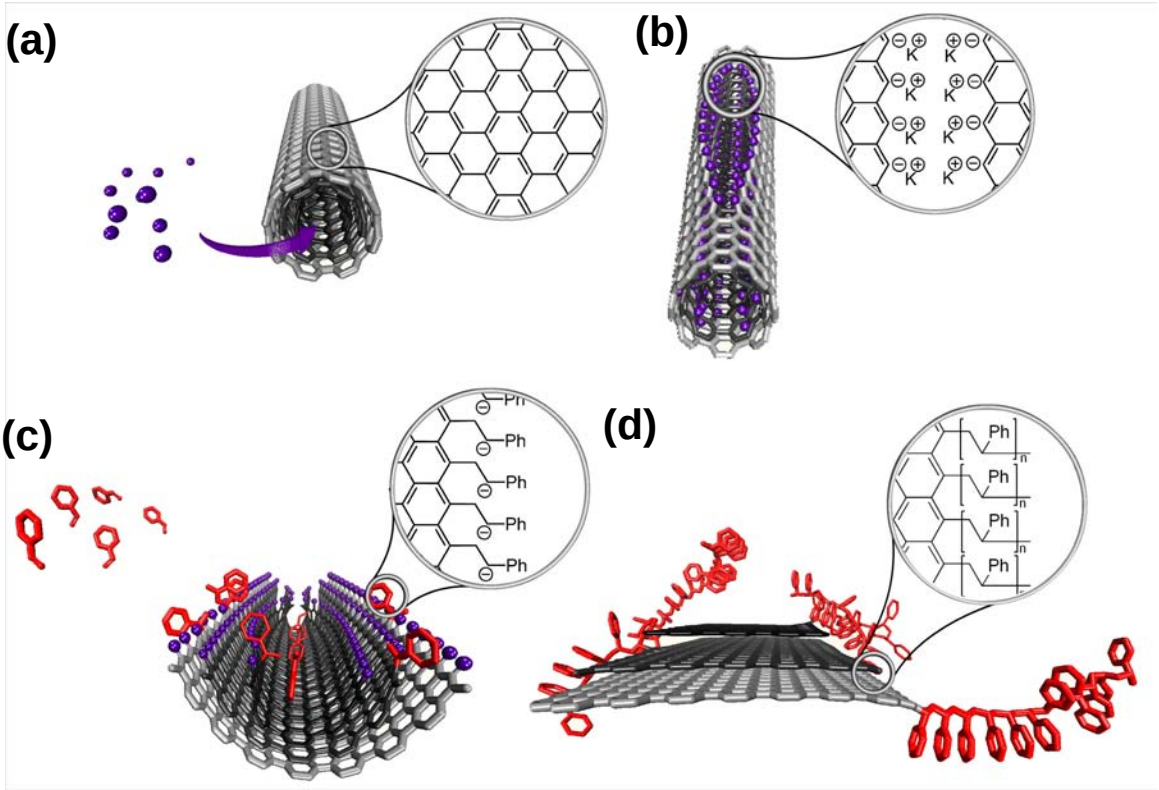

Figure 6.1 Reaction scheme for one-pot synthesis of functionalized GNRs. (a) The MWNTs are intercalated with potassium naphthalenide (blue dots). (b) A longitudinal fissure is formed in the walls of the MWCNTs due to expansion caused by intercalation of THF-stabilized potassium ions into the MWCNTs host. The edge radicals would be immediately reduced to the corresponding anions under the reducing conditions. (c) Polymerization of styrene assists in exfoliation of MWCNTs. (d) PF-GNRs are formed upon quenching.

The synthetic strategy for the one-pot synthesis of PF-GNRs used in the present study is shown in Figure 6.1. MWCNTs were converted into edge-negatively charged polymerization macroinitiators *via* intercalation and splitting. It is assumed, based on the proposed mechanism, that the edges of the split tubes are lined by aryl anions and their associated metal cations. Second, anionic polymerization of vinyl monomers starting at the negatively charged GNR edges, as was a Na/K solution method,[6] results in PF-GNRs. The vapor phase intercalation was reported earlier.[5] The liquid-phase intercalation will be only described here along with the subsequent polymerization methodology (See the Appendix F for the synthesis of polystyrene functionalized GNRs through vapor-phase intercalation). Briefly, MWCNTs, potassium metal, naphthalene and tetrahydrofuran (THF) were added to a Schlenk flask and subjected to three freeze-pump-thaw cycles to remove oxygen. As suggested by our previous work,[5] the intercalation of solvent-stabilized potassium cations into MWCNTs may lead to expansion of the *d*-space between MWCNT layers, causing the MWCNTs to partially or fully split.[5,6] The fissures in the sidewalls of the MWCNTs serve as the starting points for vinyl monomers, such as

styrene and isoprene in the present case, to anionically polymerize from the GNR edges. Due to polymerization probably proceeding between the GNR layers, only a small amount of olefin was needed to effect the exfoliation of the MWCNTs. The non-attached polymer was removed by extracting the raw product with boiling chloroform in a Soxhlet extractor. Scanning electron microscopy (SEM) was used to image the MWCNTs after intercalation and polymerization. PF-GNRs with widths in the range of several hundred nm are clearly shown in Figure 6.2 (See Figures F1-F3 in the Appendix F for additional images).

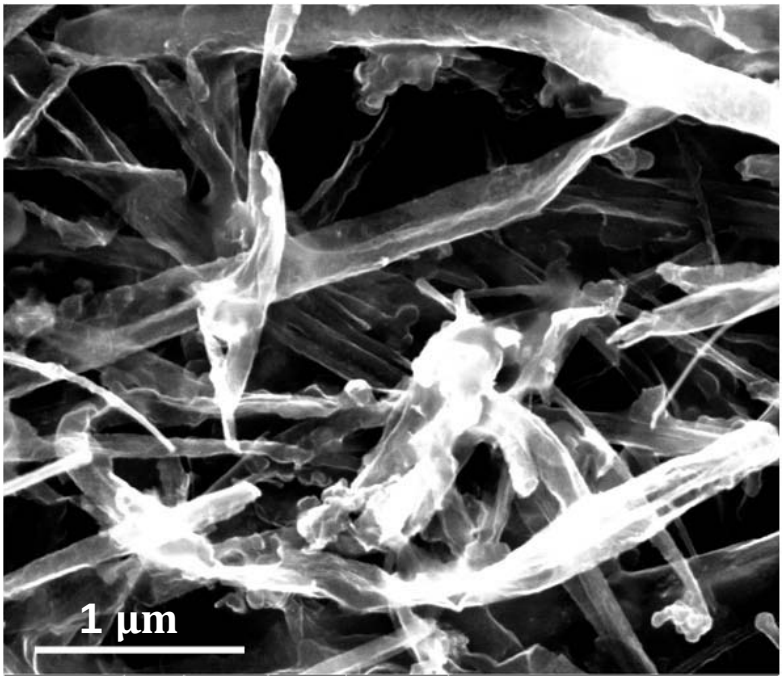

Figure 6.2 Representative SEM image of MWCNTs treated with potassium naphthalenide followed by addition of styrene (See Figure F3 in the Appendix F for the SEM image of Mitsui MWCNTs treated with potassium naphthalenide followed by addition of isoprene). GNRs can be readily identified under SEM; their width is in the range of several hundred nm. The amorphous material wrapping the GNRs or extending across neighboring GNRs is polystyrene.

Thermogravimetric mass spectrometry (TG/MS) was used to qualitatively confirm the presence of the polystyrene chains, to estimate the quantity of the monomer units, and to determine the temperature window of degradation of the PF-GNRs. To exclude the influence of the surface physisorbed components, all of the PF-GNRs were extracted with chloroform in a Soxhlet extractor for 1 week and then dried at 60 ºC overnight. The thermogravimetric analysis (TGA) thermogram (Figure 6.3a) indicates an one step weight-loss process with a total weight loss of 9% between 100 and 900 °C. Major decomposition occurred between 384 ° and 474 °C. According to MS analysis and a previous report,[8] this is the range where depolymerization of the polystyrene occurs. Charged molecule fragments with mass to charge ratios (m/z) 78, 77, 51, and 50 were observed, with intensities that are distinct for the styrene monomer, which is the one of the expected degradation products.[9] A control experiment with starting material MWNTs was also performed where no weight loss was observed (blue curve in Figure 3a). Based on the weight loss between 384 and 474°C, the weight ratio between the styrene monomer unit and carbon atoms of the graphene material was 1:136. If all of the edge carbons of the graphene nanoribbons were functionalized, these data would indicate that the average polymer chain length was only 9 units for a 3 μm × 150 nm ribbon (See Supporting Information SIII for the calculation), but it is unlikely that all sites had equal exposure to the monomer, so dramatically varied chain lengths are presumed. However, further definition of this point is not easily obtained, nor is it in the ultimate interest of our study. Raman spectroscopy was also used to characterize the graphitic structure of the GNRs. An increase in the intensity of the D band over the G band from 0.15 for MWCNTs to 0.35 for GNRs was observed in Figure 6.3b. Upon splitting of MWCNTs,

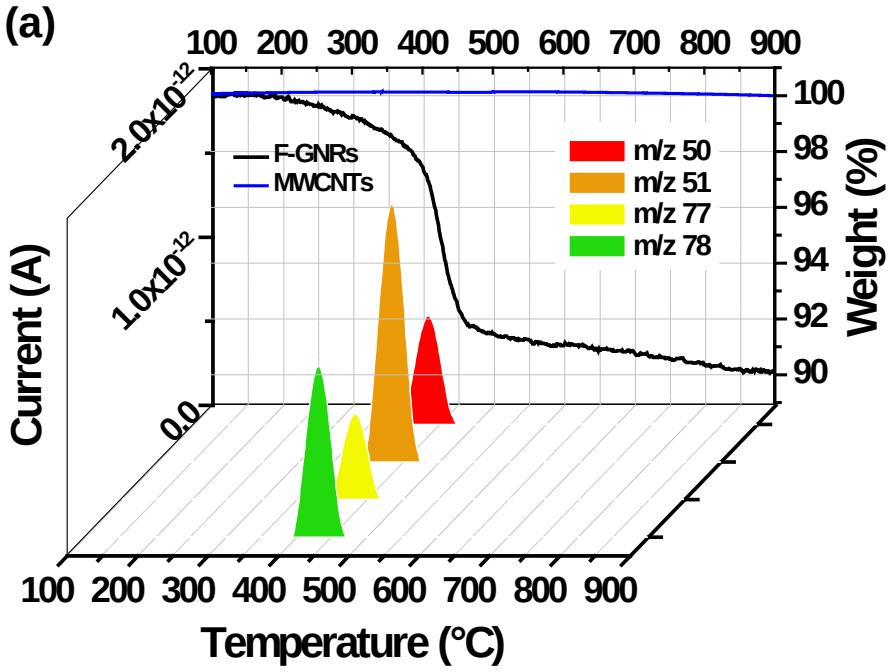
(a)
100 200 300 400 500 600 700 800 900
2.0x10-12
1.0x10-12
0.0
Current (A)
F-GNRs
MWCNTs
m/z 50
m/z 51
m/z 77
m/z 78
100
98
96
94
92
90
Weight (%)
100 200 300 400 500 600 700 800 900
Temperature (°C)

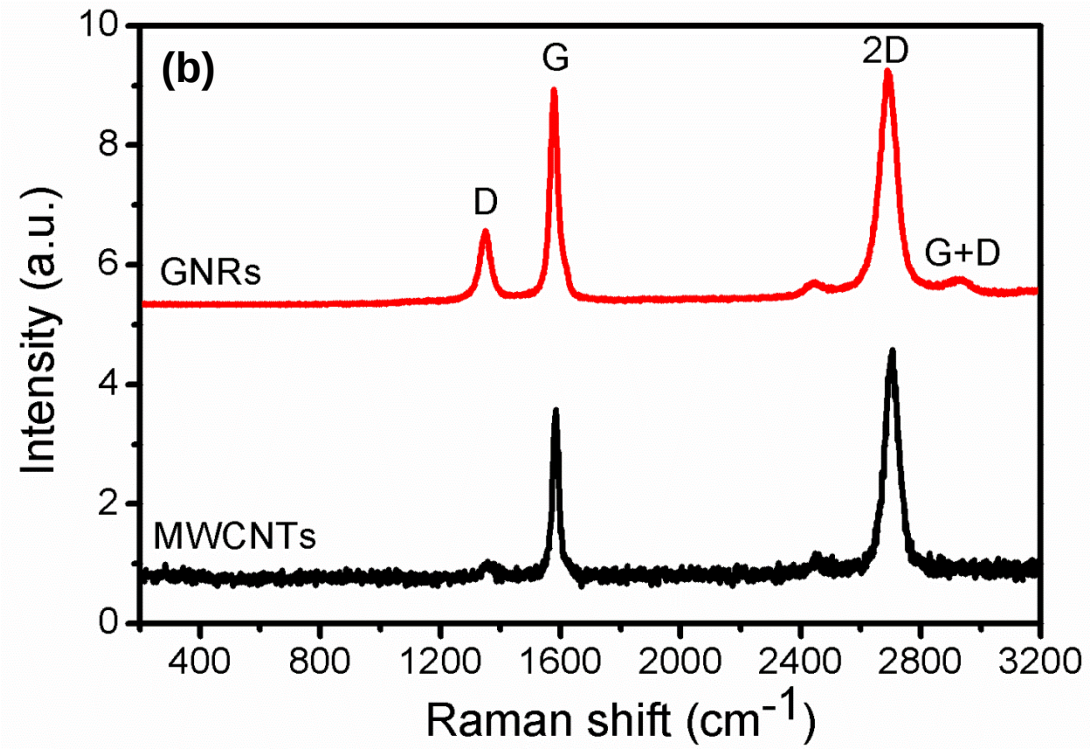
(b)
G
2D
D
G+D
GNRs
MWCNTs
10
8
6
4
2
0
Intensity (a.u.)
400 800 1200 1600 2000 2400 2800 3200
Raman shift (cm-1)

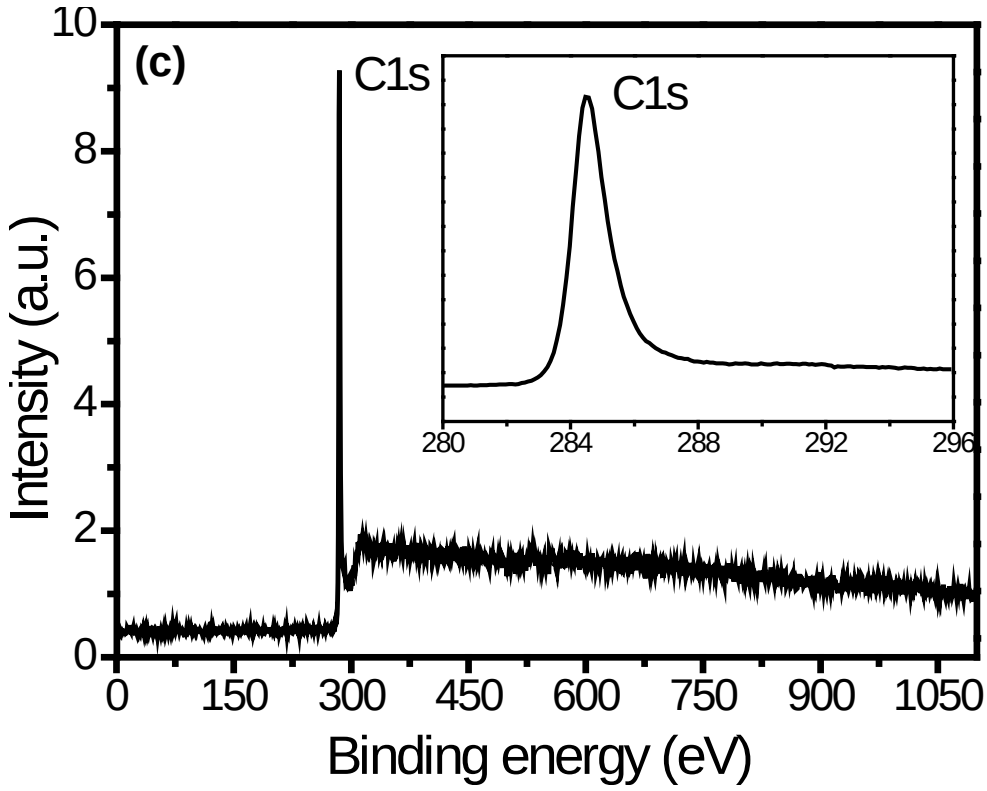

Figure 6.3 Characteristics of functionalized GNRs. (a) 3D TG-MS spectra of the gas phase in the thermal degradation of PF-GNRs and MWCNTs. Different colors represent gas products with different m/z in which m is the mass of the gas products and z is the charge. The black and blue curves correspond to the TGA profile of PF-GNRs and MWCNTs, respectively. (b) Raman spectra of PF-GNRs and MWCNTs. Disordered structure or defects were introduced onto PF-GNRs, owing to the splitting of MWCNTs caused by intercalation followed by polymerization. (c) XPS survey spectrum of GNRs. The inset is high-resolution XPS C1s spectrum of GNRs, indicating GNRs are free of oxidation.

a prominent D peak is an indication of disorder in the graphene structure due to the high edge content.[5] The disordered structure also results in a slight broadening of the G band[10]

and the 2D band,[11] as well as the combination mode of D + G band[12] at ~2700 cm^{-1} in GNRs. However, splitting of the G band,[13] corresponding to intercalated graphitic structure, is not observed in the Raman spectrum, implying that little residual intercalants, if any, or solvents were between the GNRs. X-ray photoelectron spectroscopy (XPS) was used to examine the GNR surface functionalities. The survey spectrum in Figure 6.3c shows that no oxygen was detected in the GNRs. This is further confirmed by the high-resolution XPS C1s spectrum in the inset of Figure 6.3c, as no peaks corresponding to 286 eV (C–O) or287 eV (C=O) were observed.[2]

To further explore polymerization initiated by reactive GNR anions, MWCNTs were potassium vapor-treated at 350 ºC for 24 h.[5] The product was transferred to a round-bottom flask in the glove box and styrene was added dropwise. The reaction mixture was kept at room temperature for 24 h and then at 60 ºC overnight to complete the polymerization. The potassium intercalated MWCNTs were fluffy and randomly distributed inside the flask. Addition of styrene monomer led to plastic beads with black

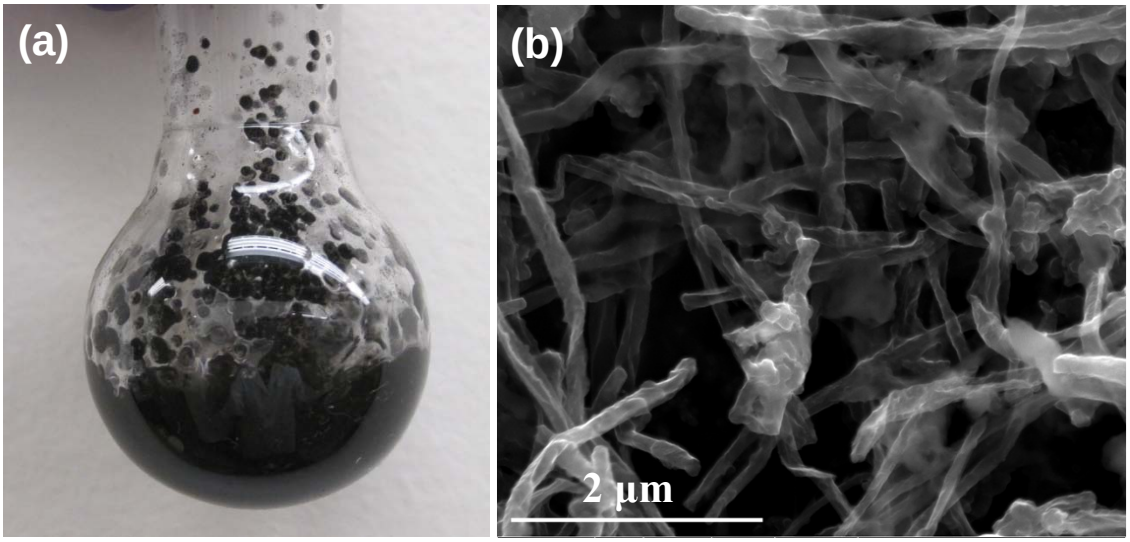

(c)

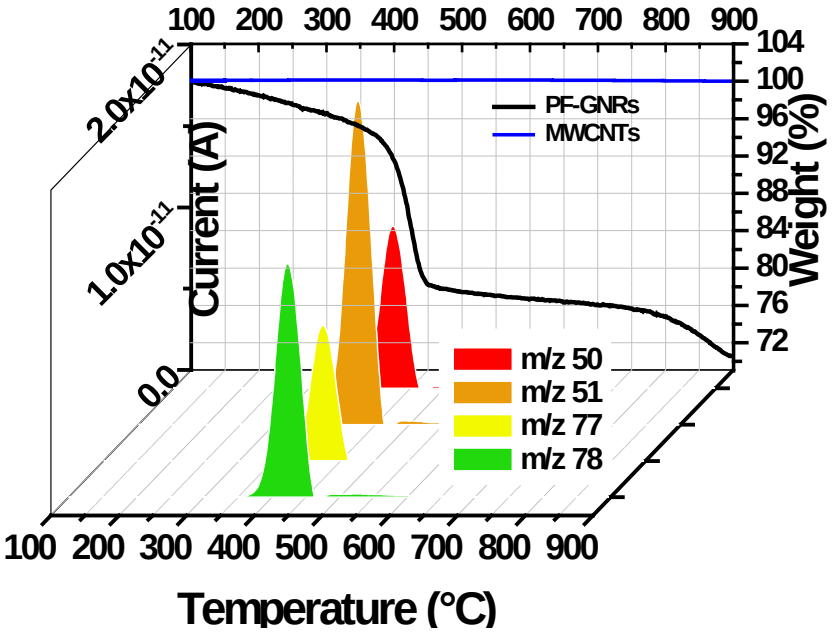

Figure 6.4 Characteristics of potassium vapor treated MWCNTs quenched with styrene. (a) Photograph of the polymerization of styrene initiated by potassium-vapor-treated MWCNTs. (b) Representative SEM image of split MWCNTs. The majority of MWCNTs were split and ribbon-like structure could be indentified in the image (See Figure F4 in the Appendix F SII for SEM images of Mitsui MWCNTs treated with potassium vapor followed by addition of isoprene). (c) 3D plot of the TG-MS results of PF-GNRs and MWCNTs. Different colors represent gas products with different m/z in which m is the mass of the gas products and z is the charge. The black and blue curves correspond to the TGA profile of PF-GNRs and MWCNTs, respectively.

centers, indicating the growth of polystyrene on MWCNTs, as shown in Figure 6.4a (See the Appendix F SI for the one-pot synthesis protocol). The MWCNTs are split and some ribbon-like structures were identified in Figure 6.4b (See Figure F4 in the Appendix F for additional images). Compared to liquid-phase intercalation followed by addition of

monomer, quenching potassium vapor-treated MWCNTs did not lead to further exfoliation of split MWCNTs. The TGA in Figure 6.4c shows that the weight loss was 22% (after extensive Soxhlet extraction with chloroform), 4 times higher than that of MWCNTs treated in liquid-phase intercalation.

To explore the flexibility of the present protocol, two other sources of MWCNTs, NanoTechLabs MWCNTs (NTL MWCNTs) and Bayer MWCNTs (Baytubes), were also subjected to the reaction conditions to compare the results to those from the Mitsui MWCNTs used for the former two experiments. Upon liquid-phase intercalation followed by polymerization, NTL MWCNTs were split but not further flattened to form

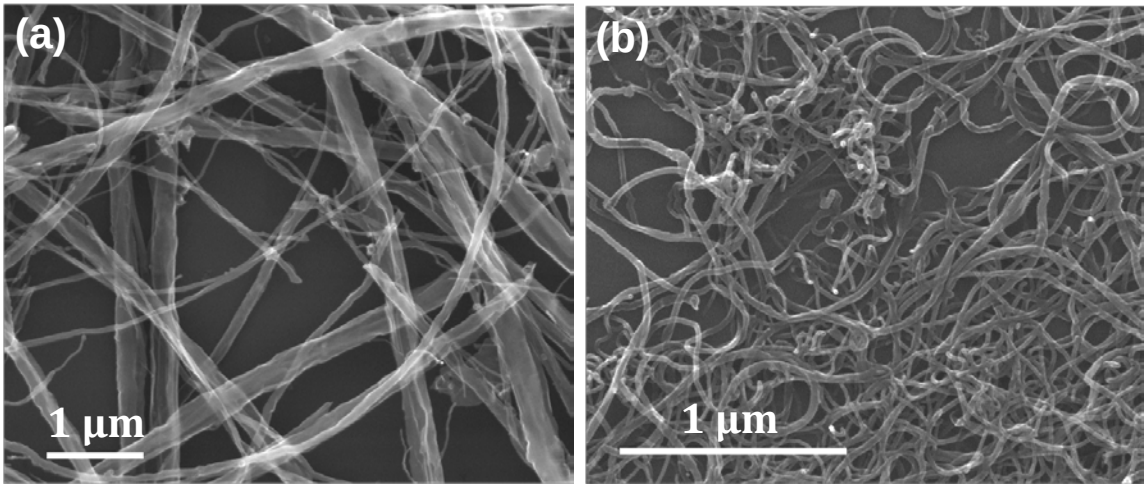

Figure 6.5 (a) SEM image of NTL MWCNTs treated with potassium naphthalenide followed by addition of styrene. The majority of NTL MWCNTs are split but they are not completely flattened to form ribbon-like structure (See Figures F5 in the Appendix F SII for SEM images of pristine NTL MWCNTs). (b) SEM image of Baytubes treated with potassium naphthalenide followed by addition of styrene. Clearly, some are split due to intercalation followed by polymerization but some still remain tube-like structure (See Figures S6 in Supporting Information SII for SEM image of pristine Baytubes).

GNRs (Figure 6.5a). With the Baytubes MWCNTs, although some partially flattened GNRs could be identified, most of the Baytubes remained intact (Figure 6.5b).

Generally, the charge transfer from naphthalene radical anions to the graphitic structure is governed by the electronic state of the host material.[14] If the host materials are highly crystalline, overlap of the valence and conduction bands will lead to two carriers, electrons and holes in the conjugated graphene plane. Therefore, the electrons, during intercalation, can be transferred from the potassium naphthalenide to the host to balance the concentration of holes, and then into the graphene conduction band. Consequently, well-defined GICs can be obtained from highly crystallized hosts. For materials with a low degree of crystallinity, unorganized intercalation structures are observed since there is no overlap between the conduction band and the valence band due to the disrupted graphitic structures. Previous work on exfoliation of GICs[15,16] suggests that forming a well-defined intercalation structure could be a prerequisite for making exfoliated GNRs via polymerization-assisted exfoliation of MWCNTs. The important link between the structural characteristics of the MWCNTs host and splitting and exfoliation of MWCNTs has been less explored, despite the fact that Mordkovich *et al*. studied the scroll carbon nanotubes *via* intercalating potassium metal into carbon nanotubes.[17] The degree of graphitization can be calculated from the interplanar *d* spacing between two graphitic layers, according to Equation 6.1[18]:

$$g = \frac{0.3440 - d_{002}}{0.3440 - 0.3354}$$

Equation 6.1 - Degree of graphitization

where g is the degree of graphitization, 0.3440 (nm) is the interlayer spacing of the fully non-graphitized carbon, 0.3354 (nm) is the d spacing of the ideal graphite crystallite and

d_{002} (nm) derived from X-ray diffraction (XRD) is the interlayer spacing corresponding to (002) planes of the graphitic material. For Mitsui MWCNTs and NTL MWCNTs g = 0.58, which is higher than that for Bayer MWCNTs, where g = 0.23 (Figure 6.6a), indicating that more facile exfoliation of the carbon host would be possible with Mitsui and NTL nanotubes. Note that the presence of any disordered structures caused by sp^3 carbon or defects that could terminate the splitting or exfoliation of MWCNTs cannot be determined from XRD patterns. Consequently, Raman spectroscopy was used to differentiate the degree of disordered structure in the host materials by calculating the ratio of the intensity of the D band to the G band.[19] The relative intensity of disorder-induced D band to crystalline G band, I_D/I_G, is 0.15 for Mitsui MWCNTs, 0.27 for NTL MWCNTs, and 0.92 for Baytubes, as shown in Figure 6.6b. Defect sites on graphene did not favor the formation of well-defined intercalation structure[14] and thus the complete exfoliation of highly defective Baytubes by intercalation is likely more difficult. This is corroborated by recent work on reductive alkylation of MWCNTs with potassium naphthalenide, in which the outer surface of highly defective MWCNTs ($I_D/I_G>1$) were functionalized with decanoic acid and no ribbon-like structure was observed in the SEM images.[20] Although NTL MWCNTs are less defective, flattening ultra-long split tubes may require further treatment. Thus, most NTL MWCNTs remained split and stacked rather than completely flattened. It is difficult to precisely establish the structural threshold (i.e. the critical value for g or I_D/I_G) that can be used to predict if the MWCNTs can be split and exfoliated, however, it is noteworthy that the higher the degree of graphitization of the carbon host (or the less defective the carbon host), the easier the exfoliation of the MWCNTs via intercalation.

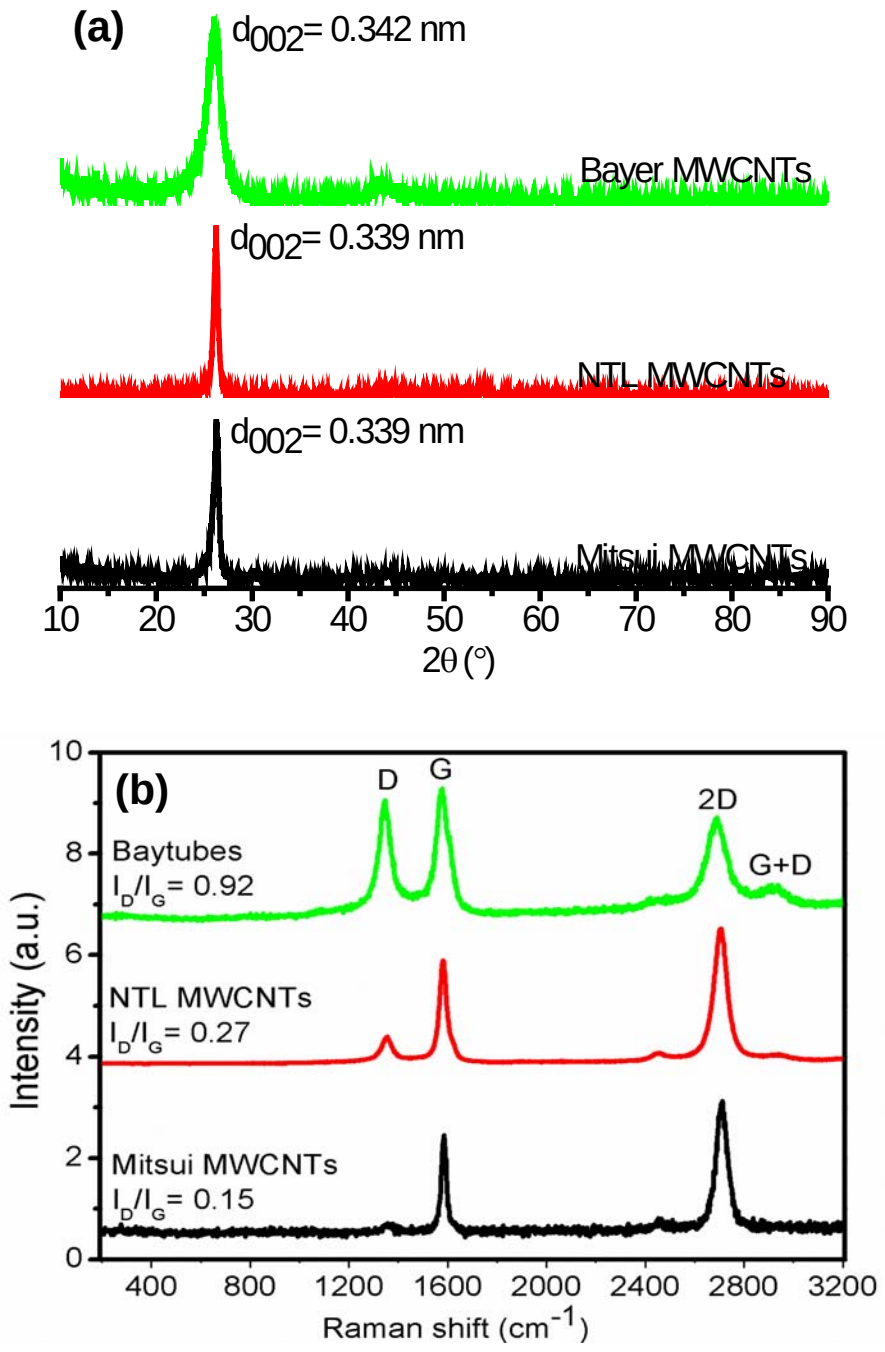

Figure 6.6 Spectral fingerprints from three different MWCNT sources. (a) XRD patterns of Mitsui MWCNTs, NTL MWCNTs and Baytubes. The d_{002} was calculated according to the Bragg's equation: $\lambda = 2d\sin\theta$, where λ is 1.54Å for Cu Kα . (b) Raman spectra of Mitsui MWCNTs, NTL MWCNTs and Baytubes. Baytubes have the highest I_D/I_G, indicating the most defective graphitic structure. Also present is the combination of G+D

band[12] induced by disorder structure, which is not observed in Mitsui MWCNTs or NTL MWCNTs.

Similar to the degree of graphitization of the starting carbon nanotubes, the ionization potential and the atomic size of the alkali metals also play an active role in intercalation and subsequent exfoliating. Since sodium naphthalenide and lithium naphthalenide have been used to make GICs[18,21] and they are also commonly used as initiators for anionic polymerization, the intercalation of solvent-stabilized sodium and lithium into MWCNTs for making functionalized GNRs was explored. However, neither of the reaction products contained significant numbers of exfoliated MWCNTs; most of the MWCNTs remained intact, as shown by the SEM images in Figure 6.7. Both lithium and sodium failed to create fissures on MWCNTs for subsequent exfoliation assisted by polymerization, as discussed in our previous work.[5]

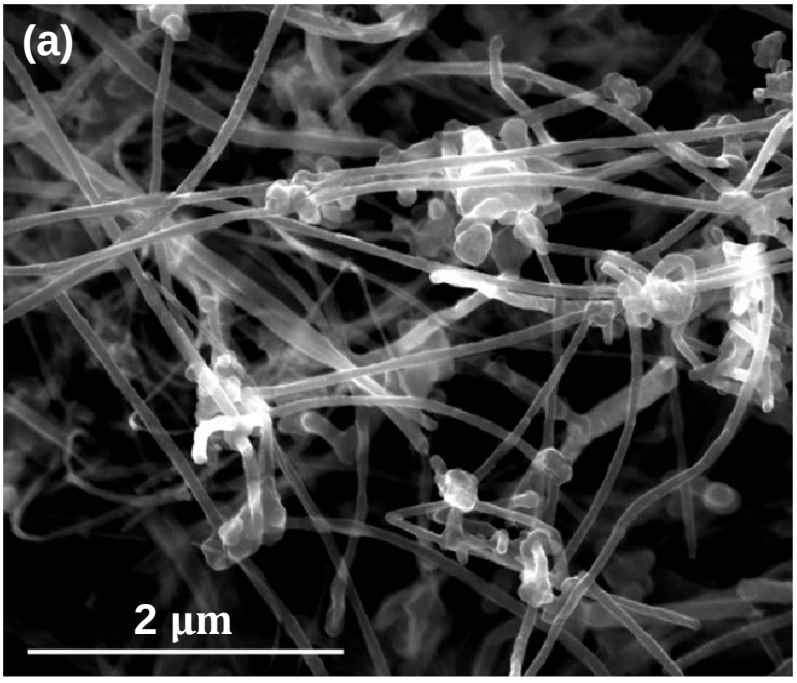

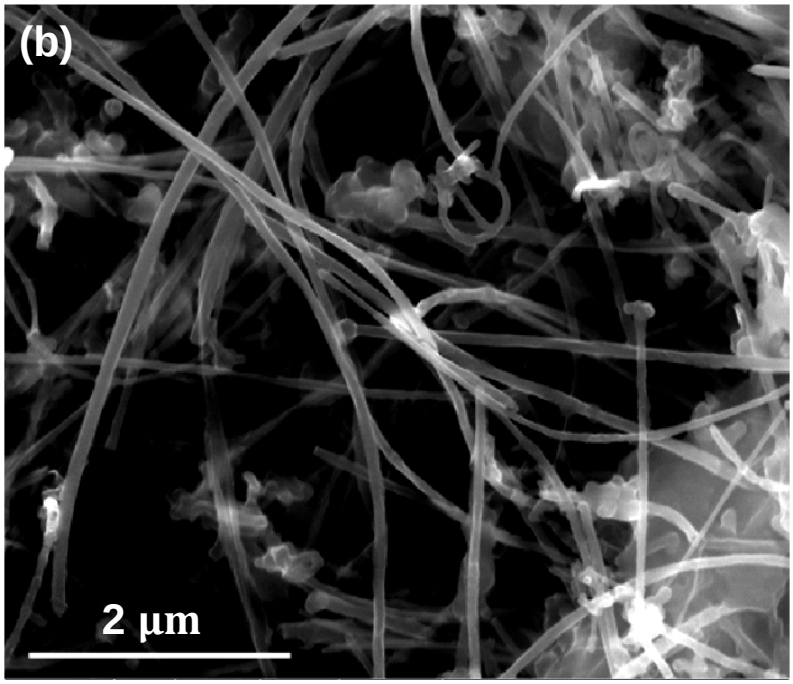

Figure 6.7 Representative SEM images of styrene treated alkali-metal intercalated MWCNTs. (a) SEM image of MWCNTs treated with sodium naphthalenide followed by styrene. (b) SEM image of MWCNTs treated with lithium naphthalenide followed by styrene. Clearly, most MWCNTs remained intact in these two cases, due to the fact that sodium naphthalenide or lithium naphthalenide failed to form fissure structures on MWCNTs for further splitting.

6.4. Conclusions

The wet chemical preparation of high-quality functionalized GNRs was achieved by polymerization-assisted exfoliation of MWCNTs in a one-pot synthesis. The *in situ* functionalized GNRs were examined by TG/MS, SEM, TEM and Raman spectroscopy. Compared to MWCNTs treated with potassium vapor followed by addition of isoprene, liquid-phase intercalation of MWCNTs and subsequent polymerization was more efficient in exfoliating MWCNTs to form functionalized GNRs, but with less polymer

bound onto the edges. Also demonstrated was the correlation between the structural characteristics of the host (the degree of graphitization and the intensity of D band over G band) and the exfoliation efficiency. The functionalized GNRs or split tubes could be used for reinforcing polymers, since the sword-in-sheath type failure of MWCNTs due to interlayer slip[22] could be retarded owing to the entangled polymer chains anchored on the edges. Through the appended polymer chains, the load might be effectively transferred from the polymer matrix to the rigid functionalized GNRs, thus making stronger composites. In addition, those PF-GNRs remain conductive, since the functionalization preferably occurs on the graphene edges generated during the intercalation process.[6] Systematic studies are underway to better understand the correlation between functionalization and conductivity of the PF-GNRs for use in making reinforced conductive composites and conductive transparent films.

6.5. Acknowledgements

We thank the Advanced Energy Consortium (BG Group, Halliburton, Conoco Phillips, BP, Shell, Total, Petrobras, Schlumberger), the AFOSR (FA9550-09-1-0581), Center of Excellence Low Carbon Technologies, Slovenia (CO NOT), Center of Excellence Advanced Materials and Technologies for the Future, Slovenia (CO NAMASTE), Sandia National Laboratory (1100745), the Lockheed Martin Corporation through the LANCER IV Program and the ONR MURI program (#00006766, N00014-09-1-1066) for funding. We thank A. Tanioka and M. Endo for the donation of the Mitsui MWCNTs, B. Katherine Price Hoelscher at MI SWACO for providing NTL MWCNTs, and H. Adams for donation of Baytubes.

6.6. References

1. Rafiee, M. A.; Lu, W.; Thomas, A. V.; Zandiatashbar, A.; Rafiee, J.; Tour, J. M.; Koratkar, N. A. *ACS Nano* **2010**, *4*, 7415–7420.
2. Kosynkin, D. V.; Higginbotham, A. L.; Sinitskii, A.; Lomeda, J. R.; Dimiev, A.; Price, B. K.; Tour, J. M. *Nature* **2009**, *458*, 872–876.
3. Cano-Márquez, A. G.; Rodríguez-Macías, F. J.; Campos-Delgado, J.; Espinosa-González, C. G.; Tristán-López, F.; Ramírez-González, D.; Cullen, D. a; Smith, D. J.; Terrones, M.; Vega-Cantú, Y. I. *Nano Letters* **2009**, *9*, 1527–1533.
4. Elías, A. L.; Botello-Méndez, A. R.; Meneses-Rodríguez, D.; Jehová González, V.; Ramírez-González, D.; Ci, L.; Muñoz-Sandoval, E.; Ajayan, P. M.; Terrones, H.; Terrones, M. *Nano Letters* **2010**, *10*, 366–372.
5. Kosynkin, D. V.; Lu, W.; Sinitskii, A.; Pera, G.; Sun, Z.; Tour, J. M. *ACS Nano* **2011**, *5*, 968–974.
6. Genorio, B.; Lu, W.; Dimiev, A. M.; Zhu, Y.; Raji, A.-R. O.; Novosel, B.; Alemany, L. B.; Tour, J. M. *ACS Nano* **2012**, *6*, 4231–4240.
7. Morelos-Gómez, A.; Vega-Díaz, S. M.; González, V. J.; Tristán-López, F.; Cruz-Silva, R.; Fujisawa, K.; Muramatsu, H.; Hayashi, T.; Mi, X.; Shi, Y.; Sakamoto, H.; Khoerunnisa, F.; Kaneko, K.; Sumpter, B. G.; Kim, Y. A.; Meunier, V.; Endo, M.; Muñoz-Sandoval, E.; Terrones, M. *ACS Nano* **2012**, *6*, 2261–2272.
8. Kaisersberger, E. *Thermochimica Acta* **1999**, *101*, 267–234.
9. Styrene: http://webbook.nist.gov/cgi/cbook.cgi?ID=C100425&Units=SI&Mask=608#Mass-Spec

10. Ferrari, A. C.; Robertson, J. *Phys. Rev. B* **2000**, *61*, 14095–14107.

11. R. Vidano, D. B. F. *J. Am. Ceram. Soc.* **1978**, *61*, 13–17.

12. Campos-Delgado, J.; Romo-Herrera, J. M.; Jia, X.; Cullen, D. a; Muramatsu, H.; Kim, Y. A.; Hayashi, T.; Ren, Z.; Smith, D. J.; Okuno, Y.; Ohba, T.; Kanoh, H.; Kaneko, K.; Endo, M.; Terrones, H.; Dresselhaus, M. S.; Terrones, M. *Nano Letters* **2008**, *8*, 2773–2778.

13. Solin, S. A. Raman *Physica* **1980**, *99B*, 443–453.

14. Inagaki, M.; Tanaike, O. *Synth. Met.* **1995**, *73*, 77–81.

15. Shih, C.-J.; Vijayaraghavan, A.; Krishnan, R.; Sharma, R.; Han, J.-H.; Ham, M.-H.; Jin, Z.; Lin, S.; Paulus, G. L. C.; Reuel, N. F.; Wang, Q. H.; Blankschtein, D.; Strano, M. S. *Nature Nanotech.* **2011**, *6*, 439–445.

16. Englert, J. M.; Dotzer, C.; Yang, G.; Schmid, M.; Papp, C.; Spiecker, E.; Hauke, F.; Hirsch, A.; Gottfried, J. M.; Steinru, H. *Nature Chem.* **2011**, *3*, 279–286.

17. Mordkovich, V. Z.; Baxendaleg, M.; Yoshjmura, S.; Chang, R. P. H. *Carbon* **1996**, *34*, 1301–1303.

18. Endo, M.; Saito, R.; Dresselhaus, M. S.; Dresselhaus, G. Ebbesen, T. W., Ed.; CRC Press: Boca Raton, FL, 1997; p. 69.

19. Nakamizo, M., Kammereck, R., Walker, P. J. J. *Carbon* **1974**, *12*, 259–267.

20. Voiry, D.; Vallés, C.; Roubeau, O.; Pénicaud, A. *Carbon* **2011**, *49*, 170–175.

21. Forsman, W. C.; Dziemianowicz, T.; Leong, K.; Carl, D. *Synth. Met.* **1983**, *5*, 77 – 100.

22. Yu, M.; Lourie, O.; Dyer, M. J.; Moloni, K.; Kelly, T. F.; Ruoff, R. S. *Science* **2000**, *287*, 637–640.

6.7. Experimental Contributions

My contribution to the experimental work in this chapter is the following: experiment design and preparation of PF-GNRs and characterization of those nanomaterials by Raman, SEM, and XRD. Gedeng Ruan optimized the synthesis of PF-GNRs and performed TGA analysis of PF-GNRs. Barbara Novosel performed TG/MS of MWCNTs and PF-GNRs. Assistance in preparation and characterization of MWCNTs and PF-GNRs was received from Bostjan Genorio and Yu Zhu.

Appendix A

The appendix corresponds to the supporting information of Chapter 1

General. Unless note otherwise, all chemicals were purchased from Sigma-Aldrich and used without further purification unless otherwise stated. Acetic acid, $CaCl_2 \cdot 2H_2O$, $MgCl_2 \cdot 6H_2O$, NaCl, KCl, $NaHCO_3$, and Na_2SO_4 were purchased from Fisher Scientific (USA). Deionized water was filtered by reverse osmosis followed by a four stage ion exchange water purification system (a Barnstead high capacity cation/anion column, two Barnstead ultra pure ion exchange columns, and a Barnstead organic removal column). Carbon black (Vulcan 9A32) was purchased from Cabot. Dialysis bags (MWCO 5,000) were purchased from CelluSep H1. SWCNTs (HPR 187.4) were purchased from HiPco Laboratory at Rice University. Centrifugation was done using an Adam Analytical Centrifuge. A dolomite core sample from a Kuwait oil well, a Berea sandstone core sample (Missisippian Age, OH) and an Iceland spar calcite sample were used in this study. The dolomite core sample was washed with toluene and methanol to reduce the amount of trapped oil and sieved. The section of ~106 – 250 μm grain range was used in this study. The Berea sandstone and Iceland spar core samples were ground and sieved to be ~106 – 250 μm grain range in the similar manner. The sandstone and calcite particles were washed five times eash with 1 wt% acetic acid and deionized water to remove clays.

Synthesis of HCCs. The HCCs used in this study were from the same batch as was recently reported.[1]

Synthesis of PEG-HCCs. The PEG-HCCs used in this study were from the same batch as was recently reported.[1]

Synthesis of PVA-HCCs. DMF (25 mL) was added to HCCs (25 mg) in a 50 mL round bottom flask equipped with a stir bar. The mixture was sonicated until the HCCs were completely dispersed in DMF. Then *N*,*N'*-dicyclohexylcarbodiimide (206 mg, 0.1 mmol) and 4-dimethylaminopyridine (2 flakes) were added, followed by 2,000 MW polyvinyl alcohol (4.2 g, 2.1 mmol). The reaction mixture was stirred for 16 h, transferred to a dialysis bag and dialyzed in standing DMF for 1 d then in running DI water for 1 week to furnish 30 mL of a PVA-HCC solution.

Synthesis of OCB. A mixture of sulfuric acid (98 %, 180 mL) and phosphoric acid (85.8 %, 20 mL) was added to CB (1 g, 83 mmol) and the mixture was stirred. Potassium permanganate (6 g, 38 mmol) was added in 3 portions over 15 min to the reaction mixture. After 15 min, the mixture was heated to 58 °C and stirred at that temperature for 1 h. The reaction mixture was cooled to room temperature and poured onto ice containing 10 mL of hydrogen peroxide (30%). Sodium hydroxide was slowly added as a fine powder into the acidic reaction mixture until the OCB precipitated out as a black solid. The OCB was collected by centrifuging at 4100 r.p.m. for 90 min. After the solution was decanted, the resulting wet OCB was redispersed in 150 mL of 10% hydrochloric acid and centrifuged again. This process was repeated twice more. Then the wet OCB was dispersed in 50 mL DI water and transferred to a dialysis bag and dialyzed in running DI water for 1 week to remove the residual acid and inorganic salts. The water was removed under reduced pressure and the damp OCB was dried in a vacuum oven at 70°C for 16 h to provide OCB (0.51 g).

Synthesis of PVA-OCB. DMF (25 mL) was added to OCB (25 mg) in a 50 mL round bottom flask equipped with a stir bar. The mixture was sonicated until the OCB was completely dispersed in DMF. Then *N*,*N*'-dicyclohexylcarbodiimide (206 mg, 0.1 mmol) and 4-dimethylaminopyridine (2 flakes) were added, followed by 2,000 MW polyvinyl alcohol (4.2 g, 2.1 mmol). The reaction mixture was stirred for 16 h, transferred to a dialysis bag and dialyzed in standing DMF for 1 d then in running DI water for 1 week to furnish 30 mL of a PVA-OCB solution with a concentration of 250 ppm, as determined by UV.

Preparation of Seawater. Salts were added to deionized water to prepare a solution with the following concentrations: CaCl2 (0.386 g/L), MgCl2 (0.523 g/L), KCl (1.478 g/L), NaCl (28.311 g/L), Na2SO4 (0.072 g/L), NaHCO3 (0.181 g/L).

Preparation of PCB*/PVA-OCB. PVA-OCB (2 mL) was diluted in seawater (47 mL) and PCB* (40 µL) was added. The mixture was stirred at rt for 3 d in the dark and then kept at 4 °C for 14 d without stirring. The mixture was then passed through a PD-10 column (GE Healthcare) to remove free PCB*. The final concentration of PCB* in the mixture was 4 ppb as determined by a scintillation measurement.

Characterization.

Instrument and Sample Preparation Information.

SEM imaging was performed on a high resolution field emission scanning electron microscope (FEI Quanta 400). The dry powders (CB, OCB and PVA-OCB) were

mounted onto the conductive tape for imaging. The hydrodynamic diameter of each nanomaterial was characterized through dynamic light scattering (Brookhaven, ZetaPALS with BI-9000AT digital autocorrelator, λ = 656 nm). The electrophoretic mobility of these aggregates was measured by phase analysis light scattering (PALS) using the ZetaPALS setup. A dip-in (Uzgiris type) electrode system with 4 mL polystyrene cuvettes was used, and measurements were taken at 20 °C. TGA was obtained on Q50 TA Instrument, using argon from room temperature to 950 °C at 10°C/min rate. UV data were collected from a Shidmadzu UV-3101 PC and samples contained in 1 mL quartz cuvettes. Samples were dispersed in deionized water upon sonication. Raman spectra were obtained on a Renishaw Raman scope using a 514 nm HeNe laser. XPS experiments were performed on a PHI Quantera SXM scanning X-ray microprobe with 26.00 eV passing energy, 45° take-off angle and a 100 µm beam size.

Determination of Extinction Coefficient at 280 nm.

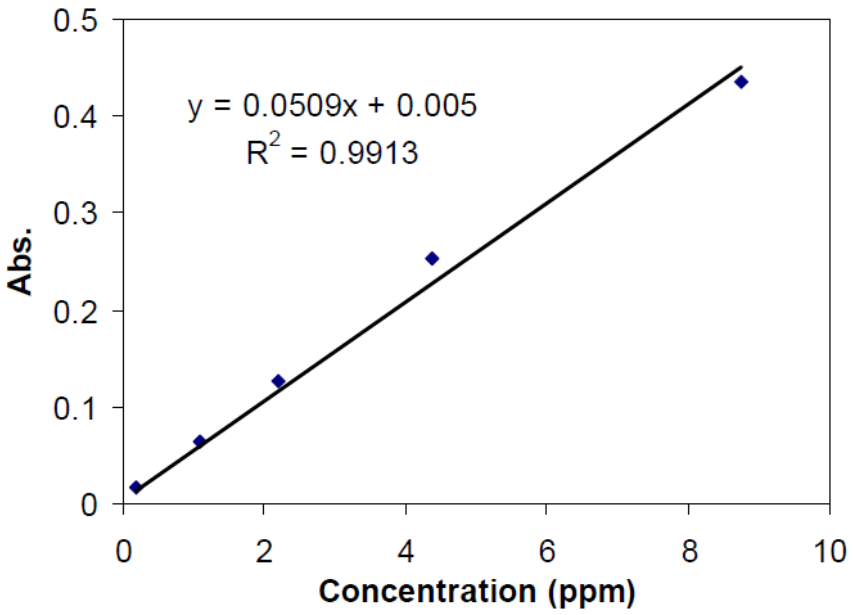

Figure A1. Calibration curve for PVA-OCB absorbance at 280 nm.

For each nanomaterial, an aqueous solution was prepared with a known concentration of the nanomaterial. A series of diluted samples were then prepared, and the absorbance of each diluted suspension was measured at λ_{max} 280 nm. The slope of the linear absorbance vs. concentration curve was used to calculate the extinction coefficient of carbon materials at λ_{max} 280 nm according to Beer's law. The calculated extinction coefficient was 0.0509 L/mg for PEG-HCCs, PVA-HCCs, and PVA-OCBs. A typical calibration curve of PVA-OCBs is shown in Fig. S1.

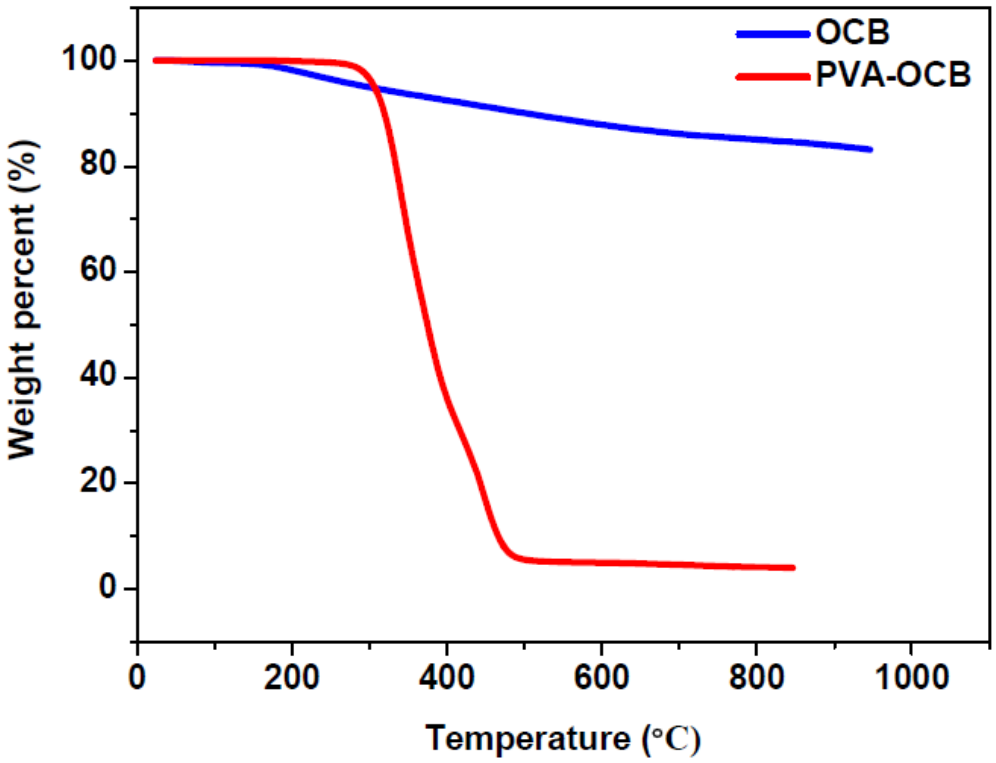

Figure A2. TGA analysis of OCB and PVA-OCB. The weight loss for OCB was 17% and for PVA-OCB it was 96%.

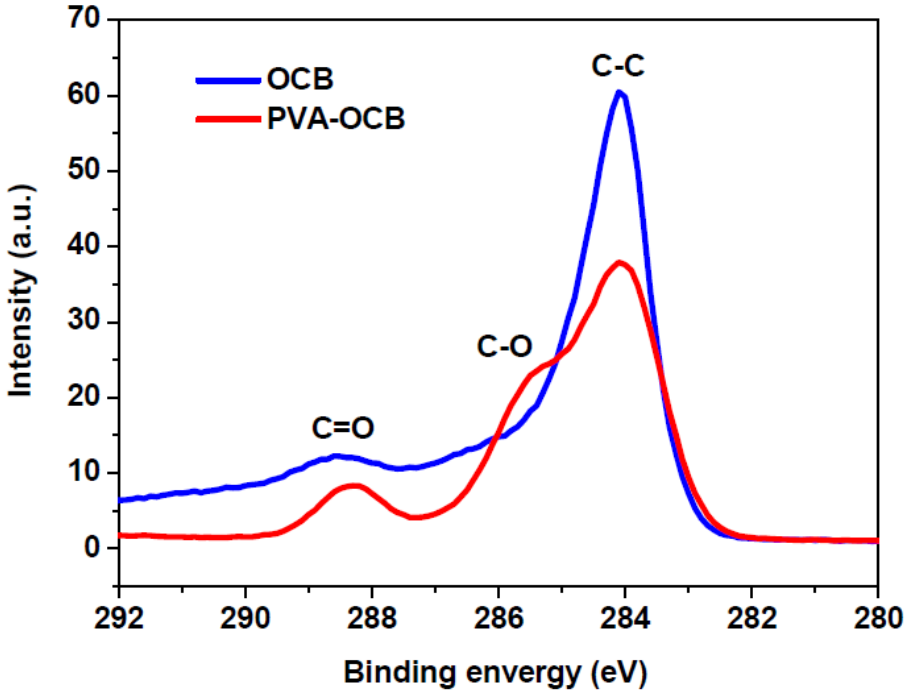

Figure A3. XPS analysis of OCB and PVA-OCB. The oxidation of the OCB is evidenced by the peak at 288.5 eV, indicative of C=O bonds. The PVA functionalization is evidenced by the new peak at 286 eV, indicative of C-O bonds.

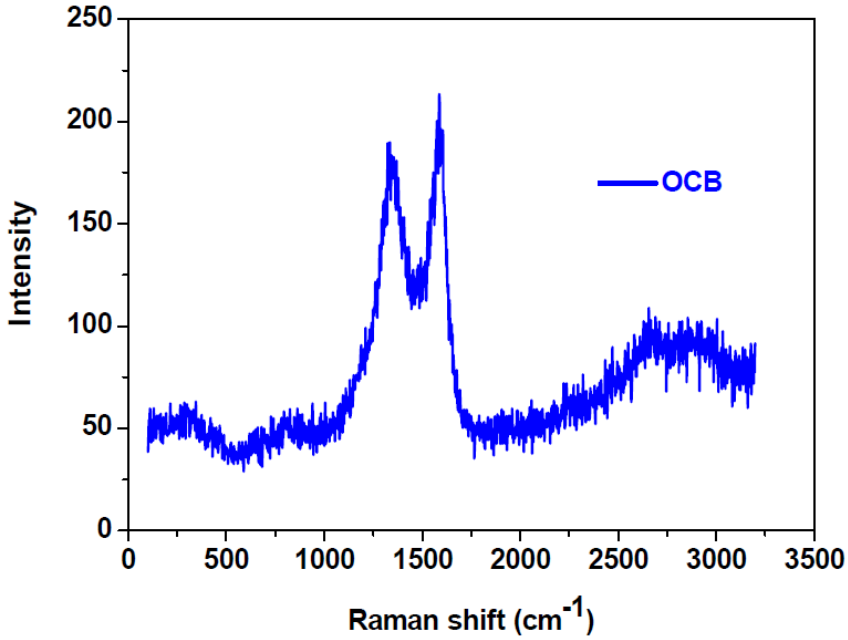

Figure A4. Raman spectrum for OCB. No Raman spectrum could be obtained for the PVA-OCB.

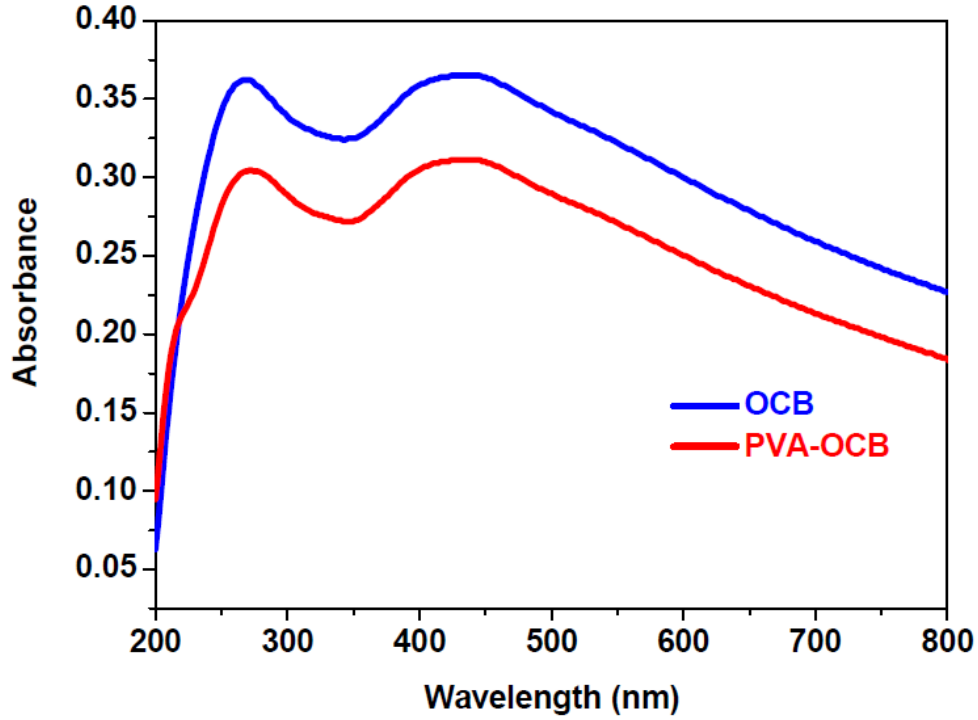

Figure A5. UV spectroscopy for OCB and PVA-OCB. The two peaks are 270 and 425 nm.

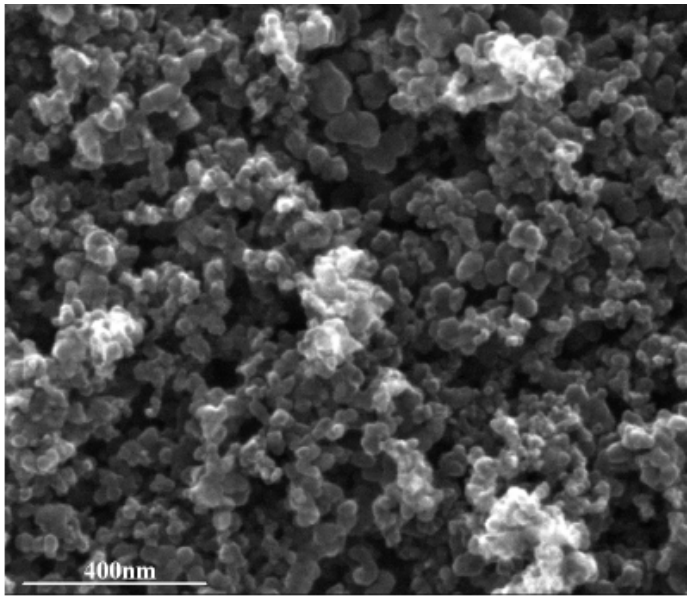

Figure A6. SEM imaging of carbon black.

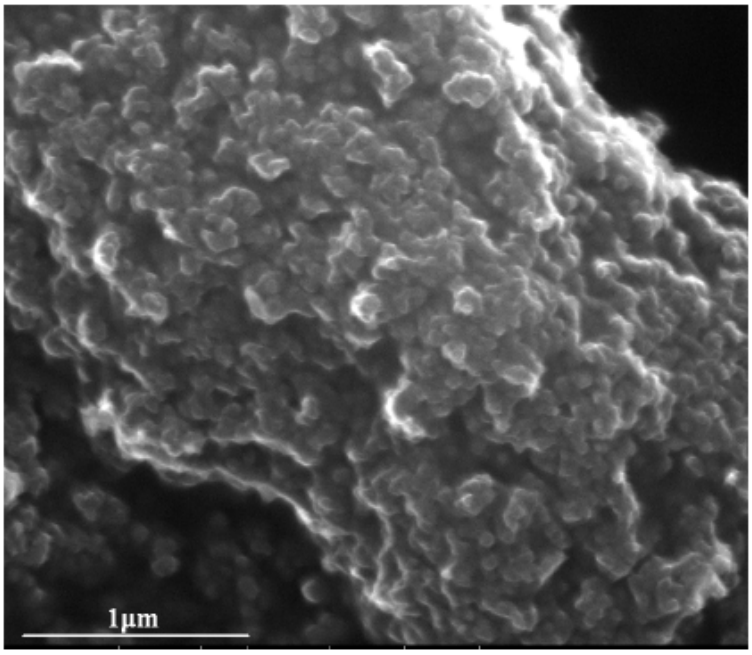

Figure A7. SEM imaging of OCB.

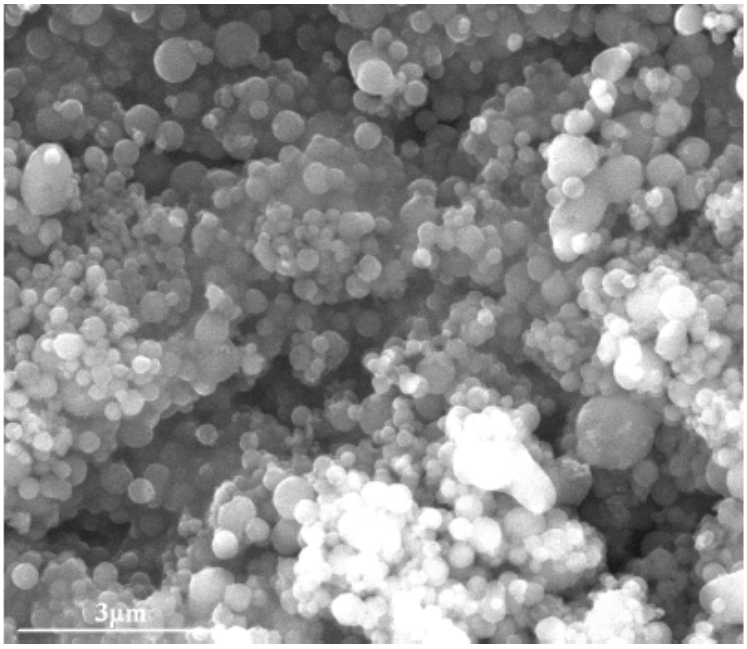

Figure A8. SEM image of PVA-OCB

Transport studies.

General Column preparation

In a typical set-up, ground rock grains were slowly packed into the glass column with a length about 6 - 7 cm (Borosilicate glass columns with an adjustable end piece, cross sectional area=0.3421 cm2, Omnifit, Bio-Chem Valve Inc., Boonton, NJ). The dry column was flushed with deionized water for several days to remove the trapped air bubbles. Porosity of columns was gravimetrically determined. A three-way valve (Omnifit) was used to connect a 60-mL plastic syringe (BD, Franklin Lakes, NJ, USA) and the column. The whole system was connected by PTFE tubing (Omnifit). A nonreactive tracer, tritiated water, was loaded into the syringe and flowed through the column. The breakthrough of tritiated water was measured to characterize the porosity and dispersity of the column. Prior to sample injection, each column was washed with sample-free solution (deionized water or synthetic seawater) for 16 h.

The characteristic parameters for each type of columns and the flow parameters are given in Table S1.

Table A1. Column properties.

	Flow rate (mL/min)	Retardation factor (R)	Dispersion coefficient (D) (cm^2/min)	Porosity (%)
Sandstone	0.13	1.21	0.03	0.52
Calcite	0.13	1.09	0.05	0.65

Dolomite	0.13	1.01	0.03	0.67

Nanomaterial Sample Preparation and Breakthrough

Before loading, the nanomaterial suspension was sonicated using an ultrasonic processor (VCW-500W, 22% output, Sonics & Materials Inc., Newtown, CT) with a titanium alloy tapered microtip (Ti-6Al-4V) and was filtered through a PES filter of 0.45 µm pore size (Whatman, USA). For nanomaterial breakthrough, a nanomaterial suspension was loaded into the syringe and was pumped (New Era Pump System Inc., Wantagh, N.Y.) to the column at a linear average pore velocity of ~0.67 cm/min. For each pore volume, the effluent from the column was collected in a 2 mL glass vial. The concentration of the nanomaterial in the effluent was determined by absorbance at 280 nm on UV-visible spectrophotometer (DR/4000, HACH Company, Loveland, CO). When the breakthrough reached a plateau or the total breakthrough was 100%, the column was flushed with the sample-free background solution.

In addition to the materials described in the main body of the manuscript, we also evaluated the breakthrough of PEGylated graphene oxide nanoribbons (PEG-GONR) and PEGylated graphene oxide (PEG-GO), but they performed poorly.

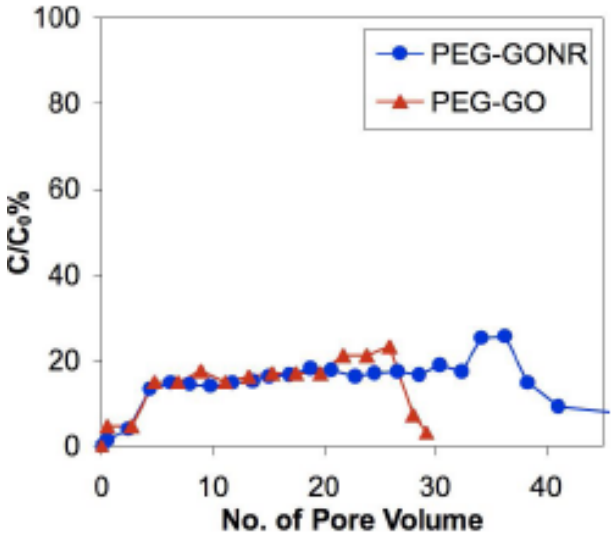

Figure A9. Breakthrough in a sandstone column of PEG-GONR and PEG-GO in seawater.

Control Studies on PCB transport

PCB*: A control PCB*/seawater sample was prepared by diluting a methanol solution (20 µL) of PCB* (23 ppm) into 50 mL of synthetic seawater at room temperature through a glass syringe equipped with a stainless steel needle. The PCB*/seawater mixture was stirred at rt for 3 d in the dark and then kept at 4 °C for 14 d without stirring. For the column experiment, the PCB*/seawater solution was loaded into a 100 mL glass syringe (Hamilton, Nevada, USA). Due to the adsorption of PCB* to glass and PTFE, the actual PCB* concentrations in the inlet and outlet flows were determined by scintillation measurement. The concentration of inlet PCB was calculated to be 8 ppb.

PCB*/PVA: In order to evaluate if PVA alone could transport PCB*, a highly concentrated aqueous solution of PVA was added to a PCB*/seawater mixture to furnish a final sample containing 8 ppb PCB* and 20 ppm PVA. The sample was then loaded

into a 100 mL glass syringe (Hamilton, Nevada, USA) and pumped into a sandstone column.

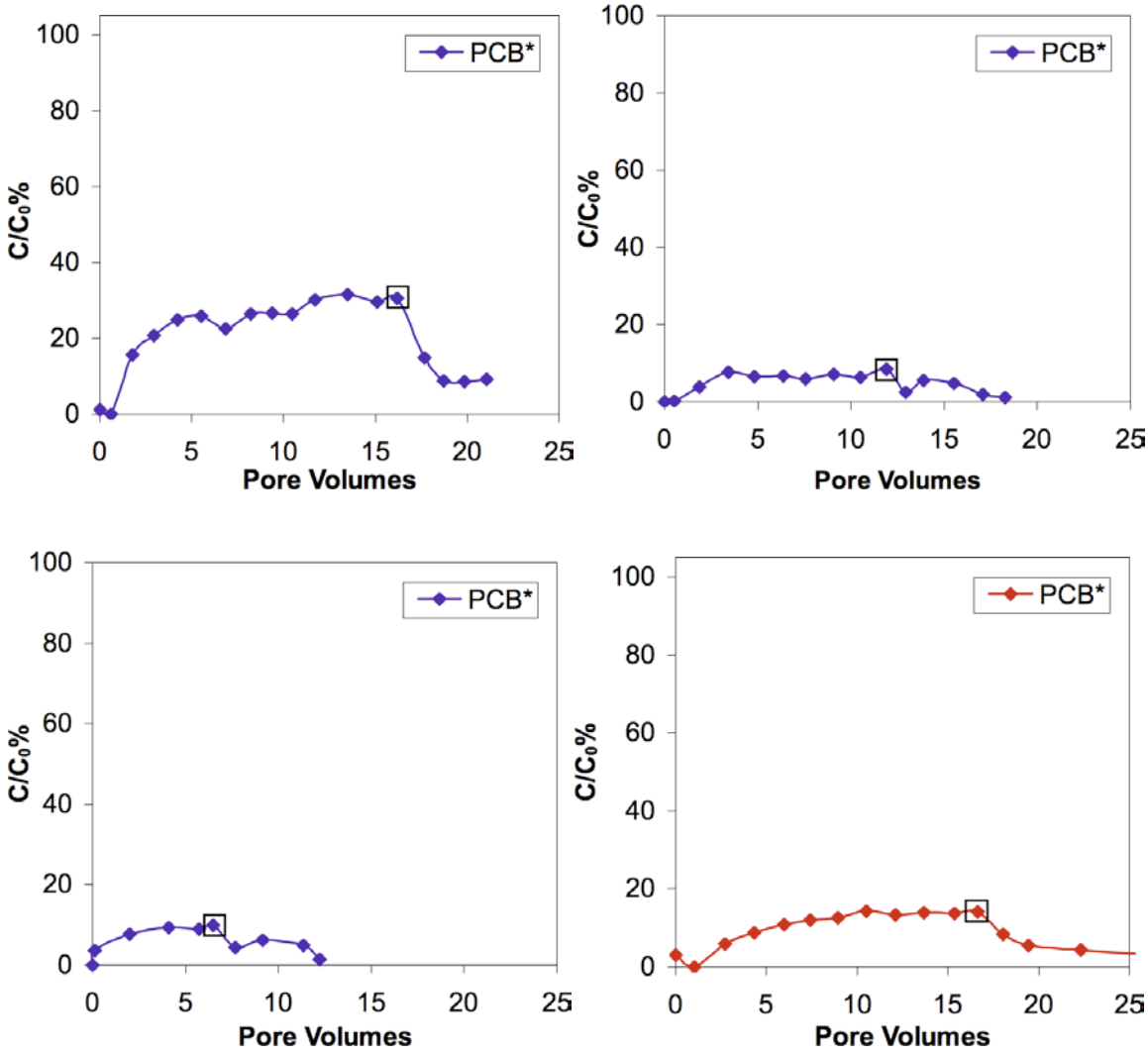

Figure A10. Breakthrough of PCB* without a nanoparticle carrier. a) Breakthrough for calcite; b) breakthrough for dolomite; c) breakthrough for sandstone; d) breakthrough when mixed with PVA for sandstone. The black boxes indicate when the flow was switched from the PEG-HCC solution to seawater.

References:

1. Berlin, J. M.; Leonard, A. D.; Pham, T. T.; Daisuke, S.; Marcano, D. C.; Yan, S.; Fiorentino, S.; Milas, Z. L.; Kosynkin, D. V.; Price, B. K.; Lucente-Shultz, R. M.; Wen, X.; Raso, M. G.; Craig, S. L.; Tran, H. T.; Myers, J. N.; Tour, J. M. *ACS Nano*, **2010**, *4*, 4621-4636.

Appendix B

The appendix corresponds to the supporting information of Chapter 2

Materials and methods

Synthesis of functionalized carbon black (fCB).

4,4'-Azobis(4-yanopentanoic acid) (ACPA) was used for the introduction of carboxyl groups onto the carbon black surface. Typically, carbon black (3.0 g, 0.25 mole) and ACPA (6.0 g, 0.021 mole) were added to THF (120 mL). The solution was stirred at 65 °C under nitrogen for 24 h. The resulting mixture was filtered and the filter cake was washed with excess THF, followed by drying at 100 °C in a vacuum oven overnight to yield carboxyl group-functionalized carbon black (fCB).

Synthesis of polyvinyl alcohol grafted fCB (PVA-fCB)

The as-synthesized fCB (15 mg) was dispersed in a 100 mL round bottom flask with anhydrous DMSO (25 mL) by sonication overnight. A separate flask containing polyvinyl alcohol (1.0 g, Mw ~ 50,000) and DMSO (25 mL) was heated to ~70 °C until the PVA was dissolved in the DMSO. When the PVA solution cooled to room temperature, it was transferred to the first round bottom flask containing the fCB in DMSO, and then *N*,*N*'-dicyclohexylcarbodiimide (DCC, 140 mg, 0.68 mmol) and 4-dimethylaminopyridine (DMAP, 20 mg, 0.16 mmol) were added. The reaction mixture was stirred at room temperature for 24 h, followed by transfer to a dialysis bag and

dialysis in standing DMSO for 3 d then in running DI water for 1 week to furnish PVA-fCB aqueous solution.

Synthesis of sulfated polyvinyl alcohol grafted fCB (sPVA-fCB)

Similar to the method used to synthesize PVA-fCB, before the second dialysis in running DI water, the resulting PVA-fCB in DMSO was further treated with 1 M $ClSO_3H$ in CH_3COOH (3.0 mL) at 60 °C for 30 min to yield lightly sulfated PVA-fCB (LsPVA-fCB), while the highly sulfated PVA-fCB (HsPVA-fCB) was obtained by treating the PVA-fCB in DMSO with 1 M $ClSO_3H$ in CH_3COOH (4.5 mL) at 75 °C for 90 min. After sulfation, the resulting solution was neutralized to ~7.0 with 1 M NaOH(aq) until the pH ~7.0. The LsPVA-fCB or HsPVA-fCB aqueous solution could be obtained after dialysis under running DI water for 1 week.

Preparation of THA/LsPVA-fCB nanoreporter

Triheptylamine (THA), a highly hydrophobic molecule due to its long alkyl chains, features an odd number of nitrogen atoms, which can be easily determined by mass spectrometry analysis according to the nitrogen rule. Here, we stirred 50 mL of the LsPVA-fCB solution with THA (~5 μL) for one day, and then passed the solution through a size exclusive column (PD-10) in order to remove any unbound THA. The remaining THA was physically adsorbed on the LsPVA-fCB hydrophobic domains, so that they would not be filtered out by the PD-10 column.

Preparation of API brine

API brine was prepared by dissolving CaCl2 (anhydrous, 10 g, 0.09 mole, 2 wt% in final solution) and NaCl (40.0 g, 0.68 mole, 8 wt% in final solution) in deionized water (450 g, 25.0 mole).

Transport studies

1. General column preparation

Ground rock grains were slowly packed into the glass column with a length about 6-7 cm (Omnifit borosilicate glass columns with an adjustable end piece, cross sectional area = 0.34 cm^2, Bio-Chem Valve Inc., Boonton, NJ). The packed rock materials were retained by 10 μm stainless steel screens (Valco Instruments Inc., Houston, TX) on both ends of the column. A three-way valve was used to connect a 60 mL plastic syringe to the column. PTFE tubing (Omnifit) was used for all tubing connections in the system. The packed columns were flushed with CO_2 (purity > 99%) for 30 min to remove the trapped air bubbles. Then the columns were flushed with API brine at a flow rate of 8 mL/h for 24 h to stabilize the rock grains. Tritiated water, as a non-reactive tracer, was injected into the columns to characterize the porosity and dispersity of the column. The pH of influent solutions in all column experiments was 6.4.

2. Isooctane-containing column preparation

After flushing the column with API brine for 24 h, the calcite column was then flooded with isooctane (Fisher Scientific, USA) at a flow rate of 6 mL/h until no water was produced in the effluent. Next, API brine was injected into the column at 8 mL/h until no more isooctane was produced in the effluent. The volume of isooctane remaining in the column was calculated by measuring the amount of isooctane produced from the

water flood. Residual isooctane saturation is the ratio of the volume of isooctane to the predetermined pore volume.

Table B1. Column properties

	Flow rate (m/24h)	Dispersion Coefficient (cm^2/min)[a]	Porosity[a]	R^2
Sandstone	9.3	0.0245 (0.0026)	0.4795 (0.0017)	0.998
Calcite	9.3	0.0416 (0.0032)	0.4500 (0.0016)	0.998

a. Numbers in parentheses are the standard deviations

3. Nanomaterial sample breakthrough

The NPs were suspended in the API brine and the mixture was filtered through a 0.45 μm pore size PES filter (Whatman, USA). The NPs suspension was then pumped (New Era Pump System Inc., Wantagh, N.Y.) to the columns at a linear average velocity of 9.3 m/d. The effluent was collected in a 2 mL glass vial. The concentration of nanoparticles was measured by UV-visible spectrophotometer (DR/4000, HACH Company, Loveland, CO) at 232 nm. When the breakthrough reached a plateau, the column was flushed with API brine.

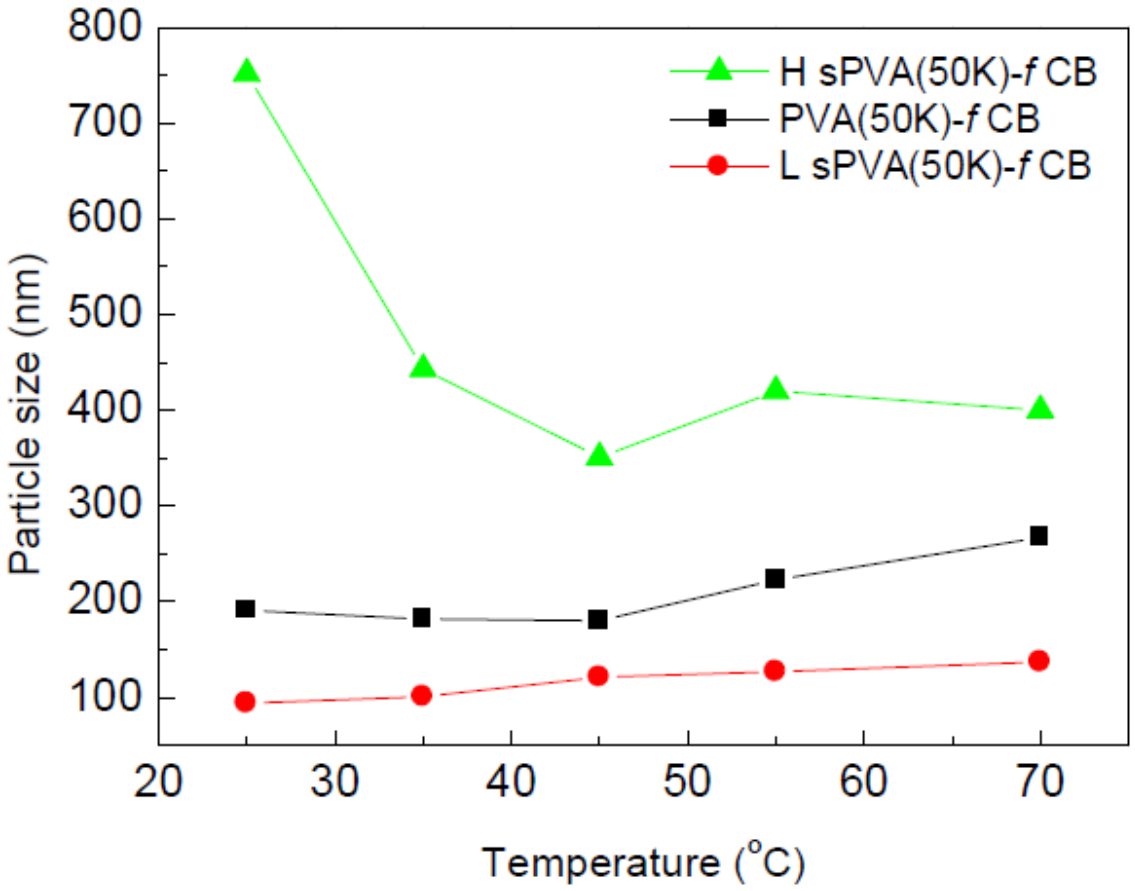

Figure B1. Dynamic light scattering (DLS) plots for the PVA(50k)-coated fCB NPs before and after the treatment with light or high sulfation. All NPs were dispersed in deionized water and the temperature was controlled from 25 °C to 70 °C.

Appendix C

The appendix corresponds to the supporting information of Chapter 3

Materials and Characterizations. Unless specified, all chemicals were purchased from Sigma-Aldrich and used without further purification. $CaCl_2 \cdot 2H_2O$, $MgCl_2 \cdot 6H_2O$, NaCl, KCl, $NaHCO_3$, and Na_2SO_4 were purchased from Fisher Scientific (USA). Carbon black (Vulcan 9A32) was donated by Cabot. Dialysis bags (MWCO 5,000) were purchased from Membrane Filtration Products, Inc. The nanoparticle solution was placed onto a carbon-coated copper grid, dried at 60 ºC overnight and imaged by a JEOL 2100 field emission gun transmission electron microscope (TEM) with an accelerating voltage of 200 kV. DSC measurements were performed on a TA instrument (DSC, Q10). The sample was capped in an aluminum pan, heated to 160 ºC at a rate of 5 ºC/min, cooled to room temperature and then heated to 160 ºC under the same conditions. The second heating curve was recorded and given in this study. Isooctane was magnetically stirred with amphiphilic OCB overnight and the oil droplets at the interface were imaged by optical microscopy (Olympus IX71). The interfacial tension was measured on a spinning drop tensiometry. Equal volumes of isooctane and amphiphilic 920 M_n PE-*b*-PEG coated OCB in synthetic sea brine were mixed and equilibrated at 90 ºC for 24 h. One drop of isooctane saturated with 920 M_n PE-*b*-PEG-OCB was used for measuring the interfacial tension at 70 °C (due to instrument limitations, the interfacial tension cannot be measured at 90 °C).

Synthesis of OCB. The OCB used in this study were from the same batch reported early.[1]

Synthesis of PE-*b*-PEG-OCB and phase transfer studies. DMF (50 mL) and OCB (50 mg) were added to a 50 mL round-bottom flask equipped with a stir bar. The mixture was sonicated in a bath sonicator (Cole-Parmer, EW-08849−00) overnight. Then, *N*,*N*'-dicyclohexylcarbodiimide (465 mg) and PE-*b*-PEG (5 g) were added, followed by 4-dimethylaminopyridine (10 flakes). The reaction was stirred at room temperature overnight, transferred to a dialysis bag and dialyzed in standing DMF for 2 d then in running DI water for 7 d to remove the unbound diblock copolymers. 145 mL of PE-*b*-PEG-OCB in DI water was collected.

Phase Transfer of PE-*b*-PEG-OCB in vials. The phase transfer of NPs was carried out by vigorously stirring or gently shaking the mixtures of 8 mL of amphiphilc OCB in the synthetic sea brine and an equal volume of isooctane (Sigma-Aldrich) at high temperatures. The typical concentration of nanoparticles in sea brine was 50 mg/L. After phase transfer, the top isooctane layer became black and the suspension was used for TEM imaging; while the bottom aqueous layer was collected and examined by a UV-vis spectrometer (Shimadzu UV-3101PC) in order to determine the concentration of NPs remaining in the aqueous phase.

Phase Transfer of PE-*b*-PEG-OCB in a sealed ampoule. 8 mL of amphiphilic OCB in DI water and 8 mL of isooctane were loaded into an ampoule that was sealed under atmospheric pressure. The sealed ampule was heated at 110 ºC in an oven and gently shaken to improve the phase transfer process.

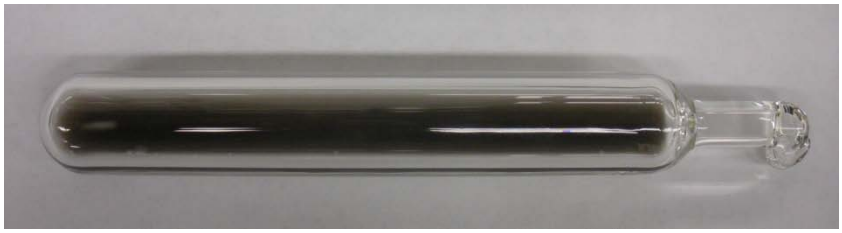

A photograph of a sealed ampoule loaded with equal volumes of PE-*b*-PEG-OCB in DI water and isooctane.

Composition of the synthetic sea brine

Chemical components	**Concentration (g/L)**
$CaCl_2$	0.386
$MgCl_2$	0.523
KCl	1.478
NaCl	28.311
Na_2SO_4	0.072
$NaHCO_3$	0.181

Table C1 Effective diameter of PE-b-PEG and PE-b-PEG in DI water and sea brine

	Effective diameter (nm)	
	DI water	Sea brine
PE-*b*-PEG (Mn = 920)	300.9 ± 2.4	333.6 ± 3.2
PE-*b*-PEG-OCB (Mn = 920)	362.2 ± 0.8	365.7 ± 7.6
PE-*b*-PEG (Mn = 1400)	348.7 ± 5.3	372.3 ± 16.1
PE-*b*-PEG-OCB (Mn = 1400)	341.7 ± 6.1	363.2 ± 9.5

Since the PE block is not soluble in water and it tends to form liquid crystal in the aqueous phase,[2] the effective diameter of diblock PE-*b*-PEG copolymers in DI water is big. The effective diameter of 920 M_n PE-*b*-PEG in DI water is smaller than that of 1400 M_n PE-*b*-PEG in DI water because of shorter polymer chain. Also, the size of diblock PE-*b*-PEG copolymers in DI water is smaller than that in the synthetic sea brine due to the "salting out" effect.[3] Correspondingly, those diblock polymers coated OCB nanoparticles in the synthetic sea brine are bigger than that in DI water. However, introducing carbon black nanoparticles or salt ions slightly increases the effective diameter of those diblock polymers in the aqueous phase.

Additional figures

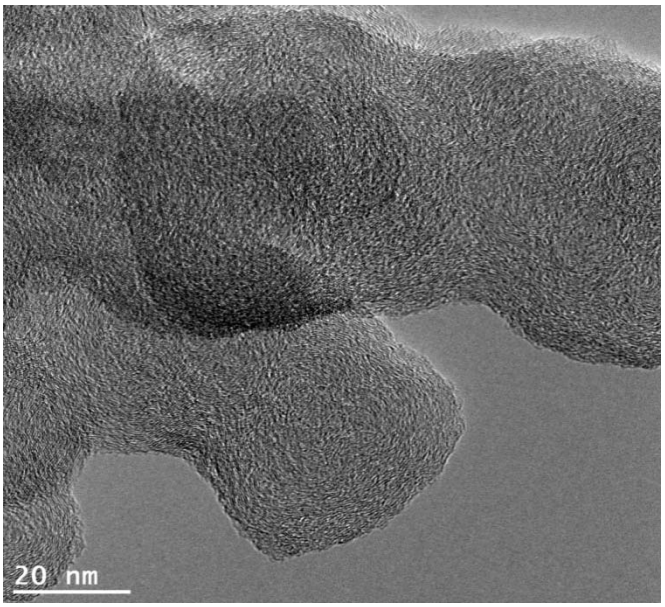

Figure C1. TEM image of OCB. The fingerprint-like structure in the image is the OCB with a diameter between 30-40 nm.

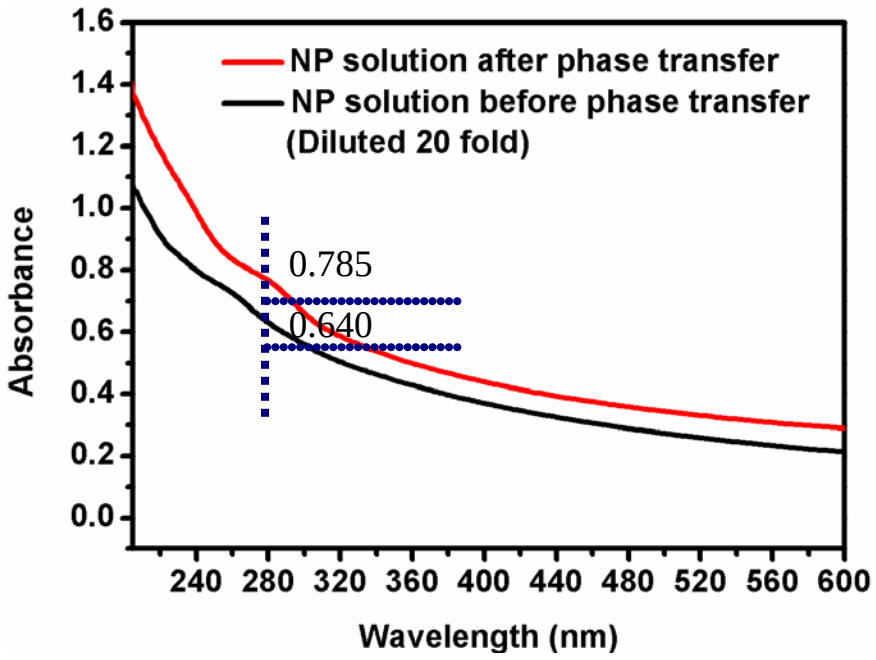

Figure C2. UV-vis spectra of NP (nanoparticle) in sea brine solution before (black solid line) and after phase transfer (red solid line). The characteristic adsorption peak of PE-*b*-PEG-OCB solution is ~ 280 nm. Based on Lambert-Beer's law, only 6% of PE-*b*-PEG-OCB remained in the sea brine solution after phase transfer.

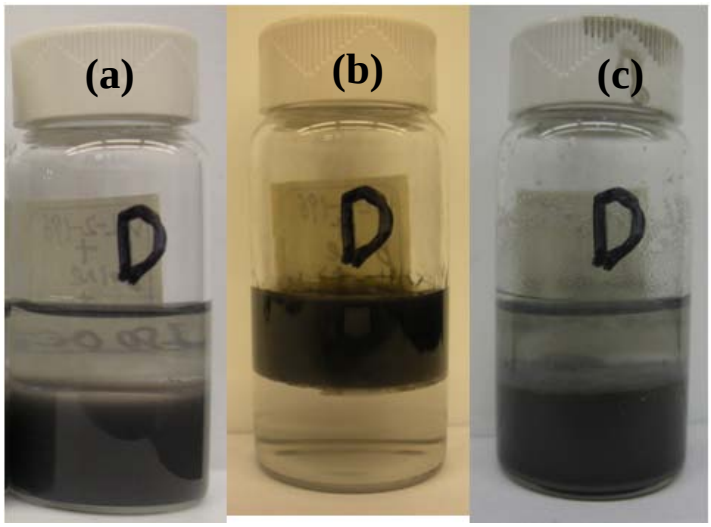

Figure C3. Phase transfer behaviour of 1400 M_n PE-*b*-PEG coated OCB in the synthetic sea brine. Photographs of a two-phase mixture of PE-b-PEG-OCB/synthetic sea brine solution (the concentration of OCB in sea brine was 50 mg/L, functionalized by 1400 M_n PE-b-PEG) and isooctane (a) before and (b) phase transfer caused by heating (a) at 90 ºC for one week, and (c) is (b) after being stirred at room temperature for 1 h upon cooling.

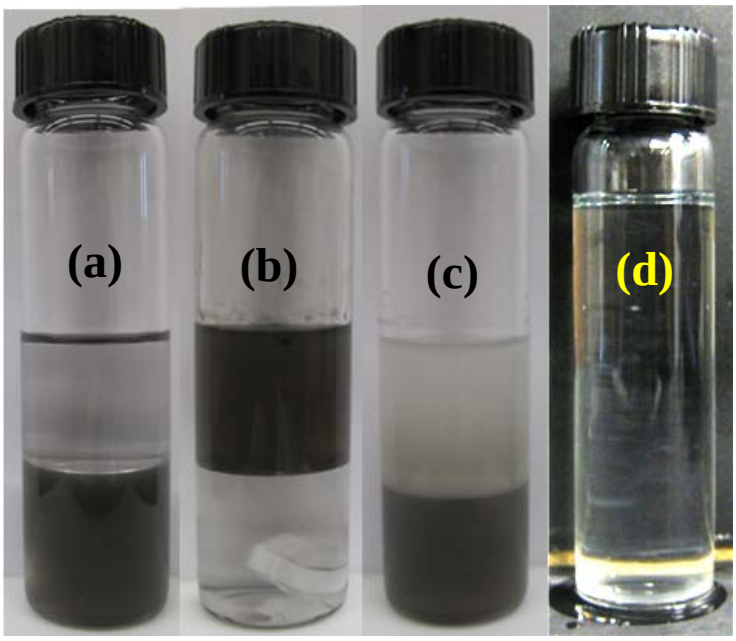

Figure C4. Phase transfer behaviour of 920 M_n PE-*b*-PEG coated OCB in the synthetic sea brine. Photographs of a two-phase mixture of PE-*b*-PEG-OCB/synthetic sea brine mixture (the concentration of OCB in the synthetic sea brine was 50 mg/L, functionalized by 920 M_n PE-*b*-PEG) and isooctane (a) before and (b) after being heating at 110 ºC for 1 h. (c) The mixture after stirring at room temperature for 1 h. The isooctane phase became turbid due to insoluble homopolymer polyethylene contamination at room temperature. (d) 920 M_n PE-*b*-PEG in isooctane (500 mg/12 mL isooctane) after being heated at 110 ºC for 1 h after gentle shaking. The clear solution indicates that the 920 M_n PE-*b*-PEG was nearly completely soluble in the isooctane at a temperature slightly higher than the melting temperature of the PE block and thus the corresponding PE-*b*-PEG-OCB NPs could move into the oil phase at higher temperatures. The sample was photographed against a dark background to show that there was no milky-white precipitate present.

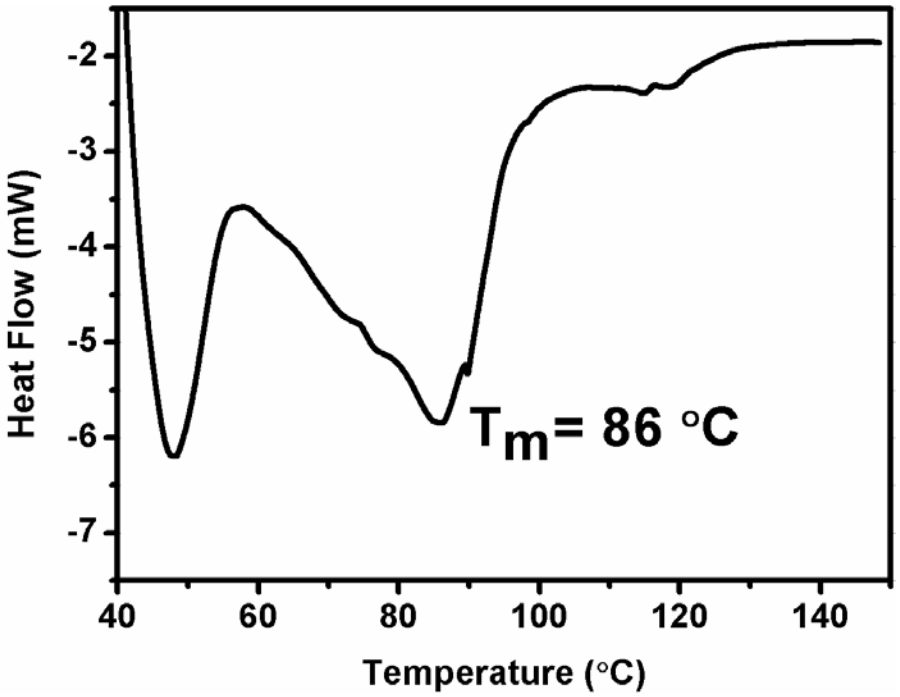

Figure C5. DSC curve of 920 M_n PE-*b*-PEG. The peak at 86 ºC is attributed to the main crystalline phase of the PE block, while the peak at 47 ºC is associated with the secondary crystalline phase of the PE block.

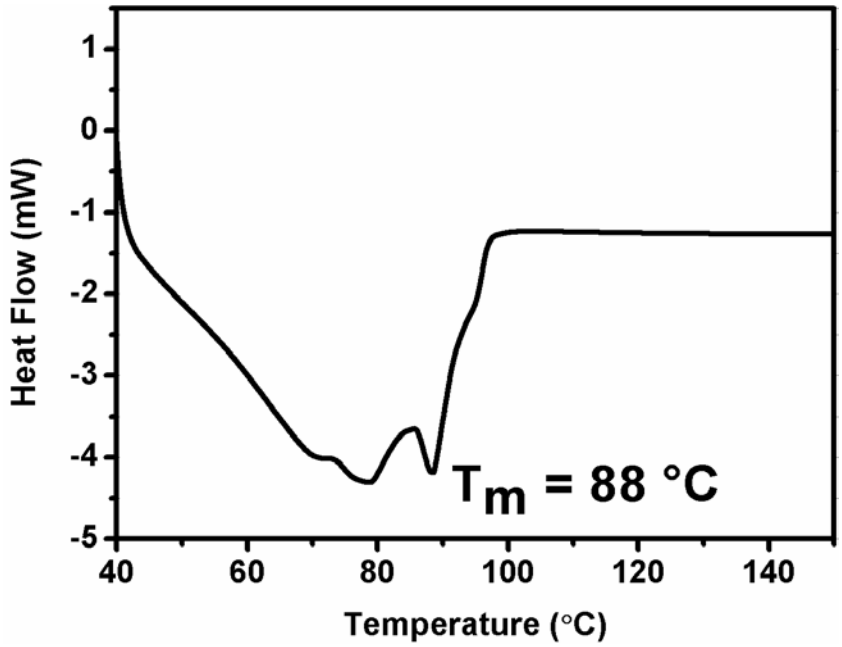

Figure C6. DSC curve of 575 M_n PE-*b*-PEG. The peak at 88 ºC is attributed to the main crystalline phase of the PE block, while the peak at 80 ºC is associated with the secondary crystalline phase of the PE block.

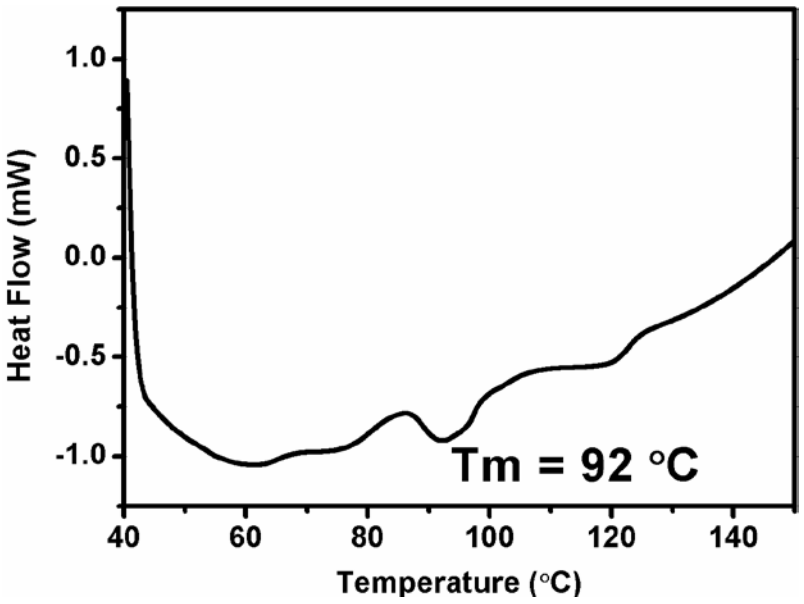

Figure C7. DSC curve of 2250 M_n PE-*b*-PEG. The peak at 92 ºC is attributed to the main crystalline phase of the PE block, while the peak at 62 ºC is associated with the secondary crystalline phase of the PE block.

References:

1 Berlin, J. M.; Yu, J.; Lu, W.; Walsh, E. E.; Zhang, L.; Zhang, P.; Chen, W.; Kan, A. T.; Wong, M. S.; Tomson, M. B.; Tour, J. M. *Energy & Environ. Sci.* **2011**, *4*, 505-509.

2 Li, T.; Wang, W. J.; Liu, R.; Liang, W. H.; Zhao, G. F.; Li, Z. Y.; Wu, Q.; Zhu, F. M. *Macromolecules* **2009**, *42*, 3804-3810.

3 Edwards, E. W.; Chanana, M.; Wang, D.; Möhwald, H. *Angew. Chem. Int. Ed.* **2008**, *120*, 326-329.

Appendix D

The appendix corresponds to the supporting information of Chapter 4

I. Additional analysis of GNRs

- **TEM images of GNRs**
- **XPS spectra of GNRs and MWCNTs**
- **UV-vis spectroscopy of GNRs and MWCNTs**

II. Comments on computational studies

I. Additional analysis of GNRs

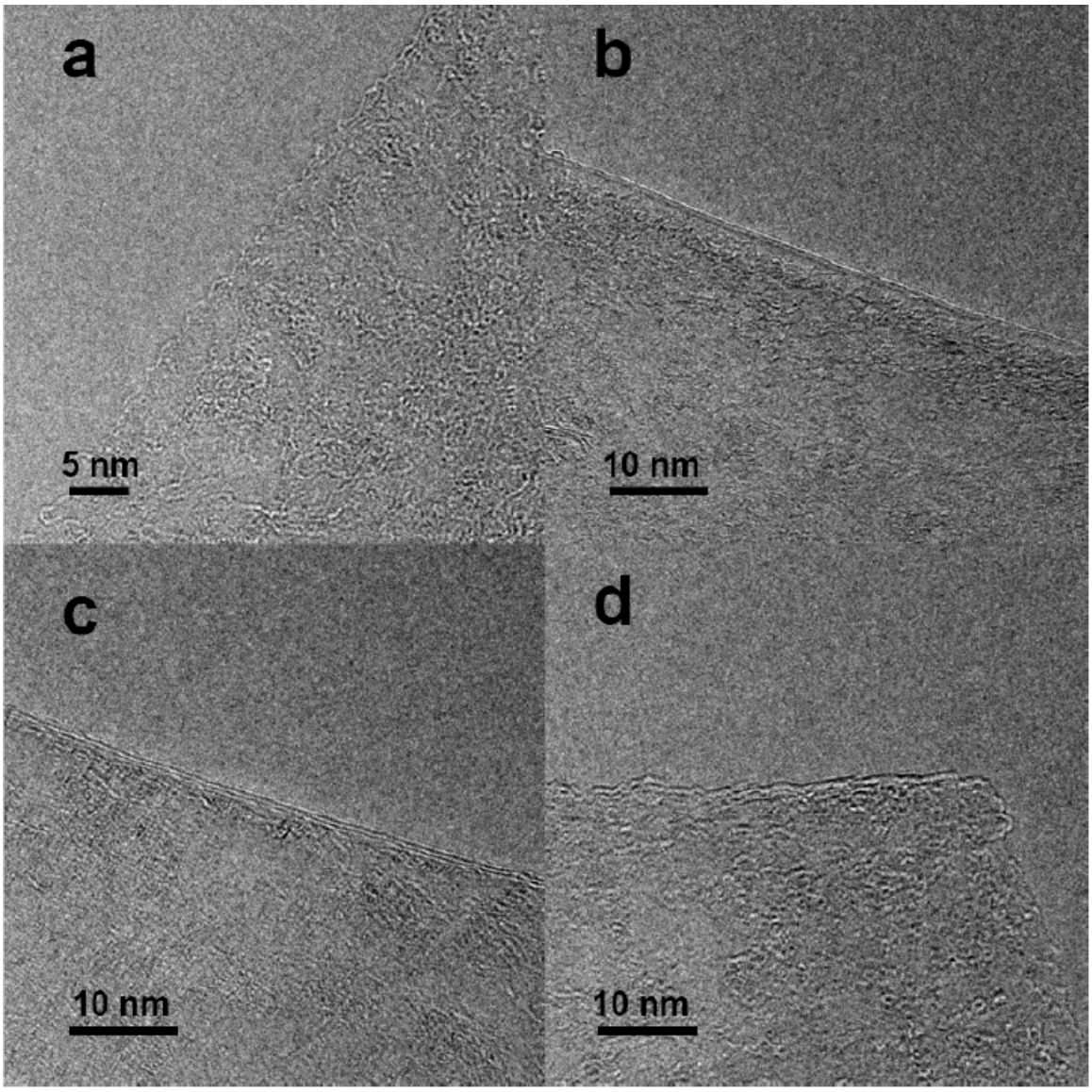

Figure D1. TEM images of graphene nanoribbons edges. a-c) Images of the edge of a bilayer GNR. d) TEM image of the edge of a trilayer GNR.

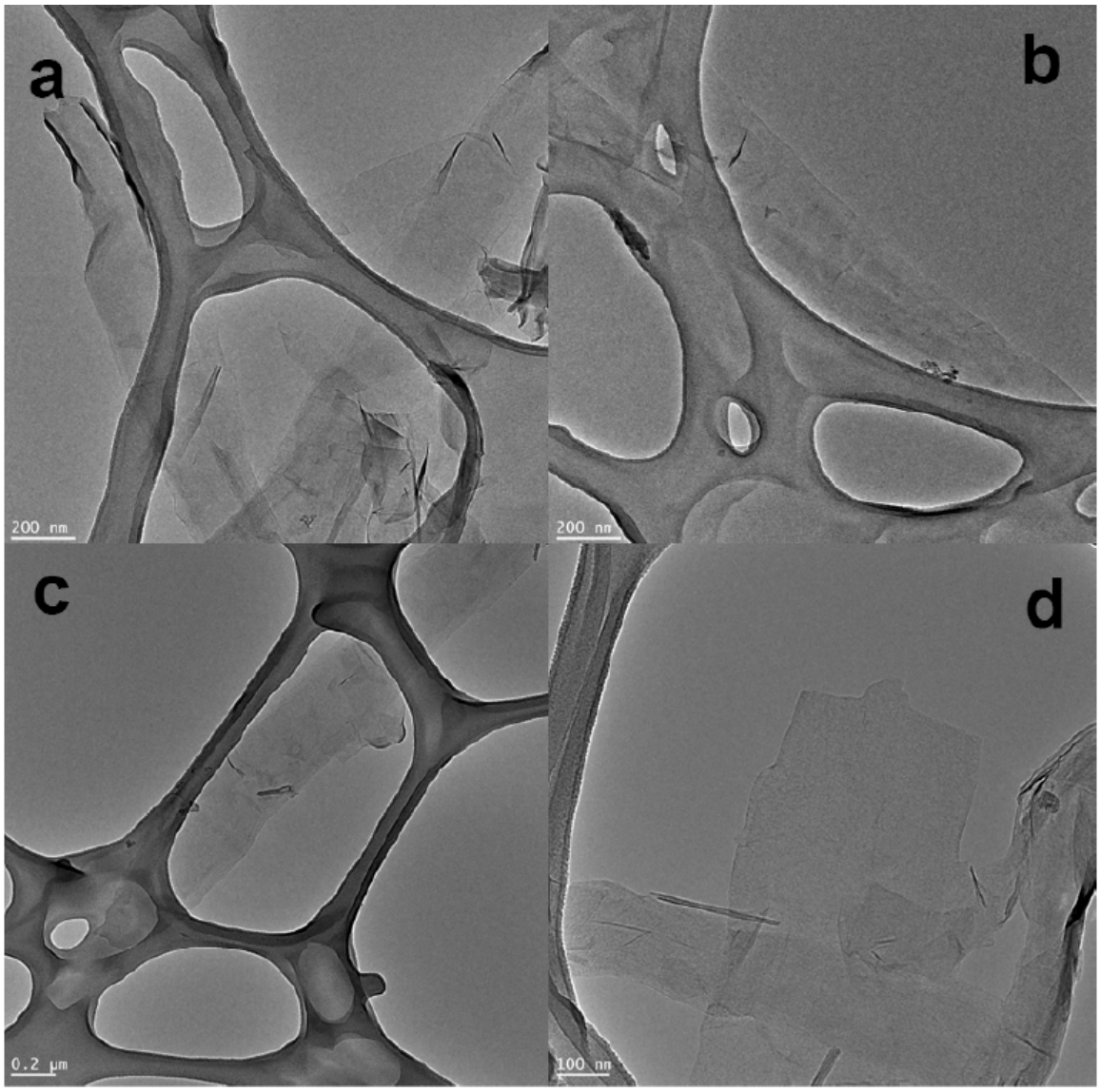

Figure D2. Additional TEM images of GNRs. a-d) TEM images (shaded areas) of few-layer GNRs atop a grid (curved structures). Complete exfoliation of MWCNTs GNRs is evident.

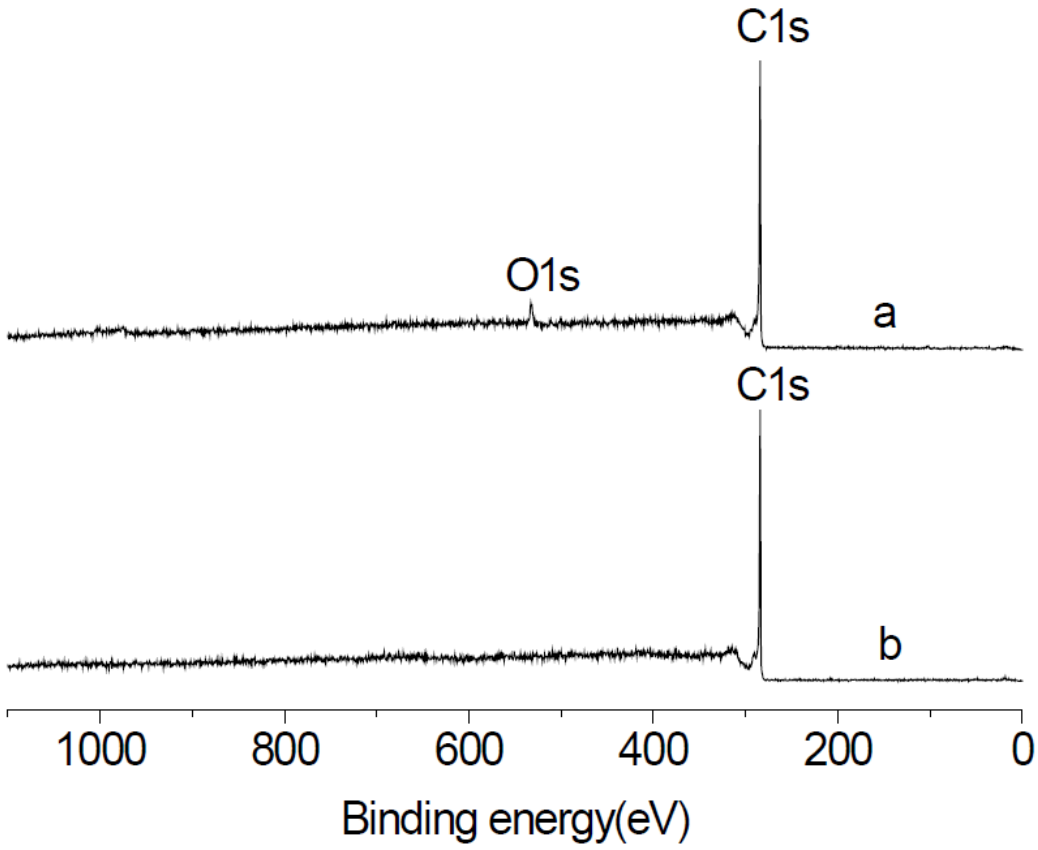

Figure D3. XPS survey data of GNRs and MWCNTs. a) XPS survey spectrum of GNRs. The signal at 532 eV could be attributed to adsorbed oxygen (see Figure D4). b) XPS survey spectrum of the original MWCNTs.

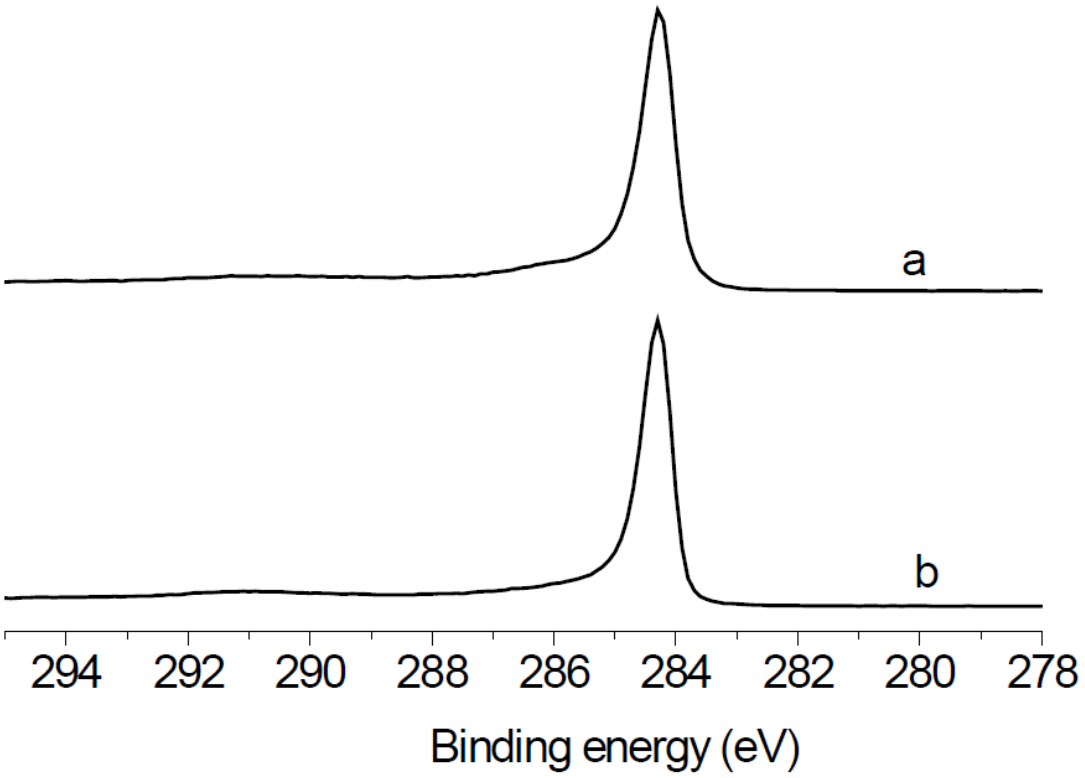

Figure D4. High-resolution XPS C1s spectra of GNRs and MWCNTs. a) XPS C1s spectrum of GNRs. No signals at 286 eV (C-O) and 287 eV (C=O) were observed. This further confirms that oxygen seen in the XPS survey data (Fig. D3) was physically adsorbed rather than chemically attached. b) XPS C1s spectrum of original MWCNTs.

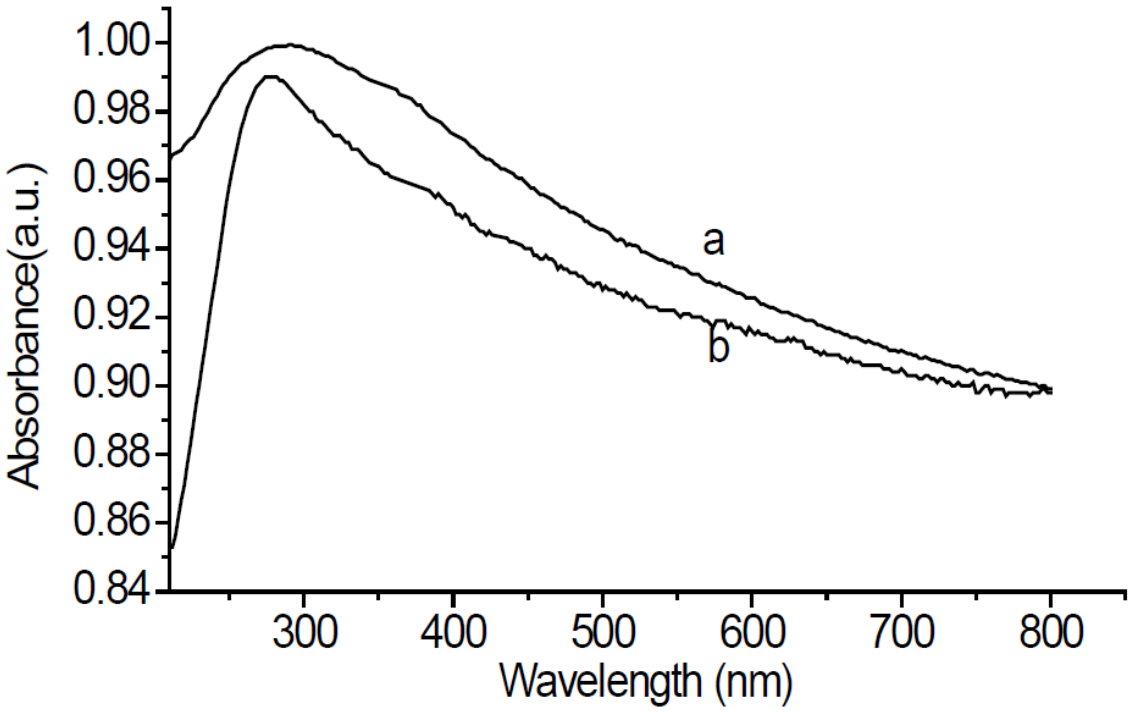

Figure D5. Comparison of UV-vis spectra of GNRs and MWCNTs dispersed in ethanol. a) MWCNTs. b) GNRs. Both absorption maxima are located at 280 nm and shifted bathochromically with respect to chemically converted graphene (270 nm)[1] suggesting better integrity of the graphene structure.

II. Comments on computational studies

The intercalation of alkali metal atoms into the interstices of MWCNTs was studied using Forcite module of Accelrys Materials Studio 4.3 using universal force field both with and without QEq charging for all models. The maximum number of iterations was set to 500. Electron transfer from the metal to graphene lattice was disregarded and atomic radii of metal atoms were not contracted to reflect their ionic character when QEq charging was not applied; therefore, the distances between the intercalated atoms and

interstitial distances between graphene sheets of the intercalates found by geometry optimization in the van der Waals approximation are likely to be unreliable.

The adequacy of our rather simplistic model for the task of illustrating possible nanoscale phenomena occurring during the metal intercalation driven splitting of MWCNTs was verified by simulating the behavior of a hexagonal, 30-atom slice (3.76 x 1.60 nm) cut from a single crystal of potassium in the (1 1 0) direction and sandwiched between two rectangular sheets (5.74 x 4.94 nm, 1147 carbon atoms each) of single layer graphene obtained by cutting a slice from AB-stacked graphite and terminating the dangling bonds with hydrogen atoms. As a result of geometry optimization in van der Waals approximation (RMS force was optimized to 2.26 x 10^{-1} kcal/mol/Å using 500 iterations and 1 min 13 s of processor time), the 0.34 nm^2 interplanar distance between the graphene sheets increased to 0.70 nm exceeding the 0.54 nm experimental value for C_8K by 30%. This disparity can be largely attributed to the excess of the van der Waals radius of potassium (0.275 nm) over its ionic radius (0.138 nm). Thus the experimentally observed spacing increment contributed to graphite by intercalating potassium atoms is 0.20 nm, which amounts to about 73% of the ionic diameter of potassium. If a species with a diameter equal to the van der Waals diameter of potassium were to contribute the same proportion of its diameter to the interplanar spacing increase, the increment would have been 0.40 nm, in a good agreement with the calculated value of 0.36 nm. Transition from AB stacking in pristine graphite to the AA arrangement in C_8K^3 was not reproduced by our model, as its influence on the values of optimized parameters of individual atoms is likely to be very small.

Application of the QEq charging improved agreement with the experiment (RMS force was optimized to 3.79 x 10^{-2} kcal/mol/Å using 500 iterations and 54 min of processor time). Therefore, the distance between the graphene sheets in the geometry optimized intercalate was 5.0 nm and the distances between the potassium atoms were around 2.9 nm *vs*. the experimental value of 4.9 nm^3 for C_8K. The carbon atoms in the immediate vicinity of the potassium had calculated negative charges of approximately 0.07 units, while at the periphery of the flakes they were almost electrically neutral. When one of the graphene sheets and all carbon atoms not constituting benzene rings within the intercalation region were removed, the chemical composition of the remainder was $C_{6.8}$ K, which is not far from the experimentally determined limit of eight carbons to one potassium. It can be reasonably assumed that the underestimation of the interplanar and potassium-potassium distances resulted from the inability of the combined influences of the small number of potassium atoms injected between the graphene sheets to counteract the van der Waals attractions of the latter in a degree observed in a C_8K crystal.

Then, the same slice of potassium was inserted between the outer and the middle layers of a 3-walled MWCNT comprising (16, 16), (11, 11) and (6, 6) hydrogen terminated SWCNTs in a coaxial arrangement. To match the curvature of the interstitial void, the potassium slice was bent with a radius of 0.916 nm during the insertion (Figure D6). After geometry optimization in the van der Waals approximation (RMS force was optimized to 6.93 x 10^{-3} kcal/mol/Å using 500 iterations and 4 min 2 s of processor time), the potassium atoms were found aligned along the axis of the MWCNT, while the immediately proximate regions of MWCNT sidewalls bulged to create a “blister” around

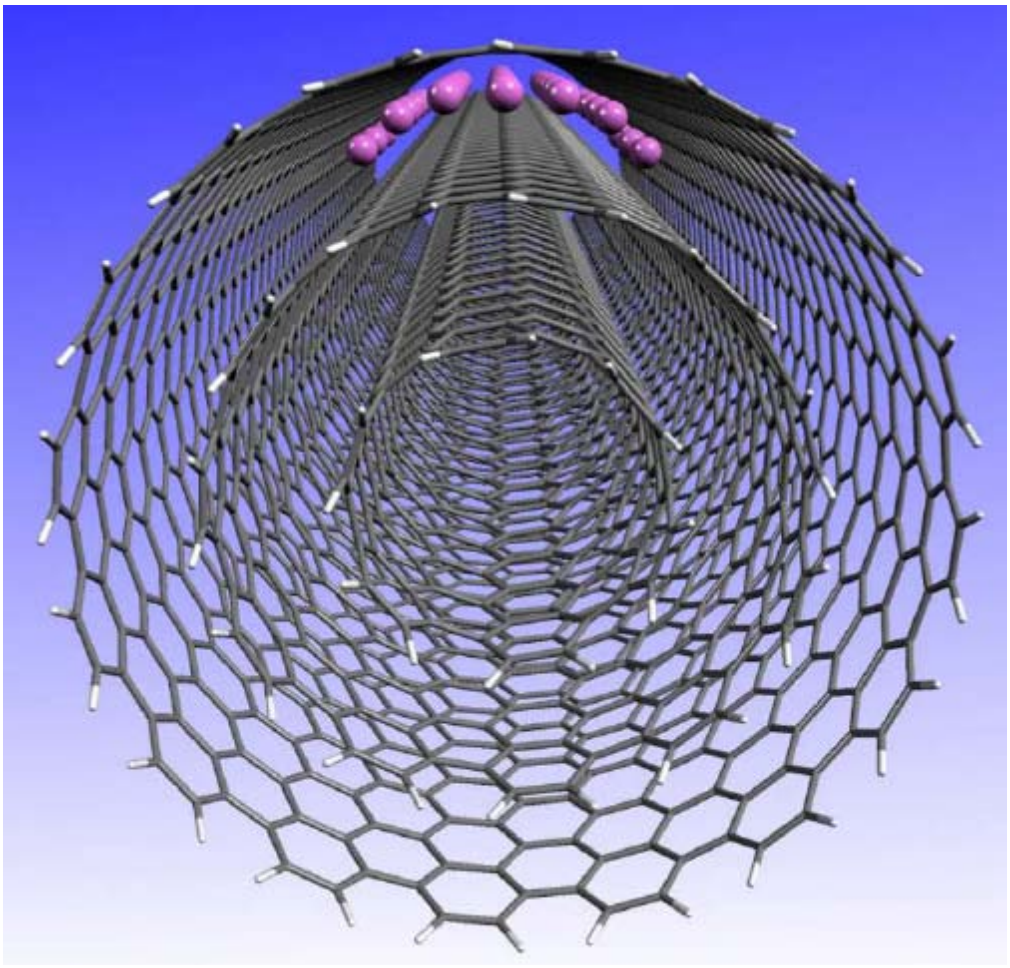

Figure D6. Model of a MWCNT with an intercalated planar cluster of 30 potassium atoms (shown as violet spheres) prior to geometry optimization.

the metal cluster. The “blister” was much more extended along the axis of the nanotubes (3.06 nm) than across its circumference (0.48 nm) and it was approximately 0.57 nm thick (Figure D7). It is noteworthy that the “blister” was formed at the expense of the middle wall depressing as much as the outer wall bulged. The increase of the interstitial spacing (0.23 nm) in comparison with the original value was much smaller than previously calculated for bilayer graphene intercalation (0.36 nm). A likely reason for

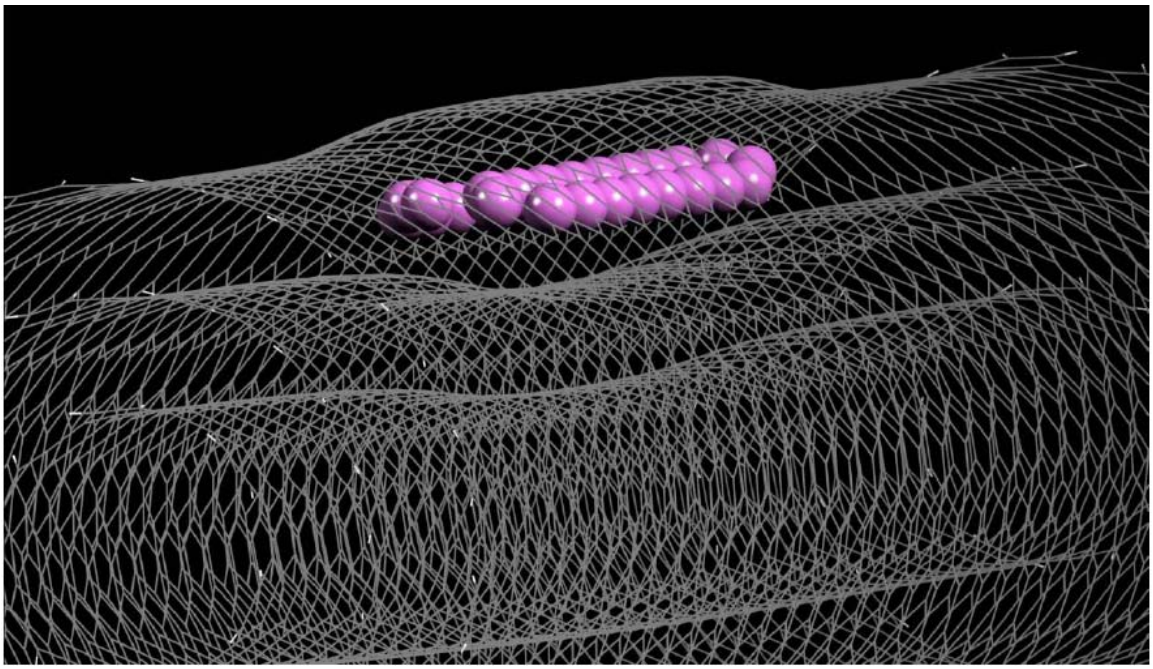

Figure D7. Orthographic view of the “blister” formed around the potassium cluster as a result of geometry optimization in van der Waals approximation. Deformations of proximate regions of inner nanotubes are clearly visible.

this discrepancy is that the interstices of the MWCNT can accommodate the incoming metal atoms only if carbon-carbon bonds are stretched, while graphene sheets of a graphite crystal can merely move apart. The carbon-carbon bonds in the top portion of the “blister” were elongated to 0.143 nm from 0.141 nm extant in the original nanotube. Although the calculated bond strain can be overestimated, its existence should not be cast in doubt because MWCNT sidewalls must make room for the incoming metal atoms regardless of their size. As the energy gain obtained during the intercalation due to the attractive interaction between the metal atoms and surrounding graphene is offset by the

energy loss caused by straining of neighboring carbon-carbon bonds, the intercalation should proceed in the direction that provides the smallest possible strain increase.

Assuming that a single intercalating atom is present in the interstitial space immediately below the outermost shell of a MWCNT, then wedge another atom into the immediate vicinity of the first one in either axial or radial proximity to it. Evidently, the axial insertion will cause a smaller strain increase than the radial one. Applying the same logic to other subsequently introduced atoms, we can see that they should form an elongated bulge provided by the model.

The next simulation step dealt with breaking a series of four parallel carbon-carbon bonds on the top of the "blister" and terminating the resulting dangling bonds with potassium atoms. The newly created carbon-potassium bonds were manually untangled to facilitate geometry optimization (RMS force was optimized to 3.12×10^{-2} kcal/mol/Å using 500 iterations and 4 min 9 s of processor time). A van der Waals approximated optimization resulted in expansion of the fissure in the sidewall of the MWCNT apparently caused by buttressing interaction of carbon-potassium bonds. The carbon-carbon bonds at the tips of the cleft were elongated to 1.48-1.52 nm. As a result of added strain, these bonds should become especially susceptible to thermally induced breakage, therefore facilitating further propagation of the fissure mainly along the axial direction of the MWCNT (Figures D8 and D9). The span of the cleft was around 0.326 nm.

Expectedly, simulations repeated on the same MWCNT models with QEq charging resulted in calculated structural parameters that were *quantitatively* different, while leaving the changes in the structure of the MWCNT *qualitatively* the same. Hence,

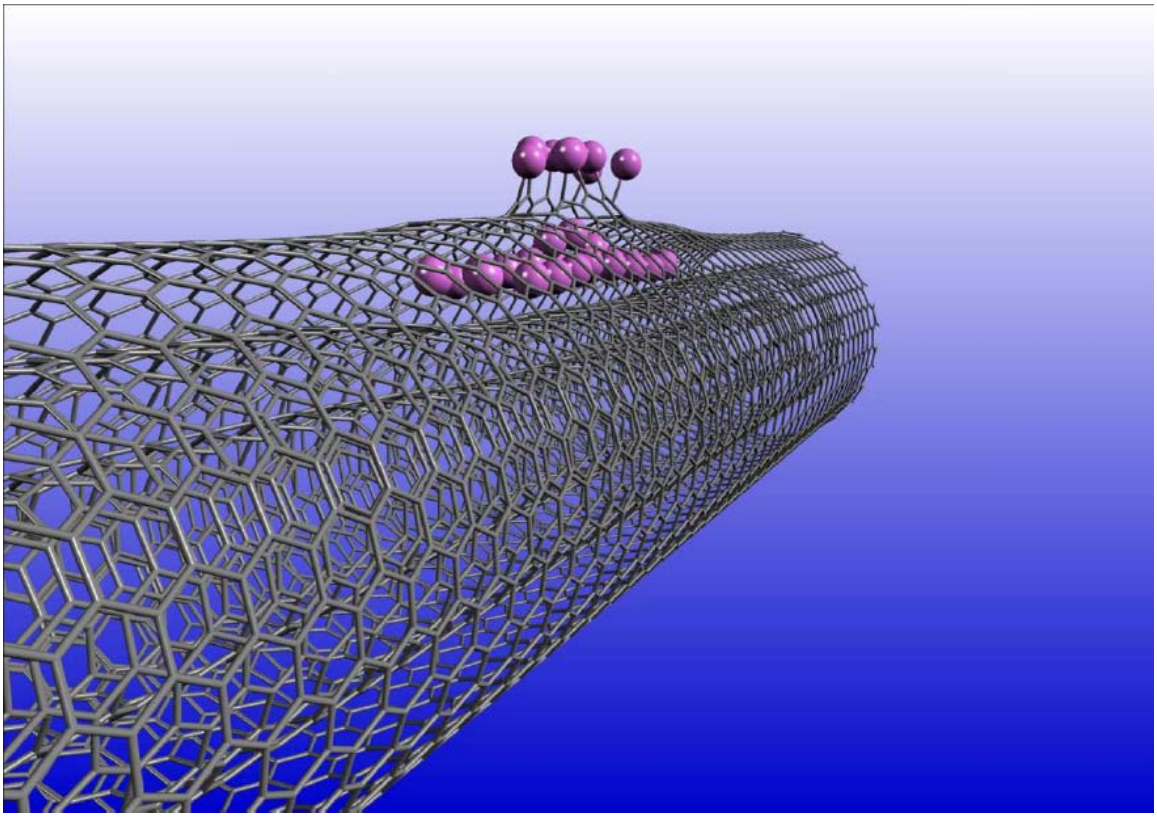

Figure D8. Cleft in the top portion of the potassium "blister" spread apart by buttressing interactions of carbon-potassium bonds simulated in van der Waals approximation.

the interstitial spacing in the "blister" decreased to 0.50 nm vs. 0.57 nm given by the van der Waals model; its length was 3.78 nm and width 1.55 nm as measured between potassium atoms farthest from each other in the particular dimension (RMS force was optimized to 3.18 x 10^{-2} kcal/mol/Å using 500 iterations and 9 h 21 min of processor time). To account for the curvature of the interstitial void, the length of an imaginary arc with the radius of 0.916 nm connecting two potassium atoms was used instead of straight line distance between them. Peculiarly, the potassium cluster failed to contract as much in the transverse direction as it did in the van der Waals model (Figure D9), but it also

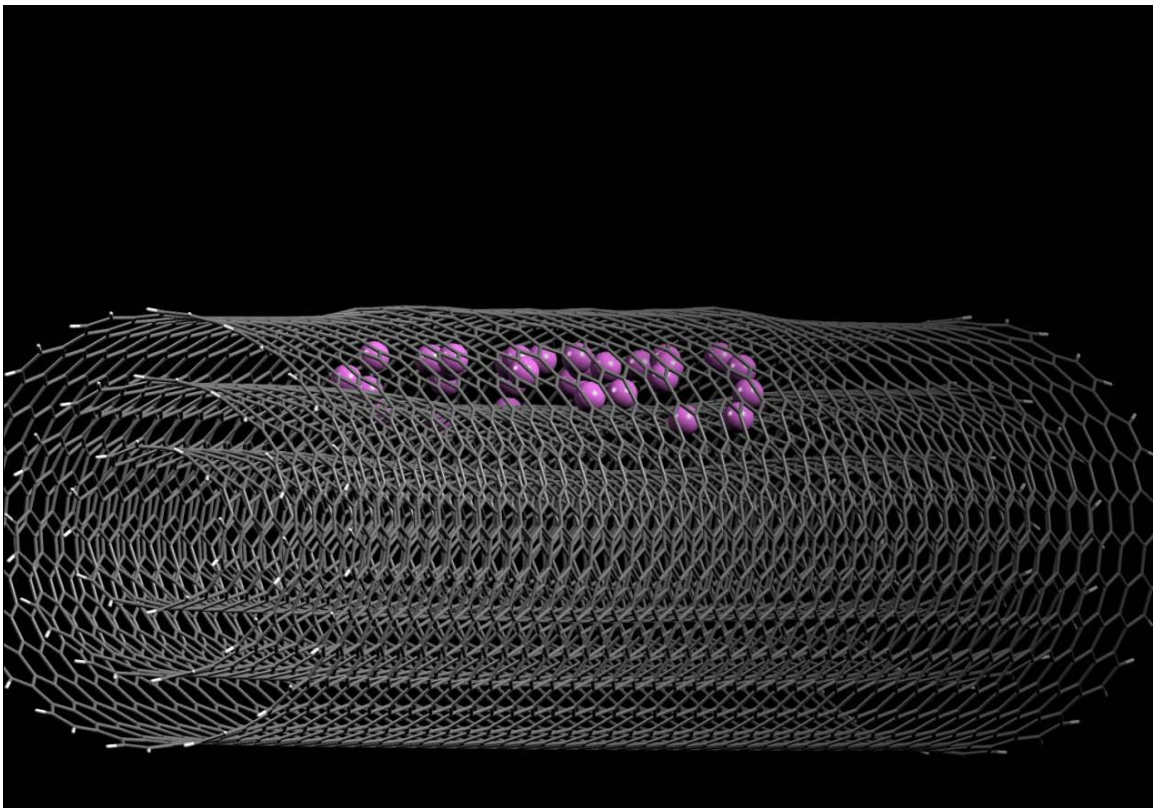

Figure D9. Orthographic view of the “blister” formed around the potassium cluster as a result of geometry optimization with charges applied.

became perceptibly longer thus bolstering the hypothesis that bulges created on the MWCNT sidewalls by metal intercalation should be elongated in the direction of the nanotube axis. The carbon-carbon bonds in the outer part of the “blister” were stretched to 0.142 – 0.143 nm in accord with the uncharged model.

When a slit in the outer wall of the “blister” was made exactly as described above and the resulting model geometry optimized using the QEq charging (RMS force was optimized to 3.79 x 10^{-2} kcal/mol/Å using 500 iterations and 9 h 21 min of processor time), several interesting differences with the van der Waals model were noted. There

was slight additional stretching of the carbon-carbon bonds at the edges of the slit (0.142-0.143 nm vs. 0.140 – 0.142 nm) and much more pronounced opening of the slit itself (0.40 nm vs. 0.32 nm), while the elongation of the carbon-carbon bonds at the tips of the slit remained similar (Figure D10). The wider separation of the edges could be attributed

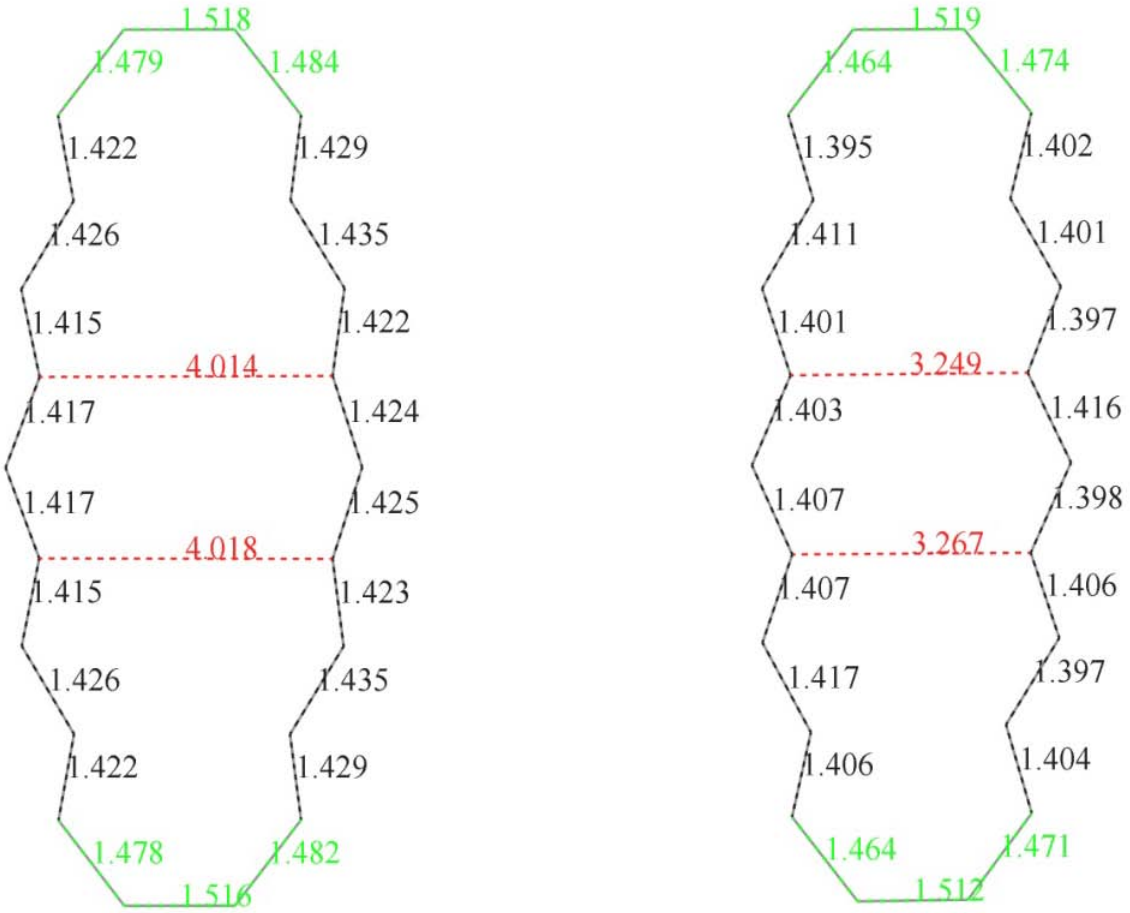

Figure D10. Comparison of interatomic distances at the edges of the cleft in charged (left) and van der Waals (right) models. The cleaved MWCNTs are aligned in the vertical direction. Especially elongated distances are labeled in red and green colors.

to significant accumulation of charges and concomitant increase in coulombic repulsion (Figure D11). Hence, the average charge borne by a carbon atom within the outer wall of

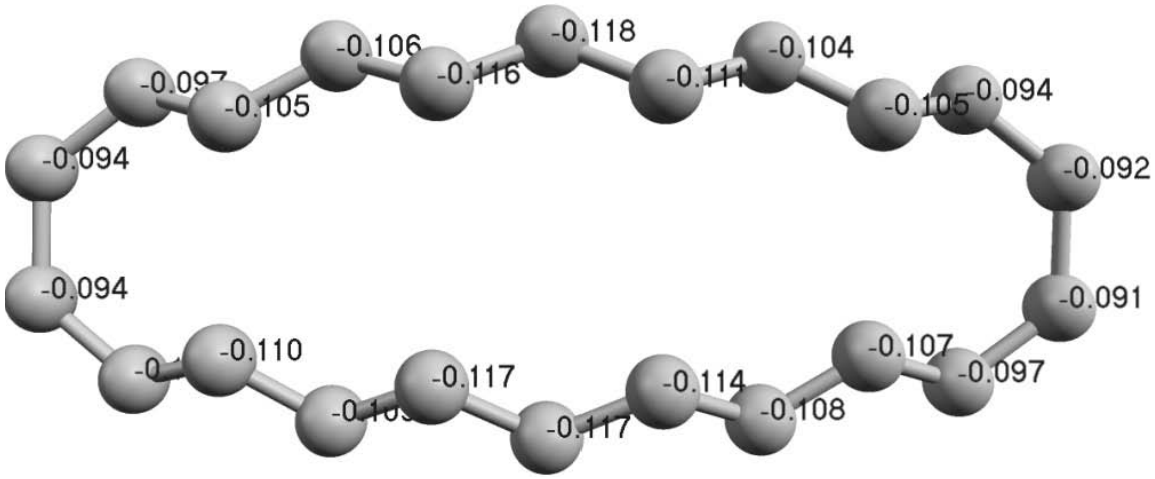

Figure D11. Distribution of charges at the edges of a cleft. The cleaved MWCNT is aligned in the horizontal direction.

the "blister" but far from the edge was around -0.07, whereas an edge atom carried a 40% higher charge of around -0.11 units. It should be noted, that partial negative charges on the sp^2-hybridized carbon atoms of graphene are located on antibonding orbitals, thus reducing the strength of bonding in proportion to their magnitude.

Particularly elongated and weakened bonds are concentrated at the tips of the cleft (Figure D12) regardless of the charges of intercalated particles, consequently giving it three most likely directions of propagation: the original one, along the nanotube axis, and two additional ones, symmetrically deviating from the axis by 30°. At this point, it would be prudent to examine possible propagation directions for an oblique cleft made in the top part of the intercalation "blister" at the 30° to the axis of the MWCNT. When a model of

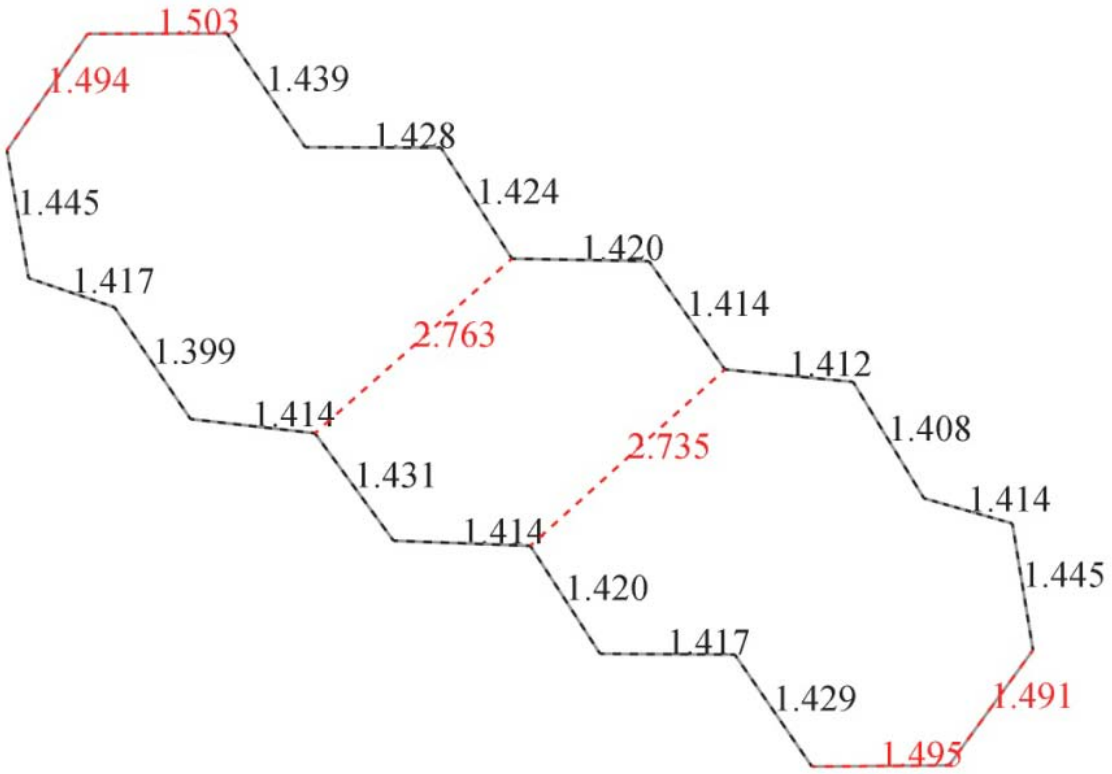

Figure D12. Interatomic distances at the edges of an oblique cleft. The cleaved MWCNT is aligned in the vertical direction. Especially elongated distances are labeled in red.

a cleaved MWCNT intercalated with potassium was prepared and geometry optimized as described above (RMS force was optimized to 1.53 x 10^{-1} kcal/mol/Å using 500 iterations and 9 h 24 min of processor time), a similar accumulation of charges was noticed at the edge of the cleft (Figure D13). There were only four especially elongated bonds in this case, breakage of which would result in the fissures propagating in either its original direction, or along the axis of the nanotube. Peculiarly, the span of the oblique cleft was significantly smaller than that of the straight one (0.27 *vs.* 0.40 nm), demonstrating that the intercalation “blister” is predominantly strained in the transverse direction.

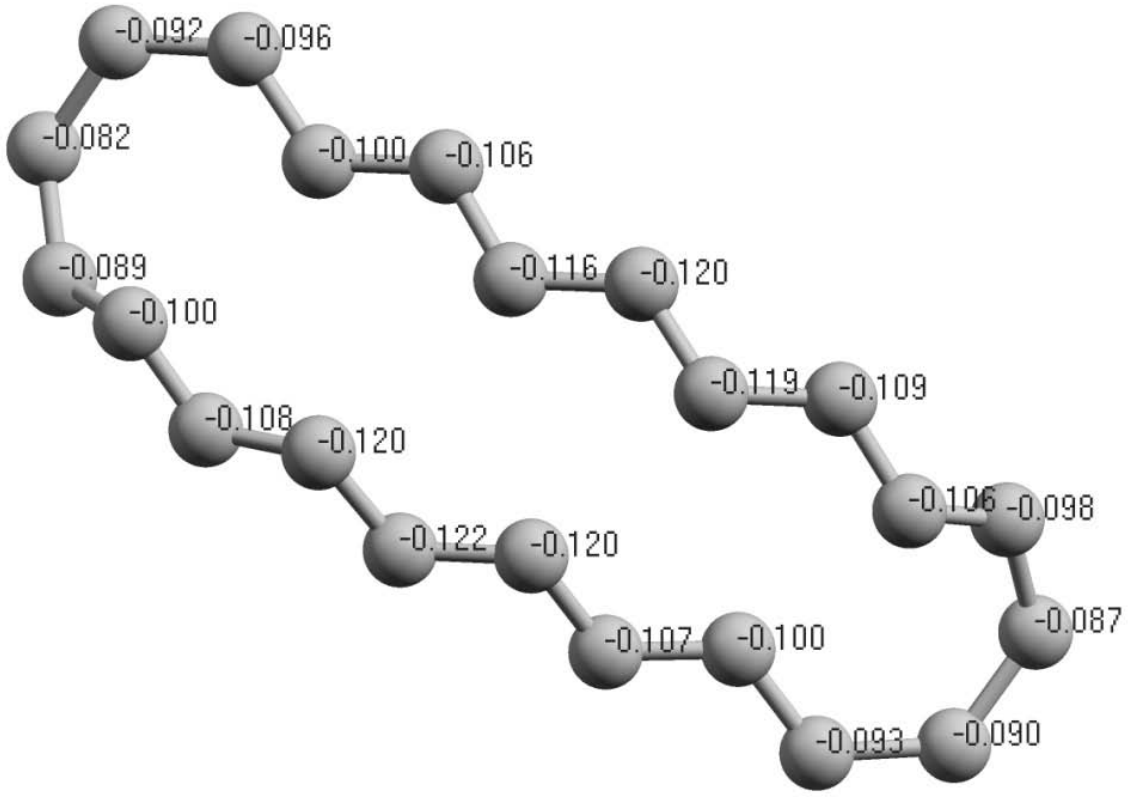

Figure D13. Distribution of charges at the edges of an oblique cleft. The cleaved MWCNT is aligned in the vertical direction.

Apparently, the magnitude of strain in the “blister” should be dependent on the ionic diameter of the intercalated metal and could be insufficient to induce carbon-carbon bond breakage if the diameter is too small. Geometry optimization performed on the same MWCNT model intercalated with Cs, Rb, Na and Li, respectively, demonstrated that the thickness of the “blister” undergoes a sharp drop on transition from potassium to sodium. There is a notable discontinuity in the ionization potential values in the series of the alkali metals also occurring upon this transition (Table D1). The much higher IP of sodium makes its intercalation less energetically favorable than that of potassium.

Table D1. Calculated Interstitial Distances in MWCNTs Intercalated With Alkali Metals.

Metal	I_c MWCNT, nm	ΔI_c, nm (%)	I_c G, nm [3]	ID, nm	IP, eV^2
Cs	0.54	0.20 (59%)	0.594	0.334	3.89
Rb	0.53	0.19 (56%)	0.568	0.304	4.17
K	0.49	0.15 (44%)	0.533	0.276	4.34
Na	0.42	0.08 (29%)	na	0.204	5.13
Li	0.37	0.03 (9%)	0.373	0.152	5.39

I_c MWCNT – calculated interstitial distance in the MWCNT intercalation compound; ΔI_c – increase of the I_c in the intercalation compound over that of graphite; I_c G – experimentally determined interplanar distance in the graphite intercalation compound; ID – cationic diameter of the metal; IP – first ionization potential of the metal.

Together with the fairly large increase in the interstitial distance of the MWCNT required to accommodate the incoming sodium atoms, the higher IP of sodium should make it an unlikely intercalant. The unusually low propensity of sodium to form intercalation compounds with graphite is well-documented.[2] For lithium, the even larger IP may be outweighed by its much smaller ionic diameter that allows the intercalation into graphite to occur without significant increase in the interplanar distance.[2] Although lithium could be expected to enter the interstitial spaces of MWCNTs with ease, the resulting increase of strain in the carbon network would scarcely be enough to induce breakage of carbon-

carbon bonds, at least below the temperatures where lithium carbide would become the major product.

Owing to their large ionic diameters and low IPs, rubidium and cesium should be even more efficient at causing longitudinal rupture of MWCNTs, provided that transient or permanent defects in the nanotube walls responsible for the passage of metal atoms into the interstitial void are large enough to let them through. Unfortunately, experimentation with Cs and Rb requires constant blanketing with argon and these metals are too expensive to be used on a large scale.

Whereas the $KMnO_4$ treatment of MWCNTs resulted in graphene nanoribbons with edges appearing perfectly straight in the SEM images over micrometer long distances,[4] the edges of the nanoribbons obtained from the intercalation-induced splitting were noticeably jagged although their general linearity was preserved (Figures 4.1). This observation indicates that chemical selectivity of the reaction or reactions resulting in the extension of the cleft in the nanotube sidewall is somewhat reduced. The origin of the lower selectivity may be traced to the fact that breaking of individual strained carbon-carbon bonds at the tips of the cleft is caused by simple thermal motions of the corresponding atoms, rather than a chemical reaction involving defined intermediates, which is likely the case with $KMnO_4$. In the environment where no other reagent or solvent is present, the free carbon-centered radicals (or anions) produced by the bond breakage will be quenched by an appropriate form of potassium, giving carbon-potassium bonds that may survive until the work-up.

References

1. Li, D.; Müller, M. B.; Gilje, S.; Kaner, R. B.; Wallace, G. G. *Nat. Nanotech.* **2007**, *3*, 101-105.
2. Novikov, Y. N.; Vol'pin, M. E. *Russ. Chem. Rev.* **1971**, *40*, 733-746.
3. Satake, M.; Iqbal, S. A. *Chemistry of P-Block Elements*, Discovery Publishing House, New Delhi,1995.
4. Kosynkin, D. V.; Higginbotham, A. L.; Sinitskii, A.; Lomeda, J. R.; Dimiev, A.; Price, B. K.; Tour, J. M. *Nature* **2009**, *458*, 872-876.

Appendix E

The appendix corresponds to the supporting information of Chapter 5

Experimental details for the synthesis of non-functionalized GNRs (H-GNRs)

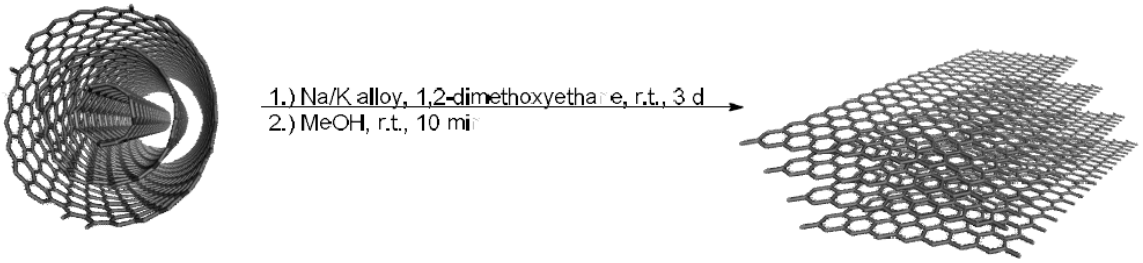

To an oven-dried 250 mL round-bottom flask containing a magnetic stir bar were added the multi-walled carbon nanotubes (MWCNTs, 100 mg, 8.3 mmol). The vessel was then transferred to a N_2 glove box where freshly distilled 1,2-dimethoxyethane (35 mL) and liquid Na/K alloy (0.29 mL) were added. The flask with the suspension was then sealed with septa and transferred out of the glove box where it was dispersed by a short 5 min ultrasonication to yield a dark greenish to red suspension. After ultrasonication, the reaction mixture was vigorously stirred (450 RPM) at room temperature for 3 d. The reaction suspension was then quenched by the addition of methanol (20 mL, 500 mmol) using a syringe and stirring was continued at room temperature for 10 min. The reaction mixture was filtered over a 0.45 μm pore size PTFE membrane. The filter cake was successively washed with THF (100 mL), i-PrOH (100 mL), H2O (100 mL), i-PrOH (20 mL), THF (20 mL), Et_2O (10 mL) and dried under in high vacuo.

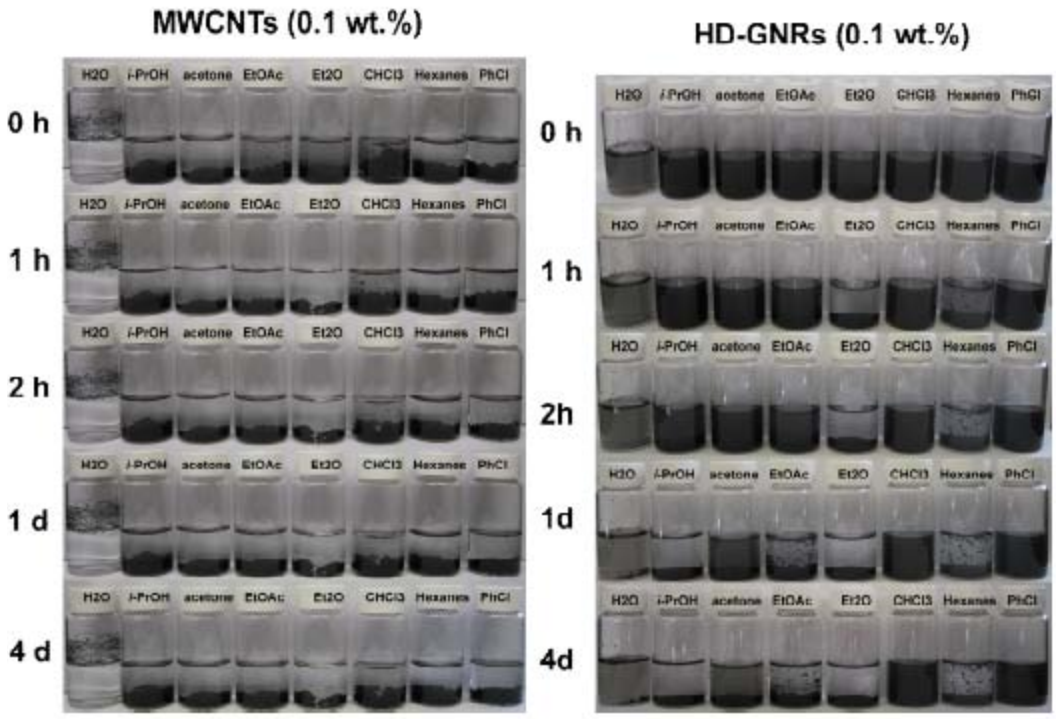

Figure E1. Comparison of solubility of 0.1 wt% starting material MWCNTs (left) and of 0.1 wt% functionalized HD-GNRs (right). Commercial MWCNTs are non-dispersible in organic solvents after short sonication using ultrasonic cleaner. HD-GNRs are well dispersible in organic solvents after short sonication.

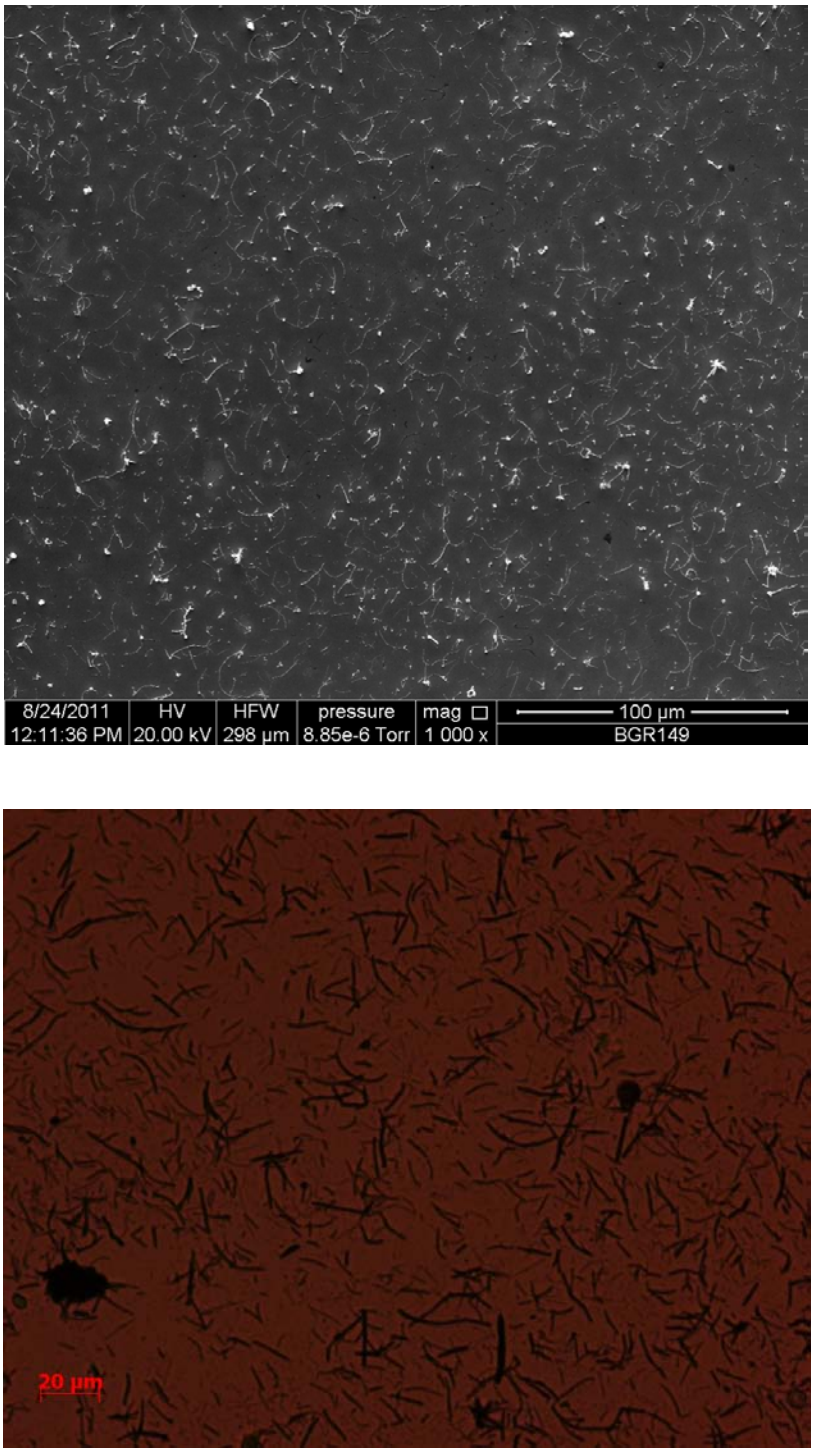

Figure E2. SEM images of functionalized GNRs. Upper image: SEM image of Mitsui-originated functionalized HD-GNRs. Lower image: Optical microscope of NTL-originated functionalized HD-GNRs.

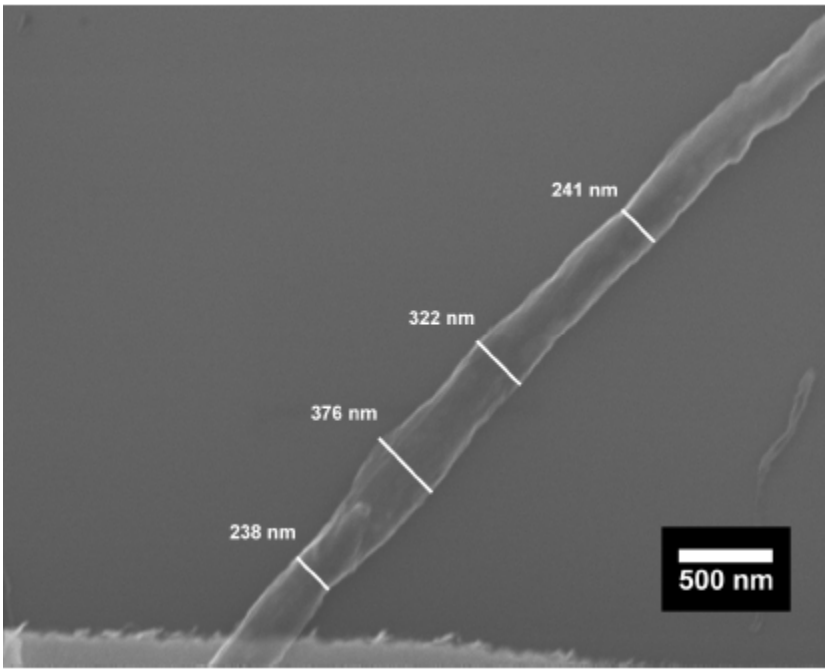

Figure E3. SEM image showing width of a single HD-GNR used in a device for conductivity measurements.

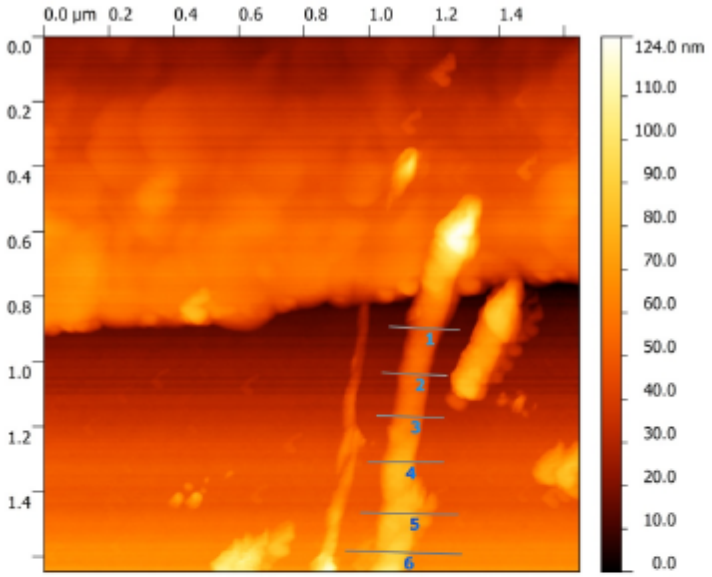

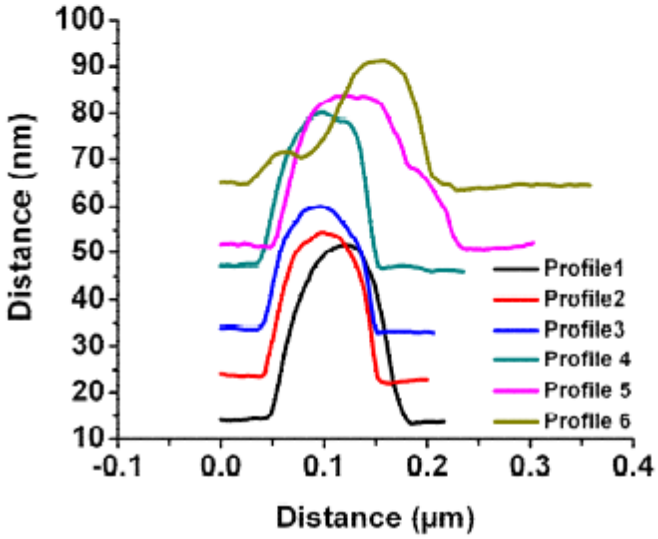

Figure E4. AFM image (top) and profile plot (bottom) showing thickness of a single HD-GNR used in device for conductivity measurements. AFM images were obtained with a Digital Instruments nanoscope IIIa, operating in tapping mode, using Si tips n-doped with 1-10 Ωcm phosphorus (Veeco, MPP-11100-140).

Equation E1. Conductivity.

$$\boldsymbol{Conductivity}\left(\frac{\boldsymbol{S}}{\boldsymbol{cm}}\right)=\frac{\boldsymbol{L}\,(\boldsymbol{cm})}{\boldsymbol{R}\,(\boldsymbol{\Omega})*\boldsymbol{t}(\mu\boldsymbol{m})*\boldsymbol{W}(\boldsymbol{cm})*\boldsymbol{0.0001}}$$

Table E1. The data used for calculating conductivity with Equation E1.

Resistance	Resistivity	Conductivity	GNR Thickness	GNR Width	GNR Length	Temperature of annealing
R (Ω)	R (Ωcm)	s(S/cm)	t (μm)	W (cm)	L (cm)	˚C
2060	0.0002347	4261.06	0.03	0.00003	0.00079	900
2480	0.0002825	3539.42	0.03	0.00003	0.00079	300
14600	0.0016633	601.22	0.03	0.00003	0.00079	25

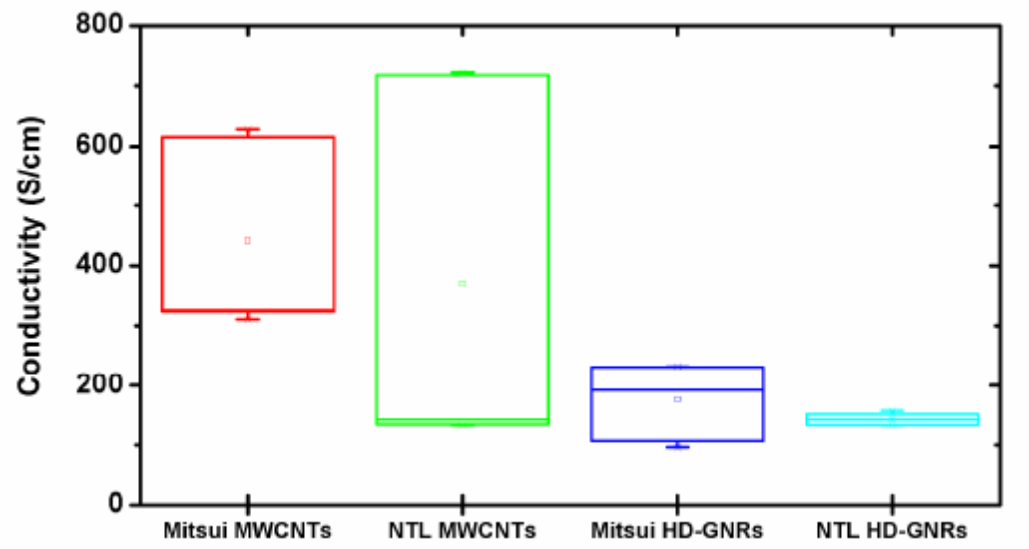

Figure E5. Statistical representation of bulk conductivities of starting material MWCNTs and functionalized HD-GNRs using a four-point probe cell. Five pellets of each sample were prepared. The pellets were pressed using a pellet die with a 13 mm diameter. 100 mg of sample was loaded into the die and pressed applying 8 T of pressure for 30 s. The solid pellet was then loaded into the four-point probe cell (Scheme E1 below) and current and potential were measured. Bulk conductivity was calculated using Equation E2.

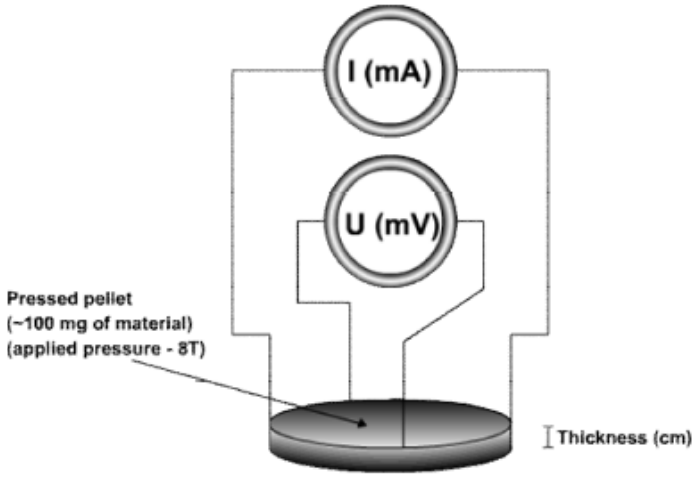

Scheme E1. The measurement of the current and potential of the solid HD-GNR pellet in the four-point probe cell.

Equation E2 Bulk conductivity

$$\sigma(Scm^{-1}) = \frac{ln2 \times I(mA)}{\pi \times \mathrm{U(mV)} \times \text{pellet thickness (cm)}}$$

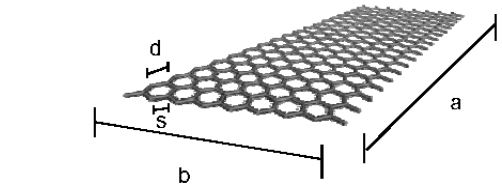

F = Functional Group
C = Carbon
$n_{C(edges)} = n_{F(edges)}$

presumption = only and all of the edges were functionalized

	value	unit
a	2700	nm
b	250	nm
d	0.246	nm
s	0.142	nm
$M_{(C)}$	12	g/mol
$M_{(F)}$	225	g/mol
$m_{(ribbon)}$	8.89E-16	g
$m_{(\Sigma F)}$	8.96E-18	g
Wt	1.00	%

for TGA comparison

	value	unit
$N_{C(all)}$	44,616,300	#atoms
$n_{C(all)}$	7.41E-17	mol
$m_{C(all)}$	8.89E-16	g

	value	unit
$N_{C(edges)}$	23,984	#atoms
$n_{C(edges)}$	3.98E-20	mol
$m_{C(edges)}$	4.78E-19	g

atomic % of the edges	0.05

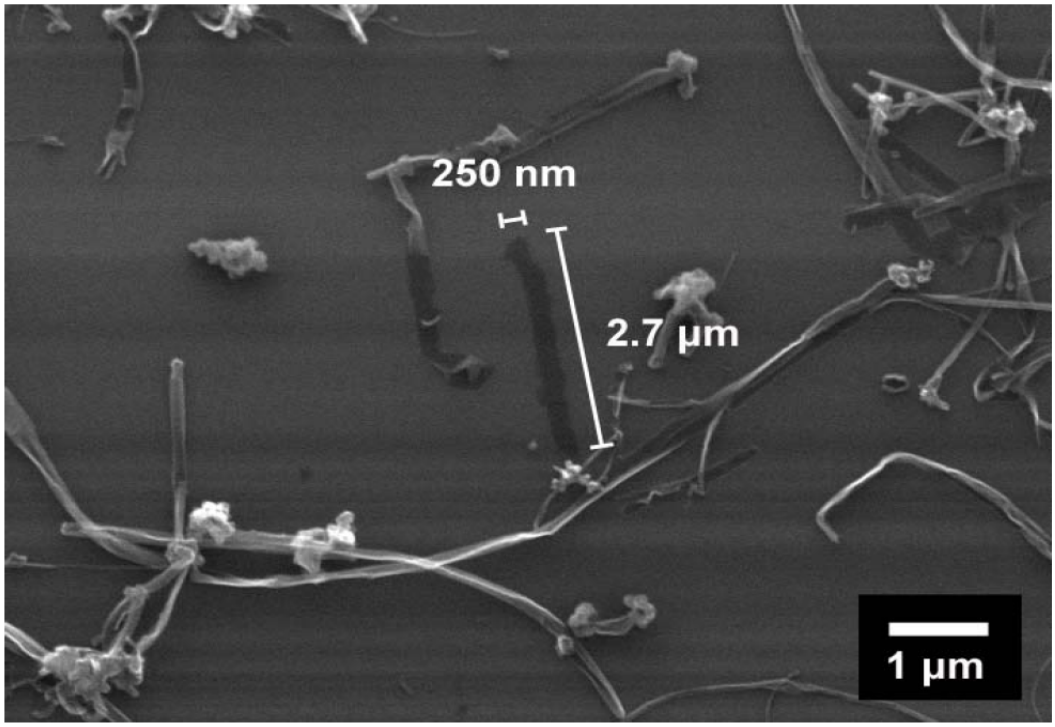

Figure E6. Calculation of the hypothetical degree of edge functionalization with HD groups (top). The length and width were estimated from the SEM image (bottom). The presumption was made that only the edge carbons are functionalized.

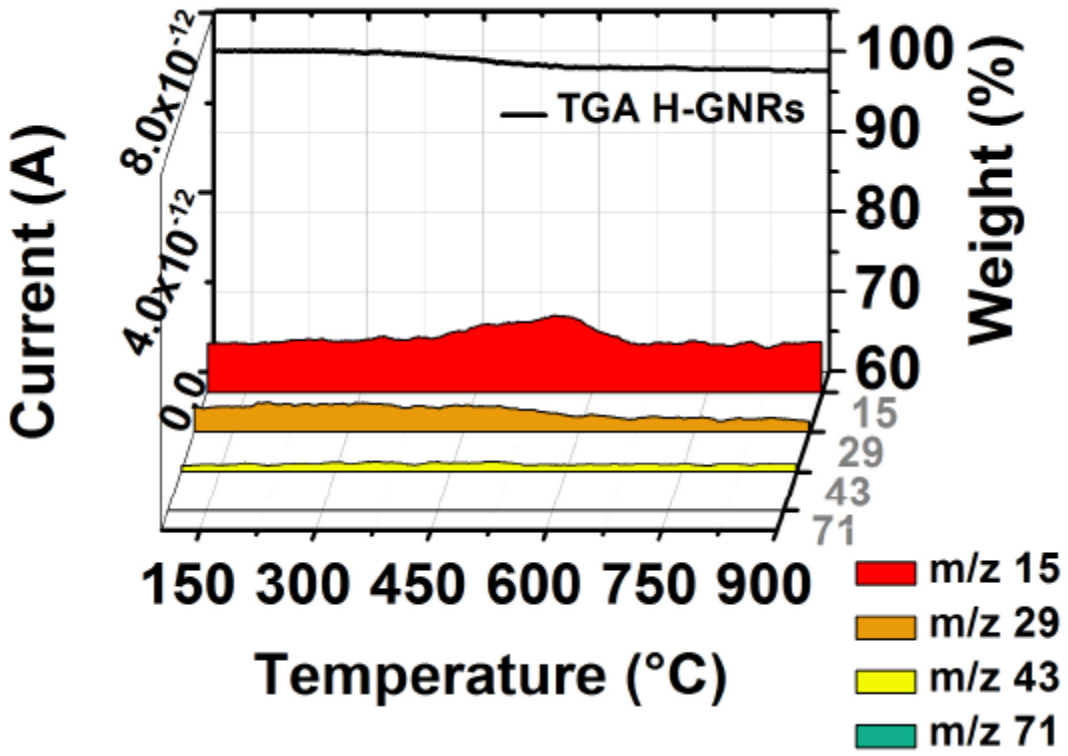

Figure E7. Evolved gas analysis for hydrogen terminated GNRs (H-GNRs). The colors represent fragments with m/z 15 (red), 29 (orange), 43 (yellow) and 71 (cyan) that correspond to alkane fragments. The black curve represents the TGA profile of the H-GNRs.

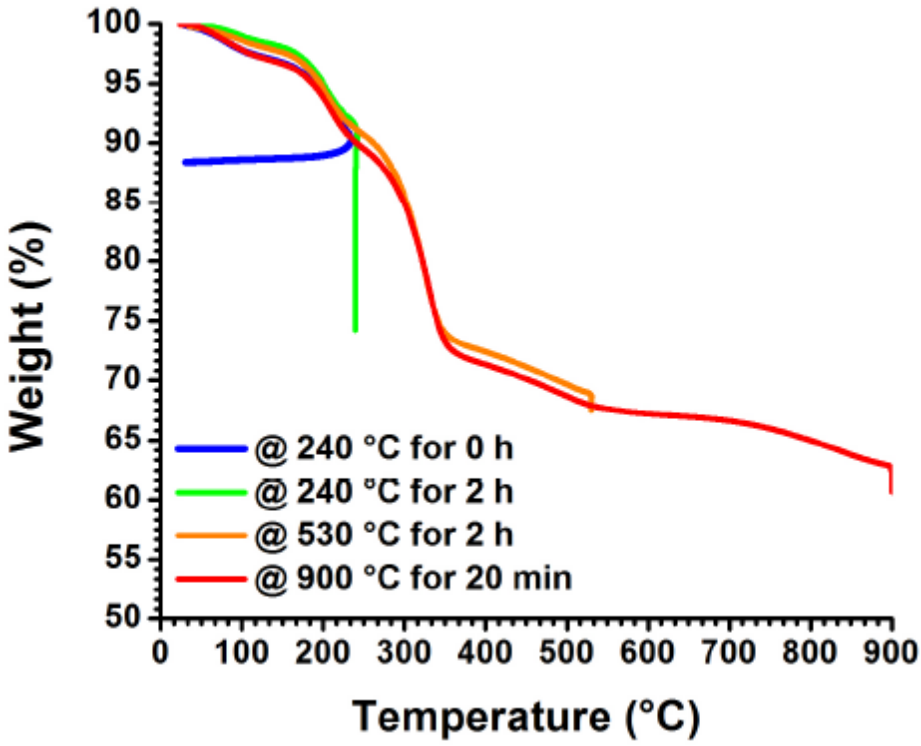

Figure E8. TGA plots of thermally treated HD-GNRs. The curves represent the weight loss of HD-GNRs thermally treated at different temperatures. Blue curve: the HD-GNRs were heated to 240 °C and then cooled to rt without holding at 240 °C; the product was partially deintercalated. Green curve: the HD-GNRs were heated at 240 °C for 2 h; the product was fully deintercalated. Orange curve: the HD-GNRs were heated at 530 °C for 2 h; the product was fully deintercalated and partially defunctionalized. Red curve: the HD-GNRs were heated at 900 °C for 20 min; the product was fully deintercalated and completely defunctionalized.

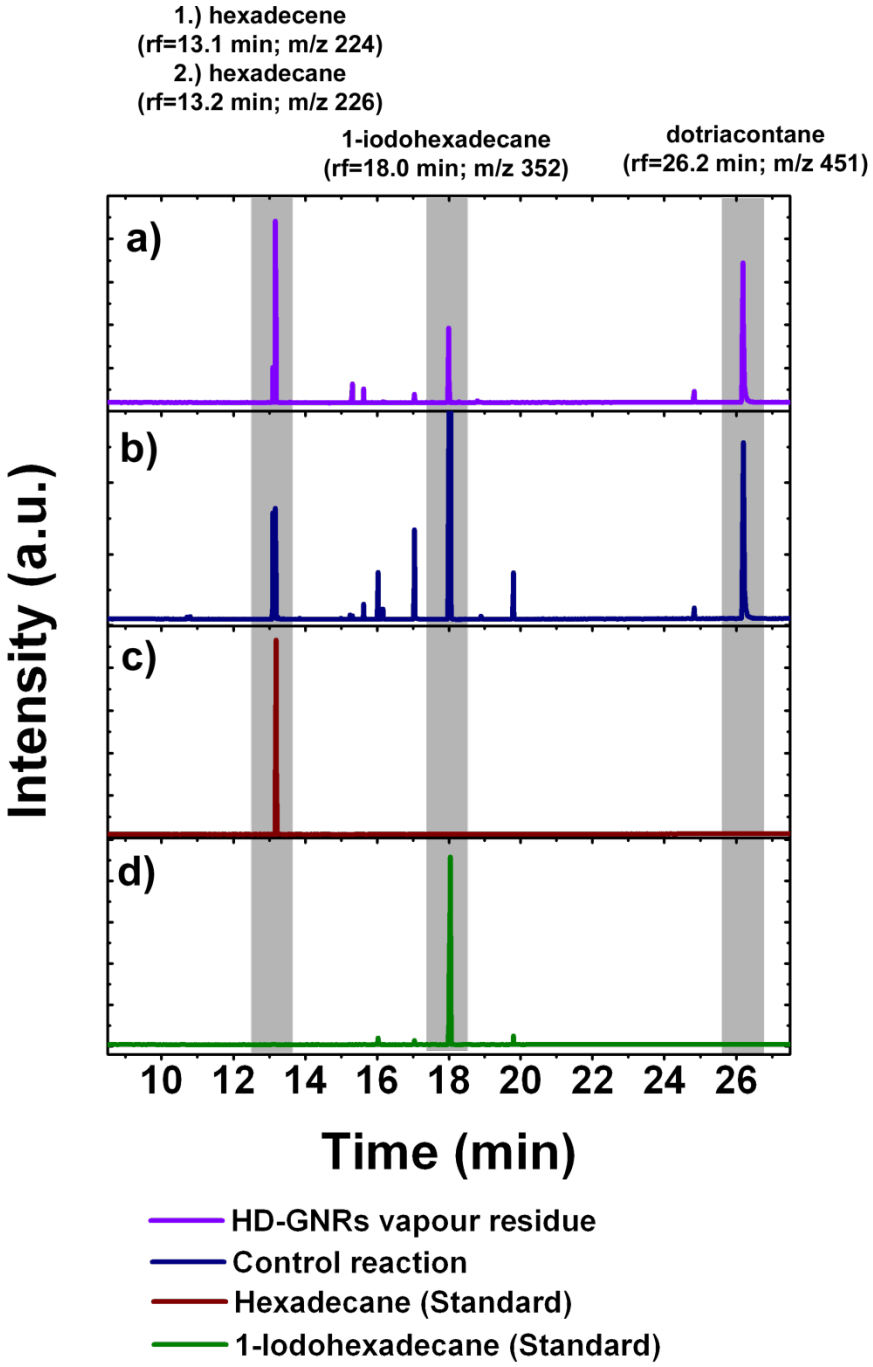

Figure E9. GC MS of control experiments for qualitative and quantitative intercalant determination. a) GC plot (purple curve) of trapped (at 0 °C) condensate from HD-GNRs heated at 150 °C in high vacuum for 1 h. The concentration of the condensate contents

was as follows: 45.1% dotriacontane, 35.1% hexadecane, 13.4% 1-iodohexadecane, and 6.4% hexadecene. Other minor components were disregarded. b) GC plot (navy blue) of control reaction (for a detailed description of the control reaction see following). The concentration of products was as follows: 59.6% dotriacontane, 20.8% hexadecene, and 19.6% hexadecane. The excess of 1-iodohexadecane (the major component) and other minor components were disregarded in calculating the percentages. c) GC plot (wine red) of hexadecane standard and d) GC plot (green) of 1-iodohexadecane standard.

Control reaction of 1-iodohexadecane with Na/K in the absence of MWCNTs

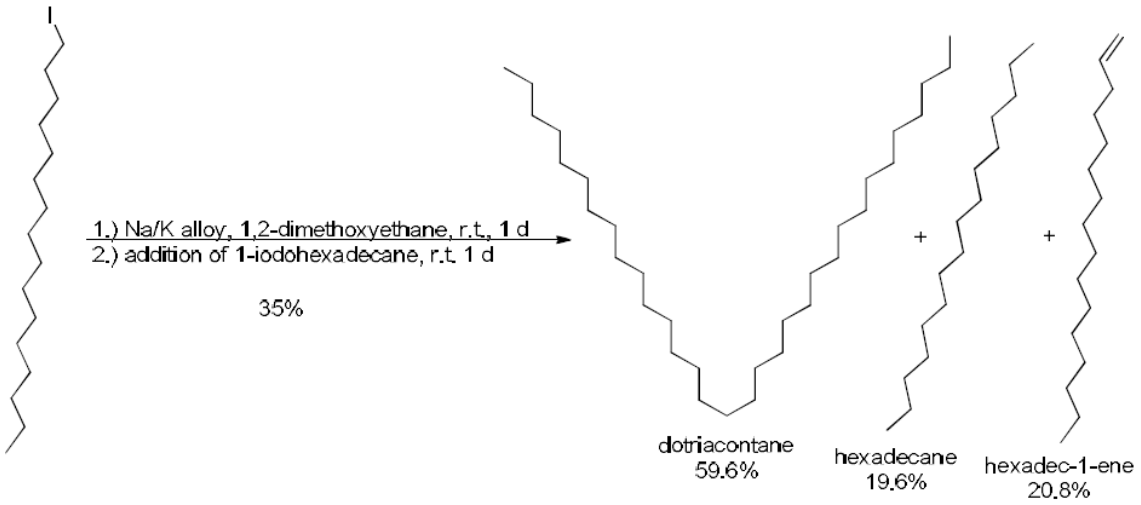

The oven-dried 5 mL RB flask containing a magnetic stir bar were transferred to a N2 glove box where freshly distilled 1,2-dimethoxyethane (DME, 40 mL) and liquid Na/K alloy (0.057 mL, 1.29 mmol) were added. The flask containing the suspension was then sealed with septa and transferred out of the glove box where the suspension was dispersed by a 5 min ultrasonication to yield a blue suspension. After ultrasonication, the reaction mixture was vigorously stirred (450 RPM) at room temperature for 1. The reaction suspension was then quenched by the addition of the 1-iodohexadecane (1 mL,

2.56 mmol) and left to stir at the room temperature for an additional d. The reaction mixture was then diluted with CH2Cl2 and GC-MS analysis was performed.

Control reaction with hexadecane and MWCNTs

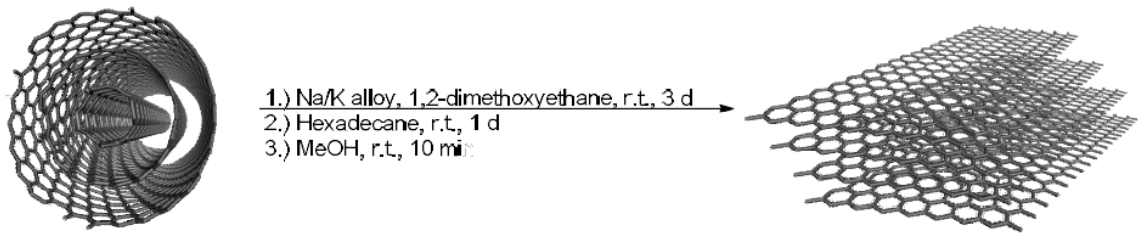

To an oven-dried 100 mL round-bottom flask and a magnetic stir bar were added the multi-walled carbon nanotubes (MWCNTs) (100 mg; 8.33mmol). The vessel was then transferred to a N_2 glove box where freshly distilled 1,2-dimethoxyethane (26 mL) and liquid Na/K alloy (0.13 mL; 3 mmol) were added. The flask containing the suspension was then sealed with septa and transferred out of the glove box where the suspension was dispersed by a short 5 min ultrasonication to yield a dark greenish to red suspension. After ultrasonication, the reaction mixture was vigorously stirred (450 RPM) at room temperature for 3 d. To the reaction suspension hexadecane (0.6 mL; 3.34 mmol) was then added using a syringe and let to stir at the room temperature for an additional day. Reaction mixture was then quenched by addition of MeOH (21 mL) and let to stir at room temperature for 10 min. For workup, the reaction mixture was filtered over a PTFE membrane with a 0.45 µm pore size. The remaining solid was successively washed with THF (100 mL), *i*-PrOH (100 mL), H_2O (100 mL), *i*-PrOH (20 mL), THF (20 mL), Et_2O (10 mL) and dried under a high vacuo.

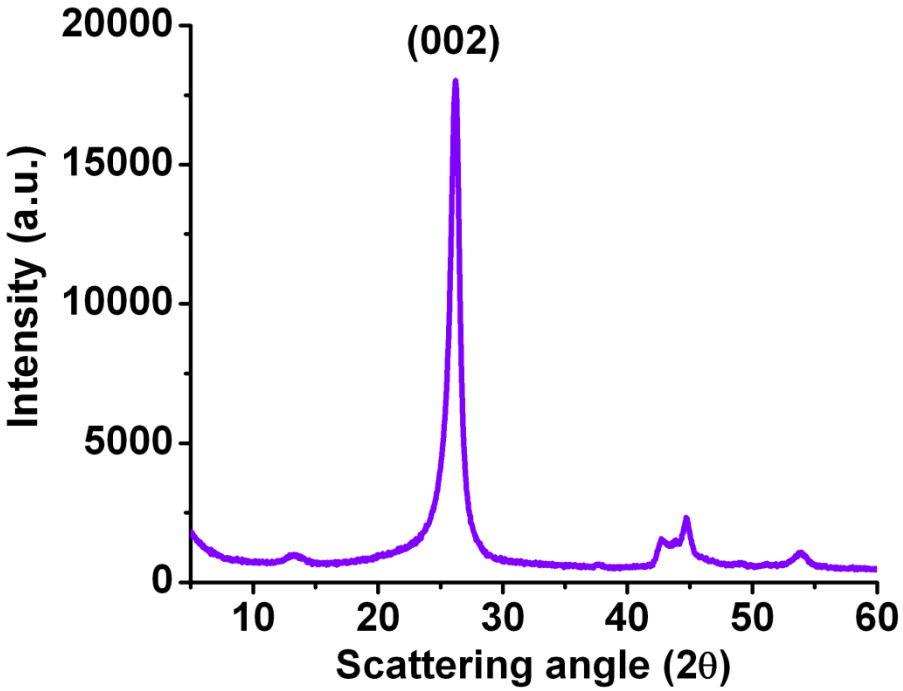

Figure E10. XRD spectrum of the product of the control reaction with hexadecane that displays a well-pronounced diffraction line at 26.2° 2θ angle. This diffraction line corresponds to the (002) signal and is similar to the spectra of N-GNRs or MWCNTs, which means that intercalation does not occur when hexadecane is used instead of 1-iodohexadecane.

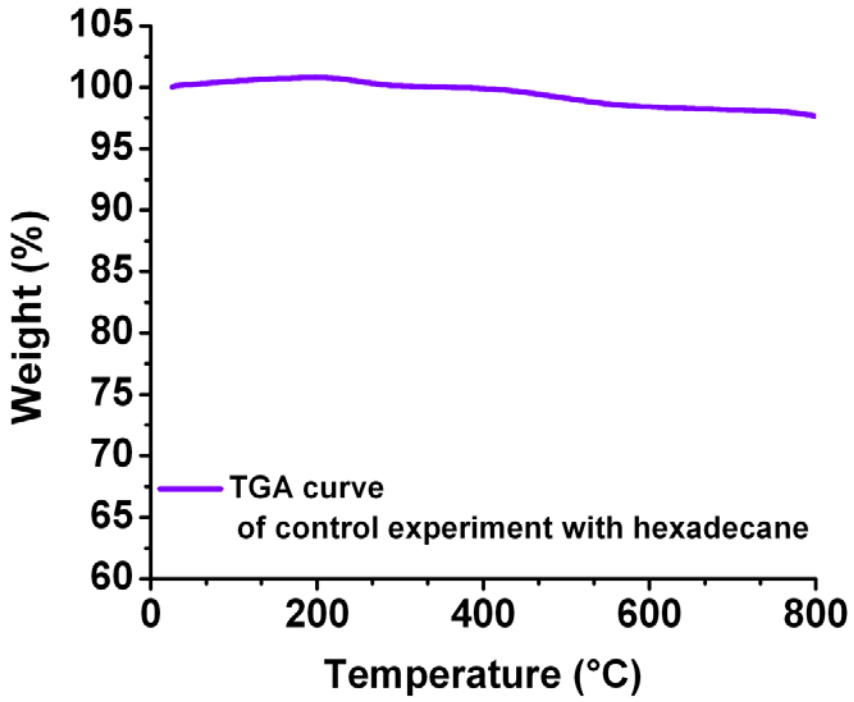

Figure E11. TGA curve of the product of control reaction with hexadecane.

Appendix F

The appendix corresponds to the supporting information of Chapter 6

Table of Contents

SI Synthesis of PF-GNRs through vapor-phase intercalation

Details of potassium intercalation of MWCNTs can be found in our previous work.[1] The sealed reaction vessel loaded with potassium intercalated MWCNTs was opened in a glove box and the intercalated tubes were transferred into a 50-ml round-bottom flask, followed by dropwise addition of 20 mL styrene monomer. The reaction mixture was taken out from the glove box and kept at room temperature for 24 hours and then heated to 60 ºC overnight for completing the polymerization. The polystyrene/PF-GNRs mixture was dissolved in chloroform, and precipitated by ethanol. After filtration, grey plastic chunks were cut into small pieces and extracted by chloroform with a Soxhlet extractor for one week. Finally, the black solid was collected on a PTFE membrane (0.45 μm), washed with THF (3 x 100 mL), ethanol (3 × 100 mL), DI water (3 × 100 mL), and acetone (50 mL), ether (50 mL), and dried in vacuum oven at 60 ºC overnight. (Alternatively, PF-GNRs can be prepared in a one-pot synthesis: heating the MWCNTs

and potassium chunks in a tightly capped Schlenk flask at 350 ºC for 24 h followed by dropwise addition of styrene or isoprene through the stopcock under nitrogen at room temperature.)

SII Additional SEM and TEM images

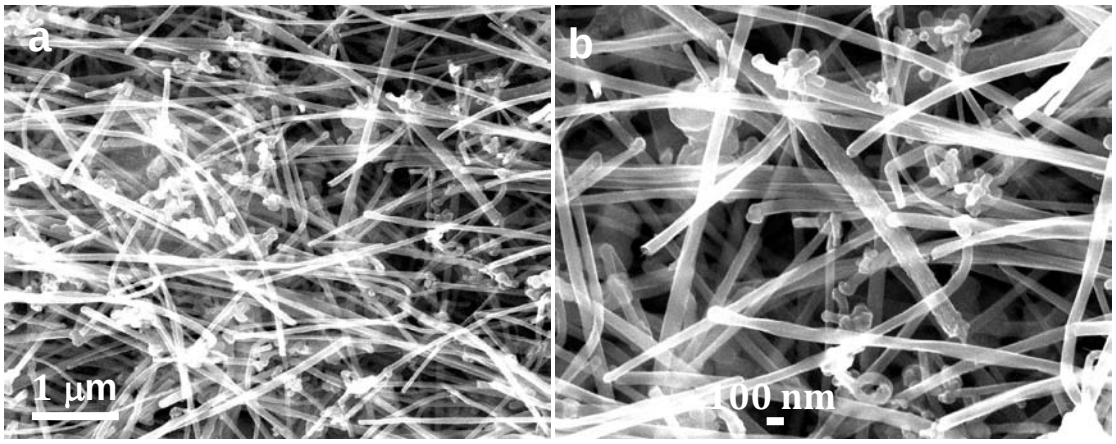

Figure F1. SEM image of Mitsui MWCNTs: (a) low-magnification and (b) high-magnification. The spherical nanoparticles are amorphous carbon. According to previous work,[2,3] thermal annealing at 2800 ºC under argon atmosphere improved not only the structural integrity of those carbon nanotubes but also removed polyaromatic hydrocabons as well as a significant amount of iron nanoparticles. The mean diameter of those tubes is 81 ± 5 nm and the mean length is 8.19 ± 1.7 μm. The detailed information about preparation and characterizations of Mitsui MWCNTs can be found in previous work.[2, 3]

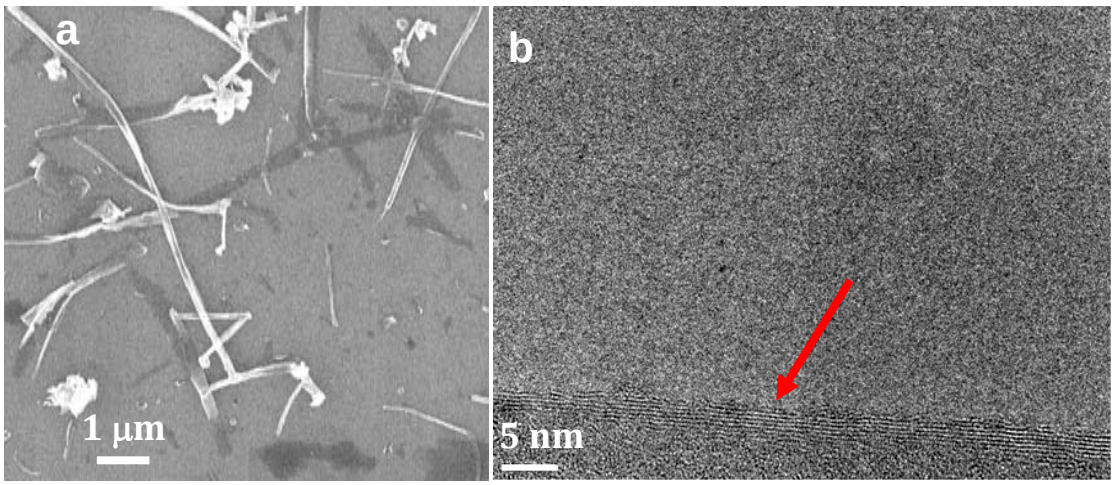

Figure F2. (a) Overview of a large area showing the conversion of MWCNTs to GNRs through liquid-phase intercalation of Mitsui MWCNTs followed by addition of styrene. (b) TEM image of the edge structure of 6-layer GNRs.

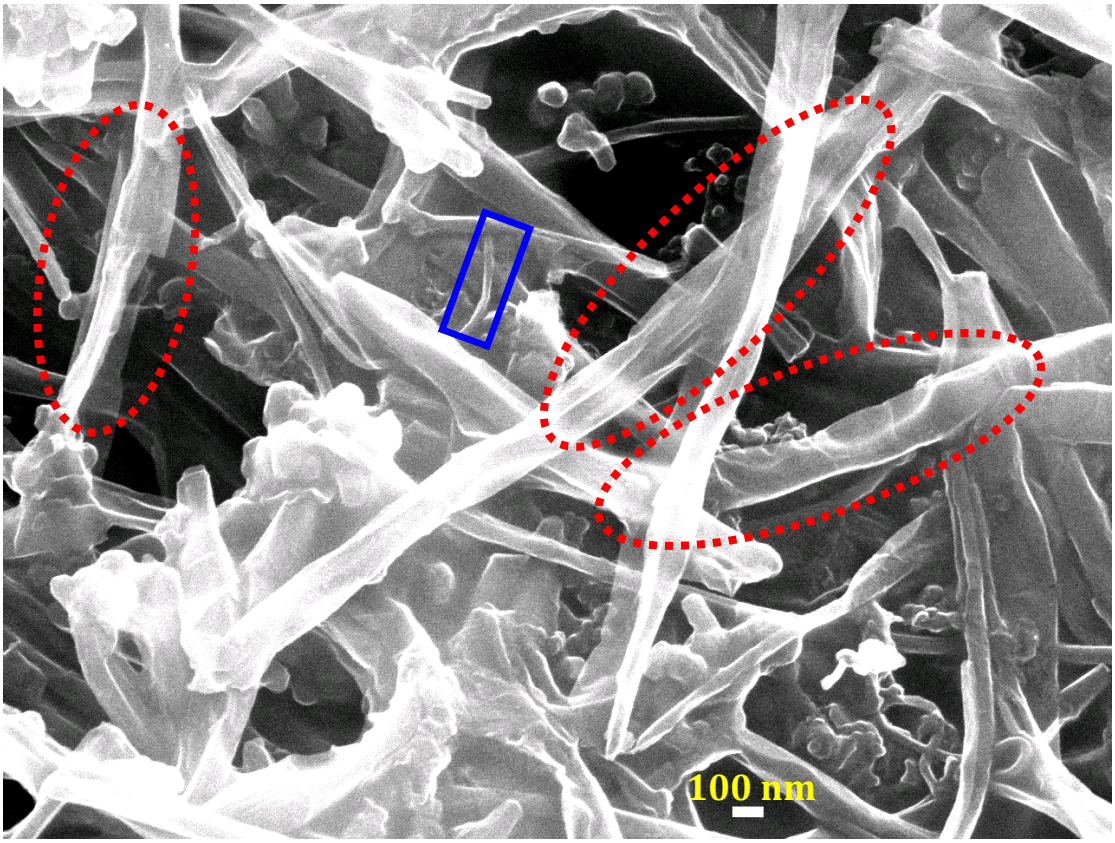

Figure F3. SEM image of Mitsui MWCNTs treated with potassium naphthalenide followed by addition of isoprene. The ribbon-like structure can be easily identified. Since the sample was imaged before extraction with chloroform, we can still see the amorphous polymer domains as well as spherical amorphous carbon.

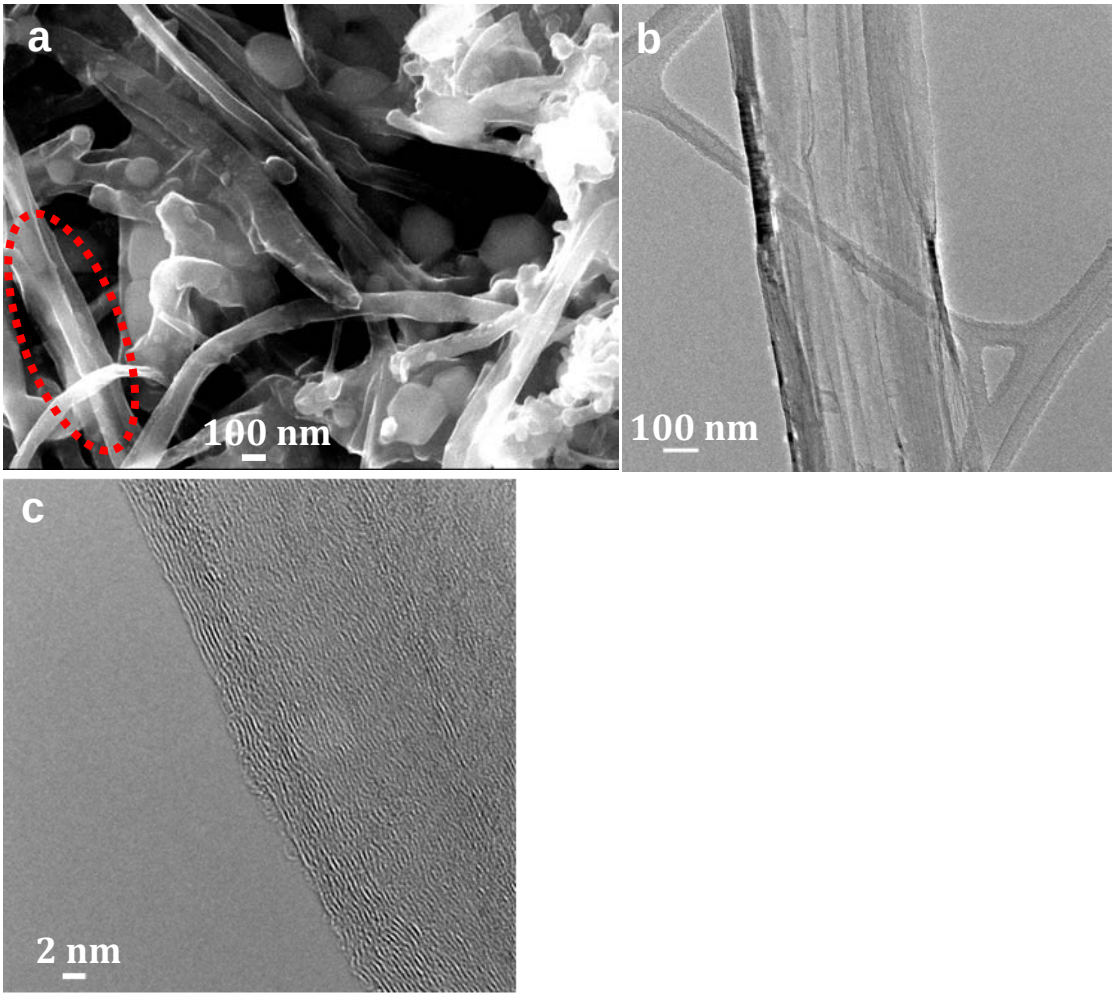

Figure F4. SEM and TEM images of treated Mitsui MWCNTs. (a) SEM image of Mitsui MWCNTs treated with potassium vapor followed by addition of isoprene. Most MWCNTs are split but they are not fully exfoliated to form GNRs. The ribbon-like structure and split MWCNTs bridged by polymer domains can be observed. Highlighted here is a partially exfoliated tube sitting on top of GNR derived from polymerization-

assisted exfoliation. (b) TEM image of an isolated PF-GNR sitting on top of a lacy carbon grid. (c) TEM image of the edge structure of multi-stack PF-GNRs.

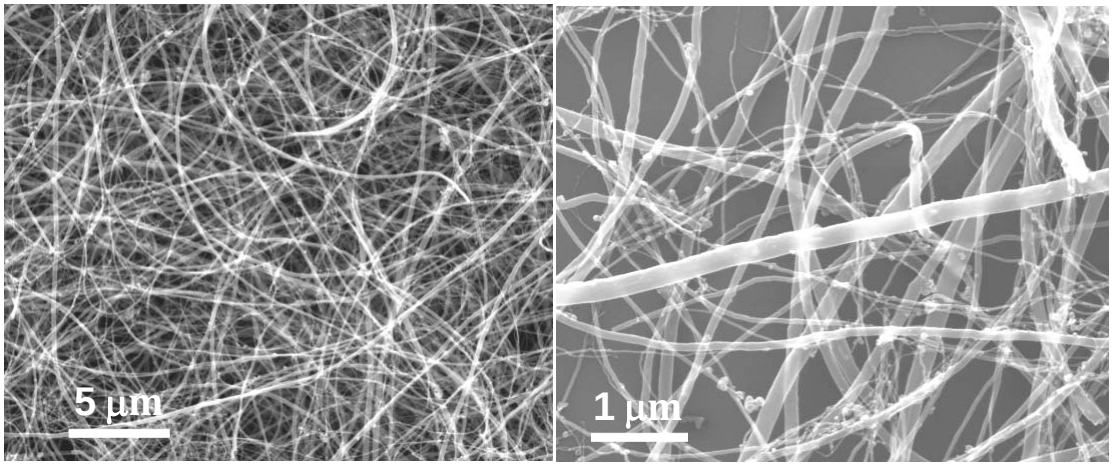

Figure F5. SEM image of NTL MWCNTs: (a) low-magnification and (b) high-magnification.

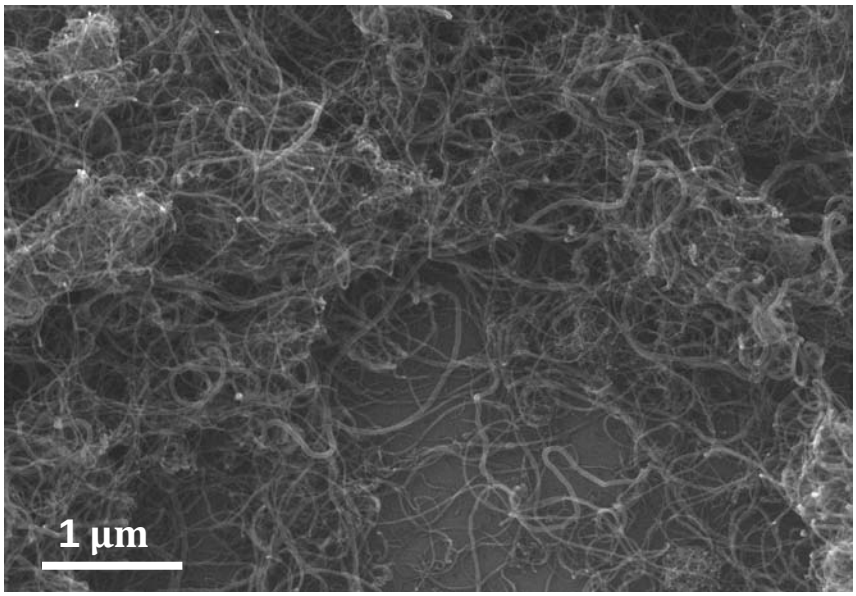

Figure F6. SEM image of pristine Baytubes that are highly defective.

SIII Calculation of carbon atoms that are functionalized with polymer

The calculation is based on the assumption that all of the edge carbons of a 3 µm × 150 nm ribbon were functionalized. The amount of polymer that was chemically attached to the GNRs is corresponding to the weight loss between 384 and 474 ºC.

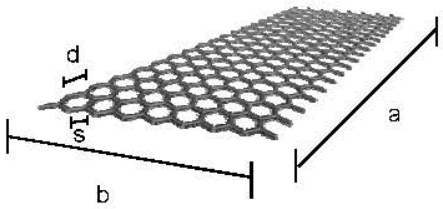

F = Functional Group
C = Carbon
$n_{C(edges)} = n_{F(edges)}$

	value	unit
a	3000	nm
b	150	nm
d	0.246	nm
s	0.142	nm
$M_{(C)}$	12	g/mol
$M_{(F)}$	104.15	g/mol
Weight loss % obtained by TGA (between 384 °C and 474 °C)	6	%

	value	unit
$N_{C(all)}$	29,744,200	#atoms
$n_{C(all)}$	4.94E-17	mol
$m_{C(all)}$	5.93E-16	g

	value	unit
$N_{C(edges)}$	25,610	#atoms
$n_{C(edges)}$	4.25E-20	mol
$m_{C(edges)}$	5.10E-19	g

atomic % of the edges	0.09

	value	unit
$n_{F(TGA)}$	0.057609217	mol
$n_{C(all\ TGA)}$	7.833333333	g

	value	unit
Average length of the polymer chain on the edges	9	monomer units

Ratio of $n_{C(all\ TGA)}$: $n_{F(TGA)}$	136 :1

Ratio of $n_{C(all)}$: $n_{c(edges)}$	1161 :1

Based on the calculation, the average polymer chain length was only 9 units for a 3 μm × 150 nm ribbon.

References

1. Kosynkin, D. V.; Lu, W.; Sinitskii, A.; Pera, G.; Sun, Z.; Tour, J. M. Highly Conductive Graphene Nanoribbons by Longitudinal Splitting of Carbon Nanotubes Using Potassium Vapor *ACS Nano* **2011**, *5*, 968-974.

2. Chen, J.; Shan, J. Y.; Tsukada, T.; Munekane, F.; Kuno A.; Matsuo, M.; Hayashi, T.; Kim, Y. A.; Endo, M. The Structural Evolution of Thin Multi-walled Carbon Nanotubes during Isothermal Annealing *Carbon* **2007**, *45*, 274-280.

3. Pacurari, M.; Yin, X. J.; Ding, M.; Leonard, S. S.; Schwegler-Berry, D.; Ducatman, B. S.; Chirila, M.; Endo, M.; Castranova, V.; Vallyathan, V. Oxidative and Molecular Interactions of Multi-wall Carbon Nanotubes (MWCNT) in Normal and Malignant Human Mesothelial Cells *Nanotoxicology* **2008**, *2*, 155-170.